# Liens entre structure interne et variations d'intensité des cyclones tropicaux : apports combinés des observations SAR et des simulations numériques à haute résolution

Léo Vinour

## To cite this version:

Léo Vinour. Liens entre structure interne et variations d'intensité des cyclones tropicaux : apports combinés des observations SAR et des simulations numériques à haute résolution. Sciences de la Terre. Université de Bretagne occidentale - Brest, 2021. Français. NNT : 2021BRES0060 . tel-03560801

HAL Id: tel-03560801
https://theses.hal.science/tel-03560801v1
Submitted on 7 Feb 2022

# THÈSE DE DOCTORAT DE

L'UNIVERSITÉ DE BRETAGNE OCCIDENTALE

ÉCOLE DOCTORALE N° 598
*Sciences de la Mer et du Littoral*
Spécialité : *Océanographie Physique et Environnement*

Par
**Léo VINOUR**

# Tropical cyclones internal structure and intensity variations : insights from high-resolution observations and modeling

**Thèse présentée et soutenue à Brest, le 13 Juillet 2021**
**Unité de recherche : IFREMER, Univ. Brest, CNRS, IRD, Laboratoire d'Océanographie Physique et Spatiale, IUEM, Plouzané, France**

## Rapporteurs avant soutenance :

| | |
|---|---|
| Michael MONTGOMERY | Professor, Dpt. of Meteorology, Naval Postgraduate School (USA) |
| Svetla HRISTOVA-VELEVA | Doctor, Radar Science and Engineering Section, Jet Propulsion Laboratory (USA) |

## Composition du Jury :

| | | |
|---|---|---|
| Président : | Xavier CARTON | Professor, UBO, LOPS |
| Examinateurs : | Michael MONTGOMERY | Professor, NPS (USA) |
| | Svetla HRISTOVA-VELEVA | Researcher, JPL (USA) |
| | Caroline MULLER | Research Director, CNRS, ENS, LMD |
| | Patrick MARCHESIELLO | Research Director, IRD, LEGOS |
| Dir. de thèse : | Claude ROY | Research Director, IRD (Emeritus) |
| Co-dir. de thèse : | Swen JULLIEN | Researcher, IFREMER, LOPS |
| | Alexis MOUCHE | Researcher, IFREMER, LOPS |

# ACKNOWLEDGEMENT

Mes remerciements et encouragements les plus chaleureux à tous les futurs thésards, stagiaires, docteurs, chercheurs et autres petites et grandes mains du monde scientifique qui auront le courage, n'ayons pas peur des mots, de se plonger dans ce manuscrit de thèse. Petite pensée émue, aussi, pour tous les francophones difficilement bilingues qui n'auront à se mettre sous la dent que ce paragraphe de remerciements et le petit résumé situé juste après le sommaire... Ainsi que de très belles images bien sûr.

Tel une miss France ou un acteur aux Oscar, je me dois maintenant de remercier toutes les personnes qui ont contribué à mener cette thèse à son terme. Et quand je dis "je me dois", je ne sous-entends bien sûr aucunement qu'il s'agisse d'une obligation académique: je pourrais très bien écrire sobrement "merci à tous" et passer à la page suivante. Mais non, non, j'y tiens. Cette thèse je ne l'ai pas faite tout seul, loin de là. Chaque jour au boulot, des fois (souvent ?) autour d'un verre, en vacances, au téléphone, en weekend... Le thésard est un écosystème précaire qui demande une attention de chaque instant.

Pour rester dans le thème, essayons de dessiner un cyclone. L'oeil d'abord: Papa, Maman, Anto, Sim, Tim. Le centre du vortex. Des vents plus calmes bien sûr, parce qu'on se voit de moins en moins et qu'on se disperse dans l'hexagone, mais malgré tout la partie essentielle, sans quoi le cyclone n'est qu'une vulgaire dépression, un coup de vent. Mettons-y aussi tout le reste de la famille: grands-parents, cousin.e.s, oncles et tantes, toute la famille dans l'oeil du cyclone bien à l'abri. Ne dit-on pas que l'oeil est le reflet de l'âme ? Ou quelque chose comme ça...

Rentrons dans le dur: le mur de l'oeil. Bien sûr, Swen et Alexis. Je ne saurais même pas faire la liste de tous les services que vous m'avez rendu, des fois où je vous ai fait faire des nuits blanches à corriger, relire, reprendre des résultats ou des phrases trop longues (serais-je en train de récidiver ? totalement); de toutes les réunions (en vrai ou en zoom), de toutes les fois où vous m'avez aidé, repêché, rattrapé, remotivé, inspiré, rectifié, calmé, encouragé, soutenu. Si il y a bien une chose que je considère comme idéale concernant cette thèse, c'est votre encadrement (et vous savez comme je peux être négatif, donc ce n'est pas rien !). Le mur de l'oeil vous va bien: vous avez été la colonne vertébrale de ces 4 années, et vous avez permis de générer les ondes de Rossby (il fallait bien que je le place) nécessaires à restaurer l'intensité du système après chaque coup de cisaillement. J'espère qu'on continuera à travailler ensemble par la suite ! A vrai dire je n'en doute pas. Alexis, j'attends avec impatience le retour des beaux jours pour le fameux barbecue face à la mer, et je sais que les images SAR continueront à rythmer ma carrière après ce qu'on a commencé. Swen, tu es venue me sortir de mon école d'ingé qui me promettait au monde (pas du tout) merveilleux du management d'entreprise pour m'envoyer à Nouméa: je te dois une sacrée fière chandelle, et j'espère qu'on se retrouvera un jour là-bas pour une petite session plongée ou kite (même si je suis plus planche à voile) entre deux séances de débugging intensif de WRF.

La bande de pluie interne maintenant: la plus proche du centre, à Brest-même. Marine, que de soirées n'est-ce pas ? 54 (Big up à Jérôme, Cricri et Maxou, et à bientôt hein), séries, festoches, discussions, tu m'as apporté tout le loisir nécessaire au soutien psychologique d'un thésard en pleine galère. Merci (très merci) pour tout ça. Gwenn, heureusement que tu fus là pour stimuler ce qu'il me restait de cerveau après une journée de travail en parlant politique. C'est important et ça change les idées, ça joint l'utile à l'agréable en somme. Merci aussi aux groovers: Manuel, Paul, Aurélien, Anto (et Alex en guest star). Cuban, Julien, Sébastien et VLM pour les quelques concerts sous la pluie (mais pas toujours). La musique c'est bon pour la santé. Et merci aux collègues et amis du labo pour les discussions, barbecues, bières, rigolades, pauses café: Clément, Victor, Huimin, Alex, Sophia, Gwendal, Luc, Marie, Hugo, Lisa, Yuan, Diane. Merci à Clément mon co-bureau et à Bertrand pour les discussions (scientifiques et parfois plus !).

Les bandes de pluie externes enfin, sans lesquelles le cyclone perd toute sa classe: Sylvain, Baptiste, P-M, Rauty (le noyau dur ça bouge pas), Lorraine (et Captain), Quentin, Benjam, Nathan (la team Sea Fairey), Elliot (tout a commencé en BE), Alex, Pedro (ces gens sont des monstres), Yves, Betti, Laeti, Mégane, Laure, Valentine et Andréas (Kanaky forevah), Cédric, Guilhem (à quand la Corse ?), Glwadys (vive le café de la Paix), Rémy et Amel, Aurel, Vaness, Jean et Anaëlle (et les oeufs à la coque), Matthis et Chabert (fellow colleagues).

Merci à tou.te.s les inconnu.e.s du quotidien, caissières ou caissiers, femmes de ménage, soignant.e.s, livreur.se.s et tant d'autres, que j'ai croisé.e.s au bureau ou à côté parfois sans même les saluer mais qui permettent grâce à leur travail le bon fonctionnement de la recherche scientifique, et de la société en général.

Merci à mon directeur Claude Roy de m'avoir apporté son soutien et son aide à chaque fois que ce fut nécessaire. Merci à Fanny Ardhuin pour son accompagnement et son soutien ainsi qu'au bureau de l'Ecole Doctorale des Sciences de la Mer et du Littoral pour leur travail et leur aide.

Un grand merci, enfin, aux membres de mon jury de thèse pour leur participatiuon à ma soutenance et l'intérêt qu'ils ont porté à mon travail: Xavier Carton, Michael Montgomery, Svetla Hristova, Caroline Muller et Patrick Marchesiello. Special thanks to Michael Montgomery for his insightful comments and corrections on my manuscript.

J'ai sans doute oublié des gens, la dynamique interne des cyclones est un sujet complexe... A ceux-là toutes mes excuses ! Et une très bonne lecture à tous les anglophones.

*"C'est comme un ouragan qui reste intact même sous le vent*
*C'est comme un papillon qui s'envole au ciel gracieusement".*

AYA NAKAMURA, *Sentiment Grandissant*

# TABLE OF CONTENTS

# RÉSUMÉ

Les cyclones tropicaux sont des événements atmosphériques extrêmes, qui coûtent chaque année des milliers de vies dans le monde en raison de leurs vents violents et des inondations et marées de tempête qu'ils provoquent. Ils sont donc une préoccupation majeure pour les scientifiques et les météorologues. Bien que fortement influencés par leur environnement au cours de leur cycle de vie, c'est la dynamique interne des cyclones qui régit leurs variations d'intensité. Dans sa phase mature (soit une fois le cyclone formé et avant son déclin), l'évolution du coeur du cyclone est en effet caractérisée par une circulation symétrique à laquelle se superposent de nombreux processus asymétriques tels que des ondes internes discrètes (appelées ondes de Rossby de Vortex) ou des perturbations locales de la circulation et de la convection telles que des mésovortex dans le mur de l'oeil ou des anomalies convectives dans la zone de vents maximum. Ces processus asymétriques, en particulier, sont étroitement liés aux variations d'intensité: ils traduisent la réponse interne du vortex aux perturbations externes. En permettant ou non la dissipation de l'énergie des perturbations par le cyclone, ils régissent sa capacité à "survivre" à ces dernières. Les variations de la structure interne sont cependant difficile à observer: elles sont en effet sporadiques, multi-échelle, et se produisent dans des zones où les vents et leurs variations spatiales sont d'une amplitude extrême. La compréhension des variations d'intensité des cyclones est donc un défi considérable au vu des technologies d'observation actuelles.

Cette thèse est centrée sur l'étude des liens entre la structure interne des cyclones et leurs variations d'intensité, dans le but d'améliorer la caractérisation de la dynamique interne et la prévisibilité du cycle de vie des cyclones. Elle repose sur l'analyse statistique d'une base de données conjointe d'observations et de simulations, composée de nouvelles mesures de vent de surface à haute résolution extraites d'images SAR (Synthetic Aperture Radar), et de simulations numériques régionales réalistes. Le travail effectué s'articule autour des questions suivantes:

— Comment les observations SAR de vents de surface permettent-elles de mesurer la dynamique interne des cyclones ?

— Ces mesures de la structure interne permettent-elles d'améliorer la caractérisation

et la prévisibilité du cycle de vie des cyclones ?
- Dans quelle mesure le modèle permet-il de compléter les observations SAR et quelle stratégie peut-on dès lors mettre en place pour améliorer le diagnostic de la dynamique interne des cyclones ?

Le travail de cette thèse a consisté dans un premier temps à mettre en place un environnement de calcul permettant de traiter identiquement les images SAR et les sorties de simulation. La procédure conçue permet d'extraire des paramètres caractérisant la variabilité radiale et azimutale du champ de vent de surface autour du centre du cyclone. Le cyclone est ainsi décrit à travers un ensemble de paramètres tels que les gradients du profil moyen dans le mur de l'oeil (entre le centre et le rayon de vent maximum) et dans la zone de vents forts (entre une et trois fois le rayon de vent maximum), ainsi que les variances et les décompositions spectrales des distributions azimutales de forme de l'oeil, gradient de vent dans le mur de l'oeil, ou vent maximum. Ces paramètres ont été définis pour être reliés à la théorie des processus de restauration de l'intensité tels que la propagation des ondes de Rossby de vortex, le mélange de vorticité entre l'oeil et le mur de l'oeil via la formation de mésovortex (qui impactent tous la variabilité azimuthale du champ de vent), ou la résilience du vortex au cisaillement externe (liée à la distribution radiale de vorticité et donc au profil de vent moyen).

Les propriétés extraites des champs de vent ont ensuite été reliées à l'intensité et au cycle de vie du cyclone, à travers les images SAR dans un premier temps. Cette analyse a permis d'observer des propriétés dynamiques telles que la contraction de la zone de vent fort, le raidissement du profil radial et la symétrisation avec l'intensité. La prédominance de nombres d'ondes élevés dans le mur de l'oeil et la couronne de vent maximum est tendanciellement plus marquée durant les phases de réintensification, ce qui est cohérent avec la littérature sur les phénomènes de restauration d'intensité via formation de mésovortex et propagation de VRWs discrètes.

Des simulations réalistes WRF à résolution kilométrique ont ensuite été utilisées pour compléter l'analyse statistique du SAR. Reproduisant les analyses effectuées sur les champs de vent de surface SAR, les simulations fournissent une continuité temporelle qui permet d'ajouter à l'analyse des variables dépendant du temps (i.e. dérivées temporelles de paramètres structurels internes), ce qui rend la mise en relation entre la structure interne et le cycle de vie plus simple et plus directe. L'anneau de vent maximum et la zone de mélange entre l'oeil et le mur de l'oeil apparaissent au travers de ces analyses temporelles comme étant reliées aux variations d'intensité à différents échelles. À courte échelle de temps (5-10 heures), les augmentations d'intensité et de taux d'intensification sont de préférence associées à un élargissement du spectre des signaux azimutaux (c'est-à-dire une homogénéisation/symétrisation azimutale du vortex), tandis que les phases de déclin et de baisse d'intensification vont de pair avec un rétrécissement du spectre vers de petits nombres d'ondes (c'est-à-dire une hétérogénéisation/asymétrisation du vortex). En comparaison, la structure radiale apparaît plus liée à l'état moyen du vortex qu'aux variations locales et de petite échelle : elle décrit la résilience du vortex au cisaillement externe et le mélange entre l'oeil et le mur de l'oeil à un instant donné, mais a une réponse plus faible aux variations d'intensité.

Une méthode de machine learning a aussi été mise en place pour mesurer l'apport des paramètres extraits de la structure interne (aussi bien du SAR que du modèle) et de la petite échelle pour la prédictabilité des changements d'intensité. L'amélioration des scores de prédiction avec l'ajout des paramètres internes (par rapport à une prédiction basée uniquement sur des paramètres de plus grande échelle tels que l'intensité ou le RMW) est constatée en particulier avec les paramètres d'asymétrie issus de la couronne de vent fort, mettant en évidence l'importance des processus asymétriques dans la dynamique cyclonique. L'ajout des paramètres temporels extraits du modèle permet aussi une amélioration des scores par rapport aux paramètres instantanés tels qu'extraits du SAR: la variation temporelle de la structure interne, notamment à travers la définition de transferts spectraux décrivant l'évolution de l'asymétrie de petite échelle, est donc pertinente pour la prévision des changements d'intensité.

A travers l'analyse statistique conjointe des images satellite SAR et des sorties de modèles dynamiques réalistes, cette thèse permet donc de mettre en évidence l'importance d'un diagnostic de la structure interne des cyclones pour la compréhension et la prévision de leurs changements d'intensité. En accord avec de nombreuses études récentes attribuant ces changements à des phénomènes de cascades d'énergie à l'intérieur du cyclone, ce travail démontre la capacité des mesures de vents de surface à diagnostiquer des processus énergétiques internes au vortex, et par extension à diagnostiquer son état à l'instant de la mesure et son évolution future. L'apport du modèle en termes de continuité temporelle met par ailleurs en valeur la nécessité d'augmenter la fréquence des observations haute résolution de surface telles que le SAR, pour la météo comme pour une meilleure compréhension de ces processus internes.

CHAPTER 1

# INTRODUCTION

## 1.1 General introduction

Take a deep breath, look into my eye (Fig. 1.1)...
Picture yourself lying quietly on a white sandy beach in Miami, Cuba, Taiwan, or Noumea, sipping a citrus cocktail, a light breeze in your hair... You've been in the sun for hours now, working on your tan. Little by little, you feel the air is getting heavier. The sky is clouding over, and waves start pounding the sand. The breeze is getting more insistent every minute. In the distance, an alarm siren is blaring. You think to yourself that it might be time to go home... And you are right !
Congratulations: you've just met a tropical cyclone (in your mind, of course). You're probably thinking to yourself that it wasn't that bad, after all. And yet, in a few hours on this beach, houses may be destroyed or flooded, roofs blown up, and trees torn down. Tropical cyclones cost the lives of 1,386 people across the planet in 2020, and caused more than $71 billions of material casualties.

Playing the role of relief valves of the tropical ocean, these extreme convective atmospheric phenomena generate an energy equivalent to half the consumption of all the power stations built by us, little humans ($10^{14}$ Watts). They measure on average 1000 km in diameter, and extend across the entire troposphere (about 15 km high).

Due to the damage they cause every year, TCs are major concerns of the weather and climate forecast, and scientific communities. The complex processes involved in their formation and evolution are also an exciting field of research. Huge progress in their understanding and forecast has been made throughout the 20th century. Forecasters "beat the hurricane" for the first time in 1928, thanks to the awareness of two ship captains, and the knowledge and expertise of Charles L. Mitchell (Shepherd, 1928). The first airplane flight over a TC was performed in 1943 (Sumner, 1943), and the first studies of TC energetics and dynamics date back to 1950 and 1951, with the works of Herbert Riehl

Figure 1.1 – Hurricane Florence (2018) has a beautiful eye, but you don't want to drown in it. Source: NASA

(Riehl, 1950), who acknowledged the role of the ocean as the heat energy supply of the TC, and Ernst Kleinschmidt (Kleinschmidt, 1951) who derived a formula for maximum wind speed.

The efforts made in the observation of TCs from aircrafts and Earth observation satellites and the gradual development of numerical models considerably improved our understanding of TCs, and our ability to predict their formation and evolution.

However, while their trajectory is now well forecasted, progress is stagnating regarding their intensity variations. These are indeed extremely complex to grasp because they involve both the external environment of the TC and its internal structure, through many multi-scale processes which, icing on the top, have the bad taste of interacting with each other.

Throughout this manuscript, I will lead you to a journey into the internal structure of tropical cyclones, their crazy steep eyewall, the swing of their eye shape, the roller coasters of their extreme wind ring... And we will try to catch some interesting science regarding these vortex attractions, and their link with the cyclone intensity variations.

## 1.2 Tropical cyclones: theoretical bases

### 1.2.1 Steady-state structure of a tropical cyclone

Viewed from space, a TC can be pictured as a vortex made of spiraling clouds and rain bands, and a central cloud-free eye (Fig. 1.2). Their vortex diameter, is on the order of 1000∼km on the horizontal. On the vertical, a TC reaches the top of the troposphere, that is around 15km. This vortex can be described both dynamically and thermodynamically.

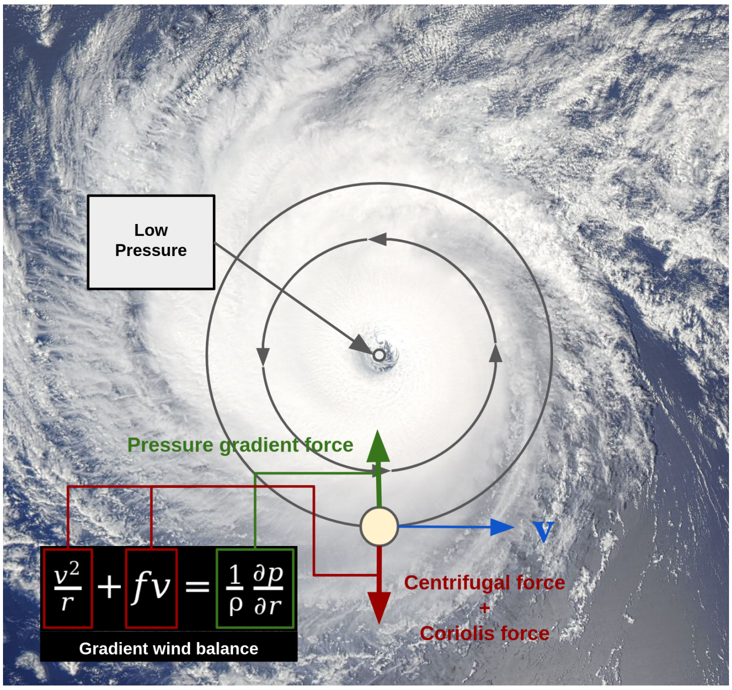

Figure 1.2 – Diagram describing the gradient wind balance governing the TC primary circulation.

#### Dynamic structure

In a first approach, the TC vortex can be approximated as symmetric around its central axis. In this perspective, it can be pictured as the superimposition of two circulations. The primary circulation is horizontal and cyclonically rotating under the effect of the gradient wind balance (i.e. balance between inward pressure gradient force and outward Coriolis and centrifugal forces, cf. Fig. 1.2). This balance derives from the Navier-Stokes equations simplified as a steady flow and neglecting radial wind and friction. It is expressed as:

$$fv + \frac{v^2}{r} = \frac{1}{\rho}\frac{\partial p}{\partial r}, \tag{1.1}$$

where $fv$ is the Coriolis force, $\frac{v^2}{r}$ is the centrifugal force, and $\frac{1}{\rho}\frac{\partial p}{\partial r}$ is the radial pressure gradient force.

To a good approximation, the hydrostatic balance also applies to the TC scales:

$$\frac{\partial p}{\partial z} = -\rho g \tag{1.2}$$

where $\frac{\partial p}{\partial z}$ is the upward pressure gradient force, $\rho$ the density and g the acceleration of gravity.

Multiplying eq. 1.1 by $\rho$ and cross-differentiating eqs. 1.1 and 1.2 yields the thermal wind balance:

$$\frac{\partial \log \rho}{\partial r} + \frac{C}{g}\frac{\partial \log \rho}{\partial z} = -\frac{1}{g}\frac{\partial C}{\partial z} \tag{1.3}$$

where $C = fv + \frac{v^2}{r}$ According to this equation, a decreasing tangential wind speed on the vertical ($\frac{\partial v}{\partial z} < 0$) would cause a positive radial gradient of density $\frac{\partial \log \rho}{\partial r} > 0$ and thus a positive radial gradient of temperature, yielding a warm-cored vortex. This implication is indeed observed on real TCs, showing the consistency of the thermal wind equation to approximate the large-scale axisymmetric structure of TCs. These dynamical balances however neglect the vertical speeds and the Boundary Layer (BL) specific dynamics, which are described through a secondary circulation.

The secondary circulation (right hand side of Fig. 1.3) is observed on a cross view of the TC. In the Boundary Layer (BL, the area close to the surface), the gradient wind balance is broken due to surface friction. The surface friction indeed reduces the tangential wind speed, which in turn reduces the Coriolis and centrifugal forces, yielding a mean inflow as the pressure gradient becomes the dominant force. The typical height of the BL is about 1km. The convergence of moist air extracting heat from the underlying warm ocean forces air parcels to ascend, and leads to convection in the central part of the TC, called the eyewall, as well as in its surroundings. This ascent is balanced by an outflow at the top of the troposphere, and the circulation becomes anticyclonic as it flows outward (i.e. beyond 200km, as observed by Smith, Montgomery, and Braun, 2019). Downdrafts of outflowing dry air complete the secondary circulation in the cloud-free areas (outside the vortex and between spiral convective rainbands), as well as in the eye.

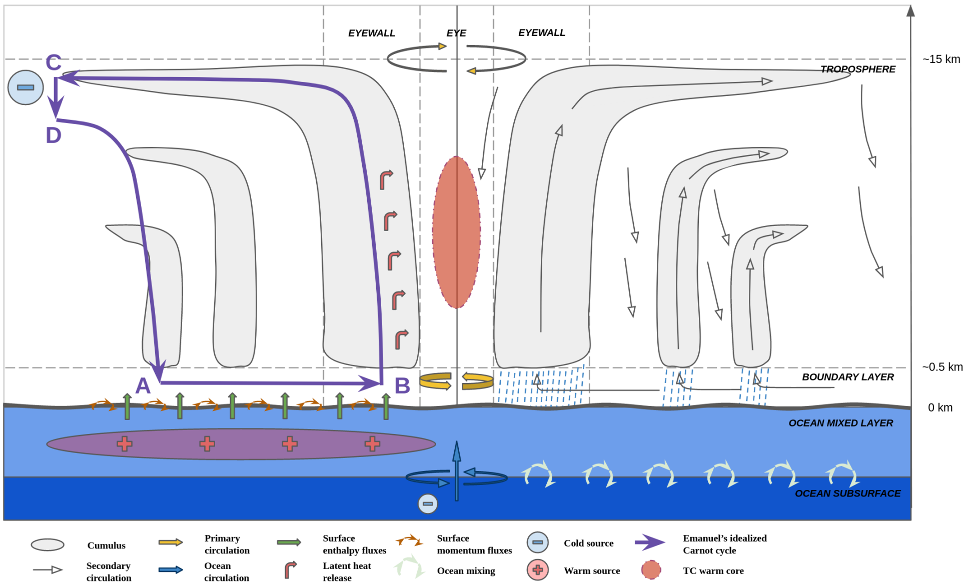

Figure 1.3 – Schematic of a TC crossview, describing the TC vertical and radial structure, secondary circulation, energetic exchanges (summarized by the idealized Carnot cycle), and ocean internal processes interacting with the TC.

The combination of these two circulations creates the well-known spirals (Fig. 1.2) observed when looking at a TC from above.

### Thermodynamic structure

The dynamic view of the TC, and particularly the secondary circulation, is also in part driven by thermodynamic exchanges between the TC and its environment.

As in many other atmospheric events such as clouds, thunderstorms or atmospheric lows, convection drives the vertical movements and environmental heat transfers of air parcels throughout the TC.

The process controlling the ascent of air parcels in TC clouds is termed moist convection. It is illustrated on Fig. 1.4. Initially, a moist air parcel is raised through the air column due to a dynamical forcing, submitted to a positive buoyancy force. During its ascension, the parcel is adiabatically cooled due to its expansion as density decreases. However, the moisture contained in the parcel mitigates this cooling: the moist-adiabatic cooling is slower than the dry-adiabatic one as, when cooling, the parcel becomes saturated in moisture, which then condensates and releases latent heat (i.e. thermic energy) inside the parcel. Thus, when the parcel gets saturated (at a level termed the Lifting

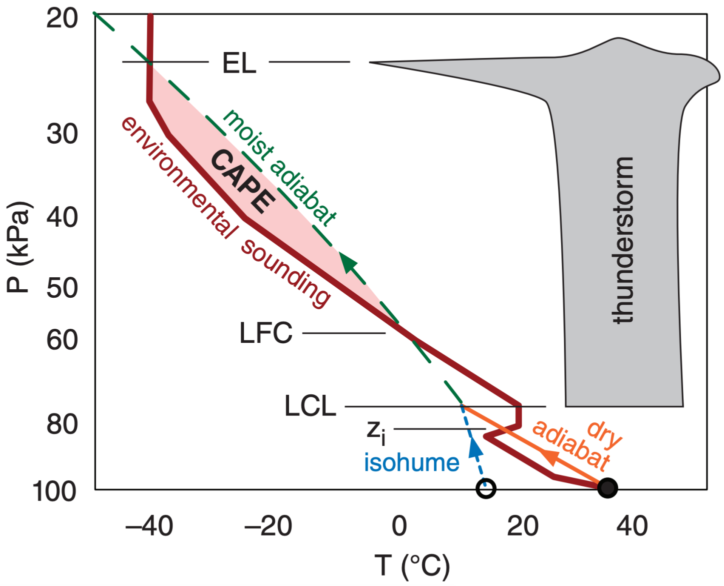

Figure 1.4 – Schematic view of the principle of moist convection and CAPE (Convective Available Potential Energy) on a skew-T diagram. Red curve is the environmental atmospheric temperature on the vertical. The moist air parcel lifted from the surface starts by following the dry adiabat (orange), then the moist adiabat reaching the Lifting Condensation Level (LCL) as it starts to condensate (forming a cloud). At some point if the parcel keeps lifting, it reaches the Level of Free Convection (LFC) where it becomes warmer than the surrounding environment [2]. The parcel thus keeps ascending releasing its latent heat up until the Equilibrium State (EL) where convection stops. The CAPE is the positive integral between the two temperature curves (i.e. air parcel and its environment).

Condensation Level (LCL)) and the moisture starts to condensate, it cools at a lower rate than its environment. Eventually, if the parcel has a sufficient vertical velocity and enough latent heat to release, it reaches the Level of Free Convection (LFC) where it gets warmer than its environment. The parcel thus keeps ascending, up to a point where all the latent heat has been released (called the Equilibrium Level (EL)). The ability of a moist parcel to ascend through the atmosphere (e.g. of convection to appear) is determined by the vertical distribution of temperature in the atmosphere.

The Convective Available Potential Energy (CAPE) is defined as the amount of work

---

[2] This diagram features the structure of a thunderstorm cloud. In a Tropical Cyclone, the ascending air parcels are warmer and the LFC is thus located lower in the troposphere, at a height of ∼1km (Smith and Montgomery, 2012).

exerted by the buoyancy force on a lifted air parcel:

$$CAPE_i = \int_{z_i}^{EL} B\,dz \tag{1.4}$$

where $z_i$ is the initial vertical level of the parcel, EL the Equilibrium Level, z is the height, and B is the buoyancy force equal to $-g\frac{\rho-\rho_a}{\rho}$ where $\rho$ is the parcel density, $\rho_a$ the atmospheric density and $g$ the acceleration of gravity. The CAPE determines the upper bound on the maximum vertical velocity achievable by the air parcel due to the buoyancy force, and thus the degree of instability of the atmosphere: a larger CAPE indicates a more convectively unstable atmosphere, and a larger amount of potential energy convertible to kinetic energy.

Moist convection thus explains how vertical air motions can ascend in clouds throughout the troposphere. It is thus a primary mechanism during TC formation, where cloud convection is still predominant in the system.

When the vortex has begun to intensify and mature, moist convection is not however the driving mechanism per se of the secondary circulation: inside a mature TC, the cloud-scale convection is then largely slaved to the symmetric vortex-scale circulation. Kerry Emanuel developed, in 1986, a model of the steady-state hurricane (Emanuel, 1986) that assimilates the TC secondary circulation to a Carnot cycle (Carnot, 1824). Initially, this ideal thermodynamic cycle was defined by Sadi Carnot to describe the operation of an engine converting heat into mechanical work. The engine is composed of two thermal sources (warm and cold) and a gas chamber that can perform work on its environment. The cycle is a sequence of four ideal thermodynamic transformations, during which (1) the gas exchanges heat with the warm source, undergoing an isothermal expansion and performing work on its surroundings then (2) it expands and cools adiabatically, still performing work on its surroundings, (3) it releases heat into the cold source in an isothermal compression (receiving work from the exterior), and (4) it compresses and warms adiabatically, receiving work from its surroundings.

In the view proposed by Emanuel, 1986, (represented on the left panel of Fig. 1.3), the warm source is assimilated to the ocean surface, and the cold source to the upper troposphere. The cycle starts at point A with air converging to the TC center (B) at the sea surface, accumulating entropy from enthalpy transfers with the underlying ocean surface at approximately constant temperature, performing work to counter surface friction. When reaching the eyewall (B), air parcels having acquired a substantial boost in entropy start a moist adiabatic ascent, releasing latent heat and following an outward slope of constant angular momentum (B-C). When reaching the tropopause, which can be seen as the cold source of the cycle (C), the air parcels release entropy at a constant temperature, dissipating energy by infrared radiation in space (C-D). Finally, the cycle is completed by a moist adiabatic descent during which the temperature increases along a constant angular momentum surface (D-A). This idealized view thus depicts the TC as an engine extracting heat from its environment (i.e. the ocean surface) and converting it to kinetic energy (i.e. vertical and tangential velocity). From this approach, Emanuel derived the theory of Maximum Potential Intensity (MPI), according to which the maximum reachable intensity of a TC can be estimated by computing its ideal work from the Carnot cycle, which depends on the temperatures of the warm and cold sources of the Carnot engine, and on the enthalpy and momentum surface fluxes responsible for energy sources and sinks of the TC engine respectively. A simplified expression of the maximum reachable wind at the sea surface is given by Emanuel, 2018 (based on Bister and Emanuel, 1998) as:

$$|V_{max}|^2 = \frac{C_k}{C_d}\frac{T_S - T_O}{T_O}(k_0^* - k), \tag{1.5}$$

where $V_{max}$ is the MPI at the sea surface, $C_k$ and $C_d$ are the enthalpy and momentum surface transfer coefficients, $T_S$ and $T_0$ are the temperature respectively at the sea surface and at the tropopause (outflow temperature), $k$ the enthalpy per unit mass and $k_0^*$ the saturation enthalpy at the sea surface. To note, equation 1.5 is a simplification with unknown members (i.e. outflow temperature, surface saturation enthalpy and boundary layer enthalpy), and limited to the sea surface (whereas the true maximum wind speed can occur above this surface). More complex formulations and discussions regarding the MPI can be found in Emanuel, 1986; Emanuel, 1988. Another debated aspect of the MPI formulation concerns the effect of dissipative heating (i.e. heating due to dissipation of kinetic energy): it was indeed included by Bister and Emanuel, 1998 through the $\frac{T_S - T_O}{T_O}$ ratio, but was recently judged to be overestimated by Kieu, 2015 (cf. discussion by Montgomery and Smith, 2017).

Emanuel's assimilation of the TC to a Carnot cycle conveniently summarizes its energetics. However, it remains a very simplified view of the system, and only describes its idealized behaviour under several drastic assumptions regarding its dynamical (neglecting dissipation both at the surface and in the eyewall), and structural (axisymmetry) properties. Smith, Montgomery, and Vogl, 2008 notably discussed the limitations of Emanuel's steady-state hurricane model, arguing that the assumption of gradient wind balance in the boundary layer is inaccurate owing to the fundamentally agradient nature of BL winds in the inner-core. They showed that a more complex representation of the BL including the outflow layer above the lower inflow layer, and the radial pressure gradient imposed by the free troposphere, could help better prescribe steady-state dynamics. These modifications of the steady-state model would also imply a different formulation of the MPI.

Beyond its steady state, the TC goes through a full life cycle, including genesis, intensification and decay phases. We describe these phases hereafter.

### 1.2.2 TC life cycle

The development and life cycle of TCs depend on various factors such as atmospheric and oceanic external conditions, the oceanic basin, the season, or internal fine scale processes. However, there is a common pattern of life cycle that describes the bulk behaviour of TCs: they form in the intertropical convergence zone, then they intensify up to a mature state in a time lasting from several hours to several days, they propagate westward under the effect of ambient atmospheric synoptic flow and planet rotation, and their trajectory gradually shifts poleward due to planetary vorticity (i.e. the beta-effect) (Holland, 1983; Holland, 1984). When reaching subtropics and mid-latitudes, TCs arrive into a less favourable environment with more vertical wind shear and colder ocean mixed layer, leading either to their collapse or to their transition to extratropical storms (Harr and Elsberry, 2000; Harr, Elsberry, and Hogan, 2000). The typical life cycle of TCs can last a few days up to several weeks. We describe hereafter the different phases of this life cycle, and the conditions governing the TC's behaviour during these phases.

#### Formation

As stated by Kerry Emanuel in a recent review on TC research (Emanuel, 2018), "no aspect of tropical cyclones has proved as vexing and intractable as their formation". The range of conditions allowing the development of such extreme events are indeed still subject to debate, and the ability to predict their formation is yet limited.

**Large-scale factors** The probability for a TC to develop in an area of the globe at a given time depends on the state of the ocean and surrounding atmosphere at that time. A warm ocean surface is a first prerequisite to TC genesis (Palmen, 1948), as the increased evaporation of ocean water allows moistening of lower atmosphere, and provides fuel for convection. The location at intertropical latitude is also a requirement as it grants a small Coriolis force, and thus allows a stronger low-level convergence. An early attempt to list environmental conditions necessary for TC formation was performed by Gray, 1975; Gray, 1979, who added sufficient low-level relative vorticity, low tropospheric vertical shear, and sufficient relative humidity and equivalent potential temperature distribution on the vertical to the two previously cited factors. Based on these environmental factors, several indices for tropical cyclogenesis have been developped since then. Menkes et al., 2012 compared four of these indices and showed that the index proposed by Tippett, Camargo, and Sobel, 2011 was overall performing the best. This index was derived from the General Potential Index (GPI) developed by Emanuel and Nolan, 2004a; Camargo, Emanuel, and Sobel, 2007, which depends on the following predictors:

- absolute vorticity, which must be high to ensure the low-level convergence and trigger deep convection
- relative humidity at 700 hPa, which must also be high to provide enough fuel for the convection
- an SST index, which includes conditions on the local SST that must be high compared to environmental SST, and other parameters such as "clipped" vorticity that limits the impact of low-level vorticity on the index above a given threshold
- vertical wind shear, which must be low to prevent disturbance of the forming convective column and upper intrusion of dry air.

Menkes et al., 2012 also showed that while such indices quite fairly represent the seasonal variability, they mostly fail at representing the interannual variability of cyclogenesis amplitude and phase, and suggest that this may be attributable to stochastic processes not accounted for in these large-scale environmental indices. These indices are regularly discussed and improved owing to new developments in the field of TC research.

These prerequisite conditions can be accompanied by other processes that favor the settlement of a mature TC: these processes are easterly waves or monsoon troughs that favour the convergence of moist air, and can trigger the transition between a mesoscale cluster of convective clouds and a deeply convective moist air column (Gray, 1968).

These circumstances are however more and more considered to be only catalysts of the cyclogenesis, instead of mandatory requirements.

**Fine-scale dynamics** Overall, the above listed criteria and processes only describe the favorable conditions for TC formation. They are necessary, but not sufficient to cause the formation of a tropical depression. As summarized by Emanuel, 2018, current observational, theoretical and modeling studies point at two main configurations for initiating a warm-core convective cyclonic vortex. In the first case, the formation of a warm-core cyclonic disturbance starts with an isolated mesoscale cold core perturbation caused by environmental cyclonic circulation (Riehl, 1963; Chen and Frank, 1993). This cold core perturbation causes mixing of moist static energy throughout the troposphere. The circulation at the surface is thus originally cold-core and potentially anticyclonic, with the presence of a cold-core TC aloft in the troposphere preventing downdrafts. Eventually, the accumulated moisture in the column launches vertical convection and low-level convergence. This triggers an inversion of the surface circulation which then becomes warm-cored and cyclonic, further fueling the deep convection.

In a second and more recent theory owing to the high resolution modeling techniques used to simulate it, the warm-core saturated air column forms due to a spontaneous self-aggregation of convection (Raymond and Sessions, 2007; Nolan, Rappin, and Emanuel, 2007; Davis, 2015; Wing, Camargo, and Sobel, 2016; Muller and Romps, 2018). Such aggregation is due to a near-surface flow from dry subsident radiatively cooled areas to moist columns with reduced radiative cooling caused by high clouds. The ocean extracted moist static energy near the surface is thus exported from dry to moist regions, yielding an upgradient energy transport.

An other recent theory regarding tropical cyclogenesis synthetizes two aspects of TC formation into a unified view (Montgomery and Smith, 2010; Kilroy, Smith, and Montgomery, 2017). The first step is the so-called "marsupial paradigm", which postulates that the formation of cyclonic tropical depressions is strongly favoured inside the Kelvin cat's eye of the critical layer of pre-existing synoptic-scale tropical easterly waves (i.e. the easterly wave "pouch"). The pouch is indeed believed to protect moist air from external dry air intrusion, while favouring the aggregation of vorticity through wave breaking and roll-up of cyclonic vorticity, while persisting in time through a feedback between the parent wave and the embedded cyclonic vorticity. This theory, first proposed by Dunkerton, Montgomery, and Wang, 2009, was verified in cloud-resolving modeling simulations by Wang, Montgomery, and Dunkerton, 2010a; Wang, Montgomery, and Dunkerton, 2010b; Montgomery, Wang, and Dunkerton, 2010 and observed by Montgomery et al., 2010. It is also the object of the Pre-Depression Investigation of Cloud-Systems in the Tropics

(PREDICT) Experiment, which proved useful to improve genesis predictability (Montgomery et al., 2012). Moreover, PREDICT observations of hurricane Karl (2010) showed the relevance of the unified theory, while the pre-existence of a cold core perturbation was invalidated in this case (Bell and Montgomery, 2019). Unlike previous theories that associated TC formation to the pre-existence of a mid-level mesoscale cyclonic vortex and required a trigger to launch deep convection, the unified theory sees TC genesis as a gradual two-way energy cascade (Montgomery and Smith, 2010): on one hand, the parent easterly wave breaking leads to a downscale cascade where vorticity goes from synoptic to mesoscale; on the other, the appearance of small-scale convective structures such as Vortical Hot Towers (VHTs) inside the wave pouch leads to an upscale aggregation of localized vortical anomalies. This merging of asymmetric vortical structures of enhanced convection is termed the rotating convective paradigm and was initially introduced by Montgomery et al., 2006 to describe the genesis of Tropical Cyclones.

The research on TC formation thus combines necessary conditions (used to define genesis indices), catalytic processes mostly linked to atmospheric large-scale circulation, and scenarios explaining the appearance of warm-core deep convection characteristic of mature TCs.

### Intensification

Once the deep convection is initiated, the vortex enters a self-sustaining process in which the average symmetric vortex intensifies through a feedback between moisture fluxes from the ocean surface and deep convection in the conditionally unstable thermodynamic environment. Several studies have attempted to describe the chain of processes controlling this feedback; they were summarized through four main paradigms by Montgomery and Smith, 2014 and reviewed by Montgomery and Smith, 2017.

The first paradigm, termed the Convective Instability of the Second Kind, (CISK), was proposed by Ooyama, 1964 and Charney and Eliassen, 1964. It relies on an axisymmetric view of the vortex in which the spinup occurs above the boundary layer through angular momentum conservation, while the energy supply for convection occurs mainly through the inflow of moist air in the BL caused by surface friction. In this view, the rate of latent heat released by deep convection is proportional to the convergence of moisture throughout the troposphere, which thus mainly occurs in the BL. The CISK paradigm thus delivers a simple view of an axisymmetric intensifying vortex based on dynamical arguments.

However, CISK has several limitations (cf. Montgomery and Smith, 2014 p. 8) that led to its modification and improvement by Ooyama, 1969 and to the introduction of the more developed Cooperative-Intensification paradigm. Similarly to CISK, the cooperative-intensification paradigm describes an axisymmetric TC approximately in thermal wind balance (i.e. hydrostatic and gradient wind balances). The intensification is then described as a feedback loop between the convectively unstable eyewall and the radial gradient of pressure and temperature: an initially weak vortex will generate inflow in the BL, causing convective activity where moist air converges in the BL, and heating in the center. To keep the vortex in thermal wind balance, a deep region of negative radial gradient of latent heating rate in the convective region draws in surfaces of constant absolute angular momentum (M) surfaces above the boundary layer while approximately materially conserving M. From the equation $V_t = \frac{M}{r} - \frac{fr}{2}$, the inward movement of M surfaces implies an amplification of the tangential winds and a lowering of the sea surface pressure in the central region via gradient wind balance. If the equivalent potential temperature in the BL is high enough and keeps increasing with decreasing radius due to surface moisture fluxes, the moist instability will be maintained: the air above the BL will thus continue to be drawn inwards and the tangential winds will continue to amplify. Unlike the CISK paradigm, this view thus limits the intensification to the degree of conditional instability of the eyewall: at some point, the release of latent heat in the eyewall warms the troposphere enough to reduce the instability to buoyant deep convection, and the increasing amount of moisture in the BL reduces the moisture flux at the sea surface; convection is thus capped.

An other approach of TC intensification was proposed by Emanuel, 1997 as the Wind-Induced Surface Heat Exchange (WISHE) paradigm. The WISHE theory relies on the steady-state hurricane model developed by Emanuel, 1986 and describes intensification essentially as a positive feedback between sea surface wind speed and the amount of heat extracted from the sea surface, which depends on the surface wind speed. WISHE thus emphasizes the importance of sea surface heat exchanges as the driving mechanism of intensification, instead of eyewall convection and latent heat release, as well as the conventional spin-up process above the BL, that are viewed as implicit (Montgomery et al., 2009).

In a more recent set of papers (Montgomery et al., 2006; Smith, Montgomery, and Van Sang, 2009; Montgomery and Smith, 2014), an asymmetric-based view of TC intensification was developed as the Rotating Convection paradigm. This paradigm is based on the principle of rotating convection already mentioned in section 1.2.2, in which local updraughts amplify the cloud-scale vorticity by one to two orders of magnitude through the process of vortex tube stretching. These highly vortical updraughts, called the Vortical Hot Towers (VHTs), eventually aggregate and thereby amplify the vorticity of the main parent vortex. They are thus believed to take a great part in vortex formation and intensification. The rotating convection paradigm thus has the particularity of acknowledging the importance of asymmetric and localized convective structures in the intensification process. This asymmetric view corresponds, when summarized to an axisymmetric view, to a revised version of the cooperative-intensification theory.

Basically, the cooperative-intensification that links the increase of near-surface equivalent potential temperature to the release of latent heat by eyewall convection remains unchanged, but the dynamics and thermodynamics of the Boundary Layer are largely revised, implying modifications of the spin-up process and axisymmetric structure of the intensifying TC as well. The rotating convection paradigm indeed goes with a new vision of TC wind spin-up in which the highest winds are located inside the BL (whereas they are located at the top of it in previous theories). This revised spin-up theory proposed by Smith, Montgomery, and Van Sang, 2009 shows that, if the air in the BL inflows faster than it is reduced by surface friction during its convergence, it spins-up and becomes supergradient, yielding higher wind speeds than in the frictionless atmosphere above the BL. In this view, the BL takes a more important role in the intensification process as it becomes the driving mechanism for the spinup of the eyewall: instead of occuring through the convergence of constant angular momentum air above the BL, the spin-up is transferred from the BL through vertical advection of angular momentum by eddy momentum fluxes. These momentum fluxes are caused by rotating deep convection: they are the result of VHTs and localized vortical poles merging and aggregating in the eyewall area, that enhance local vorticity and transfer their momentum to the inflowing air. The transfer of air from the BL to the eyewall deep convection above can only occur if the buoyancy of the eyewall is able to ventilate this air: otherwise, there would be an outflow above the BL and the vortex would spin down as in a normal convective cell. The intensification is thus limited to the fact that the convective mass flux in the eyewall has to be strong enough to ventilate the BL inflow: if the inflow becomes too important with respect to eyewall convection, the air outflows above the BL and caps the intensification.

Rotating convection paradigm thus synthesizes axisymmetric and asymmetric aspects of TC intensification to deliver a unified view of the TC vortex in which the axisymmetric feedback process between eyewall latent heat release and elevation of near-surface equivalent potential temperature by moisture fluxes appears primarily controlled by BL dynamics and by the formation and aggregation of localized rotating convective clouds. The new spin-up theory associated with the axisymmetric version of the paradigm has been validated observationally and in modeling studies, and VHTs have been extensively observed and theorized, although their role in eddy momentum fluxes distribution still requires investigation. This new paradigm is thus a considerable step in the direction of a coherent description of the TC life cycle, as it synthetizes dynamics and thermodynamics, symmetric and asymmetric properties, and describes both the formation and intensification of TCs (even the decay phase in a quiescent environment according to (Smith, Kilroy, and Montgomery, 2021)).

### Intensity variations

**Environmental factors** The most common sources of perturbation of TC intensification are surface interactions (land and ocean), and vertical wind shear. Both have been extensively studied and are not the subject of the present thesis, but a very brief summary of their known interactions with the TC vortex is provided here.

The presence of a large and intense vortex moving above the ocean surface has various effects on the ocean, the most easily observable being the so-called ocean surface "cold wake". Observational evidence indeed shows that TCs leave a cold sea surface temperature (SST) wake behind them which can be significant regarding the mean temperature (Elsberry, Fraim, and Trapnell Jr, 1976; Price, 1981) . This surface water cooling can in turn impact the TC intensity by limiting its energy supply (Ginis, 2002; Jullien et al., 2014). The mechanisms provoking this ocean surface cooling are multiple (they are illustrated on Fig. 1.3): they include Ekman pumping caused by the cyclonic circulation (Price, 1981; Shay, Goni, and Black, 2000), mixing induced by entrainment and shear instability (Elsberry, Fraim, and Trapnell Jr, 1976; Shay, Elsberry, and Black, 1989; Jaimes and Shay, 2009), surface heat fluxes (Andreas and Emanuel, 2001). The ocean response depends on several factors, as the characteristics of the TC (size and translation speed of the TC determines the intensity of Ekman pumping: the smaller and faster the TC, the lowest the Ekman-induced surface cooling), and the structure of the ocean during the TC's passage (e.g. the shallower the mixed layer, the stronger the cooling (Vincent et al., 2012; Jullien et al., 2012)). The ocean pre-existing mesoscale activity also influences the ocean response to a TC, as they feature a specific ocean stratification that modulates the ocean response, and in turn its impact on the TC intensity (Bao et al., 2000; Wu, Lee, and Lin, 2007; Jullien et al., 2014).

Vertical wind shear of the synoptic flow is another environmental factor that have considerable impact on the TC as it perturbs the vertical alignment of the TC (Frank and Ritchie, 1999; Smith, Ulrich, and Sneddon, 2000; Frank and Ritchie, 2001; Corbosiero and Molinari, 2002). The tilt processes under the effect of shear are complex, but they usually result in a perturbation of the convective column which, under the effect of vorticity, initiates a horizontal offset between the lower and upper parts of the sheared TC. This process and the interaction between the different shifted vertical layers of the TC eventually leads to the formation of Vortex Rossby Waves (VRWs, see section 1.2.2 for details), which can lead to the reformation of a coherent tilted vortex, or to the vortex collapse if the shear is too strong (Montgomery and Kallenbach, 1997; Schubert et al., 1999; Corbosiero and Molinari, 2003). The excitation of VRWs can indeed cause the intrusion of low entropy air from the exterior into the vortex at mid levels, or to downdrafts of low entropy air in the boundary layer, which can in turn impact TC intensity and make it less resilient to shear events (Reasor, Montgomery, and Grasso, 2004; Tang and Emanuel, 2010; Riemer, Montgomery, and Nicholls, 2010).

**Vortex internal processes and structure** In response to external disruptions or local scale interactions, processes internal to the vortex are triggered and interplay with intensity variations. The modification of the internal TC structure can be viewed as a departure from the bulk steady-state TC structure, often through transitory and asymmetric features. In practice, all interactions of the TC with its environment modify the structure of the wind field (and all other representative variables: pressure, precipitation, vorticity...) either locally or at a larger scale, sometimes encompassing the whole vortex. A systematic modification of the TC wind structure is for instance the wave number-1 asymmetry introduced on the symmetric vortex by its translation speed. The translation speed indeed induces a difference of wind speed between the two sides of the TC, as one side (the right one in the northern hemisphere) has tangential winds aligned with the translation speed, while the other side has opposed cyclonic and translation velocities. The resulting vortex is thus not symmetric, but features a difference of speed between its two sides equal to twice the translation speed. Vertical wind shear, as previously depicted, can tilt the vortex, generating local anomalies of wind and vorticity mixing in the eyewall, perturbations of the potential vorticity field, modifications of the radial structure, etc. Similarly, all interactions of the TC with its environment can cause distortions or perturbations of the wind field.

The processes affecting TC intensity are detailed hereafter, and illustrated on Fig. 1.5 for vortex-scale processes, and Fig. 1.6 focusing on the TC core and eye-eyewall features.

**Vortex contraction** A first feature of TC internal structure changes is the vortex contraction. This contraction is not linked to any external event, but is an intrinsic process of TCs when they intensify. Shapiro and Willoughby, 1982 showed that heat and momentum sources at the vortex center can rapidly affect the eyewall structure, and have a tendency to cause eye contraction by displacing the wind maximum progressively inside the radius of maximum wind. This contraction process is widely accepted as a general tendency of intensifying TCs (Shapiro and Willoughby, 1982; Willoughby, Clos, and Shoreibah, 1982; Stern et al., 2015; Li, Wang, and Lin, 2019). It is an important feature of the TC internal structure as it directly links intensification to a modification of the entire radial structure.

**Eye thermodynamics** The thermodynamical structure of the eye features a strong inversion between upper dry air descent caused by the outflow at the top of the troposphere, and lower moist air ascent under the combined effect of sea surface heat exchange in the eye, momentum inflow and mixing with the eyewall (Willoughby, 1998; Franklin, Lord, and Marks Jr, 1988). The location of this inversion has been related to the intensity and intensification phase of the TC (Jordan, 1961; Emanuel, 2018).

**Eyewall mesovortices** The shearing between the warm eye and the surrounding eyewall due to the strong wind speed, and potential vorticity gradients leads to the appearance of so-called eyewall mesovortices (Lewis and Hawkins, 1982; Marks et al., 2008). These mesovortices cause strong asymmetries in the eye shape and polygonal eyewalls such as the triangle shape of Fig. 1.6 (Lewis and Hawkins, 1982; Muramatsu, 1986; Marks et al., 2008; Kossin and Schubert, 2001). These polygonal eyewalls have been related in several studies (Kuo, Williams, and Chen, 1999; Wang, 2002a) to an other major feature of TC life-cycle, the Vortex Rossby Waves (VRWs).

**Vortex Rossby Waves (VRWs)** The nature and extent of the impact of VRWs on the TC life cycle is still debated and investigated. These waves rotating around the eye and propagating outward (cf Figs. 1.5 and 1.6) along potential vorticity gradients (similarly to

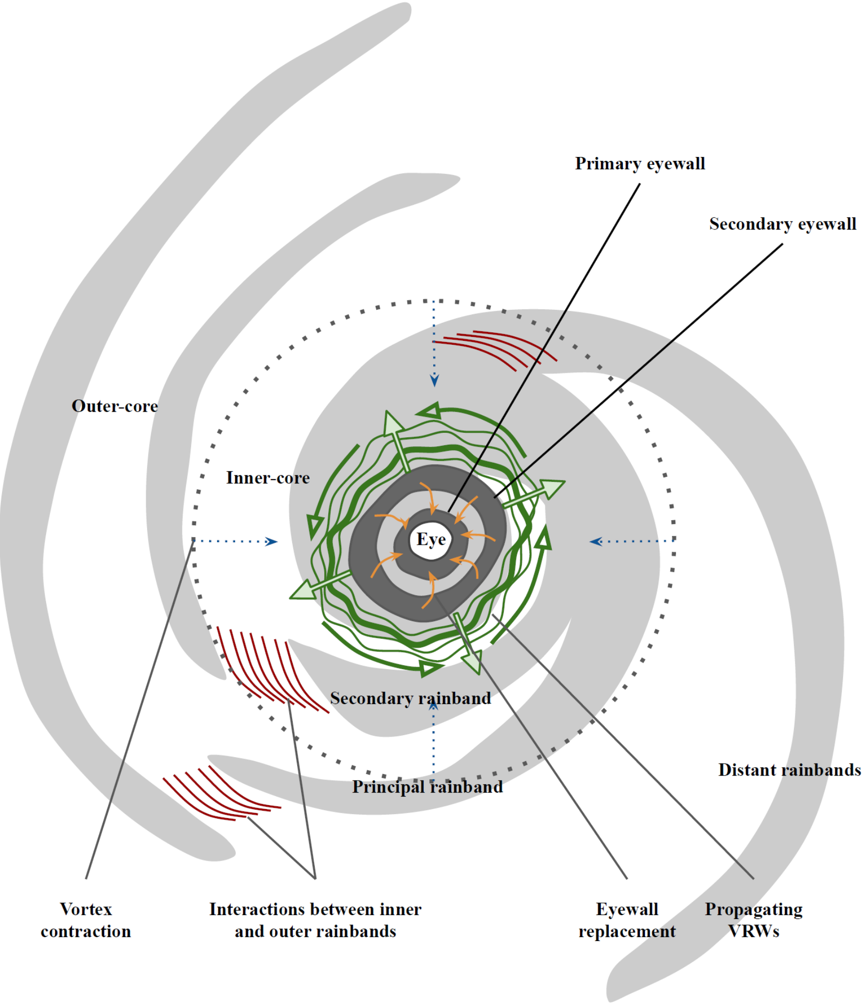

Figure 1.5 – Schematic upper-view of a TC describing vortex-scale structure and processes related to intensity variations. Adapted from Houze, 2010.

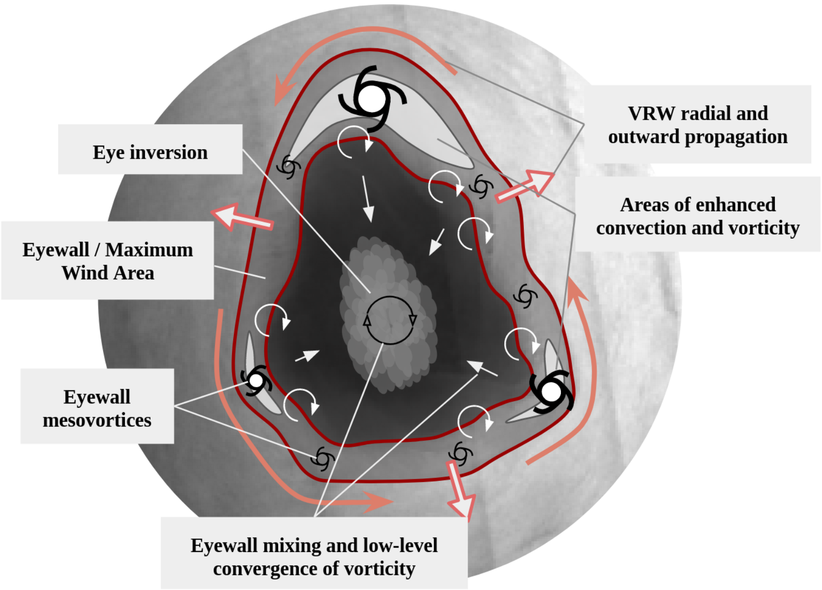

Figure 1.6 – Schematic of TC inner-core processes in the eye and eyewall area leading to eye deformation and generation of VRWs. Background is a SAR normalized radar cross-section from TC TRAMI (2018).

atmospheric Rossby waves) have been consistently theorized (Guinn and Schubert, 1993; Montgomery and Kallenbach, 1997; Wang, 2002a; Wang, 2002b; Brunet and Montgomery, 2002; McWilliams, Graves, and Montgomery, 2003) and observed (Reasor et al., 2000) in TCs. They are described as a driving mechanism of vortex axisymmetrization, restoring symmetry and possibly promoting TC intensification (Montgomery and Enagonio, 1998; Enagonio and Montgomery, 2001; Shapiro, 2000). These VRWs have strong signatures on the structure of the TC, influencing inner-core asymmetric wind field. Observational studies have linked them to low wave number (1 and 2) disturbances propagating through the vortex (Reasor et al., 2000) causing eye rotation (Kuo, Williams, and Chen, 1999) and coupling with inner rain bands (Chen and Yau, 2001). They were also simulated in numerous modeling studies (Wang, 2002a; Wang, 2002b; Wang and Wu, 2004), and their spectral distribution and extent were shown to strongly depend on model resolution (Gentry and Lackmann, 2010).

**Rainbands** TC rain bands can be divided in two categories with different associated dynamics. Inner rain bands, in the TC's inner-core, hardly visible on TC images as they are in the most cloudy area of the TC. They are convectively coupled to VRWs, and thus very related to their dynamics and propagation (Guinn and Schubert, 1993; Montgomery and Kallenbach, 1997; Li and Wang, 2012). At larger radii, VRWs propagating outward reach a critical radius at which their phase speed matches the bulk vortex frequency (Schecter and Montgomery, 2003). Inner rain bands thus disaggregate in the so-called Rapid Filamentation Zone (Rozoff et al., 2006; Wang, 2008; Li and Wang, 2012), and turn into outer rain bands, which can be spotted as large spiral bands separated by cloud-free areas. Outer rain bands are thus dynamically distinct from inner-core dynamics, but can also notably impact the vortex causing intensity and size changes or Secondary Eyewall Formations (SEFs) (Wang, 2009; Wang and Tan, 2020).

**Eyewall replacement cycles (ERCs)** Vortex spin-up added to eyewall contraction can sometimes eventually cause ERCs (Willoughby, Clos, and Shoreibah, 1982), that strongly affect the TC's intensity. This process occurs when a secondary eyewall forms outside of the Radius of Maximum Wind, and gradually contracts to replace the first eyewall. Secondary eyewalls form due to the expansion of the wind field (Abarca and Montgomery, 2013) and the increased latent heating outside the Radius of Maximum Wind (RMW) that goes with this expansion (Rozoff et al., 2012). The formation of Secondary Eyewalls that triggers ERCs might be linked to VRW propagation and rotating-convection paradigm, according to Terwey and Montgomery, 2008. Using idealized numerical simulations, they showed that Secondary Eyewall Formations (SEFs) happen through the formation of a cyclonic jet in the vorticity skirt above the RMW, which gradually intensifies into a deeply convective eyewall due to wind-wave feedback and convergence of system-scale vorticity. This jet results from axisymmetrization of vorticity anomalies that converge and aggregate into the primary eyewall by shear turbulence and VRWs. Other studies suggest that ERCs might also be triggered by external events, and interaction between the inner-core and the surrounding rainbands (Rozoff et al., 2012; Judt and Chen, 2010). ERCs can cause strong intensity fluctuations by spontaneously decreasing the TC intensity, while at the same time further broadening the wind field (Huang, Montgomery, and Wu, 2012). They are therefore a source of uncertainty for observational assessment of vortex maximum intensity and size (Combot et al., 2020).

The above listed processes and features provide a non exhaustive view of the diversity of phenomena that are currently under investigation for a better understanding of TC formation and intensity variations.

### Decline

Many events can cause the end of a TC event. As seen above, environmental events such as ocean surface cooling or vertical shear in the atmosphere can cause notable perturbations of the TC, but they must be very strong to cause the collapse of an intense formed vortex on their own, which rarely occurs in the tropical atmosphere. The most common reasons for TC decay are thus either landfall or reaching high latitudes (as the beta-effect drives their track poleward). They thus simply lose their energy supply, either reaching dry land or colder water. Higher latitudes also have higher levels of vertical shear, combining two sources of external perturbations. In some cases, however, TCs can undergo an extratropical transition and become extratropical storms by tapping into the available potential energy contained in baroclinic waves (Harr and Elsberry, 2000; Klein, Harr, and Elsberry, 2000; Jones et al., 2003). These transitions are hard to predict and can cause lots of damage at much higher latitudes than expected. They are the object of a specific field of research.

To note, a recent modeling study by Smith, Kilroy, and Montgomery, 2021 attempts to gather all aforementioned aspects of TC life cycle under a unified view based on the rotating-convection paradigm: they show that TC genesis, intensification, mature variations and final decline are all highly asymmetric phases that can be described through symmetric aspects of the asymmetric theory. Moreover, they propose a vision of the TC life cycle which, even without external interactions and in a favorable environment, is intrinsically transient. This transient character is due in their view to the gradual decrease of maximum wind speed and increase of RMW during the mature phase; and to the inevitable breaking of convection by the outflow above the BL due to insufficient ventilation by eyewall convection.

## 1.3 Studying and forecasting TCs

While our knowledge of TCs at the beginning of the 20th century was limited to their climatology, the progressive development of airborne measurements, parametric models, satellite observations, and dynamical realistic models allowed to further witness, analyze, and theorize their properties. Here we draw an overview of the most commonly used tools for TC observation and modeling.

### 1.3.1 TC Observation

The uncertain probability of occurrence, relative fast translation speed, large size, extreme weather conditions, and wide range of interacting processes governing TC dynamics makes their observation a scientific and technical challenge. There were however, in the last decades, increasing observational opportunities.

#### Land-based and airborne observations

The first observations in TCs were performed by commercial ships crossing storms. Nowadays, with improved weather forecast, ships mostly avoid these extremely violent phenomena.

**Moorings, buoys, drifters, and profilers** deployed on existing observational networks, or during dedicated field campaign, can provide measurements at the sea surface (winds, air-sea fluxes, waves), and in the ocean column (currents, temperature, salinity). These observations are however sometimes damaged or hampered by extreme wind, and wave conditions.

**Coastal radars** provide 3D observations of winds and reflectivity (Lee and Bell, 2007) (Fig. 1.7). They have an azimuth resolution of one degree and a range resolution of 0.25 km, with a range of 230 km for velocity measurements (respectively, 1km and 460km for reflectivity measurements). They operate with 14 elevation angles sampling from 0° (i.e. sea surface) up to 19.5°. Given the Earth curvature and the constant azimuth resolution, distant measurements are higher in the atmosphere and sampled at a lower resolution. Coastal radars can however encompass the whole structure of a TC if it is close enough to the radar.

**Airborne measurements** are probably the most detailed in situ measurements of TCs. Dedicated aircrafts have been adapted to fly in TC extreme conditions. They usually follow a cross flight pattern (see Fig. 1.8C) to sample the TC radial structure, and various TC quadrants. They carry several observational devices. **Dropwindsondes** are sondes that are dropped into the TC during the flight, measuring the wind, temperature, humidity, and pressure vertical profiles as they fall (see an example on Fig. 1.8A). **Dual-Doppler radars** operated from aircrafts, provide 3D kinematic and precipitation fields by measuring reflectivity and Doppler-derived wind speeds both on the vertical and horizontal thanks to their multiple antennas (Marks Jr and Houze Jr, 1984; Marks, 2003; Aberson et al., 2006; Reasor, Eastin, and Gamache, 2009) (Fig. 1.8B). These data have

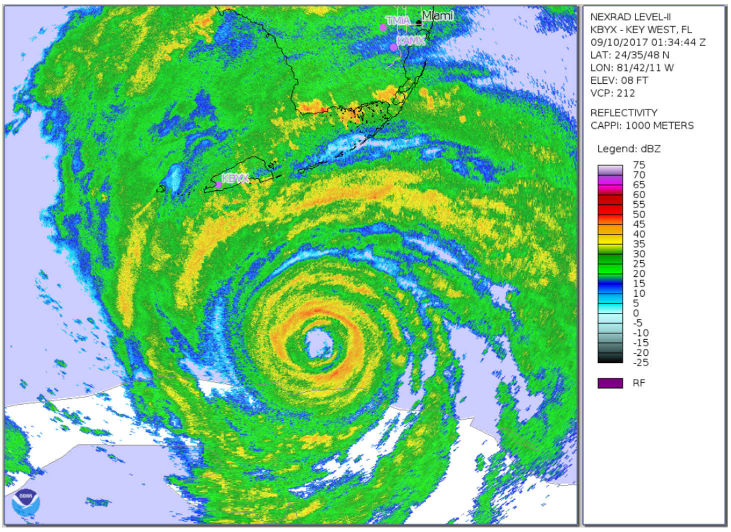

Figure 1.7 – Example of coastal radar reflectivity measurement on TC IRMA (2017) from the KBYX WSR-88D radar (Key West, Florida).

a larger coverage than dropwindsondes, and can be composited or interpolated to provide 3D-gridded wind and precipitation fields, but they can be noisy or inconsistent near the sea surface (Reasor, Eastin, and Gamache, 2009). Finally, the **Stepped Frequency Microwave Radiometer (SFMR)** is a sensor that passively acquire the microwave emissions from the atmosphere and ocean surface. SFMR retrieves surface wind speeds at the nadir (see Fig. 1.8C) from 6 different C-Band channels that measure surface relectivity (Uhlhorn et al., 2007).

Airborne measurement techniques allowed most of scientific progress between the 40s and the 70s, including our understanding of TC formation, intensification and dynamical balances (Stith et al., 2018). They are still extensively used nowadays, and are mainly operated by the National Hurricane Center in the United States, although measurements were recently made by other agencies (Fu et al., 2020). Their two main limitations are: 1) the human and economical resources they require, which limits their use to some basins or some agencies, 2) their limited geographical extent, as they don't encompass the full TC structure being limited to cross-sections, and they are limited to TCs close to US coasts (i.e. Eastern Pacific and Northern Atlantic basins surveyed by NHC).

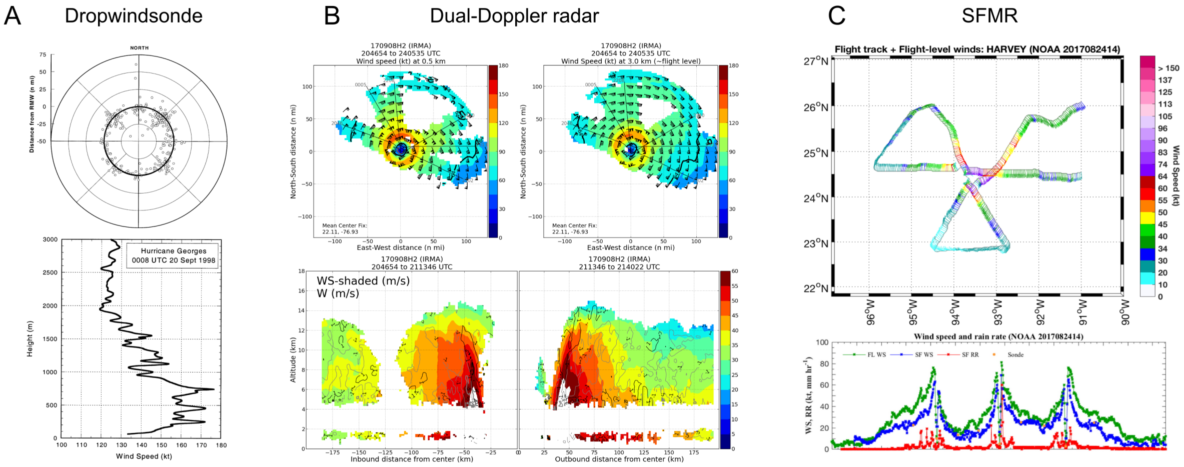

Source : Franklin et al., 2003

NOAA HRD ariborne radar data (TC IRMA, 2017)

NOAA AOML (TC HARVEY, 2017)

Figure 1.8 – Examples of aircraft acquisitions in TCs. (A) Dropwindsondes soundings: Launch locations of eyewall dropsondes during the 1997-1999 period (upper panel) and example of dropsonde vertical profile of wind speed acquired in TC GEORGES (1998), taken from Franklin, Black, and Valde, 2003. (B) Dual-Doppler radar acquisitions during TC IRMA: wind speed fields at 0.5km (upper left) and 3km (right) altitudes, and wind speed vertical cross-section (lower panels), source: NOAA HRD. (C) SFMR acquisition during TC HARVEY (2017): flight track (flight level winds in color) on the upper panel, and along-track profiles of measured flight-level (green) and surface (blue) wind speeds, and surface rain rate (red), source: NOAA

### Satellite observations

Since summer 1961, when Television Infrared Observation Satellite 3 (TIROS-3) captured the first satellite images of hurricanes (Bandeen, Kunde, and Thompson, 1964), the satellite era has brought a whole new diversity of available TC observations, and granted a global coverage of events. Various orbits and sensors allow various types of measurements with assets and drawbacks for each of them. They are summarized in Table 1.1, and detailed hereafter.

**Geostationary satellites** They provide passive measurements of the top of the cloud visible reflectivity and infrared emissions (Fig. 1.9A). A method of classification of TC intensity and life cycle phase based on an assessment of cloud features and TC morphology (and their evolution in time) from visual and infrared images has been developed by Dvorak, 1975. It is still one of the tools used by weather agencies for TC forecast. Geostationary measurements have high spatial and temporal resolutions of respectively 1 km and 1 min, but only give access to the top of the clouds.

**Low-orbiting satellites** They provide measurements around the globe with a given repeat cycle. They therefore may cross TC tracks once or several times (sometimes none, depending on the TC track velocity and direction with respect to platform orbit and swath properties). To note, NASA has recently launched a constellation of 8 micro-satellites (with small sensors using the Global Navigation Satellite Systems signal) with a specific orbit (inclination of 35°) to maximize the coverage in the Tropical band and thus reduce gaps between observations of a given TC (Ruf et al., 2012; Ruf et al., 2018). Here, I will only detail microwave sensors, which wavelength larger than visible and infrared measurements allows to penetrate through clouds. Infrared or visible sensors are also used, for instance to retrieve sea surface temperature (SST), or biogeochemical ocean surface properties such as chlorophyll-a.

**Radiometers** , which are passive microwave sensors, measure the brightness temperature. Regarding TC wind observation, they can be separated into 2 types: multi-frequency imagers, and L-band radiometers.

**Multi-frequency imagers**, such as SSMI (Fig. 1.9C) and AMSR-2, are used to retrieve surface wind speeds (Zabolotskikh, Mitnik, and Chapron, 2013), Cloud Water Vapor, cloud liquid water, and precipitation rate (Meissner and Wentz, 2009; Wang and

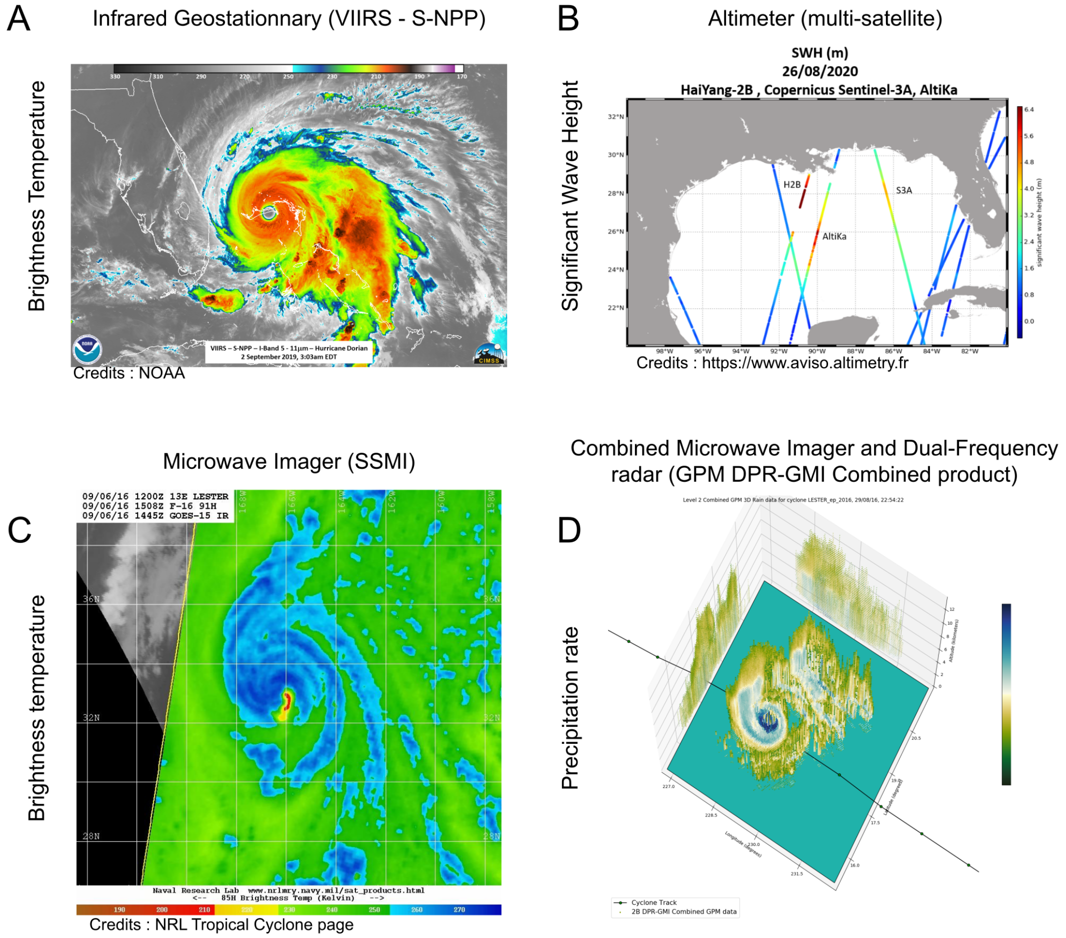

Figure 1.9 – Examples of acquisitions in TCs from several types of satellites. (A) Infrared Brightness Temperature from the Visible Infrared Imaging Radiometer Suite aboard the Suomi-NPP geostationnary satellite (NASA/NOAA) acquired on TC DORIAN (2019). (B) Significant Wave Height measured by 3 different altimeter satellites (HaiYang-2B, Copernicus Sentinel-3A, AltiKa) on TC LAURA (2020). (C) Microwave (91 GHz) Brightness Temperature measured by SSMI on TC LESTER (2016). (D) Precipitation rate from the combined DPR-GMI product measured by the Global Precipitation Measurement (GPM) program, acquired on TC LESTER (2016).

Hankes, 2016) with a resolution between 13 and 70 km depending on the frequency band. Polarimetric radiometers such as WindSat can in addition retrieve wind vectors (Gaiser et al., 2004), but with a lower accuracy than scatterometers.

**L-band radiometers** such as SMOS or SMAP provide estimates of soil moisture and ocean surface salinity by measuring the surface brightness temperature, with a resolution varying between 10 and 40 km. They were shown to be able to retrieve the intense surface wind speeds of TCs (Reul et al., 2012; Meissner, Ricciardulli, and Wentz, 2017, Fig. 1.10A). They allow to estimate the maximum surface wind intensity, and the large scale asymmetry, but not the smaller-scale features. For instance, the eye is not distinguishable for intense contracted TCs (Fig. 1.10A).

To note, radiometers also include microwave sounders, but these devices only retrieve brightness temperature and are thus used to compute atmospheric temperature and water vapor, with no access to wind speeds.

**Active radars** emit a beam and measure the intensity of the backscattered signal. **Altimeters** are nadir single beam radars designed to measure sea surface height. They also measure ocean waves height (Fig. 1.9B), and were shown to be able to retrieve surface wind speed, and precipitation rates in TCs along the altimeter track (Quilfen, Tournadre, and Chapron, 2006). **Scatterometers** (such as QuickSCAT or ASCAT) are multiple viewing angles (multiple or rotating antennas) radars, with a nominal resolution of 25 km that can be reconstructed to 12.5 km resolution estimates (Williams and Long, 2011). They allow to retrieve wind speed and direction (Fig. 1.10B). They are however more sensitive to rain and ocean impacts than L-band radiometers, and saturate at high winds. **Synthetic Aperture Radars (SAR)** use a single antenna with a "synthetic aperture" technique, which consists in processing several consecutive acquired signals to build a synthetic along-track antenna much larger than the real one. Various acquisition modes and polarizations allow to retrieve wave spectra, and wind speeds with a very high spatial resolution ranging from 10m to 1km. A comparison between SAR and SMAP or ASCAT wind fields is shown on Fig. 1.10, and highlights the better representation of the TC eyewall, the small-scale wind features and asymmetries provided by SAR. The SAR 1-km wind field data are the main source of observations used in this thesis, and will be further detailed in the chapter II.

Finally, data such as the Global Precipitation Measurement (GPM) DPR-GMI product combine active and passive sensors (i.e. radar and radiometer) to synthesize a 3D

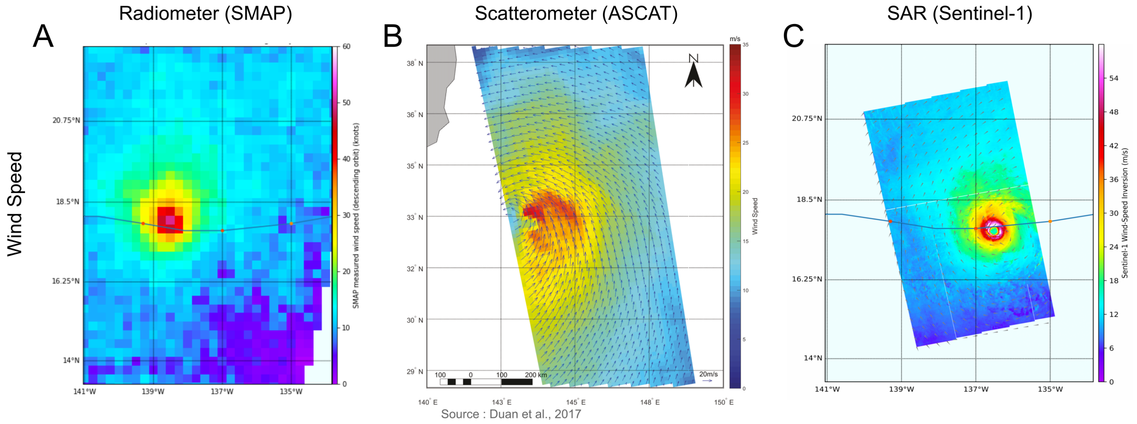

Source : Duan et al., 2017

Figure 1.10 – Examples of satellite radiometer, scatterometer and SAR wind speed retrievals. (A) SMAP radiometer acquisition on TC LESTER (2016); (B) ASCAT scatterometer acquisition on TC LIONROCK (2016) with retrieved directions indicated by black arrows; (C) Sentinel-1 SAR acquisition on TC LESTER (2016).

precipitation field at 5km horizontal and 125m vertical resolutions (Fig. 1.9D). They provide a view of the vertical structure of the vortex, with however significant uncertainty as the retrieval of vertical profiles is based either on model simulations or on observed profiles from secondary sources, which limits their reliability.

## 1.3.2 TC simulation

### Analytical models

The development of analytical idealized axisymmetric models allowed to work on the theory of TC intensification. The CISK theory that first conceptualized the intensification of a TC was the result of the modeling studies by Charney and Eliassen, 1964 and Ooyama, 1964, who modelled the relationship between low-level moisture convergence, and latent heat release in the eyewall. This simple model allowed the first forecasts of TC intensity. Later, Emanuel, 1986 and Emanuel, 1988 developed axisymmetric models to test the validity and limitations of the WISHE theory for TC intensification and the definition of MPI, which proved to be closer to observations in modeling studies than CISK-based models that usually did not reach high intensity and needed too drastic conditions for TCs to appear. Analytical models have been the verification basis for most intensification and internal dynamics theories, notably for the VRW theory developed by Montgomery and Kallenbach, 1997, as well as for the dual spin-up theory developed by Smith, Montgomery,

Table 1.1 – Comparison of different types of TC satellite observations, their main characteristics, their assets, and disadvantages.

| Observation source | Geostationnary | MW imager | L-band radiometers | Scatterometers | SAR |
|---|---|---|---|---|---|
| Band | Visible, Near Infrared and Infrared (∼300THz,∼1$\mu$m) | K to W-band (∼20-∼90 GHz, ∼15mm-∼3mm) | L-band (∼1.4 GHz; ∼20cm) | C-band (∼5.35 GHz; ∼5 cm), Ku-band (∼14 GHz; ∼2cm) | C-band (∼5.35GHz; ∼5cm) |
| Signal | Brightness T | Brightness T | Brightness T | Intensity of backscattered signal | Intensity of backscattered signal (NRCS) |
| Revisit time | - | ∼12h | ∼2-3 days | ∼7h | ∼6 days |
| Measured parameters | Cloud cover | Precipitation, Integrated Water Vapor, wind speed at the sea surface | Wind speed, temperature, integrated water vapor at the sea surface | Wind speed and direction at the sea surface | Wind Speed and direction at the sea surface |
| Product resolution | 750m | 13 km | ∼40 km | 25-50 km | 1 km |
| Assets | Frequency of acquisitions, large swath (∼3000km), can follow TC life cycle evolution, high resolution | Large swath, multiple frequency allows to measure different parameters and improve precipitation retrieval | Large swath (∼1000km), see through clouds, high wind sensitivity | Large coverage (∼800km), see through clouds, direction retrieval | High resolution, see through clouds |
| Limitations | No penetration through clouds | Impacts of rain on wind fields due to elevated frequency | Low resolution, no wind vectors | Signal sensitivity decreases at very high wind speed, Rain, ocean surface current, SST can impact NRCS | Not a large coverage, reduced opportunity to get acquisitions over TCs, Impacts of rain and waves exist |

and Van Sang, 2009.

### Parametric models

Parametric analytical models of the surface wind and pressure fields allow to reconstruct an idealized wind field based on the parameterization of the wind or pressure profile given a limited range of parameters (central and ambient pressure, outflow temperature, RMW, depending on the parameterization) (Ruiz-Salcines et al., 2019). The first conceptual view of a vortex is the Rankine vortex, which describes the vortex wind profile as linear (i.e. solid body rotation, constant vorticity) in its inner part and inversely proportional to the radius after the RMW (with zero vorticity). Later, many parametric models were developped to improve the description of the wind profile. For instance, Holland, 1980 derived a wind profile based on environmental and central pressure and RMW, while Willoughby, Darling, and Rahn, 2006 joined two sections of the profile (inner increasing portion, and outer exponentially decaying portion) on composites from aircraft observations to derive a complete parametric profile. More recently, Chavas, Lin, and Emanuel, 2015 regrouped the physical arguments developed in Emanuel et al., 2004 and Emanuel and Rotunno, 2011, relating the mean radial profile to dynamical conditions on the structure of the boundary layer and outflow, to compute and join the mean wind profile in the inner and outer core areas. Although this theory for the outflow control on TC intensity was criticized by Montgomery, Persing, and Smith, 2019; Montgomery and Smith, 2019 as having problematic aspects regarding the causality of wind spin-up and the importance given to asymmetric processes, the attempt made by Chavas, Lin, and Emanuel, 2015 to synthetize a physical theory into a parametric model is relevant regarding forecast and risk assessment improvements. Such parametric vortices are indeed widely used for storm surge and wave forecasting, as well as for ocean forcing applications.

### Dynamical models

With the increase in computer capacity, dynamical models have developed and have been increasingly used over the last decades. Dynamical models solve the Navier-Stokes (NS) equations in three dimensions on discrete time-space grid. Subgrid-scale processes, that cannot be solved are parameterized. As these models include the various processes involved in TC formation and evolution, their realism depends both on the resolution, and the parameterization of unresolved processes.

**Impact of resolution** Coarse simulations such as climate simulations run for climate change scenarii have resolutions ranging between 25 km (for high resolution runs focused on specific processes) and 200 km (for global runs). They do not correctly represent TCs producing only cyclone-like vortices, which presents some characteristics of TCs but much lower intensities (Sugi, Noda, and Sato, 2002; Camargo and Sobel, 2005; Scoccimarro et al., 2011). They also fail in some regions to accurately represent the favorable environmental conditions for tropical cyclogenesis. They can however be used to run global simulations over several years, providing useful material for climate studies. On the other tail of model spectrum, Large Eddy Simulations (LES) have a much higher resolution of a few tens of meters, which allows featuring very small-scale processes such as BL rolls (Zhu, 2008) and turbulent mesoscale eddies (Rotunno et al., 2009). Their use over a whole basin, and during an entire TC life cycle however requires unrealistic computational resources. Regional mesoscale simulations are a compromise between these two types of simulations. They can quite realistically represent the TC life cycle, its maximum intensity, and small scale processes of interest like polygonal eyewalls or VRWs (Wang, 2002a; Wang, 2002b; Gentry and Lackmann, 2010). It is the type of simulation that was used in this thesis.

**Coupled modeling** As TCs are strongly coupled systems, coupled modeling is also extensively used for TC forecast and research (Lin et al., 2005; Bender et al., 2007; Wu, Lee, and Lin, 2007). It consists in running concurrently atmosphere, ocean, and wave models, and exchange information that impact their respective solving, building a model that concurrently solves the different environments. For instance, in an ocean-atmosphere coupled model, the ocean model provides the sea surface temperature and currents to the atmospheric model, which computes the surface heat and momentum fluxes required as surface condition to the atmosphere dynamics, and provides them back to force the ocean model. Coupling consequently improves the representation of cold wakes, wave field asymmetries, and consequently sea-surface drag, air-sea surface exchanges in general, and their feedback to the TC itself (Lengaigne et al., 2019; Pianezze et al., 2018; Jullien et al., 2014). It is however computationally expensive, as it requires to run several models to solve the different Earth compartments, and this cost increases with the resolution of the different models. Coupling was not used in this thesis for the aforementioned reasons, and because the focus was not on the impact of air-sea exchanges, but it is seen as a promising perspective to improve the realism of the simulations as well as to study the impact of air-sea interactions on the studied TC internal fine scale features formation and evolution.

**Data assimilation in models** For TC forecast or reanalysis, dynamical models can also assimilate atmospheric and ocean observations to partially constrain the simulations to better match observed events. Indeed, model solutions are not perfect, they are discretized on a grid of a certain resolution, and sub-grid processes are parameterized leading to uncertainties and eventually bias of the model solutions compared to observations. On top of that, NS equation mathematical solution is unknown, and its numerical solution relies on the stochastic representation of turbulence, leading to a stochastic "nature" of the atmosphere and ocean dynamics, limiting their forecast. Assimilation of observations is thus a way to constrain the model solution towards observed data. However, as it modifies model physics, free simulations (without assimilation) are preferable to study the properties of a specific physical process.

### Statistical models

Statistical models are extensively used for TC forecasting, and were until the 2000s the most performing tools to predict TC track and intensity (DeMaria and Kaplan, 1994; DeMaria and Kaplan, 1999; DeMaria et al., 2014). They use linear statistical regression techniques to predict intensity changes, taking as inputs several parameters characterizing the current state of the TC (i.e. its maximum intensity, intensification rate and track), climatological conditions, and large-scale environmental descriptors such as vertical wind shear. The development of dynamical models over years allowed to compute these large-scale parameters directly from simulations, creating a new category of models called statistical-dynamical models, that have a lower computational cost and runtime and equivalent or better performance than dynamical models alone regarding TC intensity forecasting (Kucas, 2010; DeMaria et al., 2014; Neetu et al., 2017).

### 1.3.3 TC Forecast

TC forecasting improvement remains an important goal of TC research, as it could help reducing human and material casualties. TC forecast relies on a cooperative use of modeling and observation tools. Forecasters base their forecast on the joint analysis of available observations (in situ, and satellite), dynamical, and statistical modeling of TC events. Observations are also used as input parameters for statistical models, and for their assimilation in dynamical models: the more frequent and reliable the observations, and the more effective the assimilation techniques, the better the forecast. Ensemble numerical simulations are run to take into account the uncertainty associated to initial conditions, observations, and stochasticity to provide probability maps of track and intensity of a given event.

Track forecast has nicely improved in the last decades, with errors going down to less than 185km within 72h, and less than 55km within 12h (against respectively 740km and 140km in 1970) (DeMaria et al., 2014; Cangialosi and Franklin, 2019). TC tracks are indeed mostly determined by the synoptic flow, and in particular the combination of beta-drift and large-scale shear or tropospheric events. These large-scale processes are now quite well-resolved and represented by dynamical models. TC track forecasts have thus improved along with those of synoptic-scale.

Intensity forecasts, on the other hand, although having considerably improved (errors under 15 knots within 120h against almost 25 knots 20 years ago), still remain quite inaccurate (almost no improvement of the 12h forecast, which remains stuck around 5 knots of error), and brutal changes of intensity such as Rapid Intensifications (RI) are often badly forecast (Cangialosi and Franklin, 2019). The limited efficiency of intensity forecasts is due to a combination of factors. Our still limited understanding and representation of BL physics is one of the most limiting factors: accurate observations are rare, notably regarding the nature of fine scale BL processes under extreme wind conditions, as well as air-sea exchange processes, and their role in TC dynamics and thermodynamics. The role of the ocean subsurface structure in TC intensity predictability is also crucial (eddies, ocean mixed layer temperature and density), and still poorly observed in real-time. In the atmosphere, moist convection added to vertical wind shear disturbances can cause upscale error growths in predictability as shown by Zhang and Tao, 2013. Improving TC intensity predictability thus relies on both improved observations of TCs (notably in the BL and under the ocean surface), and improved numerical simulations (towards increased resolution, and improved resolution of turbulent and coupled processes at the air-sea interface). A better physical understanding of TC dynamics, and especially of the BL is one of the crucial point, and my work contributes to this goal.

## 1.4 Thesis problematics and outline

I summarized in this introduction the different aspects of TC dynamics, and the main challenges of TC meteorological research and forecast. TCs still lack understanding in many ways, making them both a mysterious and exciting domain of geophysics: as for many geophysical processes, their large-scale dynamics are tightly related to processes of smaller-scale, even reaching turbulence scale. Moreover, their extreme nature makes their observation difficult and, consequently, their parameterization and modeling too.

In recent years, the growing abilities in high-resolution modeling and the improvement of observational coverage and resolution under TCs has cast light upon the small-scale and asymmetric features of TC formation, intensification and intensity variations. Specifically, the unified theory on TC formation, the rotating-convective paradigm for TC intensification, the VRW theory regarding TC intensity restoration and the related theories on eyewall and eye dynamics all rely on asymmetric aspects of TCs. This recent view of the TC as an asymmetric system, strongly controlled by its Boundary Layer (through the BL spinup theory notably) and governed by energy transfers and internal waves propagating throughout its radial and vertical structure, was the conceptual basis for my thesis.

Spaceborne SAR measurements appeared as a valuable tool in this context as they allow to study the TC inner-core BL structure thanks to their surface-level, high resolution, and large spatial extent acquisitions that encompass the whole TC vortex. This thesis thus also relies on an important effort to gather these observations and analyze them concurrently with model simulations. Both observations and modeling are extensively used for TC study, but rarely in synergy: observations are used as a validation dataset for modeling studies, and models as a support to design new types of observations, but few studies rely on a joint study of both observation and modeling sources. As my lab gathers researchers with both expertises, the environment was favorable for such an approach.

The work that I did during my PhD follows three major steps: first, I set up a working environment of observation and modeling suitable for TC study; second, I figured out a procedure able to study these two data sources jointly and take out their individual advantages, while identifying and managing their drawbacks; finally, I used this joint dataset to address the relationships between the observed asymmetric fine-scale structures of the inner-core and their evolution, and the modulation of TC intensity. As TC genesis, intensification and mature life cycle are distinct domains of TC studies (although the recent theory draws numerous bridges between them notably through the rotating-convective paradigm), I focused my studies on the mature TC life cycle, i.e. the evolution of the TC when reaching the level of a Tropical Storm (above 18 m/s). This part of the TC life cycle is indeed of great interest for operational meteorology as it is both hard to predict and particularly dangerous, and is thus also more sampled by SAR acquisitions. SAR images were used as a tool to measure the wind field radial and azimuthal characteristics, notably the sharpness, size and asymmetry of the eyewall and maximum wind ring, and their energy distribution. The dynamical modeling framework set up jointly with this observational dataset was designed to provide a realistic representation of these properties, and to be comparable and complementary to SAR. In particular, it was used to assess the time evolution of the TC structure, which is not accessible from SAR observations due to the SAR sampling frequency. A statistical analysis was finally designed, using a machine learning approach, to evaluate the added-value and predictability potential of SAR and model extracted parameters.

The technical background for my thesis is thus a joint dataset including SAR surface wind speed observations, and dynamical simulations used to mimic SAR observations with a higher temporal sampling resolution. This technical support was used to address the following problems:

1. **Which aspects of TC internal dynamics can we diagnose from high resolution surface wind speeds ?**
2. **What does it bring to our understanding of TC intensity variations ?**

The overarching hypothesis is that SAR observations and joint simulations could help diagnose internal vortex properties linked to symmetric BL spinup, asymmetric convective structures (such as VHTs and eyewall mesovortices), and energetic processes (such as vorticity transport by VRWs). Thus, given the link drawn by recent theories between these interconnected features and TC intensity restoration and variations, a statistical study of SAR-extracted parameters could help improve the diagnostic and forecast of ongoing changes in the TC's internal structure and intensity. More specifically, the main diagnostics performed on SAR images and dynamical model outputs were based on these interrogations:

- **How can we estimate TC symmetric properties in order to relate them to the symmetric TC theory (spinup, resilience) ?**
- **Can surface wind asymmetries measured from SAR be related to VRW, VHT and mesovortical activity and, by extension, to TC intensity variations?**
- **What is the added value of SAR symmetric and asymmetric estimates in terms of predictability of TC intensity changes ?**

The second chapter of the thesis describes the framework and methodological steps followed to set up the database for both SAR observations and numerical simulations. SAR technology is introduced, along with the different steps of image processing, and parameter extractions allowing the estimation of inner-core parameters. The SAR database is presented, including a validation of the dataset. The modeling infrastructure is then described i.e. the WRF model, the configuration and parametrizations of our set of simulations. I finally present the statistical methods used to study SAR observations and simulations, including a machine learning algorithm designed to link SAR-extracted parameters to TC intensity variations, and a method deriving temporal variations of the internal structure from WRF simulations and linking them to vortex-scale changes.

The third chapter focuses on the exploitation of the SAR database and the statistical study of SAR-extracted TC properties, and their link with TC intensity variations. This chapter is based on an article submitted to in Journal of Atmospheric Sciences in 2020. It further describes the SAR extraction methods, and the link between intensity and both radial structure and azimuthal asymmetry. Contraction and sharpening of the radial profile, as well as decrease in azimuthal asymmetry coefficients, and broadening of the spectral decomposition towards high wave numbers are observed with increasing intensity. The machine learning method is applied to show the improvement in dissociating intensifying and declining TCs allowed by the measurement of small-scale azimuthal wavenumbers (especially WNs 4-5) composing 1-D characteristic signals such as maximum wind distribution or eye shape.

The fourth chapter intends to go further in the estimation of temporal correlation between inner-core structure and vortex-scale properties by introducing the modeling database, based on WRF regional high-resolution simulations. The temporal resolution of simulations indeed allows to improve the study of internal structure by going from snapshot-estimated diagnostics to temporal derivatives and second derivatives of these properties, and thus have access to energy propagation and WN transfers, which are essential in the frame of intensity restoration theories. The study performed on WRF outputs reproduces the analyses performed on SAR images, adding new variables to quantify temporal changes. Case studies and average properties are analyzed to highlight the connection between, notably, changes in the azimuthal spectra of the eyewall and maximum wind areas, and intensity variations. The machine learning algorithm is re-applied to assess the contribution of time-dependent structural descriptors to the classification of intensitfication rates, showing that they more significantly improve the scores than non-temporal variables.

A final chapter summarizes and synthesizes the results of both studies, and discusses several perspectives and fields of improvement for the future.

Chapter 2

# DATA AND METHODS

## 2.1 Motivation and constraints

This work relies on a dual approach combining a newly gathered database of TC SAR observations, and a set of realistic dynamical simulations.

SAR observations are still uncommon in TC studies for several reasons:

- the relevant dual polarization for TC wind retrieval is available on recently launched SARs (only Radarsat-2 launched in 2007, Sentinel-1 A and B launched in 2014 and 2016 and Gaofen-3 launched in 2016)
- algorithms of dual-polarized wind inversion are quite recent (Mouche et al., 2017)
- the availability of a relatively large number of useful acquisitions is also recent, relying on an effort made by scientists and space agencies to schedule acquisitions over TCs based on their track forecasts and other priority requirements.

Such observations have the advantage of being innovative with possible new applications in TC research and forecasting, but also require to develop new processing methods compared to more widely used observational sources.

The outstanding resolution of the SAR allows to sample small-scale structures such as eyewall mesovortices and polygonal eyewalls and convective asymmetries in the inner-core (cf. the triangular eye shape featured on Fig. 2.1A). SAR post-processing and product delivery are however associated with several issues: wind directions estimated from a mix between SAR surface wind streaks and interpolated dynamical models are not reliable for the moment; the retrieved wind field can be impacted by rain signatures that are not entirely understood and dealt with yet (see the example of rain-caused attenuation in the maximum wind area featured on Fig. 2.1A): some anomalies related to the wind inversion algorithm such as subswath signatures can still appear. Moreover and most importantly, although SARs can capture a wide range of TC events on all basins and categories, their temporal sampling is very sparse, and there is no continuity in acquisitions. Their characterization of TC surface wind speeds is thus limited to instantaneous snapshots and

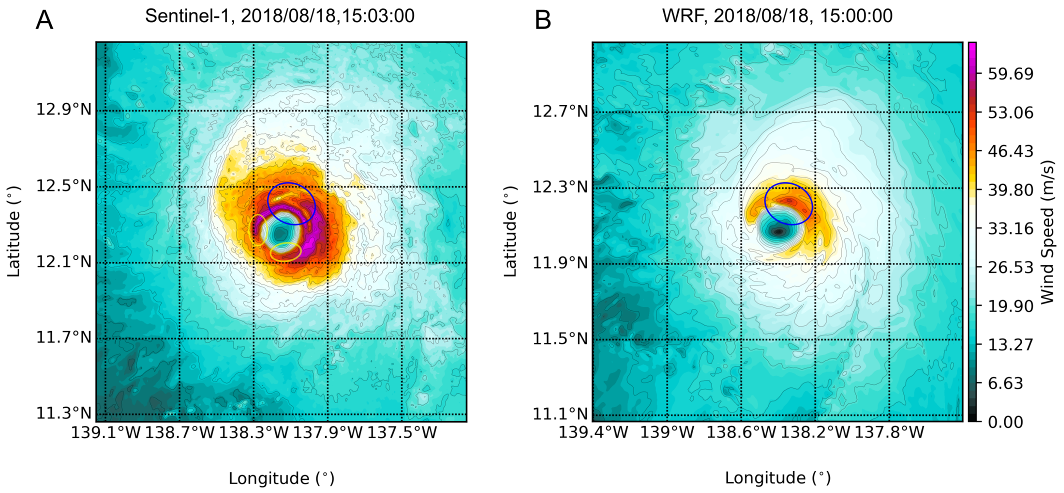

Figure 2.1 – Comparison of a SAR acquisition (A) and a WRF simulated surface wind field (B) illustrating the specificities and issues of each dataset. Red circles show the location of the maximum wind area, which is not shown by the SAR due to heavy rain attenuation. Yellow ellipses highlight distortions of the eye shape on the SAR image, characteristic of the presence of eyewall mesovortices.

only one or a few snapshots per TC event.

The study of SAR observations is thus, in the present thesis complemented by 3D realistic dynamical simulations, which are used to provide additional information for the interpretation of high-resolution TC wind fields. Dynamical modelling brings the temporal continuity missing in SAR observations, but also brings its own issues and drawbacks. For instance, the simulated wind field, although showing small-scale structures comparable with SAR, is smoother and does not reproduce the maximum intensity (Fig. 2.1B). The simulated wind fields are thus evaluated, their limitations are discussed, but overall they are used to estimate temporal changes in the TC inner-core surface wind field at short-scale (i.e. energy transfers and distortions occurring on hourly scales in the eyewall and maximum wind areas) and longer time-scale (i.e. intensity variations and structural changes at a daily or weekly scale). The access to the complete life cycle of simulated TCs is crucial in the frame of this study, as one goal is to link inner-core dynamics to intensity variations occurring either during the initial intensification, or the mature state variations, or the final decline. In the following subsections, I first describe SAR imagery technology and the modeling framework. I then describe the methodology used to characterize the TC structure and its evolution with intensity variations.

## 2.2 SAR observations

### 2.2.1 SAR overview

Synthetic Aperture Radar (SAR) technology was invented in 1951 by Carl A. Wiley and has become over the years a prominent remote sensing technique. It is a side-looking microwave sensor operating mainly in L (1-2 GHz), C (4-8 GHz) and X (8-12GHz) bands. It provides kilometer to meter-resolution two-dimensional images used for numerous applications including military surveillance, forestry, glaciology, oceanography or volcano and earthquake monitoring. SARs can estimate surface roughness by measuring the intensity of the backscattered signal, i.e. the intensity of the signal received after its emission by the radar and reflection by the Earth surface. The Normalized Radar Cross Section (NRCS), i.e. the backscattered intensity normalized according to individual scene geometry and radiometry (Small, 2011), is in practice the variable measured by SARs and will be referred to hereafter. As a radar, SAR has two substantial advantages regarding the observation of the sea surface. First, as an active sensor emitting its own source signal, it can measure water and ground surface properties indifferently by day or night, contrary to optical radiometers installed on geostationnary satellites that need an external light source to be able to record. Second, it emits in microwave wavelengths which allows a good penetration of the atmosphere, so SARs can reach the Earth surface through clouds. The first operational spaceborne SAR was launched in 1978 aboard the SEASAT-A NASA mission, later followed in the 90s by ERS-1 and ERS-2 (European missions, 1991 and 1993), JERS-1 (Japanese mission, 1992), RADARSAT 1 (Canadian mission, 1995), and ENVISAT (European mission, 2002). It has since then become a common source of spaceborne Earth surface observation.

### 2.2.2 SAR high resolution

SAR provides estimates of the sea surface wind fields at a spatial resolution of 1km. The resolution of raw NRCS data is even higher, reaching about 10 meters. Other remote sensing techniques such as scatterometers and radiometers provide retrievals of 2D surface wind speed estimation, but with much lower resolution (usually 12.5 to 25 km for scatterometers, about 40 km for radiometers). Moreover, scatterometers saturate above 15-20 $m.s^{-1}$ (Bentamy, Croize-Fillon, and Perigaud, 2008; Chou et al., 2010; Yang et al., 2011; Chou, Wu, and Lin, 2013) while SAR does not show saturation even at category 5 above

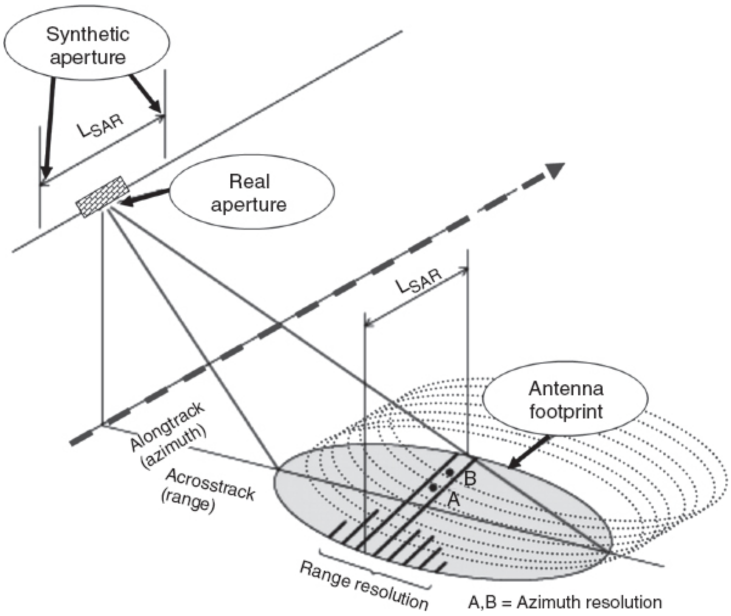

Figure 2.2 – Schematic of Synthetic Aperture Radar operation

60 $m.s^{-1}$ (Combot et al., 2020). The exceptional spatial resolution of SAR is allowed by a specific technology. The resolution is determined differently on range (cross-flight direction) and azimuth (along-flight direction) axes. The diagram on Fig. 2.2 shows the operation of SAR acquisitions and illustrates its resolution. Range resolution is directly determined by the emitted pulse frequency and time length. The position of an object on the surface located at a given range from the satellite is indeed deduced from the time between emission and reception of the signal. Given this time lapse, the incidence angle and the speed of the electromagnetic signal, the distance, and thus the position in geographic coordinates can be computed. The resolution is determined by the time necessary to emit and receive two signals at the closest and furthest ranges from the satellite (i.e. inner and outer limits of the beam on Fig. 2.2): the pulse frequency must exceed this time lapse to avoid confusion between two signals emitted and received from a given incidence angle. This threshold can be reduced by limiting the time length of the pulse, however a reduction causes a critical loss of emitted power. In practice, modulating the frequency of the emitted signal allows to gain power while lowering the pulse length, which allows to increase the range resolution up to a few meters (5 meters for Sentinel-1). Moreover, the swath width is further increased by emitting consecutively at several incidence angles, creating a ground swath composed of several aligned subswaths (the sketch on Fig. 2.2 shows only one large subswath). The azimuthal resolution is determined by a different princi-

ple called synthetic aperture. This technique consists in processing together the phase and amplitude of several consecutively emitted signals to build a synthetic along-track antenna much larger than the real one. A given point on the ground being illuminated during a given amount of time by the moving satellite (see consecutive beams on the ground on Fig. 2.2 illuminating points A and B several times), a synthetic echo can be computed using the Doppler shift between the different echoes. The point is thus virtually illuminated by an array as big as the satellite path during this time ($L_{SAR}$ on Fig. 2.2), i.e., the beam width on the ground. This increase in the antenna size narrows the beam, resulting in an increase in azimuthal resolution.

### 2.2.3 SAR operations

**Acquisition modes**

In practice, SARs can be operated with different exclusive configurations and settings to provide observations suited for various applications. In this study, we rely only on Sentinel-1 A & B, and Radarsat-2 acquisitions, which provide dual-polarization, i.e. acquire data using both co-polarization (vertical-vertical (VV) or horizontal-horizontal (HH)), and cross-polarization (vertical-horizontal (VH) or horizontal-vertical (HV)) modes. The combination of these two polarization modes to retrieve surface wind speeds was introduced by Mouche et al., 2017. The purpose is to use the lower saturation of cross-polarization at high wind speeds to compensate the saturation of co-polarization, and on the other hand to use co-polarization in low signal-to-noise areas where the cross-polarization is noisier (cf. Fig. 4 of (Mouche et al., 2017)). This combination allows a great improvement of retrieved surface wind speeds at all TC categories. We thus only describe the operating modes of these three satellites.

Sentinel-1A&B were launched respectively in 2014 and 2016 by ESA in continuity of ERS-1&2, and ENVISAT. They are on a Low Earth Orbit (LEO) of 700km, and have an orbital period of 98.6 minutes, and a revisit time of 12 days combining the 2 satellites. They operate in C-band with four different and exclusive acquisition modes summarized in Table 2.1. Only IW and EW modes are used to compute 1km surface wind gridded products used in the present work.

RADARSAT-2 was launched in 2007 by the Canadian Space Agency (CSA). It is on an 800km LEO orbit, and has an orbital period of 100.7 minutes, with a revisit time of 24 days. Similarly to Sentinel-1, it is equipped with a C-Band SAR with several ex-

Table 2.1 – Summary of Sentinel-1 SAR acquisition modes and their main characteristics

| Acqsuisition Mode | Swath width | Nominal resolution | Main ESA applications |
|---|---|---|---|
| Interferometric Wide Swath (IW) | 250km | 5x20m | Main mode, Land Imaging |
| Extra Wide Swath (EW) | 400km | 20x40m | Sea-ice, oil spill monitoring |
| Strip Map (SM) | 80km | 5x5m | Small islands, natural hazards |
| Wave Mode (WV) | 20x20km | 5x5m | Wave and ocean surface |

clusive acquisition modes. The one used to retrieve SAR wind speed products is the SCW (SCANSAR-Wide) mode resolved at 100x100m with a swath width of 500x500km. RADARSAT-2 was the first SAR to provide dual-polarization.

### Operational constraints

The memory and technical requirements relative to SAR acquisitions prevent these sensors from recording continuously. Moreover, the different acquisition modes are exclusive and cannot be activated simultaneously, while several modes can be of interest for a given event (for instance, a TC can cause natural hazards on islands, and there is a choice to make between IW, EW, or SM modes). Thus, acquisitions must be planned and respond to economical and political constraints, and the satellite must be remotely activated to record. Due to these requirements, and to the small revisit period of their low orbits, the number of SAR wind field acquisitions over TCs is reduced: not all TCs can be sampled, only one or few acquisitions are usually obtained for a given event, and fewer get to encompass the whole vortex as the forecast tracks transmitted before acquisitions may be inaccurate, leading to misses in the planned acquisitions. The operational planning of SAR acquisitions for their use in TC observation is thus a complex procedure that results from a consequent effort of coordination between meteorological forecast centers, research centers, and mission planning teams in space agencies.

### The SHOC acquisition campaign

The SAR acquisitions used for this study are the result of a cooperation between IFREMER (my employer for this thesis), CLS (an organism dedicated to satellite data collection and processing) within their VIGISAT program, and ESA-Copernicus (European Space Agency managing the Sentinel-1A and B satellites). Collection of Radarsat-2 acquisitions was also carried out thanks to a partnership between VIGISAT and the Canadian Space

Agency, which plans and processes Radarsat-2 acquisitions. This acquisition campaign named SHOC (Satellite Hurricane Observation campaign), to which I took part during my thesis, allowed over the past few years (SHOC started in 2016) to build a consequent database of SAR TC images (cf. subsection 2.2.5).

### 2.2.4 SAR processing: from acquisitions to L2 wind product

The processing of SAR images involves a specific chain of management, coordinated between space agencies and research institutes. In the case of Sentinel-1 data used in this work, the level-0 data are first processed by ESA to level-1, and then by IFREMER and CLS to level-2. The level-0 raw data collected by the satellite are processed to level-1 by projecting them on ground range coordinates, yielding pixel intensities on a regular geographic grid. The Normalized Radar Cross Section (NRCS) is computed on level-1 data through radiometric calibration of pixel intensities. The calibration consists in correcting the noise present on the recorded NRCS due to radiation, by applying coefficients that depend on the absolute range, the subswath considered, and on the range inside each subswath.

The level-2 wind field can then be retrieved by applying the Geophysical Model Function (GMF). This processing step is carried out by both IFREMER and CLS for the data used in this work. Surface wind speed is related to NRCS through momentum transfers at the sea surface, i.e. wind-induced waves that deform the sea surface increasing its roughness and thus the backscattered signal. The GMF thus computes wind speed from the NRCS considering incidence angle and satellite attitude parameters. Figure 2.3 illustrates level-1 NRCS and level-2 retrieved wind field for a TC case. It shows that the impact of the incidence angle (shown by the gradual increase of signal amplitude with range) seen on the NRCS is corrected in the retrieved wind field.

The GMFs used in our case are the CMOD5N (Hersbach, 2010) GMF (used originally for ERS-2 and ASCAT radiometers) for co-polarization mode (VV), and the MS1A-HW (Mouche et al., 2017) GMF (revised MS1A for high winds up to 70m/s) for cross-polarization mode (VH). This combination of co-and cross-polarizations intends to mitigate the disadvantages of both modes (Mouche et al., 2017): co-polarization (VV and HH) mode is less noisy and better renders wind directions but saturates at high wind, cross-polarization (VH or HV) mode has a higher signal-to-noise ratio but is more sensitive to high winds (Vachon and Wolfe, 2010; Zhang and Perrie, 2012). The GMF and retrieved winds were validated by Mouche et al., 2019. A more extensive validation was

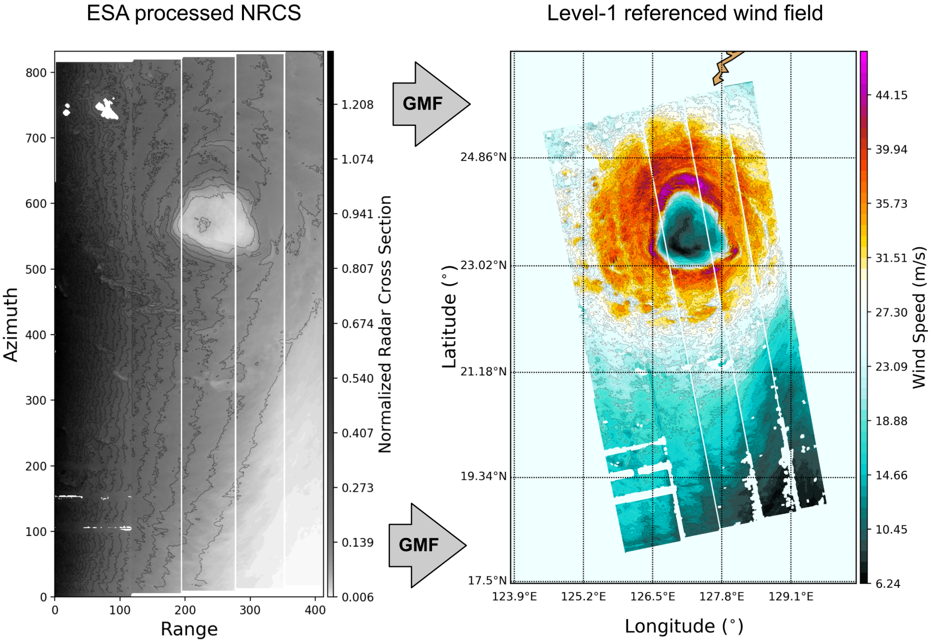

Figure 2.3 – (A) Level-1 NRCS from SAR acquisition on TC TRAMI (2019/08/28,09:35); (B) Surface wind field retrieved after application of CMOD5n-MS1A-HW GMF

performed in the study of Combot et al., 2020, which I co-authored (Appendix I), through comparison to SFMR flight high-resolution data and best track estimates and proved to be very accurate. The study conducted in Combot et al., 2020 was focused on the validation of maximum wind, RMW, and characteristic 34, 50, and 64 knots wind radii. Very good agreement between SAR and SFMR for maximum wind speed estimates was found (RMSE of $3.86 m.s^{-1}$ with SFMR, and $6.71 m.s^{-1}$ with best-tracks), as well as a fair agreement for RMW (RMSE of 3.17km with SFMR, and 11.6km with best-tracks), with however several outliers. The causes of these discrepancies between SAR and BT or SFMR were investigated, and rain impacts and secondary eyewalls were identified as the main causes of wrong estimations on SAR images, while other discrepancies were mostly attributed to best-track coarseness. This validation study was focused on best-track equivalent parameters, with no analysis of the internal structure, which is the purpose of the present work.

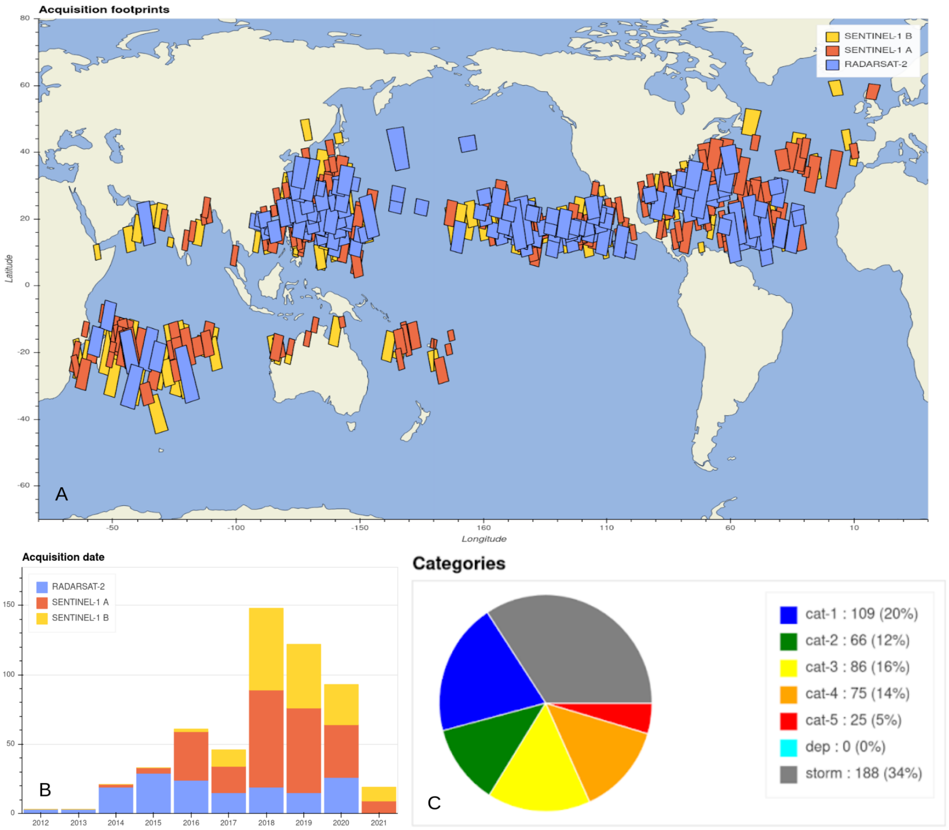

Figure 2.4 – Summary of Sentinel-1 and RADARSAT-2 acquisitions over TCs since 2012. (A) Footprints of all images colored by satellite; (B) Number of acquisition by season (colored by satellite); (C) number of acquisition by TC category. Taken from `https://cyclobs.ifremer.fr`

### 2.2.5 The SAR dataset

The SAR dataset gathered through the SHOC campaign, and processed through the dual-polarization GMF is regularly updated with the most recent TC-matching SAR acquisitions. All new upcoming acquisitions are processed through the post-processing algorithms, and added to the level-2 database of SAR images at IFREMER. The composition of this dataset to this day is summarized on Fig. 2.4, taken from the CYCLOBS data access and visualization website gathering SHOC acquisitions.

As shown by the geographical and temporal distributions represented on Fig. 2.4A,B, the dataset covers all TC ocean basins, and provides a large number of acquisitions (548 in total, 396 from Sentinel-1, and 153 from Radarsat-2), with much more Sentinel-1 acquisitions since 2016 (beginning of the SHOC campaign). The dataset also covers all TC categories (panel C). This dataset includes all images that were programmed during TC acquisitions. However, a number of them are missed acquisitions, i.e. planned to hit the TC eye on its trajectory but not matching it. These images (99 in total) were not considered in the present work as it is focused on the TC's inner core. Other images were ignored for the purpose of the analysis:

- tropical storm category (188 images, about one third of the complete dataset) was not considered, as these acquisitions often show no formed eye, and thus impede or degrade the estimation of TC properties
- acquisitons too close to land or islands were also ignored to avoid landfalling hurricanes and land interactions in the analyses (as the focus is on intensity modulations of the mature TC); they represent about 50 images from the original dataset.

The true processed dataset, although constantly evolving with the addition of new acquisitions, was thus originally composed of 173 Sentinel-1 acquisitions, and 70 Radarsat-2 images, eye-matching, above Tropical Storm category, and suited for the analysis of TC inner-core properties and intensity modulations.

## 2.3 Best-track data

Best-track files are of formatted files provided by meteorological agencies to describe the main characteristics of TC events: the center longitude and latitude, the maximum wind, the minimum pressure, the storm nature (i.e. tropical storm, depression, minor/major TC, or extratropical storm), and (if available) a few characteristic wind radius.

They are provided by various agencies which are organized to provide a complete tracking and surveillance of all TCs globally. These agencies can be national or regional meteorological centers such as the Regional Specialized Meteorological Centers (RSMCs) located in Honolulu, La Réunion, Miami, Nadi, New Delhi and Tokyo that are responsible for TC monitoring in their assigned region (for instance, Miami RSMC provides best-track information for TCs in the West Atlantic and East Pacific basins). Australia and New Zealand also have TC Warning Centers (TCWC) in Brisbane, Darwin, Perth and Wellington dedicated to TC vigilance. National agencies such as the Shanghai Typhoon Institute of the Chinese Meteorological Administration, the Hong Kong Observatory, the Australian Bureau of Meteorology or the American National Hurricane Center (NHC), Central Pacific Hurricane Center, Joint Typhoon Warning Center (JTWC) and National Center for Atmosperic Research (NCAR) also provide TC tracking files and re-analysis. These numerous sources provide partial TC information often restricted to their own region and basin of interest. Moreover, they are not all coordinated which can lead to discrepancies depending on the methods used for TC monitoring. Due to these discrepancies, and the absence of a globalized database grouping these different sources, the International Best Track Archive for Climate Stewardship (IBTrACS, Knapp et al., 2010) was developed in 2010 by the National Oceanic and Atmospheric Administration (NOAA, USA) to gather TC information, and provide a uniform and complete best-track dataset. The IBTrACS dataset gathers best-track data over a period going from 1848 to present. All sources are provided separately in the same format, except when they are coherent and can be grouped (such as different WMO agencies that are all gathered under a unique WMO ID, or USA agencies that are gathered under the USA ID). The USA source from the IBTrACs database was used in the present work as the best-track reference. In some rare cases where IBTrACS was not available (usually most recent events), the ATCF (Automated Topical Cyclone Forecasting) database was used to complete the database, but this only concerns a very small part of our dataset (3 images over the 200 composing the final database). ATCF provides near real-time provisional best-track files that are available for even the current storms and TCs, although not re-analyzed and thus less reliable than IBTrACS. It also provides re-analyzed best-track files at the end of each season, those tracks are included in the IBTrACS database.

IBTrACS is designed to be used for research purposes, and is extensively cited and used in TC scientific literature.

Best-track files were used in the first part of this work to retrieve the metadata of each SAR image, i.e. to identify the event, basin, and category of the observed storm. They are also used as a validation/comparison basis to compare statistical distributions and relationships describing the internal structure retrieved from SAR. Finally, best-track information is used in our study to estimate temporal variations of characteristic variables, given the sparse distribution of SAR acquisitions over time, and the consequent impossibility to have a temporal continuity. In the first step of our extraction method, each SAR image is thus matched with the corresponding best-track file based on the netCDF file characteristics (i.e. date and position of the image). Before even opening the SAR netCDF files and retrieving the wind field, a first estimation of maximum intensity, Radius of Maximum Wind (RMW), translation speed, and intensification rate is thus obtained by interpolating the best-track vectors at the acquisition time. Those estimations however have to be carefully considered and criticized given their coarse resolution, and the fact that they gather many different sources including some that do not describe the surface wind field (as IR images describing the cloud cover, or coarser resolved measurements from radiometers). We indeed showed in Combot et al., 2020 that several discrepancies between SAR and best-track maximum winds were caused by the interpolation of best-tracks that have a coarser resolution in their maximum wind values.

## 2.4 Numerical simulations

Given the wide representation provided by the SAR dataset (about one hundred different events are sampled, describing all intensity categories and basins), setting up a database describing the life cycle of all these events with a dynamical model, at an effective spatial resolution of about 1km (which is the SAR product resolution), was not feasible. The adopted simulation framework is thus a compromise between a statistical description of TCs (i.e. a sufficient variety of situations, basins, intensity changes), and simulating realistic internal dynamics and the corresponding life cycle changes and potential interactions between both scales, but at a reasonable computing cost. To achieve such a compromise, seven TC simulations were launched to feature seven different events, with a strategy of increased resolution close to the TC inner-core (up to 1km horizontal mesh). The focus was on the mature life cycle (TC genesis and late decline stages were not simulated), and the events were chosen to avoid external processes such as landfalls, island interactions, and extratropical transitions, and to feature long life cycles, with several re-intensifications. The Weather Research and Forecasting (WRF) model described hereafter provides a sophisticated modelling framework suitable for such range of TC realistic simulations.

### 2.4.1 The WRF model framework

The Weather Research and Forecasting (WRF) model was released in December 2000, and has since become the world's most used atmospheric model. Initially developed by the National Center for Atmospheric Research (NCAR), which is operated by the University Corporation for Atmospheric Research (UCAR), it has been designed and built as a community model. Its high adaptability and support of massively parallel computation on many different platforms makes it suitable for simulations ranging from global climate to Large Eddy Simulations (LES).

WRF solves the Navier-Stokes equations in 3D on a rectangular Arakawa-C grid. Here we use the ARW (Advanced Research WRF, Skamarock and Klemp, 2008) solver, which enhanced effective resolution allowed by high order numerical schemes is particularly suitable for mesoscale dynamics and regional simulations. The dynamical solver comes with a range of editable options, and is complemented by a physics package, where parametrizations regarding convection, microphysics, radiation, and planetary BL can be chosen among a large, and regularly updated state-of-the-art selection.

The model architecture is designed to be easily usable and editable: once the model sources are compiled, simulations can be set up through namelist text files that control physics and dynamics parametrizations, grid and domain settings, solver parameters, as well as input/output variables. The run preparation is also facilitated by the WRF Preprocessing System (WPS), which consists in configuring domains and geographical information (geogrid program), ingesting, reformating, and interpolating global analysis or model forecast files to the domains (ungrib program), putting input fields on the model's vertical levels, and generating lateral and initial conditions (metgrid program). The simulation framework used in this thesis also benefited a lot from the simulation infrastructure, tutorials, and scripts developed for coupled model simulations (but used here in the case of WRF-only simulations) by the Coastal and Regional Ocean Community Model (CROCO) team.

The simulations were run on the DATARMOR supercomputer, located in Brest (FRANCE), which is dedicated to scientific applications. This modeling framework allowed to set up a range of realistic TC simulations which characteristics are described in the following paragraph.

### 2.4.2 Model configuration

The settings adopted for WRF simulations are designed to realistically feature the entire mature life cycle of several TC events, with a spatial resolution sufficient to study the internal structure and its variations, and compare them to SAR extracted parameters.

The choice of physical parameterizations and numerical schemes was based on previous work on TC coupled simulations carried out by my advisory team (Jullien et al., 2014; Samson et al., 2014; Lengaigne et al., 2019), and myself during my Master's internship. The Betts–Miller–Janjic (BMJ) convective scheme was used for the 9km domain, (as convection is explicitly solved in the 3 and 1km nested domains); the Yonsei University (YSU) PBL with revised MM5 Monin-Obukhov was used for surface layer parameterization, the classical Charnock relation was used for the surface drag coefficient, the WRF single-moment six-class (WSM-6) for microphysics, the Dudhia scheme for shortwave radiatione, and the Rapid Radiation Transfer Model (RRTM) for long-wave radiation.

Each TC case is simulated using 3 domains: 1 parent domain at 9km resolution that encompasses the whole TC track, and two vortex-following domains at 3km, and 1km resolution. The two nested domains move every 15 minutes following the TC vortex, thanks to an automatic tracking of low pressure under 50000 Pa in a radius determined by a maximum TC translation speed of 40 m/s. Moreover, refined high resolution terrain and landuse files were added, as moving nests use by default the 9-km resolved topography of the large domain. The small size of the moving nest limits the computation cost. Conveniently, its fixed dimensions facilitate the post-processing (constant grid size is more convenient for file concatenations between different simulations). The resolution of 3km and 1km on the nested domains avoids the parameterization of convection, which is a noticeable uncertainty in regional models (Lengaigne et al., 2019), while keeping a reasonable computational cost. As shown by Fig. 2.5 showing the power spectrum computed from wind values on the 1km nested domain, the adopted configuration has an effective resolution of about 5km (denoted by the cutoff wavelength), which is close enough to SAR measurements (1-km grid smoothed with a 3-km sliding average). The $k^{-5/3}$ dependence of kinetic energy spectrum is in agreement with the observations of Skamarock, 2004 for mesoscale simulations.

Initial and boundary conditions are determined using data from the NCEP FNL. The FNL dataset is a re-analysis from the Global Data Assimilation System (GDAS) that provides atmospheric, oceanic and land surface products as global 6-hourly files at 0.25 degree spatial resolution. The re-analysis is performed by assimilating several observations from the Golbal Telecommunications System (GTS) and other sources into the Global Forecast System (GFS) model. During the simulations, the larger domain is also nudged to these re-analysis files using the WRF Four-Dimensional Data Assimilation (FDDA). The nudging is applied spectrally during the whole simulations, and in the entire larger domain only, with no direct impact on nested domains. The spectral nudging only applies to scales larger than a given wave number, presently, wave number 3: this means that scales lower than the large domain size divided by 3 (i.e. about 1000 km in this configuration) are not constrained. The nudging is also not applied in the Boundary Layer.

This configuration allows realistic simulations of TC mature life cycle: with the forcing files, moving nests, and physics parameters described here, the only modification to pro-

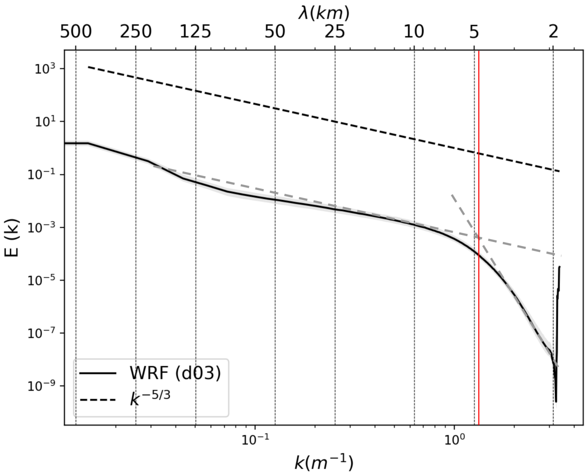

Figure 2.5 – Wavenumber spectrum of surface kinetic energy in Joules computed from WRF small domain d03 (solid curve) along with the theoretical Kolmogorov law (dashed curve) as a function of k ($m^{-1}$). Cutoff frequency of the WRF spectrum is denoted by the red vertical line.

vide when simulating different events is the extent of the large domain, and the start and end dates of the simulation. These parameters are automatically determined by extracting best-track positions of the simulated event during its mature phase (above category 1), and adding 8 degrees on each side of the track.

### 2.4.3 The TC simulations

Seven simulations were launched to model TCs in different basins, and the events were chosen based on several characteristics (details of events, domain extents, and dates are presented in chapter IV):

- the duration of the life cycle was the first criterion. The longer the TC's life cycle, the longer its mature phase, and the more likely it is to feature intensity changes, decays, and re-intensifications. TCs with a long mature phase, and no interaction with land or islands during this phase were preferred. They allow indeed to witness scale interactions, and gradual internal changes instead of brutal disturbances caused by external constraints.
- the geographical location was also a criterion: as stated before, the reliability of this study of inner-core processes, and intensity changes is largely conditioned by the variability of our database: the more numerous the situations, locations and properties, the less event-related the studied properties would be, and the more

physical meaning our interpretation would have. For this reason, the WRF dataset includes one TC in the North Atlantic ocean (IRMA), one in the East Pacific ocean (LANE), two in the West Pacific ocean (TRAMI and MANGKHUT), one in the North Indian ocean (FANI), and two in the South Indian ocean (CEBILE and JOANINHA). The case diversity ensures that statistical diagnostics of simulations are not impacted by any basin-specific feature, and that featured processes are not discriminated based on the TCs location.

— the last decisive factor was the presence of SAR acquisitions on the events. Indeed, it was thought useful to have acquisitions on the simulated events, in case direct comparisons would appear necessary for some reason. Such comparisons of SAR and WRF were excluded in our study, as direct comparison would have required a more observationally-based driven simulation framework to obtained simulated TCs very close to observed TCs. This was not the point of our study, as we focused on studying the internal processes and life cycle evolution, which requires to let the model freely evolve. Thus, while the SAR observational constraint was unnecessary in the frame of this work, we kept the possiblility to compare simulation outputs with SAR observations for other case study purposes.

As shown later in chapter IV, the comparison between simulated and real TC events shows discrepancies both in intensity, size, and sometimes track and translation speed. The simulated TCs sometimes do not reach the observed maximum intensity, or experience intensity changes that did not happen in real cases. These notable differences arise from several reasons: 1) the model uncertainties (resolution, parameterizations) that can lead to miss physical processes, 2) the stochastic nature of NS equations. However, the diversity of cases and external conditions is realistic, and allows to have TC phases ranging from category 1 to category 5, with notable intensity changes, and a significant variability in the mature TC life cycle description, which was the only request for my study.

## 2.5 A designed methodology to link TC wind field structure and TC intensity variations

The particular framework set up for my work is specifically designed for two purposes: allow a better and new understanding of TC dynamics through the joint use of high resolution observations and realistic dynamical models, and promote the use of SAR observations in the context of improving TC predictability on an operational level. Understanding the reasons why a TC reaches an intensity peak, re-intensifies, or experiences a fast intensification or a fast decline, are the main concerns of forecasters, and thereby of the scientific community as they are keys to TC dynamics understanding. The characterization of these intensity changes yields different issues for SAR and WRF.

The procedure of extraction is designed to estimate both radial and azimuthal structure properties of the inner-core, both from SAR and WRF surface wind fields. These extractions are meant to estimate relevant TC properties with regard to the literature, with a minimal amount of variables, and the sole access to surface wind speed. The main fields of research regarding intensity changes related to TC BL internal dynamics are the research on intensity restoration processes, mainly through VRWs, eyewall dynamics, and energetic processes in the inner-core. The first issue was consequently to find ways to access information regarding energy propagation in this region from non-directional surface wind fields. As neither wind direction, nor vertical velocity, and nor time continuity are available from SAR snapshots, the propagation of VRWs cannot directly be measured. However, the VRWs and energy transfers consecutive to convective bursts or eyewall perturbations have been found to generate asymmetry, and distortion in the vortex structure. Thus, although they cannot be observed directly on the wind field, VRWs sign on the eye shape and inner-core structure by perturbing its symmetry. VRWs are moreover linked or coupled with many other measurable features of the surface wind field, such as eyewall distortions caused by mesovortices and convective asymmetries. Overall, the small-scale features causing asymmetry in the wind field (and especially in the eyewall and maximum wind areas, where the TC kinetic energy is concentrated) are all impacting the energy distribution in the vortex, and actively participate to its intensity changes. The most logical and convenient way to estimate internal processes related to intensity changes at a given time is thus to study the asymmetry of the 2D wind field azimuthal structure. WRF simulations were used to furtherly assess the temporal changes in this asymmetric wind field, complementing SAR extractions with an assessment of the evolution of internal perturbations.

The processing method used to exploit SAR images, and WRF outputs was designed to work indifferently on both sources of data (SAR and WRF), so that the defined variables that describe the internal TC structure could be directly compared. It is described hereafter.

### 2.5.1 Inner-core asymmetry: parameters of interest

As VRWs are usually quantified by their wave number azimuthal decomposition of energy distribution (Montgomery and Kallenbach, 1997; Wang, 2002a; Wang, 2002b), a similar approach is adopted here. The inner-core VRW activity is approximated by a range of proxies quantifying the degree of perturbation of the inner-core, measured on four distinct extracted signals:

- the eye shape
- the distribution of mean radial wind gradient in the eye-eyewall area (a measurement of the degree of vorticity mixing in the eyewall) [1]
- the RMW distribution
- the maximum wind distribution.

These signals are all extracted from a polar projection of the geographical SAR or WRF grid, with an arbitrarily fixed azimuthal resolution of one degree, and a radial resolution matching the original grid step average value. Figure 2.6 shows the four different signals and their location in the TC wind field. As shown by the Figure, these four signals are concentrated near the center of the vortex, in the area of maximum wind. They describe two distinct areas (eyewall and maximum wind ring), and characterize two types of properties (spatial variability for eye shape and RMW distribution, and amplitude variability for eyewall radial gradient and maximum wind distribution).

#### Normalization and Smoothing

Before quantifying the asymmetry of these azimuthal distributions, all extracted signals are smoothed and normalized, so that the variations in size and amplitude does not impact the measurements of asymmetry (i.e., two identical eye shapes but at different scales will have the same variance and spectral decomposition). Smoothings are carried out mostly with a 3rd order Butterworth filter, which is a low-pass filter suitable for a wide range of applications that maximizes the flatness of the response in the passband.

---

[1] In most studies regarding eyewall mixing (Schubert et al., 1999; Kossin and Eastin, 2001; Mallen, Montgomery, and Wang, 2005), the quantity evaluated is vorticity, as it allows to better measure the mixing and assess the regime of eyewall circulation (i.e. annulus or monopole of vorticity). However, vorticity is difficult to measure on SAR as directions are not available. Moreover, these studies also explicitly relate the shape of the vorticity profile to the tangential wind profile (see for instance Fig. 7 of Kossin and Eastin, 2001). Thus, we relied on surface wind speed only, approximated as the tangential wind speed.

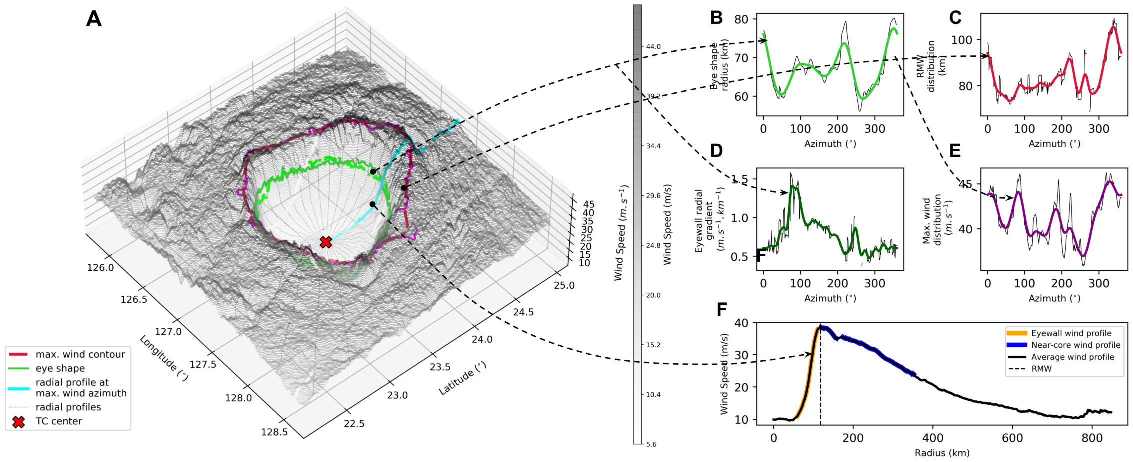

Figure 2.6 – Illustration of parameters extracted from the surface wind field on the SAR acquisition of TC TRAMI (2018/09/28,09:35). (A) Surface wind field projected on a 3-D grid (elevation=wind speed) with extracted signals superimposed. Panels (B),(C),(D),(E) respectively show raw (thin black) and smoothed (bold) extracted azimuthal distributions of eye shape, RMW, eyewall radial wind gradient, and maximum wind, with the same color code as (A). (F) shows the extracted radial mean profile and highlighted eyewall (yellow) and near-core (blue) areas.

The transfer function is the following:

$$|H(j\omega)| = \frac{1}{\sqrt{1 + (\frac{\omega}{\omega_c})^{2n}}} \tag{2.1}$$

where n is the filter order, $\omega = 2\pi f$ is the angular frequency $\omega_c = 2\pi f_c$ the cutoff angular frequency. This cutoff frequency is arbitrarily fixed in my study, and depends on the structure of the original signal. For amplitude and spatial signals, such as the ones extracted here, the cutoff frequency is computed from the signal spectrum, as the frequency corresponding to 40% of the signal's explained variance, a value that was judged to reasonably absorb local anomalies and grid step discretizations from the extracted signals, while still well rendering their variations (cf. Fig. 2.6 B,C,D,E to see the effect of smoothing on the raw signals).

### Asymmetry coefficients

To associate these signals to the energetic activity in the inner-core, asymmetry coefficients were defined as the smoothed and normalized signal variance, thus measuring the average departure of the signal from an axisymmetric distribution. Fourier decompositions were also performed on each signal to compute the power level associated to each wave number (WN) in these signals, in order to refine the study of asymmetry by dissociating several characteristic scales and processes (i.e. rainband and vortex-scale with WN 1, or polygonal eyewalls with WNs 3-4-5 for instance). Although being very partial, this description of the inner-core activity provides a relevant overview of the degree of internal perturbation across the boundary layer as it mixes measurements of spatial distortion (with the eye shape), dynamical activity (with the eyewall mixing and maximum wind distribution), and structural stability (with the RMW).

### Radial profile

The properties of the inner-core radial structure were also thoroughly analyzed to estimate the size, contraction, and stability [2] of the vortex, focusing on the eyewall area and the inner-core, between RMW and 3RMW. The inner part of the eyewall profile is the area of highest radial wind gradient in the vortex (see Fig. 2.6, the inner eyewall portion is featured in yellow on the radial profile), where crucial energy exchanges take place, and are likely to influe on the TC's behaviour. For these reasons, the measurement and study of the average radial gradient in this area was judged important for the understanding of the TC life cycle, especially considering that it is a parameter difficult to measure accurately on most other observations sources due to insufficient resolution. To the average gradient was adjoined a measurement of the inner eyewall profile curvature, defined as the difference between the mean gradient and the gradient of a linear profile between the TC center and the RMW (i.e. Rankine approximation). This variable thus normalizes the gradient with respect to the TC size, measuring the eyewall radial profile sharpness and approximating the degree of eyewall mixing: for a given value of mean radial gradient, a sharper profile with positive mean second derivative will have less mixing than a more linear one.

The outer inner-core was also investigated, mainly following the works of Reasor, Montgomery, and Grasso, 2004 and Mallen, Montgomery, and Wang, 2005, which relate this portion of the vortex structure to the TC's resilience, that is, the vortex ability

---

[2] the term "stability" is used here in the context of Reasor, Montgomery, and Grasso, 2004, who defined vortex resilience as a parameter describing the stability of the vortex regarding perturbations by external shear. It shall be regarded as an *asymmetric* property describing the stability of the vortex towards external wind shear, and it must be distinguished from the more usual "inertial stability" parameter, which is an *axisymmetric* property describing the response of a vortex to an external source of heat or momentum (Shapiro and Willoughby, 1982)

to endure external perturbations without losing too much of its stability, thus partly or entirely conserving its intensity. The shape of the radial profile is related to vortex resilience through the VRW theory: indeed, the radial distribution of potential vorticity and specifically the sign of the potential vorticity at the critical radius at which VRWs corotate with the mean vortex determines the growth or decay of tilt instabilities (Reasor, Montgomery, and Grasso, 2004). The critical radius is usually located between 1 and 3 RMW (highlighted in blue on the radial profile of Fig. 2.6 A,F), that Mallen, Montgomery, and Wang, 2005 call the near-core area. The sign of potential vorticity depends on the properties of the mean wind distribution: the faster decaying the profile, the lower the potential vorticity. In the present work, the properties of the near-core wind profile were thus estimated through the mean value of gradient between 1 and 3 RMW (i.e. mean near-core gradient), and the curvature of the near-core profile defined as the difference of gradient computed over RMW and 2RWM and computed over RMW and 3RMW, which approximates the shape of the near-core profile, and thus its decay in the near-core area.

The radial structure is thus described by two azimuthally averaged gradients (i.e. mean gradients on the yellow and blue parts of the profile on Fig. 2.6F), and two measurements of the profile's curvature, in the inner eyewall and near-core areas.

### 2.5.2 Specificities associated to SAR image treatment

SAR acquisitions are much more difficult to process than WRF model outputs, as many artifacts related to the measurement or to the post-processing chain can affect the SAR-retrieved wind field, and impact the estimation of inner-core parameters. The generic extraction method was thus implemented with numerous additional steps to take care of these issues, and ensure that the final dataset would be consistent. The steps described hereafter are specific to SAR.

#### TC center estimation

The requirement for estimating inner-core parameters is a reliable estimation of the TC center position. Most of our results indeed rely either on mean radial profiles, or on azimuthal signals such as eye shape contour, or the distribution of maximum wind speed, which both require a minimal offset of the polar grid to avoid adding artificial asymmetry to the extractions. The detailed procedure of TC center tracking is explained in chapter III 3.2.3. To sum up, it consists in iterative researches gradually approaching the TC center.

The first approximate center position is defined from the best-track positions time-serie interpolated at the acquisition time. More recent versions of the algorithm get rid of the best-track interpolation by taking a first guess as the maximum wind position computed on the 25km-smoothed SAR wind field. We then search for a low wind area around this first guess center, by recursively computing the centroid of lowest wind points in its vicinity (based on a fixed research radius). If a stable point is found (i.e. repeating the research around the centroid does not change its position), the point is retained as the TC center. If otherwise each iteration yields a centroid further from the maximum wind area until reaching the vortex periphery (and eventually the image border), the radius of research is refined and the procedure is reproduced. Thresholds on the number of iterations and the distance from the maximum wind centroid allow to limit the duration and to determine the success or failure of the procedure. In the case of WRF simulations, the small domain is already centered on the vortex, but the TC centering method was also applied to ensure a full consistency with the SAR processing.

A second step is the eye re-centering, which is an adjustment to ensure that the final TC center is located at the center of the eye. This step relies on a first polar projection of the wind field on a coarse grid, to estimate a first approximate eye shape and re-center the eye position at the centroid of this shape.

### SAR heterogeneity mask

SAR level-2 products are provided with a heterogeneity binary filter designed to mask rain signatures and local artifacts that cause anomalous wind speed values. The corrections applied on level-1 NRCS are indeed not fully efficient: subswaths signatures are attenuated by the GMF but still present on the wind field; other artefacts such as rain anomalies causing abnormal heterogeneity (which is then wrongly interpreted as abnormally low or high wind by the GMF) impact the wind field.

These heterogeneity anomalies are identified, and flagged by the level-2 processing chain, by defining a mask on grid points exceeding a certain value of local wind gradient (proxy for heterogeneity). The level-2 procedure however occasionally results in masking areas that are not affected by rain but only associated to high values of wind gradients, such as the eyewall area. Fig. 2.7 shows the field of local wind gradient, with the heterogeneity mask above it. As shown on this Figure, the eyewall and eye areas are completely masked by the heterogeneity flag, preventing the analysis of the eyewall structure and radial gradients. The heterogeneity mask thus has to be removed near the center to allow

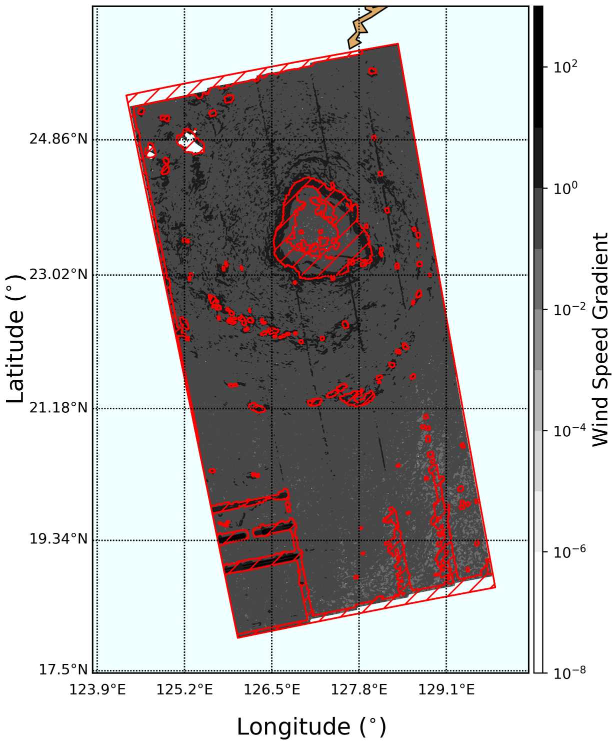

Figure 2.7 – Map of local spatial wind gradient computed on SAR acquisition of TC TRAMI (2018/09/28,09:35). Red hatched contours denote the values flagged by the heterogeneity mask

the study of eyewall structure, but this removal might unmask some rain-impacted areas. The mask is thus removed in a very reduced area close to the eye (up to 2RMW), in order to keep all rain signatures from inner-core rain bands masked as well as possible.

## Outliers

Outlier detection and masking steps are applied prior to smoothing described in section 2.5.1 every time a parameter or signal is extracted (such as the eye shape computed to re-center the eye) to ignore local outliers, distortions of azimuthal or radial signals induced by artificial local maxima or minima (cf. Fig. 2.6). Outlier detections rely on a modified Z-score method which compares each median difference to the Median Absolute Difference (MAD), and masks above a given threshold (usually 10) according to the following condition:

$$thr_{MAD} = \frac{|X - median(X)|}{median(|X - median(X)|)} \tag{2.2}$$

### Handling of image borders and double eyewalls

Finally, additional steps of the extractions are designed to handle particular cases that can prevent or degrade parameter estimations: they include masking of signals when they are too close to the image border, and completion with linear interpolation (so that incomplete signals could still provide an asymmetry estimation), and handling of double eyewalls and rain band features so that the maximum wind contours would be as continuous as possible (i.e. not switching from one eyewall to the other or from a rainband of high wind to the eyewall).

### Summary of the steps followed to build the final SAR dataset

Setting up the SAR database relies on the following sequence of stages. The first and main step is the previously described extraction procedure, composed of several algorithms that automatically and generically estimate a range of TC inner-core properties from SAR surface wind fields: average radial profiles and azimuthal distributions of characteristic signals (along with their spectral decomposition) compose the first level of the inner-core dataset. The extraction procedure takes into account many image-related issues, and rejects a notable part of the initial dataset when extractions are prevented or compromised by these issues. Many extractions are however carried out and flagged as successful despite inconsistent estimations. For instance, undetected double eyewalls or rain band features can impact the extraction of maximum wind distribution without causing any error. For these cases, a visual assessment and manual selection is thus necessary before integration into the statistical dataset. Any irrelevant estimation of shape or peculiarity in contour estimation is thus visually identified. If the issues are minor and estimated not to impact the computation of IC parameters, the image is flagged as OK for statistical database integration, otherwise the image is excluded from the following procedure steps.

After this manual selection, a netCDF file is generated which gathers all extracted parameters from the accepted Sentinel-1 and Radarsat-2 samples. The image processing procedure is now over: all extracted signals are grouped in a unique file and SAR level-1 individual netCDF files are not accessed afterwards anymore.

Once the database is generated, including aizmuthal signals and radial profiles extracted from each image along with associated best-track time series, the parameters describing these signals are computed: mean profile gradients and curvatures, azimuthal signal variances and spetcral decompositions, and intensification rates on several time references. A final processing step consists in a second manual selection this time based on statistical distributions: scatter plots of several characteristic variables are plotted (such as RMW or eye shape asymmetry versus intensity). Using an interactive tool, all outliers or surprising values can be related to the corresponding image, so that their specificity can be related either to a processing error that was not detected during the first manual filtering (which happens as the first selection does not necessarily reveal all artefacts that can impact a signal or its variance) in which case they are rejected, either to a particular dynamical or structural behaviour (such as intense TCs showing outlying low value of eyewall mean gradient due to anomalously high winds in the eye) in which case they are conserved. After this step, the database is set up with a wide range of level-2 variables relevantly describing the physical processes and structural properties of the TC inner-core. Between the opening of level-1 files and this last selection, many images were rejected from the dataset.

### 2.5.3 Assessing the time evolution of the inner-core structure

WRF simulations are processed through the same chain as SAR observations, although the SAR-specific steps are ignored. The WRF database thus has exactly the same structure as the SAR one. In addition however, hourly WRF output files grant access to both a reliable estimation of intensity changes, and a computation of temporal changes occuring inside the inner-core structure from the time series of radial and azimuthal properties. These two abilities were prevented on the SAR dataset by the limited temporal resolution (separate snapshots), and the coarse resolution and limited reliability of life cycle estimations from best-track files. They are a key to measuring and understanding TC dynamics, as theory of inner-core processes relates intensity changes to energy transfers within the vortex and thus to structural variations rather than instant characteristics. The transition from a snapshot based statistical study to a time-series based analysis however requires the definition of reliable variables to measure both vortex intensity and internal inner-core changes.

#### Choice of characteristic time scale

The first notable issue is the choice of a characteristic time scale to describe these variations: intensity time series, for instance, can show large hourly variations, with bursts lasting between one and a few hours, but the life cycle is characterized by a larger time

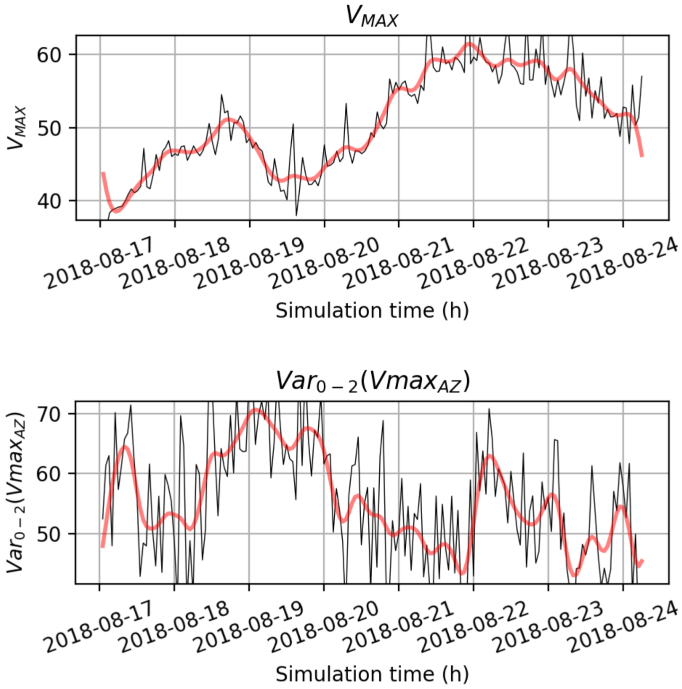

Figure 2.8 – Raw (thin black lines) and smoothed (bold red lines) signals of (A) maximum wind speed $V_{MAX}$ and (B) $Var_{0-2}(Vmax_{AZ})$, the percentage of variance explained by WNs 0+1+2 extracted from the spectral decomposition of the maximum wind distribution at each time step of the LANE WRF simulation. Smoothing of time series is carried out applying a Butterworth filter with a 12h cutoff period

scale, with phases of intensification, peak, decay, and trough lasting from about 10 hours to several days. As shown on Fig. 2.8A illustrating the effect of smoothing on the intensity time serie, the raw intensity can indeed have large variations of about 10m/s in just one hour that are not representative of the TC life cycle: for instance, on 2018/08/19, we observe a strong intensity burst from 40 to 50 m/s in one hour while the smoothed intensity with a 12h cutoff period almost does not change, and the event of the life cycle on a larger scale is an intensity trough (i.e. re-intensification). In such case, identifying this burst as an intensity peak thus seems irrelevant. The same issue exists for internal structure variables (Fig. 2.8B, in this case WNs 0-2 explained variance of the maximum wind distribution), with an additional difficulty being that the defined variables can feature large noise levels that prevent or complicate the determination of a characteristic time scale for dynamical processes. As one of the purposes is to assess predictability and as internal structure time series have a very large variability on hourly time-scales, a larger scale was chosen to extract persistent changes characterizing TC life cycle and structure instead of spontaneous changes that are not necessarily relevant. The small time scales are thus smoothed by filtering high frequencies with a cutoff period of 12h. This smoothing attenuates frequencies lower than 12h, so almost no variability is found under 6h.

### Temporal variables

Temporal variables were designed to provide a suitable match between the literature on VRWs and inner-core processes (i.e. eyewall mesovortices, vortex stability and resilience notably) and the structure of our SAR snapshot equivalent variables. Energy transfers and propagation governed by VRW propagation were approached by quantifying the temporal changes in the maximum wind ring energy distribution, i.e. the amount of energy contained in the low wave numbers (indicating an unstable stage of the maximum wind ring) with respect to the amount in the high wave numbers (indicating a balanced energy spectrum and thus a homogeneous maximum wind ring). These low and high wave number groups are based on the literature and on the author's experience of SAR and WRF processing: the vortex-scale deformations mostly sign in the wave numbers 1 and 2, while larger wave numbers denote a VRW transitional activity and, starting around wave number 5, a homogeneous distribution. As described in chapter IV, the measurement of a temporal transfer between the 1-2 "low WN" group and the 6-180 "high WNs" group indeed characterizes a physical change in the maximum wind distribution, and thus describes a dynamical process.

The same reasoning applies to other extracted azimuhtal signals such as eye shape or eyewall radial wind gradient distribution, although they do not necessarily describe the same dynamical processes, the same spatial scale, or the same stage in a re-intensification process:

- eye shape energy transfers, for instance, characterize the distortion of the eye, thus an earlier stage of intensity change-related inner-core processes more related to the appearance of eyewall mesovortices and the progressive generation of VRWs;
- eyewall radial gradient describes the structure of the eyewall, and thus, in a sense, the degree of eyewall mixing and its azimuthal distribution, hence its temporal energy transfer would denote a process of homogeneization of the eyewall, which is not necessarily followed by the generation of VRWs.

## 2.5.4 Characterizing intensity variations

### Intensification rates

### From IBTrACs

The description of intensity changes from best tracks is limited to long ranges of more than 6 hours: even though the resolution is of 3 hours, the resolution in maximum intensity is very reduced as it is a composite of several diverging sources, leading to large intensity peaks, and phases of constant intensity that can last several hours, which is clearly not realistic. This impacts the computation of temporal variables such as intensification rate: As featured on Fig. 2.9, the rates extracted from the raw best track by simple interpolation on the raw curve can be quite different from the ones extracted from a smoothed intensity curve (see black and green arrows on the figure). Due to the coarseness of best track, a phase of intensity decrease can yield an intensification rate equal to 0 if the surrounding time steps are all at the same intensity (see the second acquisition on 2017/09/07). As my work focuses on small-scale features and processes that can occur within a few hours, this coarseness of intensity time series was a limitation to my analyses. For these reasons, all analyses implicating best track intensification rates related to SAR were carried out by averaging SAR properties by groups of intensification rates. These groups were defined quite coarsely in order to absorb best-track uncertainties into categories with a lot of samples, at the expanse of sensitivity as, for instance, fast and slow intensifications were both equally considered as part of the "positive intensification" group.

### From WRF

The issue of life cycle characterization is very different with WRF outputs. Hourly timesteps indeed grant access to a continuous assessment of the internal structure as well as of large scale properties. The maximum intensity time serie does not need to be computed from another source, which eliminates any concern for misfits between the internal structure descriptors and TC intensity changes. This allows a finer characterization of these changes: all intensity variations can be considered as directly related to the ongoing changes throughout the internal structure. Moreover, the ability to study time series not only of maximum intensity, but also of any parameter extracted from the wind field (radial gradients, azimuthal asymmetry and energy distributions...), and to define time-relative variables, allows to have a much finer description of dynamical scale interactions. An intensity change of any kind can now be related to the internal structure at the same

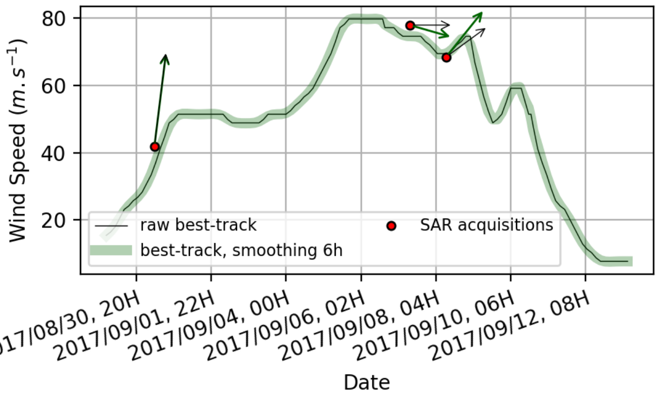

Figure 2.9 – Comparison of intensification rates extracted from raw and smoothed best-track maximum wind time series for TC IRMA (2017). Red dots are the positions of SAR acquisitions on IRMA with the corresponding estimated maximum wind value. Black (Green) arrows are the interpolated intensification rates computed from the raw (smoothed) signal

time (i.e. asymmetric/symmetric maximum wind ring for instance), or to the evolution of the internal structure at this time (i.e. homogenizing or distorting maximum wind ring), or even to the evolution of the state and evolution of the internal structure before or after this change. The accuracy of interpretations is thus greatly enhanced. This however also depends on the characterization of life cycle variations, and an accurate definition of life cycle phases.

### Definition of life cycle phases

Then, life cycle phases were defined similarly to the ones defined for IBTrACs: intensifications, declines and flat phases based on thresholds on the intensification rate, troughs, peaks and stable phases based on thresholds of secondary derivative. These phases are shown on Fig. 2.10A with the life cycle depicted by the LANE WRF simulation.

Both SAR and WRF studies required a precise characterization of intensity variations. The 12h smoothing applied to intensity time series first allows to reduce the life cycle to its notable and persistent intensity variations. Direct bivariate comparisons between intensification rate and internal parameters yielded a very large variability due either the highly variable nature of studied parameters (i.e. azimuthal signal wave number decompositions, etc.) or to uncertainties associated to parameter estimations (such as intensification rate from best-track for instance). Moreover, the raw intensification rate in itself has a large internal variability: for instance, a given value of positive intensification rate includes all kinds of intensifying TCs (before a decline, after a re-intensification, at the beginning of their life cycle or at the end, etc.). Thus, to extract consistent trends and statistical properties from the life cycle, I decided to focus the interpretation of TC life cycle on specific phases: instead of directly relating, for instance, eyewall radial gradient to interpolated best track intensification rate, I studied the average values of eyewall radial gradient in groups of intensification rate and intensity second time derivative to regroup in one specific group all TCs associated to a given behaviour. These phases were first defined by delimiting thresholds on the value of intensification rate:

— intensifying TCs for intensification rate larger than 5m/s/day,
— stationnary TCs for intensification rate between -5 and 5 m/s/day
— declining TCs under -5 m/s/day,

with a balanced number of samples in each group.

Defining these groups attenuates the impacts of potential disagreements between SAR and best track, or potential errors or oversmoothings of the IBTrACs intensity time serie, and allows a more reliable interpretation without interference with these artificial biases. However, they also coarsen the results interpretations to a more restricted extent: complex dynamical features (such as for instance varying time lags between life cycle and internal structure response) and potential biases due to internal dynamics (secondary eyewalls, stronger precipitations...) or synoptic events (external shear, land interaction or basin-related specificities) are not acknowledged and only general trends common to all TCs are observed. These general trends are one one hand more difficult to observe, as case-specific features interfere with the mean behaviour, causing a very high intra-class variability. This means, on the other hand, that any observed trend has to be considered as significant: even if standard deviations are very high, any mean behaviour trend denotes a characteristic process of TC life cycle.

This description of TC life cycle variations could be notably refined on WRF analyses, by extracting local maxima and minima to focus on the largest intensity changes. For instance, for the intensity, local maxima correspond to marked phases of decline in which the vortex is usually highly disrupted internally, and local minima correspond to re-intensifications where the TCs prepares to intensify. Maxima and minima of intensitfication rate and intensity second derivative also allow to extract time steps during which the TC experiences the most notables intensity changes.

Study of the mean values of internal structure variations for each of these phases is a good way to assess the link between internal structure and life cycle, as it shows the dynamical processes dominating the vortex's evolution through these different phases. This analysis is illustrated on Fig. 2.10: the lower panel shows the time serie of eyewall radial gradient compared to Rankine vortex (i.e. the sharpness of the eyewall radial wind profile). Superimposing this curve with the upper panel allows to relate mean trends in the radial gradient to life cycle phases. For instance, the green highlighted portion of the life cycle during the first day of simulation is associated to a strong intensification and, in the same time, to a strong increase in eyewall profile sharpness. By counting the number of time steps associated to increasing sharpness (i.e. red shaded curve on panel B) during a given life cycle phase, and during all similar phases throughout the simulations, we can estimate if, on average, the increase in eyewall radial gradient sharpness is favourably associated to specific phases of the life cycle. A finer analysis was also conducted to assess the temporal lag between temporal structure and life cycle changes: indeed, it was noted that, although connections between these two scales exist and are obvious in several cases, they are not necessarily synchronous and tend to vary significantly in time lag and amplitude depending on each case. The difficulty, however, in the WRF statistical analysis, was the structure of the dataset and its lack of representativeness. As only seven distinct events were simulated, it is difficult to study specific behaviours statistically: any feature isolated from the distribution is not necessarily representative of any TC process, it can only be the expression of specific conditions unrelated to any life cycle interaction. Thus, as for the SAR (but for different reasons), the interpretation must focus on mean behaviours over the whole dataset to extract a truly representative feature that could have applications in TC forecasting.

### The statistical approach

SAR images are widespread in time, geographic location, seasons, and events. It is thus highly complicated to contextualize a given image in its external environment and chronology, except by crossing SAR observations with other remote sensing sources with higher time resolution and/or access to vertical structure. The uncertainty associated to such cross-comparisons (due to time interpolations, differences of resolution, and reliability of the different sources) is considerable, and demands a thorough examination and processing of each source. Such work was not thought relevant regarding our goals and time resources, which is why it was preferred to consider images as samples building a TC database (i.e. assimilating different TCs to a manifestation of a unique physical process) instead of separately describing a multitude of dissociated TC events.

The comparison to dynamical models was also a determining factor to choose the statistical approach, as direct comparisons between SAR and models however turned out to have multiple limitations. Indeed, although simulated TCs were realistic and showed wind structures almost directly comparable to SAR observations, their life cycle was not necessarily realistically simulated due to uncertainties in initial and boundary conditions, model uncertainties (resolution, parameterizations), and stochastic nature of NS equations. Ensemble simulations of each event could be an option to overcome some of these issues, but the requested number of simulations to compare to all SAR images would have been very consequent, and computationally proscribed.

The adopted procedure thus consists of a dual statistical analysis of SAR and WRF databases, which was designed to circumvent most of the difficulties inherent to both datasets: the database absorbs the potential artefacts or post-processing issues impacting SAR images; it also allows to get rid of the need of perfectly realistic TC simulations. Most diagnostics of the datasets were carried out through bivariate distributions comparing in most cases a variable describing the life cycle (i.e. intensity and its first and second time derivatives), and a property of the internal structure (i.e. radial and azimuthal extracted parameters). A machine learning method was also designed to complexify the analysis by considering the entire multivariate dataset and take into account potential non-linear interactions between the variables.

### Machine learning classification method

### Motivation

The parameters extracted to describe either the radial or azimuthal structure differ in their properties, their statistical dependency on the life cycle variations, and the dynamics they describe or relate to. The information contained in each individual variable, and its significance for TC life cycle is however difficult to assess, as the study of mean behaviours restricts our interpretation to general trends with no access to dynamical content. Due to the limited representation they have from the perspective of SAR and WRF datasets as used in this work, the information contained in each individual variable, and its significance for TC life cycle is difficult to assess, and the study of mean behaviours restricts our interpretation to general trends. The assessment of the role of each extracted variable in the TC's life cycle requires a multivariate analysis taking into account all potential interactions between these variables, and evaluating them not individually but with respect to the other parameters. Intensity changes, indeed, are not solely governed by VRW processes, or external shear, or eyewall mesovortices. The vortex's stability, and ability to intensify does not only depend on its size, its radial structure, or its azimuthal symmetry and homogeneity: all these features interact in different ways and various amplitudes to govern the TC life cycle. I thus focused for the last part of my analyses on setting up a method that would take into account this mutlivariability and these potential interactions. The final goal of this approach is to assess the relative importance of each variable and, ideally, to provide TC forecast centers with a hierarchy of internal structure features that could help to better predict intensity changes. The emergence over recent years of big data science, and machine learning algorithms in the scientific community provided an adapted tool for this purpose, as machine learning methods can handle multivariate datasets, and take into account linear or non-linear interactions between all variables.

**Classes**

The purpose of my study, and the structure of SAR and WRF datasets however require a specific framework to provide consistent results. As the goal is to assess the individual impact of each extracted variable in the description of TC life cycle, and their ability to improve TC predictability, a classification method was chosen to see if the information contained in TC-extracted variables was able to dissociate TCs based on their intensity changes. The classes to separate were defined, in agreement with my previous analyses of TC life cycle, based on thresholds on the intensification rate: declining TCs, stable TCs, and intensifiying TCs. These classes allow to assess the impact on TC predictability, as if a snapshot from SAR or WRF can provide information on the intensification rate (i.e. is the TC intensifying or declining), the intensity at later times can be predicted based on this intensification rate. Although the predictability can not directly be estimated as we do not truly try to predict the intensity at later times, but only to classify TCs in raw groups of intensification rate, the method allows to estimate the potential for predictability of a given group of variables. With WRF, the analysis was pushed a little further as I used temporal variables such as azimuthal transfers for the classification (thus assuming that at a given time and for a given output, the previous states of the vortex were known), and also defined classes based on the secondary derivative of the intensity time series, thus trying to dissociate phases of re-intensification from phases of intensity weakening.

### Choosing a classification method

There is a major issue remaining with the implementation of this machine learning method. Indeed, the number of variables extracted from the internal structure is very large: radial gradients in the eyewall and near-core areas, near-core profile curvature (proxy for resilience) and eyewall comparison to Rankine, azimuthal explained variances for each wave number, asymmetry coefficients, and asymmetry coefficients for the 4 extracted azimuthal signals... In total, 48 variables were kept for the analysis as potentially containing information regarding the TC life cycle. A classification with this amount of variables and less than 200 samples (161 for SAR, 254 for WRF taking a random fourth of model outputs to decorrelate the samples) is highly overfitted, and yields irrelevant results with prediction scores of 100%.

The usual method to avoid overfitting is a dimensionality reduction such as Principal Component Analysis (PCA) or Linear Discriminant Analysis (LDA). These methods consist in projecting original vectors (i.e. variables) on new axes in a space of lower dimension corresponding to the number of classes. While PCA maximizes the variance within each class to perform its projection, LDA maximizes the separation between each class. LDA thus appears more adapted to my purpose which is a classification. However, the interest of dimensionality reduction is also its major disadvantage: by reducing the number of variables, PCA and LDA loose information regarding these variables. The final prediction score thus only displays the new vectors and their weight in the classification, but not the variables that compose these vectors, thus loosing the individual weight of each original variable in the classification. Moreover, as they only perform linear combinations to compute new vectors, potential non-linear interactions between variables are ignored. The classical approach for this kind of dataset, i.e. a dimensionality reduction followed by a classification using a machine learning algorithm, could thus not be adopted.

Another classification method that allows more visibility is the decision tree algorithm, which performs classification by fixing gradual thresholds on individual variables that allow maximal isolation of the classes. The obtained decision trees allow to witness which variables are most important in the classification, as the lower branches of the tree are the ones that allowed to isolate the largest number of samples. However, in such approach, also no interaction between variables is considered. As our purpose is not to perform the perfect classification of intensification rates, but to understand the interactions inside the internal structure, and to quantify their links with TC life cycle, this method was thus not adapted either.

The method finally adopted was inspired by a communication with colleagues working on statistics in biology, and more particularly by the work performed by (Receveur et al., 2020). Their problematic is similar to mine (i.e. dataset with high dimensionality, and need to quantify the weight of each variable). The principle is the following: instead of performing one classification over the full set of vectors, several classifications are performed based on subgroups of variables combined in all possible ways. These subgroups can then be compared based on their prediction score, which allows to identify the most important variables or combinations of variables. Non-linear interactions can be taken into account by running the classification with nonlinear predictive models (such as support vector machine, SVM), and dimensionality is not an issue anymore as subgroups can contain the desired number of variables. The classification is not performed to separate in itself the two or three classes with the best efficiency (as the lower number of variables can notably lower the classifier performances), but in the perspective of comparing the different combinations, and identify the most informative variables, which was my initial purpose. To reduce the impact of the choice of the classifier, each combination was processed through ten different classifiers, providing a "neutral" prediction score mixing linear and non-linear regression models, decision trees and random forests, and other usual classifiers. A random variable was also added to the dataset, and included in the combinations to provide a "witness" variable. This innovative framework of machine learning classification allowed a reliable comparison of different variables extracted from SAR and WRF outputs, and provided insights in their ability to monitor TC intensity variations.

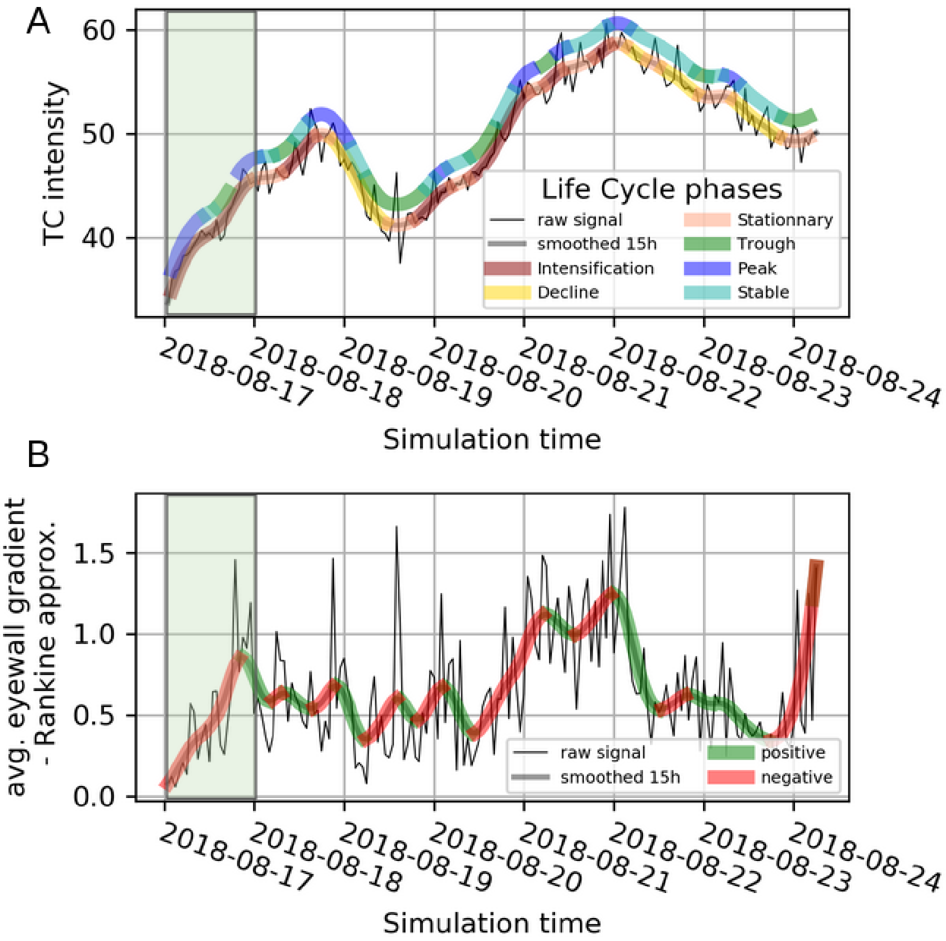

Figure 2.10 – (A) Description of life cycle phases extracted from the intensity time serie of the LANE simulation. Thin black line denotes the raw maximum intensity signal, and smoothed colored curves denote different life cycle phases defined as lower (declines and peaks) and and upper (intensifications and troughs) quarters and remaining middle values (for stationnary and stable) of the distributions of intensification rate and intensity second time derivative. (B) Same plot for the time serie of eyewall radial gradient compared to Rankine vortex, i.e. profile sharpness. Only positive and negative values of time derivative are dissociated this time. A notable phase of intensification is highlighted by a green shading a the beginning of the simulation.

Chapter 3

# OBSERVATIONS OF TROPICAL CYCLONE INNER-CORE FINE-SCALE STRUCTURE, AND ITS LINK TO INTENSITY VARIATIONS

---

This chapter content is the suject of an article under final review in Journal of Atmospheric Sciences.

## Abstract

Tropical Cyclone (TC) internal dynamics have emerged over recent decades as a key to understand their intensity variations, but are difficult to observe, as they are sporadic, multi-scale, and occur in areas of very strong wind gradients. The present work aims at describing the internal structure of TCs, as observed with newly available satellite synthetic aperture radars (SARs) wind products, and at evaluating relations between this structure and the TC life cycle. It is based on a unique dataset of 188 SAR high-resolution (1 km) images, containing 15 to 47 by intensity category. An extraction method is designed to retrieve and characterize, the TC radial profile, its azimuthal degree of asymmetry, and the energy distribution in the eyewall and maximum wind areas. Vortex contraction and sharpening of the eyewall wind radial gradient with increasing TC intensity are observed, as well as a symmetrization of energy distribution around the vortex. Eyewall high wave number structures show a dependence on the life cycle phase, supporting previous findings discussing the vortex rapid evolution with onset and propagation of eyewall mesovortices and associated vortex Rossby wave generation. A machine learning approach finally highlights that the eye shape and eyewall radial wind gradient fine-scale dynamics have the potential to improve the statistical prediction of TC intensity variations, compared to the sole use of vortex averaged parameters and synoptic information. The high-resolution radial and azimuthal coverage provided by SARs make these acquisitions a very valuable

tool for TC research and operational application.

## 3.1 Introduction

Forecast and understanding of tropical cyclone (TC) life cycle has been a critical challenge of meteorological science for decades. The development of dynamical weather forecast models, and our increasing observational capacity from space have led to a better resolution of the synoptic steering flow and to subsequent improvements in TC track and maximum potential intensity forecasts (Miller, 1958; Emanuel, 1986; Emanuel, 1987; Elsberry et al., 2013). On the other hand, the forecast of TC intensity variations has seen much less progress (Cangialosi and Franklin, 2019). TC intensification and mature-phase intensity variations are associated to multi-scale interactions (interactions between very fine and synoptic scale processes (e.g.Elsberry et al., 2013), complex internal and stochastic dynamics in the inner-core (e.g. Wang and Wu, 2004; Montgomery and Smith, 2014), and exchanges with the underlying ocean (e.g. Bender and Ginis, 2000; Wada, 2009; Jullien et al., 2014), which are more difficult to model and predict, and are not necessarily well understood.

TC intensification theories, developed since the 60s (Charney and Eliassen, 1964; Ooyama, 1964; Ooyama, 1969; Emanuel, 1986; Smith, Montgomery, and Van Sang, 2009), are still debated. They assume that TC vortex intensification occurs through the spin-up of tangential winds, which mainly takes place above the boundary layer (BL). There, the flow is assumed to be in gradient wind balance, and to converge due to eyewall deep convection causing tangential winds to increase (as angular momentum is conserved). In the BL, the assumed gradient wind balance is broken by surface friction, causing convergence of moist air which eventually releases latent heat when reaching the eyewall, and provides fuel for deep convection (Emanuel, 1986). Intensification thus occurs through a feedback between spin-up above the BL, moisture inflow in the BL, and convection in the eyewall. A more recent study (Smith, Montgomery, and Van Sang, 2009) also suggests that spin-up could occur inside the BL due to supergradient winds present in the inner-core, with the strongest winds thus located at the top of the BL and the inner-core being partly decoupled from the outer-core. Studying and observing the BL structure is thus crucial to better understand surface energy transfers and inner-core dynamics, such as wind spin-up, gradient and supergradient balances, and convectively driven inflow, that drive TC intensification.

Intensity variations of the mature TC have also been thoroughly studied: while triggered by external events such as vertical wind shear or tropospheric troughs (Uhlhorn et al., 2014), they are also tightly connected to several internal processes mainly occurring in the inner-core, eye, and eyewall areas. Eye warming (Stern and Zhang, 2013) and observed mid-level thermodynamic inversions within the eye (Jordan, 1961; Willoughby, 1998; Franklin, Lord, and Marks Jr, 1988) have been related to intensity variations as eye subsidence interacts with the eyewall convection, and modifies the dynamical balance in the BL. Eye contraction is described as a supporting mechanism to vortex intensification and stabilization (Shapiro and Willoughby, 1982; Lee and Bell, 2007). Secondary eyewalls (Holland, Belanger, and Fritz, 2010; Willoughby, Clos, and Shoreibah, 1982), and eyewall replacements (Houze et al., 2007) have been observed as a result of TC vortex destabilization and progressive re-establishment after external events affecting the TC life cycle. A range of observational studies, mainly based on coastal (Macdonald, 1968; Muramatsu, 1986; Kuo, Williams, and Chen, 1999) and airborne (Reasor et al., 2000; Corbosiero et al., 2006) dual-Doppler radar imagery, has also identified Vortex Rossby Waves (VRWs) as a progressive restoration process.

The VRW theory, first formalized by Montgomery and Kallenbach, 1997, describes internal waves propagating along potential vorticity gradients that promote vortex axisymmetrisation by propagating energy from the TC center to its periphery. The basic dispersion relation for a symmetrizing spectrally localized wave-packet of VRWs is the following:

$$\omega = n\overline{\Omega}_0 + \frac{n}{R}\frac{\bar{\zeta}_0'}{(k^2 + n^2/R^2)} \tag{3.1}$$

where $\overline{\Omega}_0$ is the mean flow angular velocity and $\bar{\zeta}_0'$ the mean flow potential vorticity gradient, R is the radius, k and n are the initial central radial and azimuthal wave numbers. Thus, given a negative potential vorticity gradient as in an idealized cyclonic monopole, the waves rotate opposedly to the mean flow rotation. Computation of the group velocity also shows that a negative potential vorticity gradient imposes an outward group velocity Montgomery and Kallenbach, 1997.

In this context, a perturbation of the eyewall convection (most often caused by external shear) can cause a breaking of the eyewall vorticity ring, leading to emergence of eyewall mesovortices (Schubert et al., 1999; Kossin and Schubert, 2001). These mesovortices modify the eye shape, induce mixing within the eye, and eventually organize, resulting in VRWs propagating around the eye and causing eye rotation. Then, they propagate outward, generating inner rainbands of higher vorticity (Macdonald, 1968), and possibly trigger the formation of outer spiral rainbands when reaching their stagnation radius (Montgomery and Kallenbach, 1997; Chen and Yau, 2001). Their propagation is suggested to allow dissipation of the center instability and reformation of the eyewall vorticity ring, thus enhancing eyewall convection and TC intensity. A complete review of VRW theory and their role in TC intensity variations is provided by Wang and Wu, 2004.

Fast structural changes of TCs, associated to the fine-scale rapid evolution of the inner part of the eyewall, and subsequent VRW propagation certainly contribute to the difficulty of forecasting TC intensity changes. Usual operational statistical-dynamical forecast models (DeMaria and Kaplan, 1994; DeMaria and Kaplan, 1999; Knaff, Sampson, and DeMaria, 2005; Knaff and Sampson, 2009) use linear regression techniques to predict intensity changes from large-scale climatological fields (temperature, humidity, maximum potential intensity, shear...), TC intensity, and rate of change at the forecast initial time. The observational limitations regarding TC internal small-scales (lack of spatial and temporal resolution) have prevent their use in such statistical models. Based on a numerical study, Judt, Chen, and Berner, 2016 suggested that forecast errors rapidly grow on small scales, limiting their predictability. However, the tight relation between mesovortices generated in the eyewall inner-edge, induced mixing and spin-up within the eyewall (Schubert et al., 1999; Kossin and Eastin, 2001; Nguyen et al., 2011) foresees towards a potential improvement of TC variation predictability with a better assessment of such fine-scale structures and associated dynamics.

The wide range of interacting processes that induce TC intensity variations, including external large-scale events, eye and eyewall instabilities, VRW generation and propagation, involve synoptic to turbulence scales ranging from days to seconds temporally, from hundreds of kilometers to meters spatially, and from the troposphere to the sea surface vertically. Observing the TC structure evolution associated to these intensity modulation processes thus requires a combination of high temporal and spatial resolution, together with a large coverage, and a cloud-penetrating technology. The definition of a sensor or a network of complementary sensors able to achieve comprehensive observations of TCs at global scale thus remains a challenge.

The most prevalent TC observation source is geostationary satellite imagery; it provides high resolution, extended geographical and temporal coverage and is widely used for TC intensity monitoring and forecast (Dvorak, 1975; Olander and Velden, 2007). However, geostationary observations are limited to top-of-the-cloud information (as they operate in visible and infrared wavelength), and cannot directly retrieve the BL evolution. Other available satellite observations for wind measurements are those of L-band or multi-frequency radiometers and scatterometers (cloud-penetrating microwave wavelength). They are able to provide a direct estimate of the wind speed at the ocean surface(Meissner and Wentz, 2009; Zabolotskikh, Reul, and Chapron, 2015; Katsaros et al., 2002; Reul et al., 2017) and thus valuable information on the TC structure. However, they are limited by their spatial resolution (usually 40-50 km) preventing their use for studying the TC inner-core structure. Small-scale BL observations are thus usually only obtained with airborne Doppler radars, dropsondes, and ground-based radars. These observations provide high resolution measurements in the BL (Marks, 2003), but with limited geographic extent and sampling capacity: airborne observations have a very partial coverage of the azimuthal structure (Reasor et al., 2000; Uhlhorn et al., 2014), and time lags between passes that limit the temporal coverage, and coastal radars do not have access to the entire TC life cycle due to their limited radial extent.

The technology of Synthetic Aperture Radars (SAR) provides an adapted complement to these techniques. It is indeed the only satellite remote sensing technique that allows probing the sea surface at very high resolution, and can provide estimates of 2D wind fields with kilometer resolution (Katsaros et al., 2002). However, SAR data are not commonly used for TC observations for several reasons: 1) over open ocean there is no systematic SAR acquisition and some of the acquisition modes do not allow for TC wind retrieval, 2) to date the planning of TC acquisitions in the adequate mode is not a priority for SAR missions' objectives, and is only performed on request, and if other higher priority acquisitions are not planned, 3) the wind retrieval from SAR images in TCs requests a dedicated treatment, which has only been recently developed (Zhang et al., 2016; Mouche et al., 2017), and 4) SAR data are currently not available in real-time limiting their potential use to post-event reanalysis only. Nevertheless, SAR data have been shown to allow the retrieval of several TC properties: TC center, eye shape (Lee et al., 2016; Du and Vachon, 2003; Jin, Wang, and Li, 2014; Liu et al., 2014), rainbands and precipitation (Long and Nie, 2017; Jin et al., 2017; Zhang and Li, 2017), convective cells (Zhang and Li, 2017), BL rolls (Foster, 2005), and surface wind speed (Zhang et al., 2016; Zhang and Perrie, 2017; Yang et al., 2017). Based on a set of 83 net radar cross section (NRCS) SAR acquisitions, Li et al., 2013 adopted a statistical approach to link hurricane eye derived morphology to TC intensity. They associated a reduction of the evaluated eye area, and a decrease of the evaluated main wavenumber characterizing the eye shape, with eye contraction and eye shape symmetrization processes with increasing TC intensity. As most wind inversion algorithms under high winds are new or still under validation, most existing SAR studies have focused on surface roughness data for the estimation of TC properties (eye shape, BL rolls, rain bands or mesovortices), and are often limited to weak TCs.

The present study takes advantage of a new consequent database of TC SAR observations, which has been gathered from two SAR missions (Sentinel-1 and RADARSAT-2) over a four-year period extending from 2016 to 2019. This database covers a wide range of TC cases. It has been used to set up a new wind inversion algorithm (Mouche et al., 2017), and has been validated against the International Best Track Archive for Climate Stewardship (IBTrACS), the National Oceanic and Atmospheric Administration (NOAA) airborne measurements, and the L-band radiometer wind estimations (Combot et al., 2020; Mouche et al., 2017; Mouche et al., 2019). Based on this new consequent database of SAR wind speed retrievals in TCs, the present study describes a methodology developed to extract TC structural properties (e.g. eye and ring of maximum wind shapes, surface wind gradients), and energy repartition within the TC vortex (characterized through surface wind intensity spectral decomposition).

Our analyses then demonstrate the ability to describe and characterize, with such acquisitions, the TC inner-core, through its radial profile, its azimuthal degree of asymmetry, and the energy distribution in the eyewall and maximum wind areas. These results have strong implications for operational and research applications, as the near real-time estimation of typical TC characteristics (maximum wind speed, radius of maximum winds, inner-core and near-core wind gradients, vortex asymmetries), which can be used for TC forecast, high wave and storm surge forecast, and observational research on inner-core dynamics and intensity restoration processes. Our analyses also suggest potential use of our wind profiles for estimating mean wind profiles, or fitted 2D wind structures, which could be used as forcing for operational risk assessment or other research applications. A second objective of our statistical analyses is to investigate the importance of the fine-scale variability of the eyewall and area of maximum wind for understanding the TC intensity fluctuations, and their potential to improve our ability to dissociate intensification phases. As SAR acquisitions are snapshots, with a relatively sparse sampling, they do not allow for a continuous monitoring of each TC evolution, and prevent for an estimate of the short-range dynamical changes in the internal structure. However, here we propose to evaluate their predictability potential by assessing the relation of TC SAR-extracted parameters (intensity, size, radial profiles, azimuthal degree of asymmetry and energy distribution) to the 12h on-going TC intensity change. An evaluation of their added-value in an actual statistical forecast model is beyond the scope of this paper, but may be an exciting perspective.

The paper is organized as follows. Section 3.2 describes the dataset and the methodology of processing of SAR images, Section 3.3 then describes the TC radial and azimuthal structures and investigates their evolution as a function of TC intensity, with a focus on the inner-core and the eyewall area, and compares these new SAR observations to previous studies. The benefit of observing these internal structural properties to depict the TC life cycle and its predictability is assessed in the last part of Section 3.3, using a methodology based on machine learning classification. Finally, Section 3.4 discusses our results and the technical limitations of our dataset and Section 3.5 draws the conclusions.

## 3.2 Data and Methods

### 3.2.1 SAR dataset

The SAR dataset used in this study is the result of the Satellite Hurricane Observation Campaign (SHOC) started in 2016 by the European Space Agency (ESA). Following the first promising SAR observations made with Radarsat-1 in TCs (Friedman and Li, 2000; Katsaros et al., 2000; Du and Vachon, 2003), SHOC aims at programming acquisitions over TCs with Sentinel-1 and Radarsat-2 SAR missions based on TC track forecasts.

SAR is a side-looking microwave active sensor, which measures the backscatter signal to estimate sea surface roughness. The synthetic aperture principle consists in processing together the phase and amplitude of several consecutive acquired signals to build a synthetic along-track antenna much larger than the real one. The high sampling frequency and the synthetic aperture therefore provide a spatial resolution that ranges from 10m to 1 km (depending on the acquisition mode). The drawback of SAR high resolution is that the raw data volume is very high, and consequently the satellite is not in continuous acquisition mode.

Both Sentinel-1 and Radarsat-2 are C-Band SARs. The acquisitions are carried out in wide swath mode to encompass the whole TC structure, and in both co- and cross-polarization modes, which have been shown to complement one another in retrieving wind speed and direction. Indeed, as outlined by Mouche et al., 2017, the cross-polarization implemented on both Sentinel-1 and Rardarsat-2 is much more sensitive to high wind gradients, allowing a better resolution of the TC wind field (characterized by large wind gradients and wind speeds exceeding 35m.s$^{-1}$). On the other hand, cross-polarization is also more sensitive to noise (due to swath junctions or precipitation in the atmospheric column). The co-polarization is thus used to validate or replace cross-polarized data in the low to moderate wind regimes, and will help retrieving wind streaks for estimation of the wind direction. This latter capacity is however not fully implemented yet, and therefore it is not available for the present study. The geophysical model functions (GMFs) used are CMod5n for co-polarized and MS1A for cross-polarized data, as described in Mouche et al., 2017.

The validity of the SAR TC wind field database used in the present study was thoroughly evaluated against the National Oceanic and Atmospheric Administration (NOAA) airborne measurements using the Stepped Frequency Microwave Radiometer (SFMR), L-band radiometer wind estimations, and the International Best Track Archive for Climate Stewardship (IBTrACS) by Mouche et al., 2017; Mouche et al., 2019 and Combot et al., 2020. Mouche et al., 2017; Mouche et al., 2019 described and validated the wind inversion algorithm against L-band radiometer data, and SFMR data. Combot et al., 2020 examined and validate the SAR database (TC maximum wind intensity (Vmax), Radius of Maximum Winds (RMW), and characteristic 34-, 50-, 64-kt wind radii (R34, R50, R64)) against IBTrACS and SFMR data. Overall, these 3 papers showed an excellent agreement of the wind intensity retrieved from SAR with all compared datasets (IBTrACS, SFMR, L-band radiometers). Combot et al., 2020 found a 0.87 correlation between SAR and best track (BT) Vmax, with an 8.76m.s$^{-1}$ RMSE, and an even higher agreement with SFMR data (correlation of 0.9, RMSE of 4.85 m.s$^{-1}$, bias lower than 0.5m.s$^{-1}$). They associated the better agreement found with SFMR to BT estimate errors in cases of rapid intensifications (not well captured), or to eye replacements cycles. Some differences were also spotted as a consequence of rain artifacts in SAR data, which can cause inconsistent wind peaks. 14% of the cases were found significantly affected by rain, with a mean computed intensity variation of 6.2m.s$^{-1}$. Rain impacts on SAR wind retrievals are challenging issues, and have to be kept in mind when analyzing the SAR wind field. However, they usually cause very localized anomalies, and the methodology that we developed in the present study was designed to minimize their potential impact on the results (see section 3.2.3).

Combot et al., 2020 further evaluated the spatial structure of SAR retrieved wind fields by comparing the retrieved characteristic wind radii (RMW, R34, R50, R64). RMW comparisons with SFMR revealed excellent agreement (correlation of 0.95 and bias of 3.5km, except for the case of TC Florence), while comparisons with BT showed stronger discrepancies (0.47 correlation, 25km RMSE, improving to 11.6 km when discarding the cases of double eyewalls). BT RMW retrievals are however notoriously bad in the absence of aircraft data, as they are derived from indirect methods or low-orbit satellite missions using medium to low resolution observations. Additionally, radii associated to higher winds might have a higher temporal variability possibly not captured by the 6 hourly BT analysis. R34 and R50 comparison with BTs showed a correlation higher than 0.85, and a low normalized bias of ~3%, and of ~10% for R64 (larger differences in R64 being associated to same reasons than RMW discrepancies). The present SAR dataset is thus considered to satisfactorily allow for TC surface wind field characterization, and will be shown, in this study, to offer a unique opportunity to capture inner- and near-core wind structure of the TC vortex, thanks to its high-resolution and spatial extent.

From the beginning of SHOC campaign in 2016, 279 eye-matching TC acquisitions were gathered. 188 of these acquisitions successfully passed our parameter extraction procedure (described in the following section 3.2.3), and were used in the present study. Other cases which were withdrawn are usually associated to partially covered vortex structure, a too large portion covered by land, or weak distorted TCs preventing parameter estimation. Figure 3.1 shows that a wide range of TC characteristics (intensity, basin, position, size, intensification rate, translation speed) is represented in the 188-case dataset. These characteristics are computed from the images themselves, except for intensification rate and translation speed which are computed from best track data described in the following paragraph.

### 3.2.2 Best-track (BT) data

We use the International Best Track Archive for Climate Stewardship (IBTrACS; Knapp et al., 2010) that combines the best-track (BT) data from various meteorological centers (Regional Specialized Meteorological Centers responsible for TC forecast in the different basins, and country agencies) into one common format. In a few cases, IBTrACS database does not completely cover the extent of an event. In these cases, the Automated Tropical Cyclone Forecast System (ATCF, Miller et al., 1990) is used to retrieve BT parameters. It may be noted that the most recent tracks from IBTrACS and ATCF are provisional, meaning that they have not been reprocessed with all available observations.

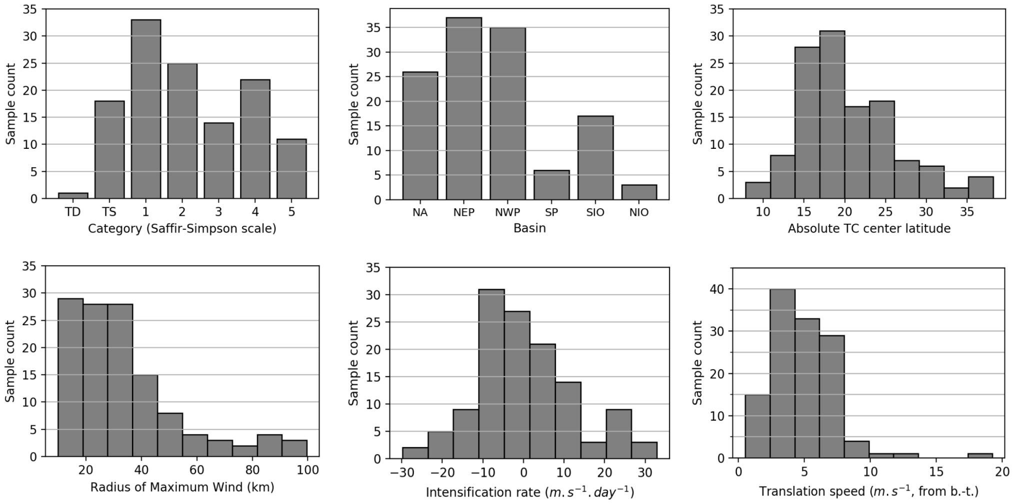

Figure 3.1 – Overview of the SAR TC database (number of samples) in terms of TC category, basin, absolute latitude, radius of maximum wind (km), intensification rate (m.s$^{-1}$.day$^{-1}$), and translation speed. The two latter are retrieved from best track data, while other parameters are retrieved from SAR images. Basin codes are the following: Northern Atlantic (NA), Northern Eastern Pacific (NEP), Northern Western Pacific (NWP), Southern Pacific (SP), Southern Indian Ocean (SIO), Northern Indian Ocean (NIO).

The BT position, Radius of Maximum Wind (RMW$_{\mathrm{BT}}$) and 34kt-radius (R34) are used for image processing (in particular for retrieving the TC eye and maximum wind areas). BT data (position and intensity (Vmax$_{\mathrm{BT}}$)) are also used to characterize the TC life-cycle, in particular the intensification rate, as no linear and continuous temporal dimension exists in SAR data due to a temporally sparse sampling of acquisitions. To provide the closest BT temporal parameter estimates for each SAR acquisition, the BT data are linearly interpolated at the acquisition time. The temporal resolution of BTs is limited to 3 hours for IBTrACS and 6 hours for ATCF, and the resolution in Vmax$_{\mathrm{BT}}$ is respectively 1 m.s$^{-1}$ for IBTrACS and 5 m.s$^{-1}$ for ATCF data, yielding to a limited precision of the interpolated tracks. We will show in the next section that a first important step in SAR image processing is to retrieve the TC center on the image itself, as the BT interpolated TC center positions can be rather far from the true center. The intensification rate is defined as the time derivative of Vmax$_{\mathrm{BT}}$ between t-6h and t+6h, t being the acquisition time.

In the next sections, parameters extracted from BTs are noted with a BT subset (e.g. RMW$_{\mathrm{BT}}$) to differentiate them from those retrieved from SAR.

### 3.2.3 Methodology of TC parameters extraction from SAR images

We designed a methodology to extract, from SAR-retrieved surface wind field, four characteristic azimuthal signals describing the TC: the maximum surface wind ring intensity and its shape, the eyewall surface wind gradient, and the eye shape. To do so, several steps are performed to ensure their best estimate, and to circumvent most of the eventual errors in SAR measurements. The first step consists in masking potential areas of erroneous signal, the second step consists in detecting the TC center, the third step is to project and interpolate the SAR image on a polar grid centered on the extracted TC center. Then, the four azimuthal signals are extracted with a procedure detailed in the following. Finally, the last step consists in a completion of partially cut signals (due to image border) and a smoothing. These different steps are detailed hereafter.

#### Masking: subswaths, outliers, and rain signatures

- Subswaths and outliers
  Subswath signatures can be identified in the SAR wind speed retrievals, indicating that wind values in their vicinity are probably erroneous. We therefore detect these subswath signatures based on their high value of column-wise average wind gradient, and mask them (Fig. 3.2A, blue lines). Subswaths and issues with the acquisition can sometimes cause larger signatures in the wind field, for which this filtering step may not be sufficient, but it overall removes most of the subswath signatures, which could hamper our azimuthal signals extraction. A second masking procedure is applied consisting of a pixel-wise mask to remove any eventual pixel outlier (e.g. spike pixel values in the wind field not corresponding to a realistic wind structure).
- Heterogeneity mask and rain signatures
  Additionally, the SAR wind product includes a heterogeneity mask designed to remove non-wind-related features associated with high local gradient values (Fig. 3.2A, gray contours). Such structures are often due to heavy rain impacting the SAR Net Radar Cross Section (NRCS) signal. Rain impact on SAR measurements is indeed a preoccupying feature of SAR inversion algorithms. Mouche et al., 2019 showed, in the case of hurricane Irma, that heavy rain can either attenuate or enhance the NRCS signal but concluded that: *"at this stage, there is not enough*

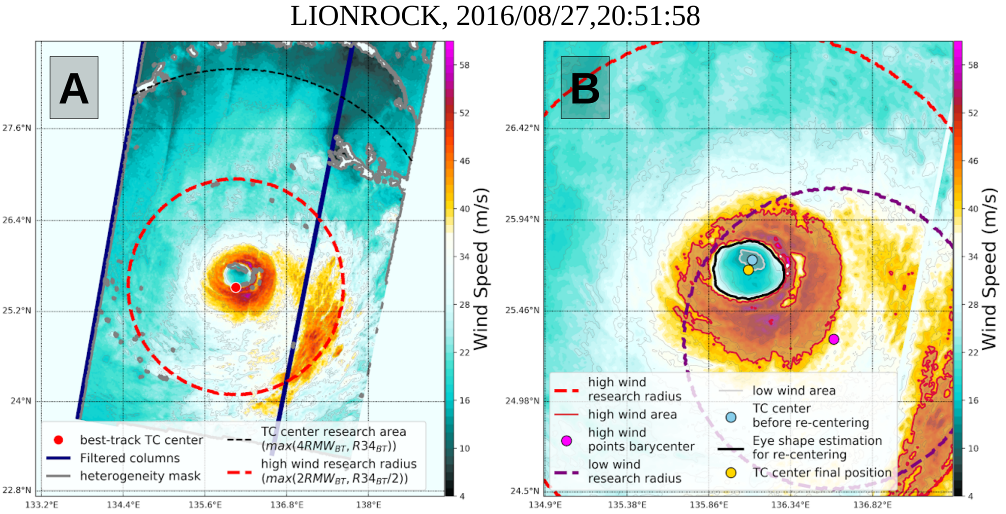

Figure 3.2 – Illustration of the TC center research algorithm on the case of TC LIONROCK (Western Pacific) observed with Sentinel-1 SAR on the 27th of August 2016 . The TC wind field (m.s$^{-1}$) as retrieved from the SAR is shaded in (A) and (B); (B) is a zoom over the TC eye. In (A) the heterogeneity mask (masking high gradient values of the backscatter signal) is represented with grey contours, the black dashed circle denotes the radius at which the heterogeneity mask is removed, the subswath signatures are identified with dark blue lines, and the red dot locates the interpolated BT TC center. The red dashed circle in (A) and (B) denotes the first research area for TC center. In (B) the detected high wind points are contoured in red, their centroid is located with the magenta dot, the second research circle is featured by the purple dashed line, the low wind points are contoured in light grey, and their centroid is located with the cyan dot. The raw eye shape signal is depicted by the black contour, and the final TC center is located with the yellow dot.

*evidence to conclude if these overall signal changes are solely due to rain impacts, to wind changes, or to their combined effects"*. Combot et al., 2020 also conducted a statistical assessment of rain impact on the SAR estimation of $V_{MAX}$ and RMW using rain rate estimates inferred from IMERG (Integrated Multi-satellitE Retrievals for GPM) product co-located with SAR acquisitions in time and space (±10 km around the SAR-derived RMW). They found 14% of their cases to be significantly affected by rain with a mean computed intensity variation of 6.2m.s$^{-1}$. On another hand, they also showed that their SAR-derived RMW were generally insensitive to rain issues.

Automated removal of rain artifacts is however quite difficult, and in-depth dedicated research is requested to address this issue. The heterogeneity mask, used in the present study, removes part of the rain-induced artifacts of the SAR wind field, and eventual remaining rain artifacts are considered to not significantly impact our analyses. Indeed, visual inspection of several case studies have shown that remaining rain signatures are mostly external to the maximum wind ring, and additionally the smoothing step applied on our extracted signals, and the statistical analyses performed on numerous cases limit the impact of local anomalies in SAR wind fields. A complementary discussion of rain impacts is provided in section 3.4.3.

### Locating the TC center

The second step of SAR image processing is to detect the TC center. Indeed, even though the TC center derived from BT has been interpolated, it is not always co-located with the center of the TC eye, as illustrated in Fig. 3.2A. The step of TC center positioning is crucial for our study, because all TC properties are then described in a polar grid referenced on the TC center. Its retrieval is designed to be generic and automatic, working on level-2 data. The procedure consists in the following steps, and is illustrated in Fig. 3.2 for a Sentinel-1 SAR acquisition performed on the 27th of August, 2016 on TC LIONROCK (Western Pacific).

As the TC eye is a region of strong wind gradient, it is often partially masked by the heterogeneity mask described in the previous paragraph (see gray contours in Fig. 3.2A). For this step of TC center research, we thus temporarily remove the heterogeneity mask around the BT interpolated TC center, in a radius defined as $max(4\mathrm{RMW}_{\mathrm{BT}}, R34_{\mathrm{BT}})$ (Fig. 3.2A, black dashed line). The heterogeneity mask is later reapplied on the polar-projected data out of $1.5 * \mathrm{RMW}_{\mathrm{SAR}}$.

Several TC center extraction algorithms have been developed for SAR images. Most of them rely on a wavelet analysis of the level-1 surface roughness images to find the TC center (Zheng et al., 2017). In the present study, as we use level-2 wind speed data, a new method is designed based on several wind speed thresholds to gradually approach the TC center. First, the pixels corresponding to the highest wind speed values, defined as the upper 80% of the wind range in a radius of $max(2\mathrm{RMW}_{\mathrm{BT}}, R34_{\mathrm{BT}}/2)$ around the BT center (Fig. 3.2A,B, red dashed line), are identified (Fig. 3.2B, red contour), and their centroid is located (magenta dot). Then, in a similar way, the centroid (cyan dot) of the low wind area (lower 20% of the wind speed range, gray contour) in a radius of $2\mathrm{RMW}_{\mathrm{BT}}$ around the high wind centroid (magenta dashed line) is located. This low wind centroid is then iteratively recomputed, in a radius of $2\mathrm{RMW}_{\mathrm{BT}}$ around the last estimated low wind centroid to ensure finding a stable location. Indeed, in some cases, the first low wind centroid guess might fall outside the eye, in the high wind vicinity. In such cases, the iterative procedure locates the centroid further from the high wind area and no stability is found. If so, the low wind centroid research is re-processed within a smaller radius of research around the high wind centroid until finding a stable low wind centroid. This procedure manages to find the TC center in a vast majority of cases, although some exceptions can occur. Finally, to prevent errors in the polar projection in cases where the low wind centroid is eccentric with respect to the vortex structure (mostly when the eye is large and distorted or when the eye distribution in the eye is not uniform), a re-centering step is carried out. This last step consists in locating the centroid (yellow dot) of the eye shape, defined as the maximal radial wind gradient for each azimuth (black line in Fig. 3.2B) around the low wind centroid. In cases where the eye shape centroid falls outside of the polygon (when the eye is distorted and the polygon is concave), the final TC center is defined as the pole of inaccessibility of the polygon, i.e. the "most distant internal point from the polygon outline". The final TC center is thus defined as the eye shape polygon centroid (or pole of inaccessibility in concave eye configuration).

### Extracting azimuthal signals

The SAR image is then projected and interpolated on a polar grid centered on the extracted TC center. The azimuthal resolution of the polar grid is set to one degree, and the radial vector is defined between 0 and $10 * \mathrm{RMW}_{\mathrm{SAR}}$ with a resolution matching the one from the original Cartesian grid of the image. The polar grid is geographically oriented with an easterly zero azimuth (the extracted signals are thus not oriented to the TC direction of motion).

Four characteristic azimuthal signals are extracted: two characterizing the TC intensity distribution, the eyewall wind gradient and the maximum wind azimuthal distributions; and two characterizing the TC shape, the eye shape and the maximum wind contour shape.

— Maximum wind distribution ($\mathrm{Vmax}_{\mathrm{AZ}}$)

The azimuthal distribution of maximum wind intensity is retrieved by extracting for each azimuth the maximum wind value. To avoid local outliers in the distribution, these maximum wind values are computed using a sliding average algorithm: for each azimuth, the profile used to compute maximum wind is averaged with its 6 closest neighbors. The retrieved signal is hereafter noted $\mathrm{Vmax}_{\mathrm{AZ}}$.

— Maximum wind shape ($\mathrm{RMW}_{\mathrm{AZ}}$)

The contour of maximum winds is defined by the distance between the TC center and the maximum wind location for each azimuth. This azimuthal distribution of RMW is hereafter referred to as $\mathrm{RMW}_{\mathrm{AZ}}$.

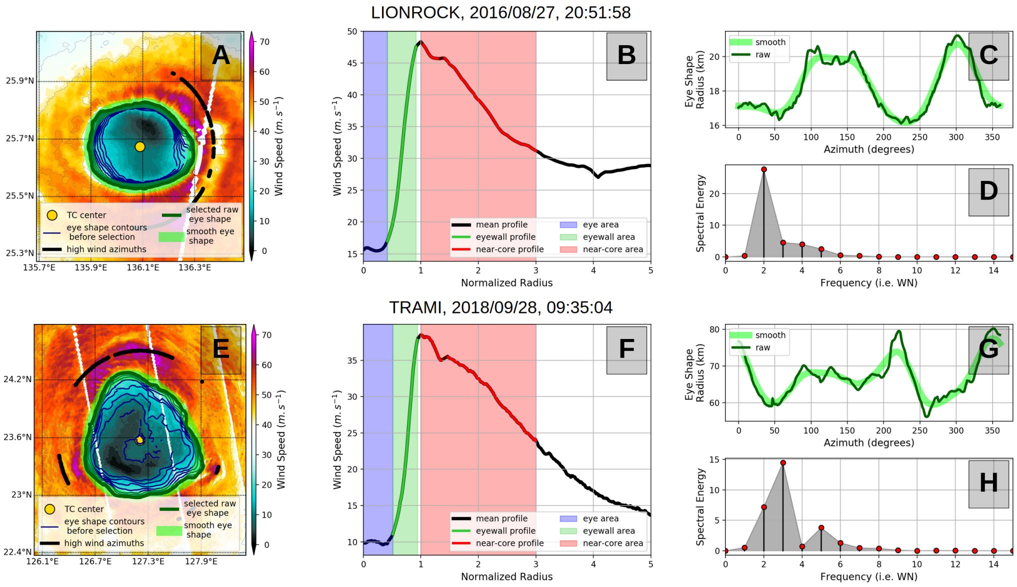

Figure 3.3 – Illustration of the azimuthal signal processing detailed in sections 3.2.3 and 3.2.3 (here for the eye shape) for 2 acquisitions on LIONROCK (Western Pacific, 27th of August 2016) and TRAMI (Western Pacific, 28th of September 2018). Panels A and E show the SAR 2D wind field and contour of the extracted eye shape (thin dark green contour), and the smoothed eye shape (thick green contour), with highlighted high wind azimuths (black dots) used to compute the maximum radial gradient; the TC center is indicated with a yellow dot. Panels B and F show azimuthal-mean wind profiles with shaded characteristic wind areas (eye area in blue, eyewall in green and near-core in red) and highlighted eyewall (green) and near-core(red) profiles used to compute mean gradient values. Panels C and G show the azimuthal distribution of the eye shape, i.e. the radius between the eye shape contour and the TC center. Panels D and H show the spectral decomposition of the normalized smoothed eye shape radius (the first 15 components are represented).

— Eyewall wind gradient ($\mathrm{dV/dR}_{\mathrm{AZ}}$)

We define the eyewall as the region located between the minimum and the maximum of the second derivative of the radial profile between the TC center and $\mathrm{RMW}_{\mathrm{AZ}}$ (see Fig. 3.3 B and F), so that the eyewall does not include the "flat" wind areas located in the eye and near the peak of the wind profile. The azimuthal eyewall wind gradient, $\mathrm{dV/dR_{AZ}}$, is then defined at each azimuth, $\theta$, as the gradient $\mathrm{dV/dR_{AZ}}(\theta) = [\Delta \mathrm{V}_{r\theta}/\Delta r_\theta]_{r_{\theta min} \rightarrow r_{\theta max}}$, where $\mathrm{V}_{r\theta}$ is the radial wind speed profile for each azimuth, $r_\theta$ is the radius, $r_{\theta min}$ and $r_{\theta max}$ are the values corresponding to the minimum and the maximum of the wind profile second derivative. We also define $\mathrm{dV/dR_{EW}}$ as the mean value of radial gradient in the eyewall computed on the azimuthally-averaged wind profile. This parameter is thus a single value (instead of a 1-D signal) estimating the average radial wind gradient in the eyewall.

— Eye shape

The eye shape is defined as a closed contour of wind located between the maximum radial wind gradient and the TC center. The maximum radial wind gradient is computed for a subset of radial profiles located at high wind azimuths (corresponding to wind values between 99.5% and 99.9% of the image, denoted by black dots on Fig. 3.3). For each of these profiles, the wind value matching the maximum wind gradient is retrieved. These values are averaged and a wind contour matching this average value is extracted, along with 9 other contours matching lower wind values (for cases with incomplete contours, see blue contours inside the eye on Fig. 3.3). The most exterior contour encompassing more than 70% of all azimuths is taken as the final shape.

The four previously extracted azimuthal signals are then smoothed by applying a 3rd order Butterworth filter with a critical frequency of 0.03 (an example is shown in Fig. 3.3b). A signal completion is also performed when the signals are partially cut by image border, by linearly interpolating the azimuthal signal.

### Computing variance and spectral decomposition

After normalizing the signals by their mean value, their variance is computed to characterize the overall asymmetry of the TC shape (relatively to a circle), and the distribution of energy (relatively to a homogeneous ring of wind). Then, a wavenumber spectral decomposition is performed to assess the power level of each wavenumber composing the signal (Fig. 3.3). A re-centering around the respective polygon centroid is applied to the two spatial signals (eye shape and $\mathrm{RMW_{AZ}}$) prior to the spectral decomposition, as our purpose is to characterize the relative azimuthal distribution and not the decentering of the structure, which would strongly sign in wave number 1. The relative power levels therefore describe the shape characteristics (for instance, a relatively elliptical eye is characterized by the predominance of wave number 2 as shown in Fig. 3.3A,C, while a more polygonal eye is characterized by a broader spectrum with strong wave numbers 3 and 5 as shown on the example of Fig. 3.3d,f). For the intensity signals ($\mathrm{Vmax}_{\mathrm{AZ}}$, $\mathrm{dV/dR}_{\mathrm{AZ}}$), the spectral decomposition characterizes the energy distribution: the predominance of low wavenumbers indicates local maxima, while a broader spectrum with higher relative importance of high wavenumbers represents a more distributed energy.

The variance, being the sum of the spectral components, a large value can be associated either with a large amplitude of only one wavenumber (a distortion of the shape, or local energy maxima), or with a smaller amplitude but a larger number of components (which could describe a shape with more noise but closer to a circle in average). In practice though, the smoothing applied to azimuthal signals and the structure of the TC vortex causes the variance to be more likely associated to predominance of large wavenumber amplitudes than to a broader spectrum as displayed in Fig. 3.3, where the upper eye shape is more elongated and has a higher variance than the lower one, which is more polygonal but is closer to a circle on average.

### Vortex averaged properties

The maximum TC intensity ($\mathrm{V}_{\mathrm{MAX}}$) extracted from the SAR images is estimated as the maximum of the azimuthal maximum wind distribution, $\mathrm{V}_{\mathrm{MAX}} = max(\mathrm{Vmax}_{\mathrm{AZ}})$.

A mean radial profile is also computed for each image by performing an azimuthal average. A vortex averaged RMW, as well as an averaged eyewall wind gradient, $\mathrm{dV/dR}_{\mathrm{EW}}$, and an averaged near-core radial gradient, $\mathrm{dV/dR}_{\mathrm{NC}} = [\Delta \mathrm{V}_r / \Delta r]_{RMW \rightarrow 3RMW}$, are computed from this averaged radial profile. The three distinct areas of the radial profile, used to describe the inner core region of the vortex in the following, are thus:

- the eyewall area (green shading on Fig. 3.3B and F): it includes all points where the local radial gradient is higher than 20% of the distribution of radial gradient values for R < RMW ; this ensures to consider the linear part of the eyewall, and avoid the flat areas in the eye and near the maximum wind
- the eye area (blue shading on Fig. 3.3B and F): it is defined as the region between the TC center and the inner edge of the eyewall
- the near-core area (red shading on Fig. 3.3B and F): it extends between the RMW and 3 RMW; this definition of the near-core is also used by Mallen, Montgomery, and Wang, 2005 as it usually contains a critical radius used for the estimation of vortex resilience.

The TC parameters extracted from SAR images are summarized in Table 3.1.

Table 3.1 – Table summarizing the TC parameters extracted from the SAR images, as described in Section 3.2.3

| SAR-extracted parameters abbreviation | Brief description |
|---|---|
| $\mathrm{Vmax}_{\mathrm{AZ}}$ | maximum wind intensity at each azimuth |
| $\mathrm{RMW}_{\mathrm{AZ}}$ | radius of maximum wind speed at each azimuth |
| $\mathrm{dV/dR}_{\mathrm{AZ}}$ | eyewall wind gradient at each azimuth: $\mathrm{dV/dR}_{\mathrm{AZ}}(\theta) = [\Delta \mathrm{V}_{r\theta}/\Delta r_\theta]_{r_{\theta min} \rightarrow r_{\theta max}}$ |
| Eye shape | Outermost closed contour of wind located between the maximum radial wind gradient and the TC center |
| $\mathrm{V}_{\mathrm{MAX}}$ | Vortex maximum wind intensity: $\mathrm{V}_{\mathrm{MAX}} = max(\mathrm{Vmax}_{\mathrm{AZ}})$ |
| $\mathrm{RMW}_{\mathrm{SAR}}$ or RMW | Vortex averaged RMW: $RMW = mean(\mathrm{RMW}_{\mathrm{AZ}})$ |
| $\mathrm{dV/dR}_{\mathrm{EW}}$ | Vortex eyewall wind gradient: eyewall gradient of the azimuthally-averaged wind profile: $\mathrm{dV/dR}_{\mathrm{EW}} = [\Delta \overline{\mathrm{V}}_r/\Delta r]_{r_{min} \rightarrow r_{max}}$ |
| $\mathrm{dV/dR}_{\mathrm{NC}}$ | Vortex averaged near-core radial gradient: $\mathrm{dV/dR}_{\mathrm{NC}} = [\Delta \overline{\mathrm{V}}_r/\Delta r]_{RMW \rightarrow 3RMW}$ |

### 3.2.4 Statistical classification of intensification rates

The potential of SAR-extracted parameters to statistically predict TC intensification rate is assessed in the last part of our results (section 3.3.3) by using a statistical classification, the predictor being the intensification phase: intensification or decay. Two groups of intensification rates are identified: intensification rates above 5 $\mathrm{m.s^{-1}.day^{-1}}$, and decay rates under -5 $\mathrm{m.s^{-1}.day^{-1}}$. The number of images used for this statistical classification is therefore 100 (over the 188 available images), as medium values of intensification rate (between -5 and 5 $\mathrm{m.s^{-1}.day^{-1}}$) are ignored.

The SAR-extracted variables used as predictors for the classifications are: the TC center absolute latitude, $\mathrm{V}_{\mathrm{MAX}}$, RMW, $\mathrm{dV/dR}_{\mathrm{EW}}$, and variance and percentages of explained variance of the 5 first wavenumbers of the 4 azimuthal signals (eye shape, $\mathrm{RMW}_{\mathrm{AZ}}$, $\mathrm{dV/dR}_{\mathrm{AZ}}$, $\mathrm{Vmax}_{\mathrm{AZ}}$). All these variables have a correlation factor lower than 0.7, ensuring their independency. Only the near-core wind gradient, $\mathrm{dV/dR}_{\mathrm{NC}}$, was discarded from the analysis, due to its too large correlation with the eyewall gradient. Given the limited amount of samples (100) and the elevated number of variables (28) composing our dataset, an evaluation of the incremental added value of each variable was not possible. We thus designed a methodology to estimate the relative contribution of each variable to discriminate intensifications vs. decays. Fig. 3.4 illustrates the flow chart of this methodology.

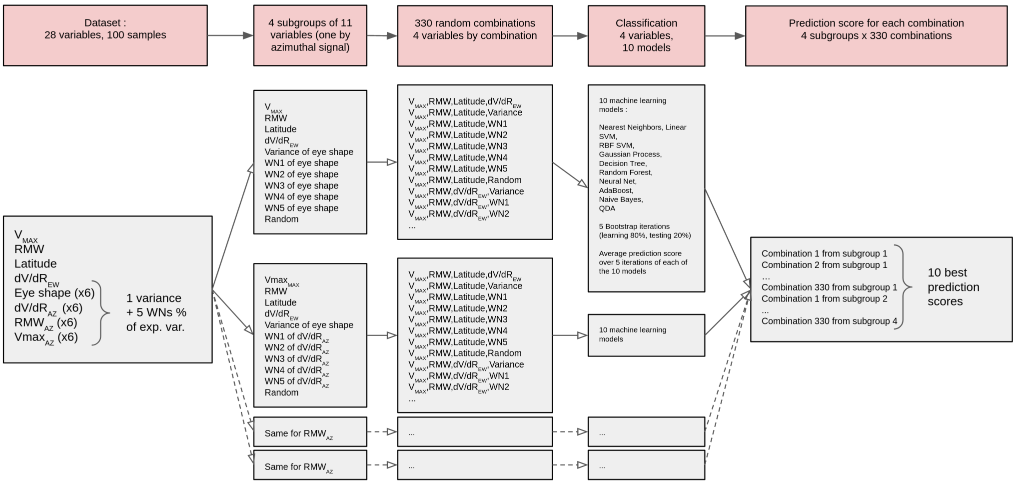

Figure 3.4 – Flow chart detailing the different steps of the statistical classification methodology.

The first step consists in reducing the number of variables (initially 28) by dividing the dataset into 4 groups based on the 4 azimuthal signals: eye shape, $\mathrm{RMW_{AZ}}$, $\mathrm{dV/dR_{AZ}}$, $\mathrm{Vmax_{AZ}}$. Each subgroup contains the variance and the 5 first wavenumbers explained variance percentages of the given azimuthal signal, as well as the vortex averaged properties (TC center absolute latitude, $\mathrm{V_{MAX}}$, RMW, $\mathrm{dV/dR_{EW}}$). A random variable is added to each group as a control variable, yielding to 4 groups of 11 variables. Then, to further reduce the number of variables for the classification (number of samples vs. variables issue), random combinations of 5 variables among the 11 in each group are classified separately. 330 random combinations and associated classifications are performed for each group.

The classification itself is performed using ten usual machine learning models (they are detailed in the 4th column of Fig. 3.4). These models feature a wide range of different methods of machine learning, including regression methods, tree classifiers or neural nets. These different models allow to take into account a wide range of possible relations between variables, including non-linear relations. The classification is performed with a bootstrap method (learning on 80% of the dataset and testing the remaining 20%, then iterating 5 times with an exclusive 20% each time).

The average prediction score is obtained for each combination of variables by averaging the 10 models prediction scores. Combinations are then sorted by order of performance, and the best combinations are detailed.

## 3.3 Results

### 3.3.1 TC vortex parameters and radial profile as observed with SAR

The kilometer-resolution SAR surface wind retrieval allows a detailed 2D characterization of the TC inner-core region, the most intense area of the TC vortex. First, maximum wind speed ($V_{MAX}$) and averaged radius of maximum wind (RMW), extracted from the SAR images, are analysed and compared to previously published results, then a detailed description of the radial and azimuthal wind structures is assessed.

#### Maximum wind speed ($V_{MAX}$) and radius of maximum wind (RMW)

The relationship between SAR-derived $V_{MAX}$ and SAR-derived RMW is illustrated on Fig. 3.5A. In agreement with previous results from airborne and SAR measurements (e.g. Shea and Gray, 1973, Weatherford and Gray, 1988b, Li et al., 2013, Combot et al., 2020), the RMW shows a decreasing trend, along with a decreasing variability as intensity increases: RMW extends from 10 to 100 km for TCs weaker than category 3 (50 m.s-1), while it is restricted to values lower than 50 km for stronger TCs (above category 3). This RMW decreasing trend with intensity can be associated to the eye contraction process described as contributing to TC intensification (e.g. Shapiro and Willoughby, 1982; Stern et al., 2015).

The variability of RMW values observed for moderate (<cat. 3) TCs being quite large, while the one for intense (≥ cat. 3) TCs being smaller, we separate the following analyses into 3 TC groups: moderate and large TCs ($V_{MAX}$ < cat. 3, RMW ≥ 50km), moderate and small TCs ($V_{MAX}$ < cat. 3, RMW < 50km), intense and small TCs ($V_{MAX} \geq cat.3, RMW <$ 50km). The RMW histograms of these 3 categories are shown in Fig. 3.5B. The moderate TC distribution features a relatively clear distinction between the moderate small and moderate large categories at 50km, while intense TCs display RMWs distributed between 10 and 50km with more numerous TCs in the lowest RMW categories. The standard deviations for both small moderate and intense TCs are similar (∼13km), while large moderate TCs have a larger spreading (std=31.5km), partly explained by the lower number of events in this category.

The events lying outside of the overall standard deviation in Fig. 3.5A mostly belong to this moderate large category, and are usually associated to highly asymmetrical TCs

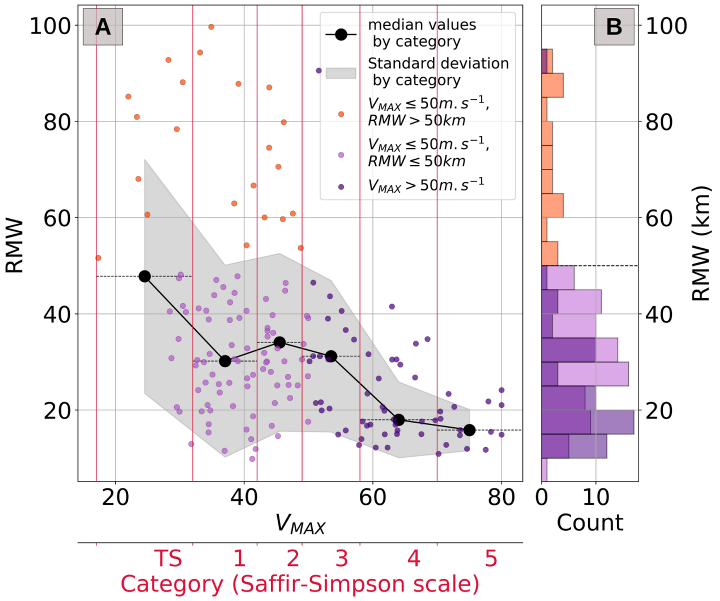

Figure 3.5 – (A) Distribution of SAR-extracted Radius of Maximum Wind (RMW) as a function of maximum wind value ($V_{MAX}$). Dots represent individual images, the black line features the binned median value by category (with horizontal lines indicating the bin extent), and the grey shading the corresponding standard deviation. Dot colors denote the division in 3 groups based on threshold values (50 m.s$^{-1}$ for $V_{MAX}$ and 50km for RMW). (B) Histogram of RMW values for the 3 aforementioned groups.

(see suppl. S1), for which high winds are mostly confined to one sector of the TC vortex. It can be noted that these cases are particularly challenging for RMW retrieval in BT data, which often provide erroneous too low estimates of the RMW (see suppl. S1), while our SAR retrieved RMW seems to be more faithfully estimated.

### Radial wind profile

From the 188 SAR images of our dataset, we compute the average radial wind profile for each TC category (Fig. 3.6A). It shows a strong dependence on TC intensity, with tropical storms (TS, blue curve) having an almost linear profile between the center and the RMW, and strongest TCs (orange and red curves) having a so-called U-shape profile separated in two regions, the eye with a constant low wind value and the eyewall with a sharp wind gradient. The eyewall area denoted by cross markers on Fig. 3.6A tends to move towards the maximum wind area, as indicated by both inner and outer markers being further from the TC center when intensity increases (with a marked distinction

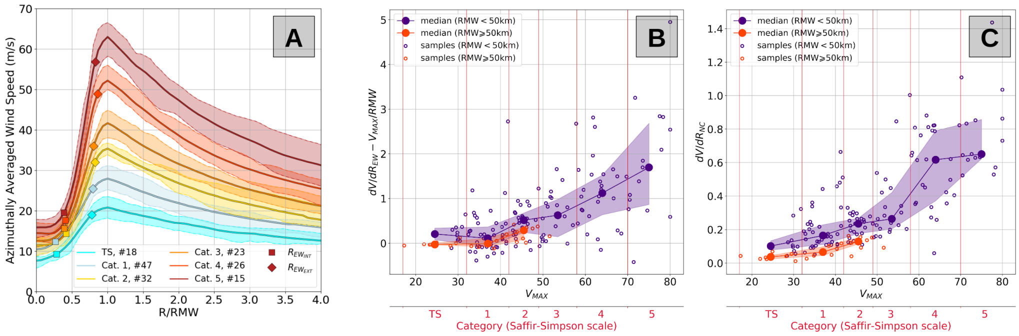

Figure 3.6 – (A) Mean radial wind profiles computed by TC category (Saffir-Simpson). Colored shading indicate the upper and lower quartiles for each profile, and the number of samples by category (#) is indicated in the legend. The x-axis is normalized by the RMW. Markers on the profiles denote mean positions of the eye inner and outer edge by category. (B) Difference between the eyewall radial wind gradient and the Rankine vortex wind gradient approximation: $(dV/dR)_{EW} - V_{MAX}/RMW$, as a function of maximum wind ($V_{MAX}$, $m.s^{-1}$). Small circle markers represent individual images, thick lines with large dark dots and shaded areas respectively denote the binned mean and quartiles by category. Colors represent two subcategories of RMW: RMW<50km in orange, RMW≥50km in purple. (C) Same as (B) but for the near-core radial wind gradient, $(dV/dR)_{NC}$.

between categories 1-2 and 3-4-5 regarding the inner eyewall edge), indicating a reduction of the eyewall extent and a relative increase of the clear eye area with intensity. These observations are consistent with theoretical results which suggest that the eye formation, and sharpening of the eyewall radial wind profile act as stabilizing processes to the TC, favoring its intensification to high categories. Emanuel, 1997 describes the eyewall flow as highly frontogenetic, due to the effect of surface friction: although this frontogenesis can collapse and lead to radial momentum transport into the eye, the feedback between surface wind and surface friction mechanically leads to a mean increase in the frontogenesis of the eyewall flow with intensity.

To further characterize the eyewall wind gradient and its sharpening, it is compared to the Rankine vortex approximation, which assumes a solid-body rotation and a linear profile between $V=0m.s^{-1}$ at R=0 and $V=V_{MAX}$ at R=RMW. As detailed in section 3.2.3, the eyewall wind gradient, $dV/dR_{EW}$, is computed over the quasi-linear region of the eyewall (delimited by the green shading on Figure 3.3B and F) avoiding the flattened areas in the eye and close to the wind peak. Figure 3.6B shows that $dV/dR_{EW}$ progressively departs from the Rankine vortex approximation as intensity increases. The spreading denoted by the interquartile range also increases with intensity, and is the highest for category 5 TCs (though partly explained by the lower number of samples). As previously suggested (Fig. 3.5), moderate TC categories can be separated into 2 sub-categories depending on their RMW. Large TCs show a gentler eyewall radial wind gradient (purple curve) in average compared to smaller TCs (orange curve) for a given intensity.

The progressive increase of the difference between the eyewall wind gradient and the Rankine approximation, as well as the separation between the two RMW sub-categories and outward displacement of the eyewall area, highlight the fact that small and intense TCs have on average a relatively wider eye with respect to their RMW (e.g. the eye external border and RMW are relatively closer to each other), and a sharper radially normalized eyewall wind profile than weaker and larger TCs. However, the large spreading of the data at strong intensity (Fig. 3.6) also denotes a diversity of inner-core situations with a few very intense TCs not having the typical U-shape with a strong eyewall radial gradient and a clearly separated eye. Kossin and Eastin, 2001 also observed, in two aircraft sampled hurricanes, the existence of two distinct regimes of eyewall dynamics, one being characterized by a well-formed eyewall with a clear eye, and the second more similar to a Rankine-like vortex with increased horizontal mixing within the eye. They showed that the TC vortex can alternate between these two regimes in very short time ranges (1h), and linked these transitions to important thermodynamic changes within the vortex structure. Nguyen et al., 2011 also documented such transitions modeling hurricane Katrina and showed that U-shape profile phases were associated with faster intensifications. These two latter studies, as well as Schubert et al., 1999 and Kossin and Schubert, 2001 further discussed how these profile transitions are related to the formation of eyewall mesovortices and subsequent vorticity mixing within the eye, and VRW generation. The shape of the radial wind profile thus also depends on evolution of eyewall mesovortices. These aspects will be further examined in the next section which describes the azimuthal structure and repartition of energy within the observed TCs.

To complement the study of the radial structure, the near-core radial gradient, $(\mathrm{dV/dR})_{\mathrm{NC}}$, in the outer vicinity of the RMW (grey shaded area in Fig. 3.6A), is also computed (Fig. 3.6C). This near-core area is directly linked to the broadness of the primary circulation, also associated to the strength of the TC (Weatherford and Gray, 1988b), and has also been shown to characterize the vortex resilience to external forcing (Mallen, Montgomery, and Wang, 2005). The near core radial gradient in our database is found to increase with TC intensity (Fig. 3.6C). A stronger increase is observed for TC categories 2-5 than for lower TC categories. As for the eyewall wind gradient, at a given intensity, the larger TCs

(RMW≥40km) have a weaker near-core radial wind gradient. Overall, both eyewall and near-core wind gradient analyses illustrate an increased contraction of the high wind area towards the RMW for more intense TCs.

### 3.3.2 Azimuthal TC structure and distribution of energy: insights from SAR

The radial profile analysis has provided an azimuthally-averaged view of the TCs showing that stronger TCs tend to have a wider eye, a sharper eyewall radial wind profile, and a smaller, more contracted vortex. However, vortex asymmetry and azimuthal repartition of energy have been shown to be important components of the intensification mechanisms (cf. asymmetric theories of intensification reviewed by Montgomery and Smith, 2014). We therefore extract, from SAR 2D surface wind fields, the TC eye and RMW shapes to describe the spatial asymmetry (compared to a circle), and the eyewall wind gradient and maximum wind for each azimuth to describe the intensity distribution around the vortex.

Figure 3.7 A and B show decreasing variances of the eye shape and RMW for increasing TC categories, denoting an axisymmetrization of TCs with intensity. The large TCs (purple on Fig. 3.7) feature higher mean values and larger spreading of variances than smaller TCs. These results suggest that axisymmetrization is a condition for TCs to reach category 4 or above, in addition to contraction of the structure, and sharpening of the eyewall radial wind profile.

The variances of eyewall wind gradient and maximum wind speed found around the vortex (Fig. 3.7C,D) also show decreasing trends with TC intensity, illustrating that in addition to the vortex axisymmetrization, the amplitude distribution is homogenized when intensity increases. To further describe this energy distribution, a wavenumber spectral decomposition is performed on the azimuthal eyewall wind gradient and maximum wind signals (see methods section 3.2.3). The wavenumbers (WNs) are gathered into 3 groups: low WNs (1 and 2), which represent the main components of TC asymmetry including signature of translation speed and planetary vorticity; medium WNs (3-5), which represent smaller-scale asymmetries not necessarily related to large-scale interactions; and high WNs (6-180), which describe the spreading of energy towards the tail of the spectrum but have been much less studied, as they are more difficult to observe and may be impacted by noise in the observations (in our case in SAR wind speed estimates).

Figure 3.8 shows a distinct evolution of the eyewall wind gradient and the maximum

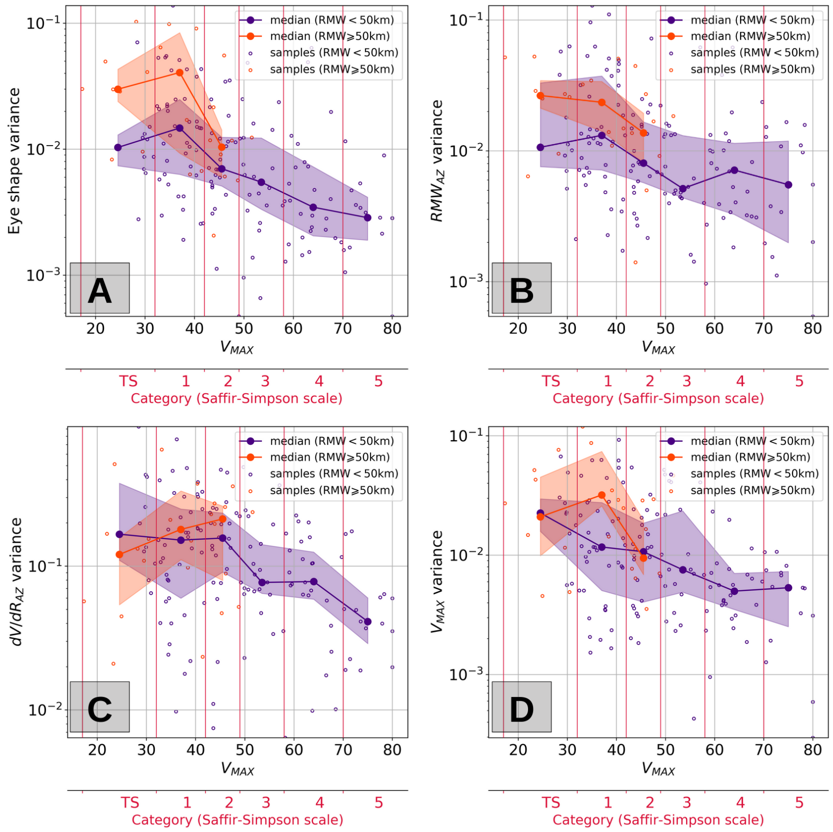

Figure 3.7 – Log-normal distribution of normalized variance of four azimuthal signals as a function of maximum wind: (A) eye shape, (B) RMW$_{AZ}$, (C) dV/dR$_{AZ}$, (D) Vmax$_{AZ}$. Small circle markers represent individual images, thick lines with large dark dots and shaded areas respectively feature the binned median and quartiles. Colors represent two subcategories of RMW: RMW<50km in orange, RMW≥50km in purple.

wind decompositions with TC intensity. On one hand, the maximum winds (green curves) feature a transfer of energy between low and high WNs, with WNs 1-2 explaining 65% of the variance at low intensity and decreasing to 55% at category 5, while medium and high WNs explained variances respectively increase from 23 to 25 % and from 12 to 18%. On the other hand, the eyewall radial wind profile sharpness (blue curves), although showing a small transfer of energy from WNs 1-2 to WNs 3-5 between cat.<1 and category 3, has a much more balanced distribution with similar WN levels at weak and strong TC intensity. The energy distribution thus appears less related to the TC intensity in the eyewall than in the maximum wind area. The energy in the maximum wind area tends to be localized in one or two maxima for weak TCs and to homogenize for stronger TCs, while the eyewall sharpness is already more homogeneously distributed for weak TCs. The

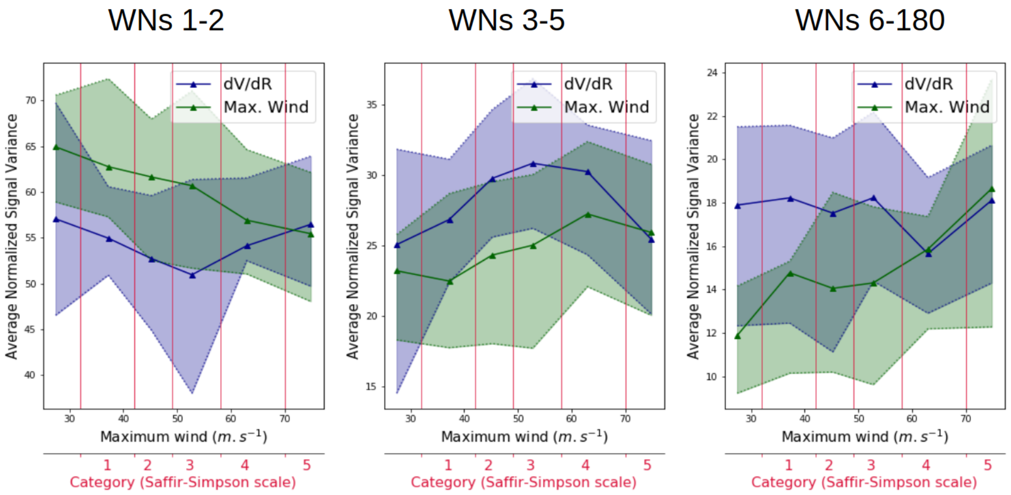

Figure 3.8 – Percentage of variance explained by wavenumbers (A) 1 and 2, (B) 3 to 5, and (C) 6 to 180, for dV/dR$_{AZ}$ (blue) and Vmax$_{AZ}$ (green) azimuthal signals as a function of TC category. Thick lines and shaded areas respectively denote the binned median and quartiles.

broader energy spectrum of the eyewall could also indicate the presence of mesovortices that may locally modify the vorticity mixing between the eye and the eyewall and thus the energy distribution, as discussed in the studies of Schubert et al., 1999, Kossin and Schubert, 2001 and Nguyen et al., 2011. This highlights that the dynamics of the eyewall are not directly coupled with the maximum wind area and may have a separate behavior.

### 3.3.3 Linking SAR-extracted characteristics to TC intensification

In the previous section, we have depicted the TC radial surface wind profile, as well as the azimuthal characteristics of the eye and maximum wind ring shapes, and the azimuthal distribution of energy around the vortex. We have in particular highlighted that very intense TCs feature specific properties (sharper eyewall, more contracted and axisymmetric vortex, broader energy spectrum), which we have suggested could promote or constrain TC intensification. However, we have not yet assessed their direct relation with the intensification rate. This is the purpose of the next sections. As SAR acquisitions are snapshots, with a relatively sparse sampling, they do not allow for a continuous monitoring of each TC evolution, and the fine scale structures observed in SAR images are certainly related to high-frequency intensity changes. We however here try to evaluate if SAR-extracted TC parameters allow to better characterize the TC life cycle and its intensity changes on relatively large time scales (12h here), in the view of assessing the potential use of SAR images for TC forecast issues and statistical models. The intensification rates are here computed from BT data and over a 12h time window (from 6h before to 6h after the TC SAR acquisition), and are separated into 3 classes: intensifying (>5m.s$^{-1}$.day$^{-1}$), stable (between -5 and +5m.s$^{-1}$.day$^{-1}$), and declining (<-5m.s$^{-1}$.day$^{-1}$) phases.

### Life cycle variations

First, we focus our analysis on intensity variations in the mature phase of TCs. Indeed, forming and dying TCs may have very asymmetric structures but are more strongly constrained in forecast systems, notably due to their zonal location and associated environment, e.g. stronger shear when reaching mid-latitudes. Consequently, considering these TCs introduces additional biases that may mislead our interpretations of TC intensity variations.

The evolution of TC contraction with intensification is assessed by evaluating the eyewall radial wind gradient (relative to the Rankine approximation) and near-core radial wind gradient as a function of TC intensification rate (IR) for the 3 TC size-intensity groups (Fig. 3.9). One can first notice that moderate large TCs ($V_{MAX}$<Cat.3, RMW≥50km, orange bars on Fig. 3.9) are all decaying or stable TCs, which may indicate an issue in the representativeness of our dataset but also that most decaying TCs are larger than intensifying ones partly due to the higher latitudes at which TCs decay. The trends obtained for the 2 other groups (small moderate and intense TCs, light and dark purple bars on Fig. 3.9) are similar (but with stronger gradient values for more intense TCs). The eyewall gradient significantly increases, being further from the Rankine profile, from decays (<-5m.s$^{-1}$.day$^{-1}$) to intensifications (≥ 5m.s$^{-1}$.day$^{-1}$). The eyewall radial wind profile sharpness thus appears to be connected to TC intensity life cycle, and could be a determinant factor in the differentiation of decaying and intensifying TCs. This is consistent with previous findings from Schubert et al., 1999; Nguyen et al., 2011 showing that more U-shaped profiles associated with ring-like vorticity distribution favour fast intensifications.

The near-core gradient also shows an increased median value for intensifying TCs, even if the quartile bars denote some overlap for intense TCs indicating a larger variability. The sharper near-core (and eyewall) trend for intensifying TCs indicate a reduced broadness

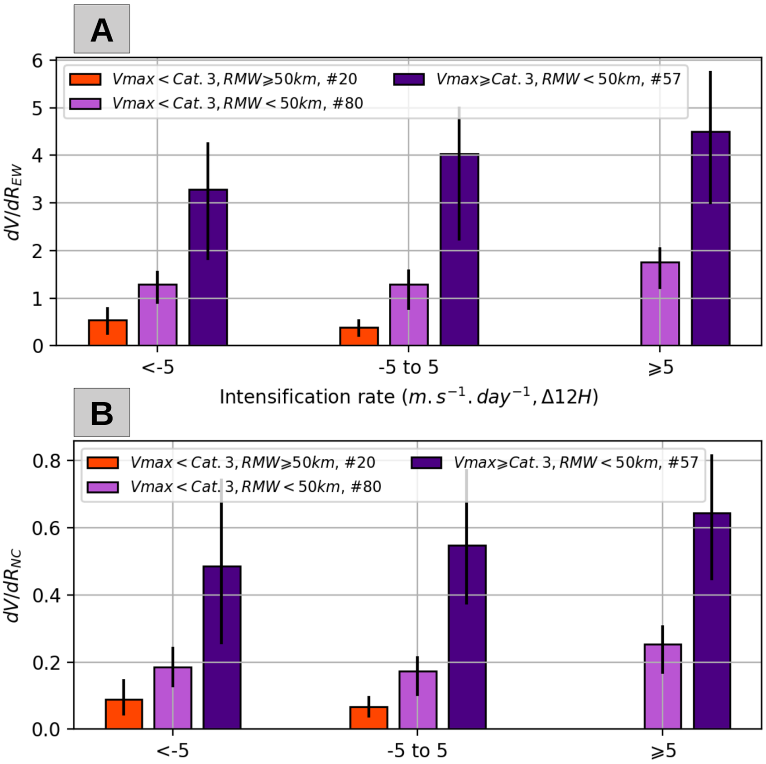

Figure 3.9 – (A) Eyewall radial gradient ($dV/dR_{EW}$, $m.s^{-1}.km^{-1}$), and (B) near-core radial gradient $dV/dR_{NC}$, $m.s^{-1}.km^{-1}$), as a function of intensification rate ($m.s^{-1}.day^{-1}$) for 3 subcategories of RMW and maximum wind: $V_{MAX}$ <cat.3 and RMW≥50km (orange), $V_{MAX}$ <cat.3 and RMW<50km (light purple), $V_{MAX}$ ≥cat.3 and RMW<50km (dark purple). Bars and errorbars respectively denote the median and the quartile.

of the primary circulation, which has been suggested to confer lower resilience of the vortex to wind shear events following (Reasor, Montgomery, and Grasso, 2004; Mallen, Montgomery, and Wang, 2005).

The TC asymmetry, characterized by the azimuthal normalized variances of shape (eye and RMW) and energy distribution around the vortex (eyewall sharpness and maximum wind), does not show any direct relation with the IR (not shown). However, a separation into different life cycle phases reveals several noticeable features (Fig. 3.10. Intensity troughs (IR negative before, and positive after acquisition time, cyan bars) are notably more symmetric and homogeneous than other life phases, while the most asymmetric and heterogeneous phases are decline (negative IR before and after acquisition time, green bars) and intensification (positive IR before and after acquisition time, violet bars). An analysis of stronger TCs only (≥ cat. 3) highlights a higher asymmetry of declining TCs

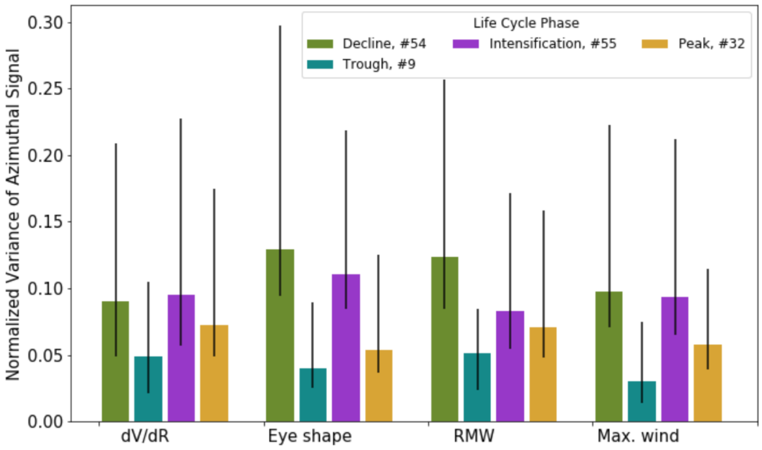

Figure 3.10 – Normalized variance of the 4 azimuthal signals (dV/dR, eye shape, RMW, and $V_{MAX}$) for four life cycle phases: stable intensification (purple), stable decline (green), intensity peak (yellow), and intensity trough (cyan). Bars and errorbars respectively denote the median and the quartiles.

over intensifying ones (not shown). The significant difference between declines and troughs shows the importance of vortex symmetry in the intensification process: both phases correspond to a negative intensification rate before acquisition, but TCs that re-intensify are much more symmetric than TCs that continue to decline. The asymmetry associated with intensity peaks (IR positive before acquisition time and negative after, yellow bars) is higher than that of intensity troughs, which might be quite surprising at a first glance, as peaks are usually more intense phases than troughs, and as more intense TCs have been shown to have a higher symmetry (see Fig. 3.7). However, this result is interesting as it might suggest that the observed asymmetry could be a predictor of the subsequent decline after a peak. Intensity peaks are often perturbed and unstable life cycle phases, where interactions of the vortex with its environment (shear, SST, islands) would result in their following decline. These interactions may consequently enhance the internal activity.

### Machine-learning classification: contribution of fine-scale extracted wind structures

Finally, in a predictability perspective, we assess the potential contribution of SAR-extracted TC parameters to a machine-learning statistical classification of positive ($>+5\text{m.s}^{-1}.\text{day}^{-1}$) and negative ($<-5\text{m.s}^{-1}.\text{day}^{-1}$) intensification rates. The method described in section 3.2.4 and Fig. 3.4 is applied to evaluate the prediction score of different combinations of ex-

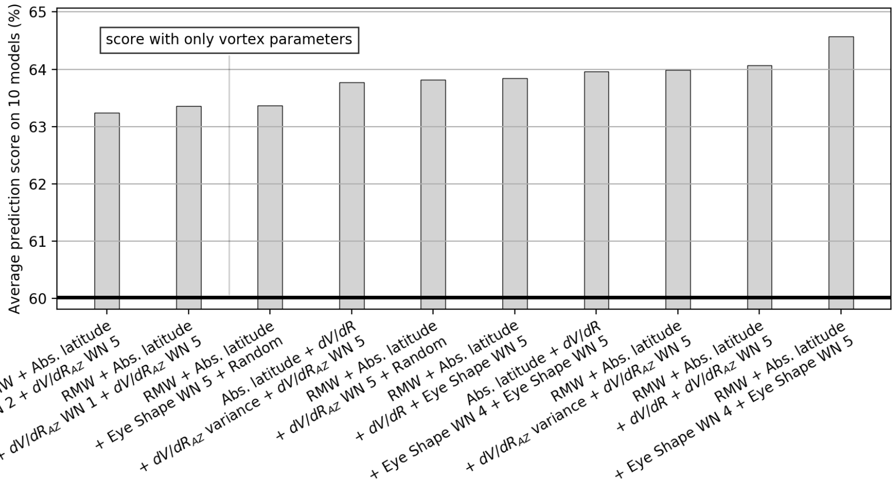

Figure 3.11 – Average prediction scores (in %) obtained over 10 machine learning models for the 10 best random combinations of 4 SAR-extracted parameters. The x-axis features the variables composing each combination. The black horizontal line denotes the score obtained for the combination containing only mean vortex-averaged parameters (Latitude, $V_{MAX}$, RMW and $dV/dR_{EW}$).

tracted variables. The 10 best combinations are shown on Fig. 3.11. For each combination, the score is an average over the 10 different machine learning algorithms.

Interestingly, only a few subset of the 28 variables used as predictors appear in these 10 best combinations: the latitude of the TC center, the RMW, 2 components of the eye shape decomposition (WNs 4 and 5), and several parameters characterizing the eyewall wind gradient (its mean value dV/dR, its azimuthal variance, its WNSs 1, 2, and 5). The latitude of the TC center is the most prominent parameter, appearing in each of the 10 best combinations. The typical life cycle of TCs with an intensification in the tropical latitudes and a decay in the mid-latitudes explains this prominence. The RMW is the second most frequent parameter appearing in 8 or the 10 best combinations. RMW may also be associated to the typical life cycle as it is influenced by the planetary vorticity, but we also showed in section 3.3.1 that the RMW is strongly associated to the intensity of the cyclone, and we suggested that this might be related to vortex contraction processes during intensification. This seems to be also supported by the strong contribution of the eyewall radial wind profile sharpness (dV/dR) in the classification, which appears in numerous combinations through its different components (mean value, azimuthal variance, WN decomposition). Notably, high WNs of the eyewall wind gradient and of the eye shape are majorly represented in the best combinations (e.g. WN 5 present in respectively 6 and 4 combinations for the eyewall gradient and the eye shape). These wave numbers correspond to small-scale dynamic processes in the eyewall such as convective bursts and mesovortices (Schubert et al., 1999; Kossin and Schubert, 2001). Signals characterizing the ring of maximum winds ($\mathrm{RMW}_{\mathrm{AZ}}$ and $\mathrm{Vmax}_{\mathrm{AZ}}$), on the other hand, do not appear in these 10 best combinations.

More generally, the scores associated to these 10 combinations range between 63 and almost 65 %. In comparison, the score associated to the combination of vortex averaged parameters (i.e. latitude, RMW, $\mathrm{V}_{\mathrm{MAX}}$ and $\mathrm{dV/dR}_{\mathrm{EW}}$), featured by the horizontal black line on Fig. 3.11), is 60%, and the score of the worst combination is around 43%. It should be reminded here that the method is not designed to bring the best possible prediction score (as a limited number of variable is used in each combination), but to assess the potential contribution of our SAR-extracted parameters. In addition, while these score variations might seem small, they can be considered as true indicators of an improvement in the classification as they are averaged over 10 models, performing bootstrap methods for each models, and iterated 10 times each with a different random control variable, ensuring to take into account the variability associated to the machine learning approach.

The prevalence of high wave numbers describing eye shape and $\mathrm{dV/dR}_{\mathrm{AZ}}$, the two signals estimated in the eyewall area (while $\mathrm{RMW}_{\mathrm{AZ}}$ and $\mathrm{Vmax}_{\mathrm{AZ}}$ describe the maximum wind ring), indicates a contribution of inner-core internal dynamics to the classification. Indeed, these wave numbers correspond to small-scale dynamic processes: eyewall processes such as convective bursts and mesovortices, for instance, sign on such small scales (Schubert et al., 1999; Kossin and Schubert, 2001), while smaller wave numbers represent a more general measure of asymmetry at the vortex scale. It can also be noted that the lowest score is associated to combinations containing $\mathrm{dV/dR}_{\mathrm{AZ}}$ wave numbers 1 and 2 (these lowest combinations are not shown on the figure). Thus, a true scale separation occurs between this vortex scale and the smaller scale describing localized structures in the eyewall.

We thus show with this machine learning approach that eyewall small-scale dynamics (characterized through the eye shape and eyewall radial gradient spectral decomposition) have the potential to improve a statistical prediction of TC intensity variations, compared to the sole use of vortex averaged parameters and synoptic information.

## 3.4 Summary and Discussion

In this study, we have analyzed 188 high-resolution (1km) SAR images of TCs. In addition to their outstanding resolution, these images present the advantage of having a large spatial extent allowing for a characterization of the whole 2D TC wind structure at the sea surface. The wind retrieval is performed using the dual-polarization capacity of Sentinel-1 and Radarsat-2 SARs, which has been shown to faithfully retrieve TC high wind speeds (Mouche et al., 2017). Taking advantage of this newly available dataset, which contains at least 15 images for each TC intensity category, our study demonstrates the ability to describe and characterize, with such acquisitions, the TC inner-core, through its radial profile, its azimuthal degree of asymmetry, and the energy distribution in the eyewall and maximum wind areas.

### 3.4.1 SAR observations and TC internal dynamics

The statistical analysis evidences a TC size reduction, and a sharpening of the eyewall radial wind profile with intensity, consistent with previous studies (Shea and Gray, 1973; Shapiro and Willoughby, 1982; Willoughby, Clos, and Shoreibah, 1982; Willoughby, 1990). Willoughby, Clos, and Shoreibah, 1982; Willoughby, 1990; Schubert and Hack, 1982 described TC contraction as resulting from the increased wind gradient in the inner edge of the maximum wind area (this increased gradient itself associated to latent heat release and isobaric height fall in the inner side of the convective ring). Studies by Schubert et al., 1999, Kossin and Eastin, 2001 and Nguyen et al., 2011 further discussed the role played by mesovortices generated in the eyewall inner-edge, which induce mixing and consequently spin-up within the eye, and then increased convective available potential energy in the vicinity of the ring of maximum winds when these mesovortices fade and move outwards as VRWs. During this process, the vortex transitions from U-shape to a Rankine-like vortex, and back to a U-shape vortex. Our observations support these previous results. We show a variety of observed wind profiles and shapes, even at high intensity. In average, a relationship between eyewall gradients and intensification rates is evidenced, and inner-core wind gradients are shown to increase faster than intensity, as illustrated by the gradually increased departure from the likely solid-body rotation profile. Such sharper gradients may also be seen as a consequence of the BL spin-up process (Smith, Montgomery, and Vogl, 2008; Montgomery and Smith, 2017), as supergradient winds near the RMW would increase the radial gradient. This process, supposed to increase with intensity (Stern and

Nolan, 2011), could explain the increased departure from the solid-body rotation that we observe. In a recent analytical model development, Chavas, Lin, and Emanuel, 2015 proposed to adjust their inner-core profile towards a slightly superlinear solution to avoid an overestimation of the wind in the eye, and better fit observations. Our results suggest that such an adjustment should depend on TC intensity, and that SAR observations could help further constraining TC parametric wind models.

The near-core wind profile radial gradient (computed from RMW to 3 RMW) is also of interest, as it characterizes the broadness of the azimuthal-mean wind peak, and the decay rate of the outer profile, which are useful for risk assessment (Croxford and Barnes, 2002), and related to the vortex resilience to external shear (Reasor, Montgomery, and Grasso, 2004). The analysis of Mallen, Montgomery, and Wang, 2005, from flight-level aircraft observations, linked the vortex resilience to the near-core profile shapes. Our analysis of near-core gradients SAR-extracted profiles is in agreement with their results, showing a near-core radial gradient increasing faster than TC intensity. Further analyses could certainly help evaluating the primary circulation broadness and the TC stability with respect to shear effects and possibly provide new guidance for TC forecasters.

Our analyses also revealed a lower sensitivity of the near-core gradient to the intensification rate compared to the eyewall gradient, suggesting a partial decoupling between these two areas. The generation of mesovortices in the eyewall area, observed in several of our images, and also discussed in previous studies (Schubert et al., 1999; Nguyen et al., 2011; Li et al., 2013), indicate a very reactive dynamics of the inner eyewall area, therefore more correlated to intensity variations. The observed decoupling may also advocate for the dual spin-up theory proposed by Smith, Montgomery, and Van Sang, 2009 and reviewed by (Montgomery and Smith, 2017), which suggests that inner-core and outer-core dynamics are monitored by two distinct kinds of spin-up, the former occurring in the BL with supergradient winds, and the latter occurring above the BL in classical gradient wind balance. In this regard, SAR appears as a very valuable observational dataset as it allows to study very small scale boundary layer processes related to these supergradient winds. In particular, the work of (Foster, 2005) focusing on BL rolls and their interaction with BL dynamics could certainly benefit from the reliability of our inversion algorithm at very high wind speeds and the representativeness of our dataset especially at high intensity.

The investigation of spectral energy distributions in the eyewall and in the maximum wind area further reveals this decoupling. While the azimuthal distribution of the eyewall radial wind gradient shows no notable sensitivity to intensity, the maximum wind contour is found to homogenize (broadening of its energy spectrum towards large wavenumbers) with intensity. In addition, the analysis of both eye shape and $\mathrm{RMW}_{\mathrm{AZ}}$ variance shows an axisymmetrization of the TC shape. These two features seem in agreement with the VRWs theory. By propagating energy from the vortex center to its upper and outer boundaries, VRWs act to restore the TC structure from interactions of the main vortex with inner-core mesovortices (Nolan and Montgomery, 2002) or external events such as vertical wind shear (Montgomery and Kallenbach, 1997), that may prevent TC intensification by tilting the vortex (Reasor, Montgomery, and Grasso, 2004). VRWs generate asymmetries in the eyewall and high wind area (Schubert et al., 1999), causing barotropic instabilities that can limit the TC intensity while reducing the eyewall tilt (Yang, Wang, and Wang, 2007). Our analyses show that intense TCs have a more symmetric structure and distributed energy spectrum, indicating less intense VRW activity. The assessment of VRWs propagation from our database is however limited by the instantaneous nature of SAR images and the lack of continuity in TC sampling.

Overall, SAR provides unique observations of TC inner-core structures and dynamics from space, which complement and converges with previous researches focused on eyewall dynamics (inner-core BL spin-up, mesovortices generation and associated vorticity mixing, and their relationship to intensity changes), vortex strength and resilience, and intensity restoration processes in the inner-core such as VRWs. They allow a statistical characterization of these properties on a relatively large range of cases. Our interpretation is however still limited by the sampling of acquisitions which prevent studying dynamical evolution, and by the fact that the current SAR wind product does not provide reliable wind directions, preventing a computation of the vorticity distribution.

### 3.4.2 SAR observations and TC life cycle variations

Our study finally assessed the potential of TC inner-core SAR-extracted parameters (radial profile, azimuthal and energetic distributions) in characterizing the on-going TC intensity variations in a future perspective of predictability improvement.

A comparison of radial eyewall and near-core gradients for 3 distinct intensification regimes (decays ($<$-5m.s$^{-1}$.day$^{-1}$), stable phases, and intensifications ($>$+5m.s$^{-1}$.day$^{-1}$)) showed increased gradients with intensification. This indicates a trend towards a U-shape profile, and a reduced broadness of the primary circulation for intensifying TCs. These results are consistent with the modeling studies of Nguyen et al., 2011 and Kossin and Eastin, 2001, which found "symmetric" phases of lower mesovortical activity (phase A for Kossin and Eastin, 2001) to be more favourable to fast intensifications. The observed increase of the near-core gradient during intensification phases also suggests a reduced broadness of the primary circulation, and a lower resilience to external events as suggested by Mallen, Montgomery, and Wang, 2005.

The evolution of TC shape or energetic azimuthal signals with intensification rate and TC life phases reveals that TCs in a transition phase towards re-intensification (after a decline phase) are the most symmetric. This result supports the VRW axisymmetrization theory according to which intensity restoration occurs through re-distribution of asymmetric potential vorticity anomalies throughout the structure (Montgomery and Kallenbach, 1997): the re-intensification can only occur if the axisymmetrization was successful, which in our case is traced by a reduced variance of azimuthal signals. To further estimate the contribution of all SAR-extracted parameters in TC life cycle prediction, we designed a machine learning approach, which classifies intensifying and decaying TC phases. The contribution of the various extracted parameters was then assessed by sorting the prediction scores obtained from different combinations of variables. The best combinations revealed a notable contribution of the eye shape and eyewall wind gradient high wave numbers (WNs 4 and 5), improving by 4.5% (from 60 to 64.5 %) the score obtained with vortex averaged parameters only.

This improvement highlights the importance of small-scale processes in the prediction of intensity variations. Indeed, wave numbers 4 and 5 in the eye shape correspond to localized structures with a reduced spatial scale, such as convective asymmetries and rain bands perturbing the eyewall. Judt, Chen, and Berner, 2016 referred to wave numbers 2-5 as the "rain band scale", and Schubert and Hack, 1982 modelled a wave number 4 disturbance and related it to the formation of mesovortices. These small-scale features may also be linked to the propagation of VRWs (Schubert et al., 1999; Wang, 2002a). In the literature, only low wavenumbers (1 and 2) are usually studied (Reasor et al., 2000; Wang, 2002b) due to observational limitations (lack of azimuthal resolution for aircrafts, lack of spatial resolution for satellite radiometers and scatterometers). Numerical studies suggest that these wave numbers are the most influent for vortex evolution (Wang, 2001; Wang, 2002a) as they are directly related to the environmental forcing.

However, rapid intensity variations are still a challenge to forecast, and may be related to these fine-scale dynamics. Our first assessment of the predictability potential of the inner-core fine-scale properties shows that including high wavenumber signals improves the characterization and classification of intensity changes. Usual operational statistical-dynamical forecast models (DeMaria and Kaplan, 1994; DeMaria and Kaplan, 1999; Knaff, Sampson, and DeMaria, 2005; Knaff and Sampson, 2009) use linear regression techniques to predict intensity changes from large-scale climatological fields (temperature, humidity, maximum potential intensity, shear...), TC intensity, and rate of change at the forecast initial time. Neetu et al., 2017 showed that the most important predictors of these statistical-dynamical models are the intensity and its rate of change. An accurate estimation of both of these parameters is therefore required (and SAR proves useful for TC intensity retrieval), but our classification suggests that including other finer-scale internal structure parameters (in particular the eye shape and eyewall gradient high wave numbers) might eventually improve this type of statistical forecast, especially on short time scales. Our dataset is though limited to a relatively low number of events and a large number of descriptors for a statistical classification. We therefore could not assess the true added value of each extracted parameter, but rather the more-likely best parameters to consider for predicting TC life cycle. In addition, our machine learning approach was not designed to actually work as an operational statistical forecast model, which would require to include all available parameters including large-scale environmental fields (temperature, humidity, shear, etc) along with our fine-scale observations to fully assess forecast issues and effectiveness.

### 3.4.3 SAR observation limitations

Besides the potential of new high-resolution SAR wind retrievals, they still have several limitations.

Our description of the TC inner-core does not include the eye area (but only the eyewall, maximum wind, and near-core areas), while it could be of interest as the eye dynamics and the degree of convection in the eye are closely related to TC intensification (see Emanuel, 2018, part 3.e.). Limitations in the inversion algorithm used for ocean surface wind retrieval from SAR observations acquired in dual-polarizations may arise in the eye region. They are associated to discrepancies between co- and cross-polarization signals due to the low backscatter signal in this area, and the particularly low signal to noise ratio of the cross-polarization. To compensate for those discrepancies, wind values from the European Centre for Medium range Weather Forecast (ECMWF) model are combined with the dual-polarization data (Mouche et al., 2017). However, ECMWF winds may not be perfectly co-located with the observed TC. In such cases, the eye wind retrieval may therefore be polluted by higher wind values from the model in the eye, yielding to overestimated wind values. Eyewall and the surrounding high wind area, are not subject to this limitation, as the weight of the model is almost zero in these areas (the algorithm taking benefit of the dual polarization). This limit of the inversion algorithm prevents us from studying the wind distribution inside the eye. It can be noted that high values of radar backscattered intensities can actually be measured in the eye of a TC (Li et al., 2013). They have been interpreted as a signature of abnormally high rain or wind, or wind sea-swell interaction in the eye. The inversion algorithm might thus not be the only cause of this inconsistency.

The understanding of rain impacts on ocean scenes acquired by SAR systems is a particularly active subject of debate and investigation in the SAR community (Melsheimer, Alpers, and Gade, 1998; Atlas, 1994a; Atlas, 1994b) and more specifically for TCs (Katsaros et al., 2000; Mouche et al., 2019; Combot et al., 2020). These signatures can significantly impact the wind field, but their characteristics vary a lot depending on rain and wind field properties. Backscattered signal can be affected through modifications of the surface roughness (waves damping by raindrop-induced turbulence in the water or increased roughness by rain droplets impinging the surface) or contributions from the atmosphere (attenuation and scattering from hydrometeors).

The result on the wind field can take several forms. The most common is an underestimation of the wind speed surrounding the maximum wind area, where the rains are the heaviest. This "eyebrows-like" signature is typical of major hurricanes (see Mouche et al., 2019, or the example of TC Lionrock in Fig. 3A). These signatures are however usually located outward from the ring of maximum wind (Fig. 3.3A,B), and have a small radial extent. Their impact on the retrieved inner-core signals is thus very limited and no impacted case was identified. On the contrary, for weaker TCs or in outer rainbands, one can have overestimation of the wind speed (see the example shown in suppl. S1 Fig. SF1-F). Such cases may impact our estimates of the maximum wind speed distribution and radial gradients, but they are very rare (only 2 were identified in our dataset).

Moreover, these individual impacts were either attenuated or removed by our preliminary smoothing and masking steps, and by the definition of vortex-averaged and integrated variables such as azimuthal variances and radial mean gradients. They are thus assumed to not noticeably impact our statistical analysis. The study of rain impact on SAR wind retrieval is still however a question to be addressed. To date, this field of research still lacks concurrent reference high-resolution measurements of wind and rain co-located with SAR data to fully quantify the rain impact on a statistical basis and yield to more reliable wind inversion algorithm.

Overall, the use of SAR acquisitions in dual-polarization is recent and further work is certainly required to improve the signal quality (especially in cross-polarization and at subswath limits), the relationship between ocean surface wind and backscattered intensity, the possible rain and waves signatures that can co-exist, the wind direction estimation, and more generally, the inversion scheme.

Another limiting factor of our study concerns the intensity variation assessment is the absence of temporal continuity in SAR acquisitions. This prevents an estimate of the short-range changes in the internal structure, and of the dynamics of extracted small-scale properties directly from the SAR data. In this study, the temporal variation of TC along with its life cycle is thus given by the BT data. Linear interpolation is performed to align in time the two sources of data, but this does not prevent from possible inconsistency between the two datasets, and may degrade the relationship between the SAR-derived parameters and TC intensity variations.

The recently published SATCON database (Velden and Herndon, 2020) provides hourly TC intensity estimates based on a combination of infrared and microwave satellite measurements with an objective algorithm. Such a dataset could allow further analysis of the relationship between TC temporal variability and SAR small-scale variability within short intervals to possibly evaluate the benefit of this complementary temporal information for TC intensity variation predictability. Such an objective would require a prior in-depth validation of wind estimates from the two data sources, and thus a dedicated study which is beyond the scope of this paper.

Finally, our dataset, though being quite consequent and covering all TC categories, is still insufficient to fully capture the full spread of situations, and to fully describe the TC evolution. Additional observations would certainly allow to refine the life cycle phases characterization and strengthen the statistical analyses.

## 3.5 Conclusions

The present work aimed at describing the internal structure of TCs as observed from SAR imagery, and at evaluating relationships between this structure and the TC life cycle. It took advantage of acquisitions performed with two satellite SARs (Sentinel-1 and Radarsat-2), which were targeting TC events. These two instruments are C-Band SARs operating in both co- and cross-polarization modes, which have been shown to complement one another in retrieving high wind speeds Mouche et al., 2017, particularly as the cross-polarization implemented on both Sentinel-1 and Rardarsat-2 is much more sensitive to high wind gradients. Other SAR missions such as ALOS-2, TerraSAR-X, or Gaofen-3 that are currently operating, do not provide, to our knowledge, the facilities and supporting programs to order TC acquisitions on short notice (which is a constrain due to relatively short time range in TC forecast), but could contribute to the TC monitoring at high resolution. Several space agencies also plan the launch of other SAR missions in the coming years (e.g. Sentinel-1 Next-Generation and ROSE-L at ESA, ALOS-3 at JAXA and NISAR at NASA-ISRO), and the TC community would certainly benefit from them, if TC monitoring could become one of their targeted applications. Some of these missions are using SAR operated in other acquisition bands (L-band or X-band). This would require additional research to develop robust high wind retrieval algorithms but could also bring new insights for radar image interpretation, certainly contributing to improve our understanding of the various components impacting the imaging mechanisms.

Our study shows SAR large coverage together with its ability to probe the sea surface at very high resolution, make this sensor very valuable for TC research, as well as for operational applications and risk assessment, especially as the importance of spatial resolution grows with TC intensity. This urges the need for moving toward an operational SAR acquisition strategy, and for further developments on wind retrieval algorithm over TCs.

The interpretations and results provided in the present study reveal the importance of radial resolution for the description of the eyewall and near-core areas, with possible implications for the understanding of TC intensity fluctuations and future perspective in the improvement of parametric models. They also highlight links between TC asymmetry, size and intensity, and the importance of azimuthal resolution as resolving high wave numbers to improve our ability to dissociate intensification phases. Including some of the SAR-extracted parameters (in particular the eye shape and eyewall gradient high wave numbers) into statistical forecast models is suggested to have a potential of predictability improvement.

Future work will focus on dynamical models to include the temporal evolution of TC small-scale structure and relate it to intensity changes. Analysis of future SAR observations will also continue to improve our understanding of this new measurement technics and further assess its potential.

# S1 - Supplemental Material: Examples and discussion of observed large RMW TC cases

The distribution of RMW values as a function of maximum wind speed revealed a quite large variability for moderate (<cat. 3) TCs, notably with cases with very large RMW (up to 100km). We thus further illustrate here some of these. Fig. 3.12 shows that they are usually associated to highly asymmetrical TCs for which high winds are mostly confined to one sector of the TC vortex.

It is interesting to note that such cases typically show disagreement between BT and SAR RMW estimates, with differences of more than 30km. BT RMW falls inside the TC eye (see dark blue circles), far from the maximum wind area, while SAR-extracted RMW (yellow circle) seems to more faithfully characterize the asymmetrical high wind area. We thus assume that BT estimation is in such cases inaccurate, possibly attributing a too low RMW, precisely because BTs use RMW indirect estimation based on the usual RMW-$V_{MAX}$ relation, which in such cases no longer holds. The case of Sergio shows a different behavior, with SAR and BT RMW estimates being in relatively good agreement, though with a large value of RMW (90km). This case features a ring of high winds more distributed around its vortex, that may favor the good agreement between both datasets.

The case of TC Joaninha (Fig. 3.12-F), which is the most intense case with large RMW that we observed may however be biased. It indeed shows a large discrepancy between SAR-extracted $V_{MAX}$ and BT $V_{MAX}$ (~20m.s$^{-1}$ difference). In this case, we assume that the $V_{MAX}$ SAR estimate may be erroneous as the SAR wind field features a quite strange "line" of intense winds in the south-west quadrant of the TC, which may be associated to a localized rain event. Indeed, the heterogeneity mask shows a little area of heterogeneity just north of this intense wind "line", which may indicate the presence of strong rain in the area (which is however not detected as heterogeneity and masked over the whole area, and which would here cause anomalously high winds). This example shows that rain issues are not easy to detect and may still impact our wind field retrievals (such cases are however rare, and are assumed to not significantly impact our statistical estimates). On another hand, the SAR RMW estimate seems not to be strongly impacted by this potential rain issue. The BT RMW estimate, on the other hand, seems unrealistic, falling inside the TC eye, where no high wind is observed.

Overall this overview of specific cases shows that large RMW can be observed for moderate TCs, and are mostly associated to very asymmetrical TCs.

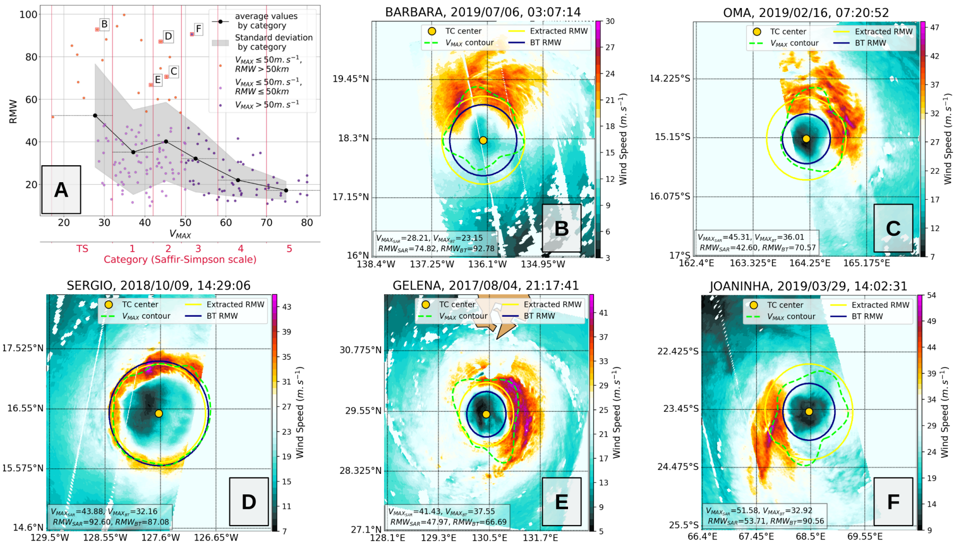

Figure 3.12 – Comparison of SAR and BT RMW estimates for 5 SAR acquisitions featuring particularly large RMWs. (A) is a reproduction of Fig. 5 in which the 5 cases are labelled; (B-F) show respectively TC BARBARA, OMA, SERGIO, GELENA, and JOANHINA. The SAR- retrieved wind field is shaded. The yellow dot locates the SAR TC center position, the green dotted line is the extracted Vmax$_{AZ}$ contour, the yellow circle represents the SAR azimuthally averaged RMW, and the dark blue circle the BT RMW.

CHAPTER 4

# TC FINE-SCALE STRUCTURE EVOLUTION WITH INTENSITY VARIATIONS: INSIGHTS FROM 3D REALISTIC SIMULATIONS

---

This chapter is the subject of an article to be submitted.

## 4.1 Introduction

Forecasting and understanding the life cycle of Tropical Cyclones (TCs) are primary concerns for meteorological science, as they cause important casualties every year. While TC tracks are relatively well forecasted, maximum intensity, and its variations are more difficult to predict (Elsberry, Lambert, and Boothe, 2007; DeMaria et al., 2014; Emanuel and Zhang, 2016). These intensity changes can be caused by interactions of the vortex with its external environment such as vertical wind shear (Smith, Ulrich, and Sneddon, 2000; Reasor, Montgomery, and Grasso, 2004; Corbosiero and Molinari, 2002), ocean surface (Elsberry, Fraim, and Trapnell Jr, 1976; Price, 1981; Ginis, 2002), or by local internal processes such as rain band interactions (Rozoff et al., 2006; Wang, 2008; Wang, 2009; Li and Wang, 2012), or convective bursts (Steranka, Rodgers, and Gentry, 1986; Hazelton, Hart, and Rogers, 2017; Wadler, Rogers, and Reasor, 2018).

These perturbations cause asymmetric distortions of the vortex, and anomalies in the TC wind and vorticity fields. The TC may thus feature polygonal eyewalls (Lewis and Hawkins, 1982; Muramatsu, 1986; Menelaou, Yau, and Martinez, 2013b), appearance of eyewall mesovortices, vortical hot towers (Black, 1991; Hendricks, Montgomery, and Davis, 2004; Montgomery et al., 2006; Van Sang, Smith, and Montgomery, 2008), or interactions between inner (Jorgensen, 1984) and outer rainbands (Wang, 2009; Li and Wang, 2012). Eventually, these modifications of the vortex structure can lead to TC intensity restoration. Eyewall vorticity mixing, for instance, has been shown to trigger Vortex Rossby

Waves (VRWs) generation, which transport and dissipate vorticity perturbations from the vortex center to its periphery eventually restoring its symmetry and intensity (Guinn and Schubert, 1993; Montgomery and Kallenbach, 1997; Möller and Montgomery, 1999). Outer rain bands have also been spotted as a driving mechanism for secondary eyewall formation, and eyewall replacements (Judt and Chen, 2010; Wang and Tan, 2020), which were shown as a restoring process for major TCs (Kuo et al., 2004; Kuo et al., 2008; Nguyen et al., 2011).

The vortex radial structure also impacts its ability to resist external perturbations. A broader ring of maximum wind, and a lower decay rate of the wind profile in the near-core area were shown as factors increasing its resilience (Reasor, Montgomery, and Grasso, 2004; Mallen, Montgomery, and Wang, 2005). The radial profile shape was also related to the radial propagation of VRWs along potential vorticity gradients (Schecter, Montgomery, and Reasor, 2002; Menelaou, Yau, and Martinez, 2013a). Moreover, TCs with a smaller size, and a thinner primary circulation have been documented as more likely to experience fast intensifications (Bryan and Rotunno, 2009; Xu and Wang, 2018; LI and WANG, 2021).

The dynamics behind intensity restoration and maintenance are thus governed by complex interactions between different spatial and temporal scales. They are consequently hard to observe, model, and understand. In particular, assessing the very fine scale evolution in the eyewall area is a challenge for both observations, and modeling.

Airborne radars, dropwindsondes, coastal radars, and satellite measurements provide support and material for the understanding of TCs (cf. Emanuel, 2018 for a quick summary and Stith et al., 2018; Ackerman et al., 2019; Fu et al., 2019 for reviews of atmospheric observation techniques). These observations are however often sparse, and assessing the life cycle evolution, and intensity variations is therefore limited with these data.

Idealized numerical models have allowed considerable progress in the understanding of TC intensification (Ooyama, 1964; Emanuel, 1986; Montgomery and Smith, 2014; Peng, Rotunno, and Bryan, 2018), and internal dynamics, such as the role of asymmetry and axisymmetrization processes (Smith and Montgomery, 1995; Thomsen, Smith, and Montgomery, 2015), eyewall mesovortices, potential vorticity mixing (Schubert et al., 1999; Kossin and Schubert, 2001; Hendricks et al., 2014), or VRW nature and propagation (Montgomery and Kallenbach, 1997; Wang, 2002a; Wang, 2002b). These idealized models allow to study a specific process, isolate its properties, and effects.

With the increase of computing capacity, 3-D high-resolution full-physics dynamical models have emerged. While eventually suffering from uncertainties in their parameterizations of sub-grid scale physics, and limits in their effective resolution (Gentry and Lackmann, 2010), they were shown to represent the complexity of internal interactions, and their multi-scale characteristics. Processes such as vortex contraction (Xu and Wang, 2010b; Xu and Wang, 2010a; Stern et al., 2015; Li, Wang, and Lin, 2019), eyewall dynamics (Chen and Yau, 2001; Yau et al., 2004; Kwon and Frank, 2008; Yang, Wang, and Wang, 2007; Wu et al., 2009; Nguyen et al., 2011; Menelaou, Yau, and Martinez, 2013b), VRWs (Chen and Yau, 2001; Wang, 2002a; Wang, 2002b; Chen, Brunet, and Yau, 2003; Hall et al., 2013; Schecter, 2015), and secondary eyewall replacements (Abarca and Corbosiero, 2011; Rozoff et al., 2012; Abarca and Montgomery, 2013; Wang et al., 2019; Wang and Tan, 2020) were reproduced. The realism of 3-D dynamical models, and their accurate representation of TC life cycle dynamics makes them comparable and complementary to high resolution observations.

In the operational community, forecasts are produced with a synthesis of real-time observations, dynamical models, and statistical-dynamical models that predict future changes from current intensity, intensification rate, and large-scale environmental parameters such as vertical wind shear, sea surface temperature (SST), or mid-tropospheric relative humidity (Kucas, 2010; DeMaria, Knaff, and Sampson, 2007; DeMaria et al., 2014; Kaplan et al., 2015; Neetu et al., 2020). Such statistical-dynamical models are still viewed by meteorological centers as competitive with full-physics dynamical models. Modern statistical models also implement sophisticated machine learning methods in order to improve the forecasts (Jin et al., 2019; Su et al., 2020; Chen, Zhang, and Wang, 2020; Neetu et al., 2020).

Statistical models however still rarely take as input parameters of the internal vortex structure, apart from the large-scale asymmetry (cf. Bhalachandran et al., 2019 assessment of WN-1 asymmetry influence on intensity changes), the maximum wind, or some characteristic wind radii. A recent study (Vinour et al., 2021) showed that newly available kilometer-resolution surface wind fields retrieved from Synthetic Aperture Radar (SAR) have the potential to improve the statistical predictability of TC intensification rates. The improvement is mainly associated to the inclusion of variables describing the fine-scale inner-core structure, in particular the eyewall gradient, and the azimuthal wind distribution.

In the present study, we intend to pursue this work by evaluating the added-value of having the temporal evolution of these fine-scale inner-core structures to further analyze the connections between vortex internal changes, and TC intensity modulation. We will here rely on seven full-physics high resolution dynamical model simulations, and model outputs that are similar to the parameters that can be extracted from SAR images (Vinour et al., 2021). We intend to study the TC internal structure through a synthetic view of the surface wind field, that can be estimated from numerical models as well as surface wind measurements, and that can be easily included in statistical models.

The article is organized as follows: the modeling framework, and the studied parameters are described in section 2; we then assess the realism of these simulations, and their statistical representativeness by comparing model outputs to SAR images and best-track files in section 3; the temporal changes throughout the TC internal structure are studied in section 4 by relating these changes to TC life cycle in various ways; a final discussion and conclusions are provided in section 5.

## 4.2 Materials and Methods

### 4.2.1 Datasets

#### WRF model

The Weather Research and Forecasting (WRF) model version 3.7.1 is used in this study with the Advanced Research WRF (ARW) dynamic solver (Skamarock and Klemp, 2008). The configurations are designed to model TC inner-core on a 1 km horizontal grid. This high-resolution is achieved using the vortex-following algorithm provided by WRF with a two-way nesting procedure composed of 3 domains: a large domain at 9 km resolution encompassing the whole TC track (it is defined as a rectangular box including the track plus 8 degrees on each side); and two vortex-following embedded domains gradually increasing the resolution to 3 and 1 km. The intermediate vortex-following domain is set as an 8 degree square box around the TC center, and the finer domain as a 4 degree square box around the TC center. The two nested domains move every 15 minutes following the TC vortex, thanks to an automatic tracking of low pressure under 50000 Pa, in a radius determined by a maximum TC translation speed of 40 m/s. Refined high resolution terrain and landuse files were additionally used for moving nests (which otherwise use the default the 9-km resolved topography of the large domain, limiting the realism of crossed islands and mainlands). On the vertical, all the domains have the same vertical grid composed of 32 terrain-following levels with refinement in the planetary boundary layer (PBL), and at the top of the model (set at 5000Pa). The set of parameterizations used is the following: Betts–Miller–Janjic (BMJ) convective scheme for the 9km domain, while convection is explicitly solved in the 3 and 1km nested domains; the Yonsei University (YSU) PBL with revised MM5 Monin-Obukhov surface layer parameterization, the classical Charnock relation for the surface drag coefficient, the WRF single-moment six-class microphysics scheme (WSM-6), the Dudhia shortwave radiation scheme, and the Rapid Radiation Transfer Model (RRTM) for long-wave radiation.

Horizontal and vertical resolutions, as well as all parameterization settings are identical for all TC simulations. Initial, surface, and boundary conditions are prescribed with the 0.25 degree NCEP Final (NCEP FNL) operational global analysis using the Global Data Assimilation System (GDAS, `https://rda.ucar.edu/datasets/ds094.0/`). A spectral nudging, using the WRF Four-Dimensional Data Assimilation (FDDA) scheme, towards these re-analysis data is also applied during the whole simulations, on the parent 9km resolution domain, and above the BL only, with no direct impact on nested domains. It ensures a better consistency of the modelled synoptic flow with observations, limiting the TC track deviations, without constraining the TC physics in the nested domains (Wang, Wang, and Xu, 2013). The spectral nudging only applies to large scales of the domain (approximately 1000 km in our case, i.e. the large domain size divided by 3).

The horizontal resolution of the 2 inner domains is a compromise between computational cost and a resolution comparable to the SAR images that are resolved at 1-km and re-sampled (averaged) on a 3-km grid.

### Synthetic Aperture Radar (SAR) observations

SAR observations provide 2-D non-directional ocean surface wind products under TCs at a high resolution of 1km, with a spatial extent of 200 to 400 km depending on the acquisition mode. The database used in this study is the same as the one presented in Vinour et al., 2021. It is composed of 188 images acquired over TCs between 2014 and 2019 by Sentinel-1 A and B, and RADARSAT-2 satellites during the Satellite Hurricane Observation Campaign (SHOC) conducted by the European Space Agency (ESA), the Collecte Localisation Satellites (CLS) group, and the French national institute for ocean science (Ifremer). This SAR database statistically represents a wide range of TC events, in all basins and at all categories. It is used here to compare observed and modeled TC internal structure. SAR is a microwave active sensor, which measures the backscatter signal at C-band to estimate the sea surface roughness with a spatial resolution that ranges from 10 m to 1 km (depending on the acquisition mode). The wind field is retrieved using co- and cross-polarizations channels with a dedicated inversion algorithm developed by Mouche et al., 2017 to mitigate the signal saturation observed in co-polarization (as for scatterometers). Mouche et al., 2017; Mouche et al., 2019, and Combot et al., 2020 showed that SAR provides very reliable estimates of TC maximum intensity, and characteristic wind radii. Vinour et al., 2021 showed that they allow to measure many properties of the internal TC structure such as the eyewall and near-core surface wind gradients, and inner-core wind azimuthal asymmetries.

#### Best Track (BT) dataset

The International Best Track Archive for Climate Stewardship (IBTrACS; Knapp et al., 2010) combines the best-track (BT) data (TC location, maximum wind speed, and characteristic wind radii) from various meteorological centers (Regional Specialized Meteorological Centers responsible for TC forecast in the different basins, and government agencies) into a common format. US centers BT data with a 6h time resolution are used in the present study to assess the representativeness of our simulations in terms of TC characteristics (location, maximum intensity, intensification rate, translation speed).

### 4.2.2 Methods

#### Surface wind field parameters of interest

One objective of our study being to estimate the added-value of TC internal structure time evolution compared to snapshot observations, we needed to analyze model outputs similarly to SAR available observations. The TC internal structure is thus described from the surface wind speed only, and following the methodology designed by Vinour et al., 2021. This methodology assesses the properties of the 2-D surface wind field in a TC-centered relative frame, and extracts radial and azimuthal parameters, which are detailed hereafter and illustrated on Fig. 4.1.

The radial structure is described by its radial surface wind gradients computed from the azimuthally-averaged profile in two characteristic areas: the eyewall area (between the eye and the radius of maximum winds (RMW), yellow on Fig. 4.1F) , and the near-core area (between 1 and 3 RMW, blue on Fig. 4.1F).In the eyewall, the radial gradient is also compared to a Rankine-like vortex to better estimate the eyewall profile sharpness with respect to the RMW. Rankine-like vortex eyewall gradient is defined as a linear

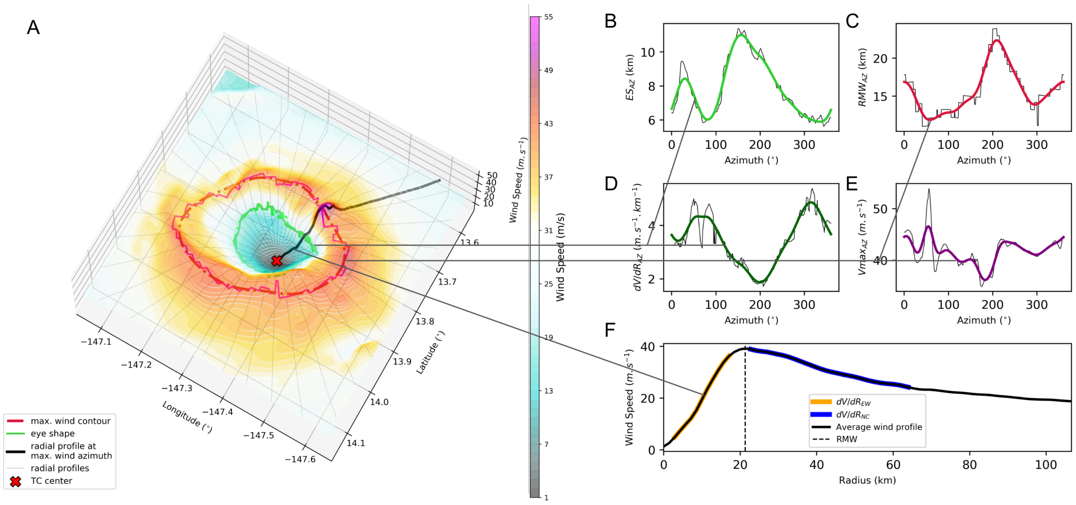

Figure 4.1 – Illustration of parameters extracted from the surface wind field from an output of the LANE simulation on 2018/08/20,07:00. (A) Surface wind field projected on a 3-D grid (elevation=wind speed) with extracted signals superimposed. Panels (B),(C),(D),(E) respectively show raw (thin black) and smoothed (bold) extracted azimuthal distributions of eye shape, RMW, eyewall radial wind gradient, and maximum wind, with the same color code as (A). (F) shows the extracted radial mean profile and highlighted eyewall (yellow) and near-core (blue) areas

profile between 0 $m.s^{-1}$ in the eye, and the maximum wind at the RMW. In the near-core area, the radial profile is also further described by a variable measuring the profile curvature, defined as: $Res_{NC} = \frac{V_{3RMW} - V_{RMW}}{3RMW - RMW} - \frac{V_{2RMW} - V_{RMW}}{2RMW - RMW}$, where V is the wind speed, and the subscripts describe the distance from the eye where it is evaluated . $Res_{NC}$ is used as a proxy for the vortex resilience, as Reasor, Montgomery, and Grasso, 2004; Mallen, Montgomery, and Wang, 2005 showed that the broadness of the primary circulation is correlated to the vortex stability, and resilience to external shear.

The azimuthal structure is described by extracting at each azimuth four characteristic parameters, composing four 1-D azimuthal signals: the eye shape (noted $ES_{AZ}$ hereafter, Fig. 4.1B), the ring of maximum wind shape ($RMW_{AZ}$ hereafter, Fig. 4.1C), the distribution of eyewall radial gradient ($dV/dR_{AZ}$ hereafter, Fig. 4.1D), and the intensity distribution of maximum wind ($Vmax_{AZ}$ hereafter, Fig. 4.1E). These azimuthal distributions are then smoothed to absorb local anomalies and polar grid discretization (see for instance the effect of smoothing on $Vmax_{AZ}$ in Fig. 4.1C). The description of asymmetry is then quantified by the total variance of these signals, and by their spectral decomposition. For each signal, the percentages of explained variance of each wavenumber (WN) of the spectral decomposition, from 1 to 180, are computed. They are then gathered into 3 distinct groups: "low" WNs (WNs 1 and 2) describing the vortex-scale asymmetry often related to large-scale dynamics in the literature; "mid" WNs (WNs from 3 to 5) associated to smaller-scale processes and characteristic of restoration processes such as eyewall mesovortices or VRWs in the most disturbed phases of the TC life cycle; "high" WNs (WNs from 6 to 180) containing the rest of the energy distribution, and thus describing more generally the azimuthal energetic homogeneity. Grouped percentages of explained variance are hereafter noted $Var_{0-2}$, $Var_{3-5}$, and $Var_{6-180}$.

The radial and azimuthal descriptors are estimated at each hourly model output for all simulations.

### Estimation of inner-core temporal changes

Three variables are considered to measure intensity variations: maximum intensity ($V_{MAX}$), its first time derivative (i.e. intensification rate, hereafter noted $\partial_t(V_{MAX})$), and its second time derivative (i.e. increase or decrease of intensification rate, hereafter noted $\partial_t^2(V_{MAX})$). Their extrema characterize different specific phases of the TC life cycle: peaks and troughs of $V_{MAX}$; strongest intensifications and declines ($\partial_t(V_{MAX})$ maxima and minima); re-intensifications and weakening of intensification ($\partial_t^2(V_{MAX})$ maxima and minima, that correspond to concave and convex parts of the $V_{MAX}$ time series). To assess the evolution of the TC internal structure in regards to these TC life cycle changes, time derivatives of the radial and azimuthal descriptors are evaluated. In addition, to measure the variations in the energy distribution of the azimuthal structure, the transfer of energy between low and high wave numbers is computed for the 4 azimuthal signals (eyewall gradient, eye shape, maximum wind, and RMW). WN transfers (noted WNT hereafter) are thus defined for a given azimuthal signal $S_{AZ}$, as:

$$WNT(S_{AZ}) = \partial_t(Var_{6-180}(S_{AZ})) - \partial_t(Var_{0-2}(S_{AZ})) \tag{4.1}$$

where $\partial_t(Var_{0-2}(S_{AZ}))$ and $\partial_t(Var_{6-180}(S_{AZ}))$ denote the time derivatives of the smoothed signals of $S_{AZ}$ $Var_{0-2}$ and $Var_{6-180}$. Note that WNT is not defined if the two transfers are of the same sign. WNT is thus positive (negative) when the variance explained by high WNs is increasing (decreasing), while that explained by low WNs is concurrently decreasing (increasing). These energy transfers measure the broadening or narrowing of the energy spectrum over time, that is in a way the homogenization or heterogenization of azimuthal signals.

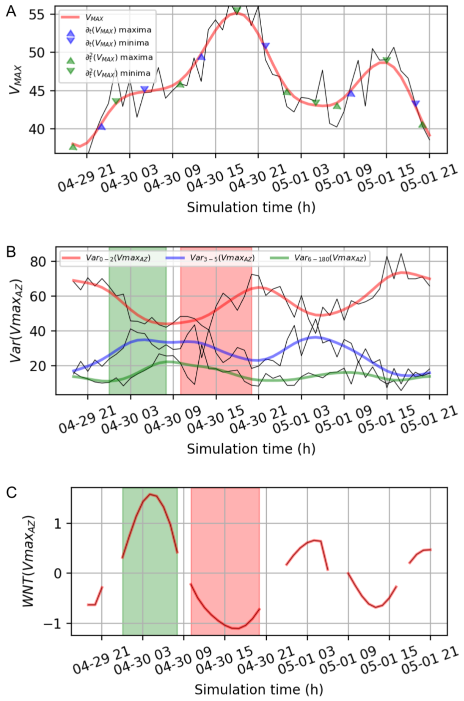

Figure 4.2 – Illustration of temporal changes estimations on the simulation of TC FANI. (A) Intensity raw time serie (thin black line) and smoothed with a 12-H cutoff period Butterworth filter (bold red), along with extracted local minima and maxima of $\partial_t(V_{MAX})$ and $\partial_t^2(V_{MAX})$ computed from the smoothed curve denoted by red and blue triangles. (B) Time series of smoothed $Var_{0-2}(Vmax_{AZ})$ (red), $Var_{3-5}(Vmax_{AZ})$ (blue) and $Var_{6-180}(Vmax_{AZ})$ (green) computed from raw signals (thin black curves). (C) Time serie of $WNT(Vmax_{AZ})$ computed from $\partial_t(Var_{0-2}(Vmax_{AZ}))$ and $\partial_t(Var_{6-180}(Vmax_{AZ}))$. The maximum positive and minimum negative phases of $WNT(Vmax_{AZ})$ are highlighted in green and red shadings on (B) and (C)

A smoothing of the time series is performed to only consider persistent variations of the parameters of interest, and ignore short localized variations. The effect of smoothing on $V_{MAX}$, and azimuthal variances is shown on Fig. 4.2. As can be inferred, the variability of raw time series can be very large (cf. thin black lines on Fig. 4.2A,B), preventing the extraction of life cycle phases or computation of meaningful time derivatives. The smoothing was thus chosen, after a sensitivity test, to absorb the high time variability, while being representative of intensity changes (peaks, troughs, increase, or decrease in intensification rates). It is applied using a Butterworth filter with a 12h cutoff period. All time derivatives are computed over the smoothed signals, allowing a much clearer estimation of intensity variations (see triangle markers on Fig. 4.2A). The smoothing also allows to extract consistent phases of negative and positive WNTs, such as those highlighted by the green and red rectangle, that go with changes in $Var_{0-2}(Vmax_{AZ})$ and $Var_{6-180}$ that are barely visible on raw signals.

### Classification

A machine learning classification method is used to assess the predictive potential of the extracted TC descriptors. The objective is to evaluate if these descriptors provide significant information to dissociate the TC life cycle phases. The classification here focuses on dissociating positive and negative values of $\partial_t(V_{MAX})$, and $\partial_t^2(V_{MAX})$, with classes defined under the 1/3 and above the 2/3 quantiles of their distribution.

We follow the classification method developed in Vinour et al., 2021, which is adapted to a dataset with a limited amount of samples (254 in this case, taking a random fourth of all WRF outputs to avoid overfitting), and a large number of variables describing the dataset (#48). The classification is performed on 756 random combinations of four variables, and with 10 machine learning models (this allows to account for a wide range of possible connections between variables, including non-linear ones). The average score of the 10 models is computed for each combination. Studying the composition of the best combinations then allows to identify the most decisive variables to dissociate intensification phases.

A sensitivity analysis of the classification results to the time smoothing of signals is performed. Classifications with descriptors computed from signals smoothed with 1, 3, 6, 12, and 18h cutoff periods are compared.

# 4.3 Modeled cases and validation

## 4.3.1 Description of simulations

Seven distinct events were simulated, in various basins, and with various characteristics: IRMA (2017, North Atlantic), CEBILE (2018, South Indian), LANE (2018, North-East Pacific), MANGKHUT (2018, North-West Pacific), TRAMI (2018, North-West Pacific), JOANINHA (2019, South Indian), and FANI (2019, North Indian).

They are detailed in Table 4.1 and Fig. 4.3, along with the geographic extent of the model parent domain. These simulations were chosen to describe major TCs (category 4

Table 4.1 – Summary of WRF simulated events and domain extents

| Event name | Start date - end date | Basin | Category (WRF) | Category (obs.) | Outer domain extent |
|---|---|---|---|---|---|
| IRMA | 2017/08/31 - 2017/09/11 | Northern Atlantic | 4 | 5 | 99.9°W-24.1°W 8.3°N-35.5°N |
| CEBILE | 2018/01/27 - 2018/02/04 | Southern Indian | 5 | 4 | 67.6°E-92.5°E 29.9°S-4.1°S |
| LANE | 2018/08/16 - 2018/08/24 | Eastern Pacific | 5 | 5 | 166.0°W-120.5°W 2.7°N-27.0°N |
| MANGKHUT | 2018/09/08 - 2018/09/16 | Western Pacific | 4 | 5 | 102.7°E-164.1°E 5.7°N-30.3°N |
| TRAMI | 2018/09/22 - 2018/09/30 | Western Pacific | 4 | 4 | 118.7°E-146.0°E 8.9°N-43.7°N |
| JOANINHA | 2019/03/23 - 2019/03/30 | Southern Indian | 5 | 4 | 53.6°E-77.4°E 32.8°S-8.7°S |
| FANI | 2019/04/29 - 2019/05/03 | Northern Indian | 3 | 4 | 75.9°E-95.1°E 2.7°N-27.6°N |

and 5) in different basins, and with a wide range of life cycle evolutions including several intensity changes during their mature phases. In addition, TCs with few interactions with land were preferred, as they allow to witness scale interactions, and gradual internal changes instead of brutal disturbances caused by external constraints. These simulations were not designed to reproduce the most realistic TCs, but to provide a sufficiently diverse database to study the inner-core structural changes in relation to the TC intensity changes during the mature phase of the TC life cycle.

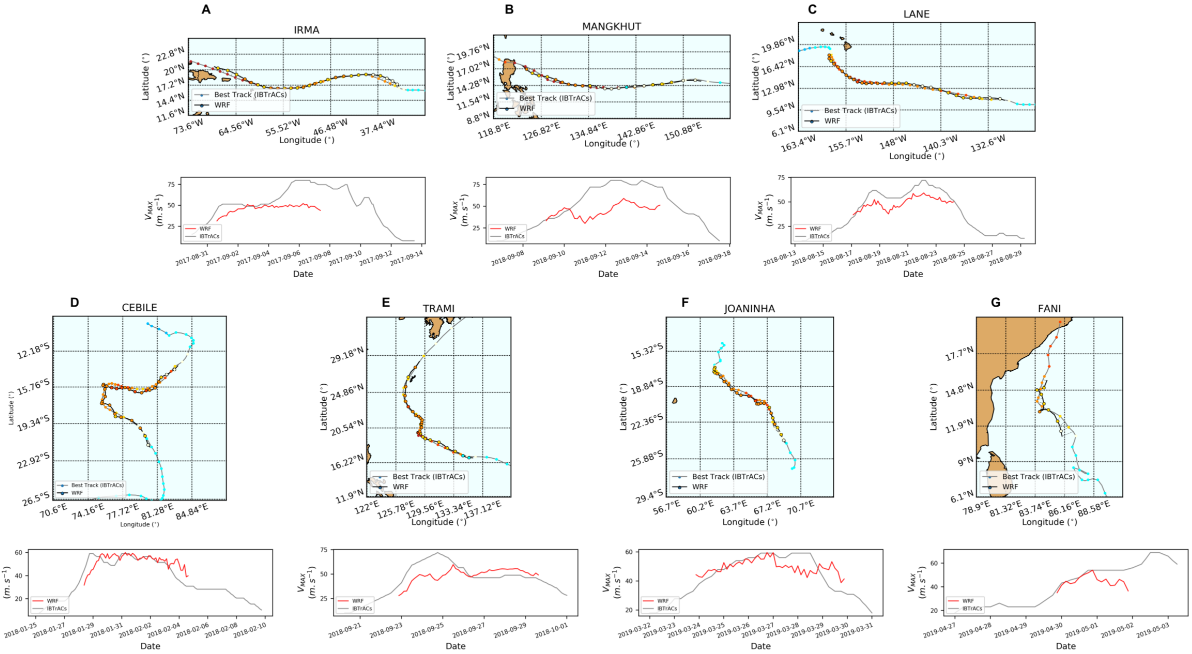

Figure 4.3 – Summary of WRF simulated tracks and intensity times series for the seven simulations compared to IBTrACs.

Figure 4.3 shows the 7 modeled TC tracks and $V_{MAX}$ time series. All tracks match well the BT data, as spectral nudging applied on the large domain ensures synoptic dynamics close to observations. Simulated maximum wind, on the other hand, can be quite different from BT data. The maximum reached intensity is underestimated for IRMA, MANGKHUT, TRAMI, and LANE, and overestimated for CEBILE, while FANI does not maintain its intensity before landfall, and JOANINHA does not capture the maximum intensity peak although matching the first intensification. Time steps above category 4 are rare; this can be a bias induced by the horizontal resolution, which is probably still too coarse to properly solve these very intense phases. The maximum wind time series also reveal some lagged or missed changes in intensity, or similar changes but of lower intensity (for LANE). Such discrepancies were however expected. They arise from several reasons: 1) the model uncertainties (resolution, parameterizations) that can lead to miss physical processes, 2) the stochastic nature of the Navier-Stokes equations. However, all simulated TCs intensify to mature TCs, and all of them feature either long mature phases with short-range intensity fluctuations around the peak intensity (IRMA and CEBILE), or notable declines and re-intensifications with secondary intensity peaks (TRAMI, MANGKHUT, FANI, LANE, JOANINHA). The diversity of cases and external conditions is satisfying, and allows to have TCs with notable intensity changes and a significant variability in the mature TC life cycle description, which was the request for our study. Figure 4.4 statistically compares the simulation database to the SAR and BT databases. It shows the chosen bias of simulating major TCs in their mature phases with therefore a normalized distribution of maximum wind centered around 55m/s, a latitude distribution centered around 15°, and translation speed centered around $5m.s^{-1}$. More importantly, the intensification rate distribution is well represented.

The statistical validation of our simulations and extracted parameters of interest against SAR observations is further detailed in the next section.

### 4.3.2 Statistical validation against SAR

The radial and azimuthal parameters describing the TC surface wind field in the present study are validated against SAR observations.

The distributions of the inner-core and near-core radial gradients shown on Fig. 4.5 shows that the model misses the strongest radial gradients. The azimuthal variances of the eye shape (B), and the RMW (E) are relatively well represented, and distributions of the eyewall gradient (C), and maximum wind ring (F) azimuthal variances are slight

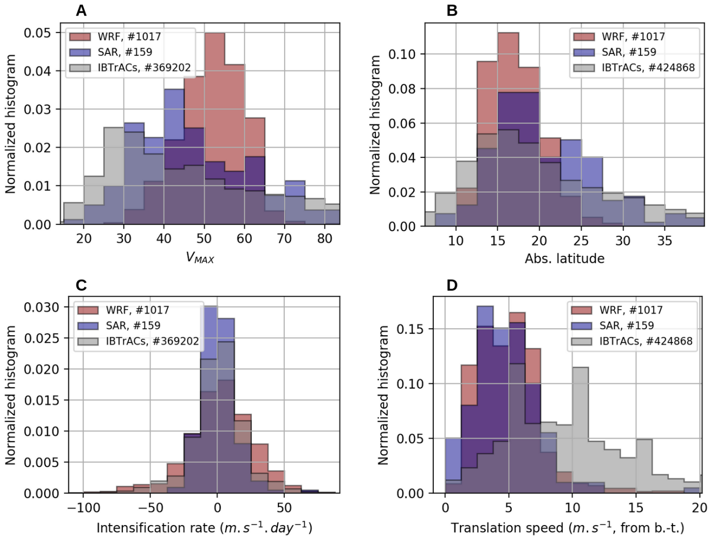

Figure 4.4 – Comparison of histograms between WRF (red, 1017 samples), SAR (blue, 159 samples) and IBTrACs (grey, 369202 samples) showing distributions of (A) $V_{MAX}$, (B) Absolute Latitude, (C) $\partial_t(V_{MAX})$ and (D) Translation Speed. Time-dependent variables ((C) and (D)) are estimated from IBTrACs for the SAR distribution.

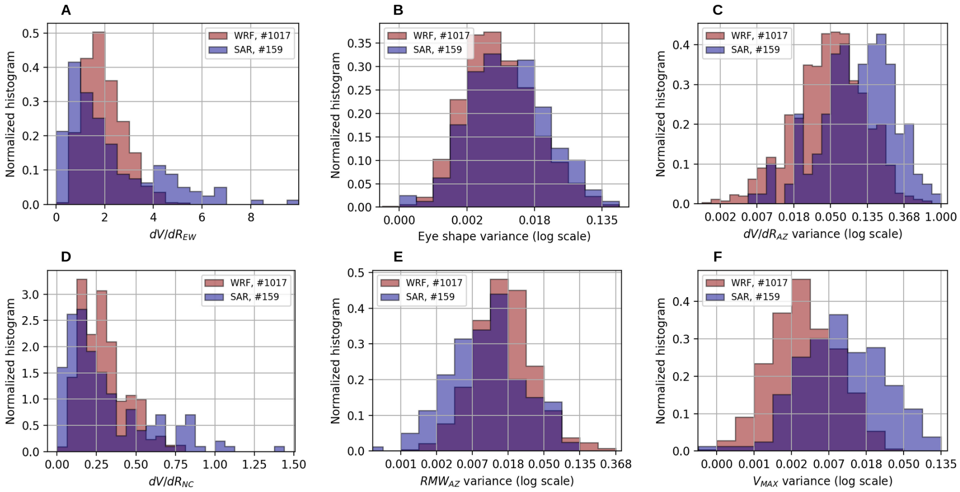

Figure 4.5 – Comparison of histograms between WRF (red, 1017 samples) and SAR (blue, 159 samples) showing distributions of (A) $dV/dR_{EW}$, (B) $dV/dR_{NC}$, (C) $Var(ES_{AZ})$, (D) $Var(RMW_{AZ})$, (E) $Var(dV/dR_{AZ}$ and (F) $Var(Vmax_{AZ}$

shifted towards lower values than SAR observations indicating a possible underestimation of the maximum wind and eyewall gradient variability. But overall, modeled distributions are satisfactorily close enough to observations.

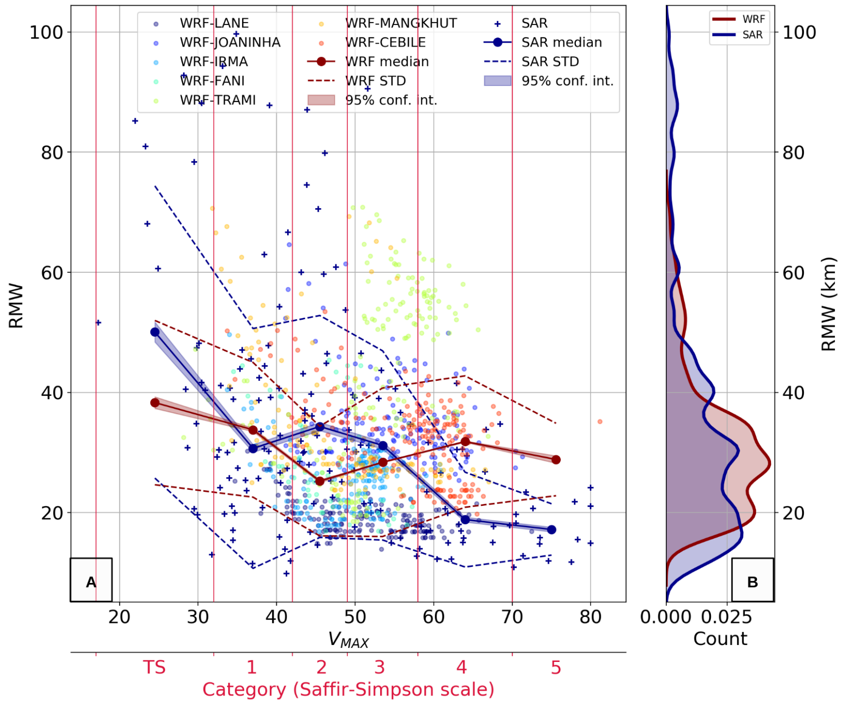

Figure 4.6 – (A) Comparison of RMW distributions with respect to $V_{MAX}$ between SAR and WRF. SAR samples and binned medan values and quartiles are denoted by blue crosses, lines and shading. WRF samples are denoted by small dots coloured according to the simulated event. WRF binned median values and quartiles are denoted by red line and shading. (B) WRF (red) and SAR (blue) PDF distributions of RMW values

The model ability to represent inner-core observed TC structure is further illustrated with the relation between RMW and maximum wind on Fig. 4.6. This relation is a good way to get a first view of the TC dynamics, as the TC vortex is expected to contract inward when intensifying under the effect of gradient wind balance and angular momentum conservation. This relation was clearly observed in SAR observations (Vinour et al., 2021), and is represented in blue in Fig. 4.6. Our simulations also show a decrease of RMW with $V_{MAX}$, but at a weaker rate, with a median value of 40 km for tropical storms (about 50km in SAR data), and 25 km for category 4 TCs (compared to about 18km in SAR data). Here again, the highest intensities appear as probably less well resolved in the model due to resolution issues. On another hand, the limit in statistical representativeness of the 7 cases is also visible, as the individual simulations can impact the median values for a given category: for instance, the high values of RMW for category 3 are mostly all attributable to TRAMI, which kept a strong intensity while it reached relatively high latitudes, and therefore dilated in size. However, the range of TC simulations overall allows to feature the average TC eye contraction.

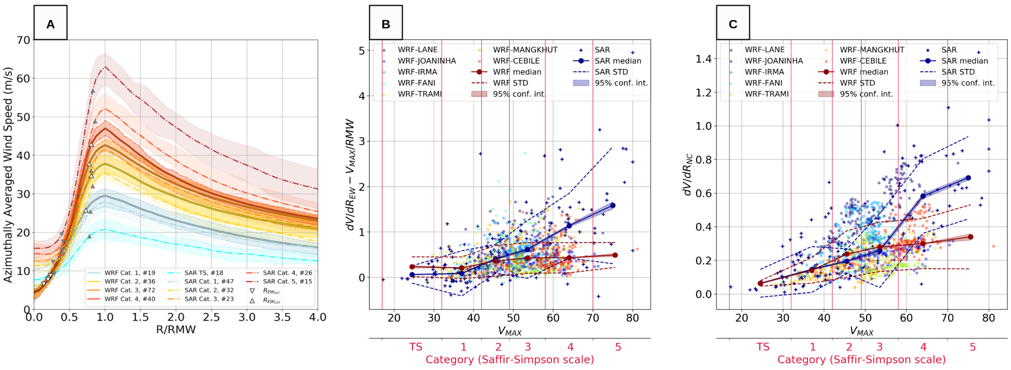

Figure 4.7 – (A) Comparison of WRF (solid) and SAR (dashed) mean radial profiles composited by intensity category, with shadings denoting the quartiles of each category. Upper (lower) triangle markers show the positions of outer (inner) limits of the eyewall maximum gradient area delimited by maximum and minimum values of curvature for WRF (white) and SAR (grey). (B) and (C) are the same as Fig. 4.6A for the distributions of $dV/dR_{EW} - V_{MAX}/RMW$ and $dV/dR_{NC}$.

The properties of the radial radial mean profile of simulated TCs are also compared to the SAR distributions studied in Vinour et al., 2021, and shown on Fig. 4.7. The composite radial profiles by TC intensity category (Fig. 4.7A) show a fair agreement between WRF and SAR apart from category 4 which is much lower on WRF due to the unbalanced distribution of wind values in category 4. It is however notable that WRF profiles are slightly more intense (by approx. 2m/s) on average than SAR ones for both categories 1, 2, and 3. This suggests that WRF TCs have a more homogeneous wind distribution: as the category is determined by the maximum wind value, the average profile for a given category reflects the proximity of other wind values to this maximum wind. It thus appears that SAR images contain lower wind values in their distribution for a given category than WRF. Another remarkable difference between WRF and SAR profiles is the eye area. Indeed, all WRF profiles have a much lower central wind value (around 6 m/s versus more than 10m/s for SAR at categories 1-3). This might be related to overestimations of wind values in the eye by SAR (an issue related to SAR wind inversion that was discussed in Vinour et al., 2021).

Looking at the eyewall gradient sharpness, TC simulations are shown to slightly depart from the Rankine-like profile (Fig. 4.7B), but much less than SAR observations for TC intensities above category 3. Similarly, the near-core area (Fig. 4.7C) shows a smoother profile than SAR observations for TC timesteps of category 4 and 5. This indicates a limit in WRF ability to resolve sharp wind gradient due to its resolution.

## 4.4 Links between life cycle and internal structure

### 4.4.1 Time scales

The TC life cycle variations are characterized with 3 time series: the TC intensity ($V_{MAX}$), its time derivative (intensification rate, $\partial_t(V_{MAX})$), and its time second derivative (variations of intensification rate, $\partial_t^2(V_{MAX})$). As shown by the time spectral decomposition of these signals featured on Fig. 4.8A, the 3 time series obviously describe the life cycle evolution at various scales with peak periods of respectively 164, 32, and 20h. Thus, the intensity characterizes the intensification and decaying phases on the whole life cycle time scale, and shows very little energy under 24h. On the other hand, its derivatives have significant signal up to 12h related to shorter variations of daily or half-daily timescales. The effect of the 12h-smoothing is evidenced with almost no power spectrum density found under 12h for all signals.

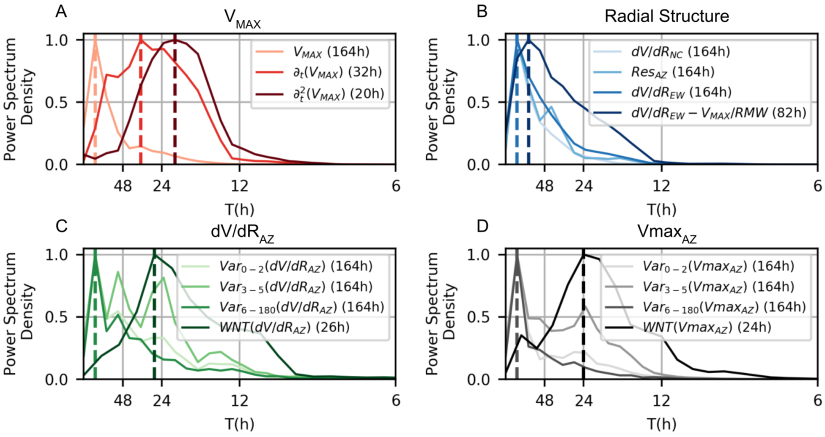

Figure 4.8 – Power spectra of WRF-extracted time series as a function of period in hours, with peak periods denoted by dashed vertical lines. (A) Intensity variations descriptors: $V_{MAX}$ (light), $\partial_t(V_{MAX})$ (medium) & $\partial_t^2(V_{MAX})$ (dark). (B) Radial profile descriptors: $dV/dRNC$, $Res_{AZ}$, $dV/dR_{EW}$ and $dV/dR_{EW} - V_{MAX}/RMW$. (C) Eyewall radial gradient azimuthal descriptors: $Var_{0-2}(dV/dR_{AZ})$,$Var_{3-5}(dV/dR_{AZ})$,$Var_{6-180}(dV/dR_{AZ})$ and $WNT(dV/dR_{AZ})$. (D) same as (C) for $Vmax_{AZ}$.

The parameters extracted to describe the TC surface wind field structure (radial gradients, azimuthal variances, spectral decompositions, and energy transfers within the spectrum) are also found to vary at different time scales. $dV/dR_{EW}$ and $dV/dR_{NC}$ evolve on a characteristic time period similar to the intensity (164h, Fig. 4.8B). This is in agreement with the relation found between intensity and radial gradient observed on Fig. 4.7. The estimation of the curvature of the eyewall profile ($dV/dR_{EW} - V_{MAX}/RMW$) shows a broader spectrum towards smaller scales, with a peak period of 82h. It is indeed the radial parameter the most related to smaller scales, in particular eyewall mixing. The azimuthal explained variances $dV/dR_{AZ}$ and $Vmax_{AZ}$ are shown to have peak period similar to the intensity (164h, Fig. 4.8C&D). However, they also have secondary peaks at shorter timescales, notably at 24h, and a broader spectrum towards short timescales than radial parameters. The wave number transfers (WNTs) within these azimuthal signals are found to evolve on short timescales only, with a spectrum centered around 24h, and significant spectral density up to about 10 h. WNTs thus focus on shorter-scale changes through the azimuthal structure, matching the time scale of $\partial_t(V_{MAX})$ and $\partial_t^2(V_{MAX})$.

### 4.4.2 Case studies

The time series of $dV/dR_{NC}$, $Res_{NC}$, $Var_{0-2}(VmaxAZ)$ and $Var_{6-180}(VmaxAZ)$ superimposed with the $V_{MAX}$ time serie during the LANE simulation are shown on Fig. 4.9.

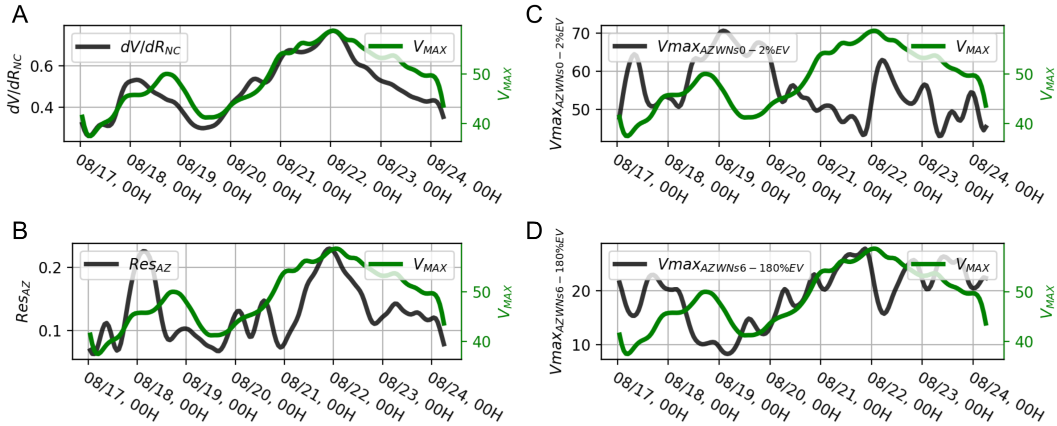

Figure 4.9 – Time series of (A) $dV/dR_{NC}$, (B) $Res_{NC}$, (C) $Var_{0-2}(VmaxAZ)$ and (D) $Var_{6-180}(VmaxAZ)$ (green curves) superimposed with the $V_{MAX}$ time serie (black curves) during the LANE simulation.

For a given TC case, the correlation between TC intensity and radial gradients time series is remarkable (0.9 cross-correlation with $dV/dR_{NC}$, 0.56 with $Res_{NC}$, Fig. 4.9A,B). The near-core radial profile follows the evolution of intensity (higher intensity goes with sharper wind profile, cf. panels A & B). On the other hand, the correlation between azimuthal variances and life cycle evolution is lower (0.53 cross-correlation with $Var_{6-180}(VmaxAZ)$, Fig. 4.9C, D). It is however notable that the increase in intensity towards the $V_{MAX}$ peaks goes with a higher explained variance in WNs 6-180 (Fig. 4.9D), that is with a more homogeneous distribution of winds around the vortex, and a concurrent decrease in WNs 0-2 explained variance (Fig. 4.9C).

Looking closely at wave number transfers (WNTs) on specific phases from the LANE and FANI events displayed on Fig. 4.10 yields several notable observations. For each simulation, the phases of maximum positive and minimum negative WNT are highlighted (red shaded areas), and snapshots of the WRF 10-m wind speed are shown at the limits of these phases. The FANI simulation (Fig. 4.10A) shows a clear alternation between positive and negative $WNT(Vmax_{AZ})$: positive transfers occur during phases of re-intensification, and negative transfers before and during intensity peaks, i.e. when intensification decreases. The time lag between $WNT(Vmax_{AZ})$ and $V_{MAX}$ is negative. Focusing on the two highlighted phases (red shaded), the first positive transfer starts approximately 10 h before the beginning of the re-intensification, and the negative transfer also starts about 10 h before the intensity peak. All other local maxima and minima of WNTs are also nearly synchronized with the inflection points of the intensity curve.

The evolution of LANE shown on Fig. 4.10B is more complex. It is much longer with shorter and more numerous re-intensification and weakening phases. However, the two highlighted phases show similar features than the FANI life cycle. The maximum of positive $WNT(Vmax_{AZ})$ on 08/20 occurs right before a marked re-intensification. It is followed by a very short and small amplitude negative transfer, and an other notable positive transfer that accompanies the fast intensification. The minimum of negative $WNT(Vmax_{AZ})$ is in turn simultaneous with the maximum intensity peak on 08/22, at the beginning of the decline phase. During the four highlighted phases, the snapshots show marked changes in the distribution of maximum wind related to $WNT(Vmax_{AZ})$ minima and maxima. During negative transfers, the TC usually goes from an asymmetric wind distribution to more balanced one, while positive transfers show the opposite. These two cases studies thus indicate that marked changes in the maximum wind distribution are connected to intensity changes, although the time lag can vary significantly in each

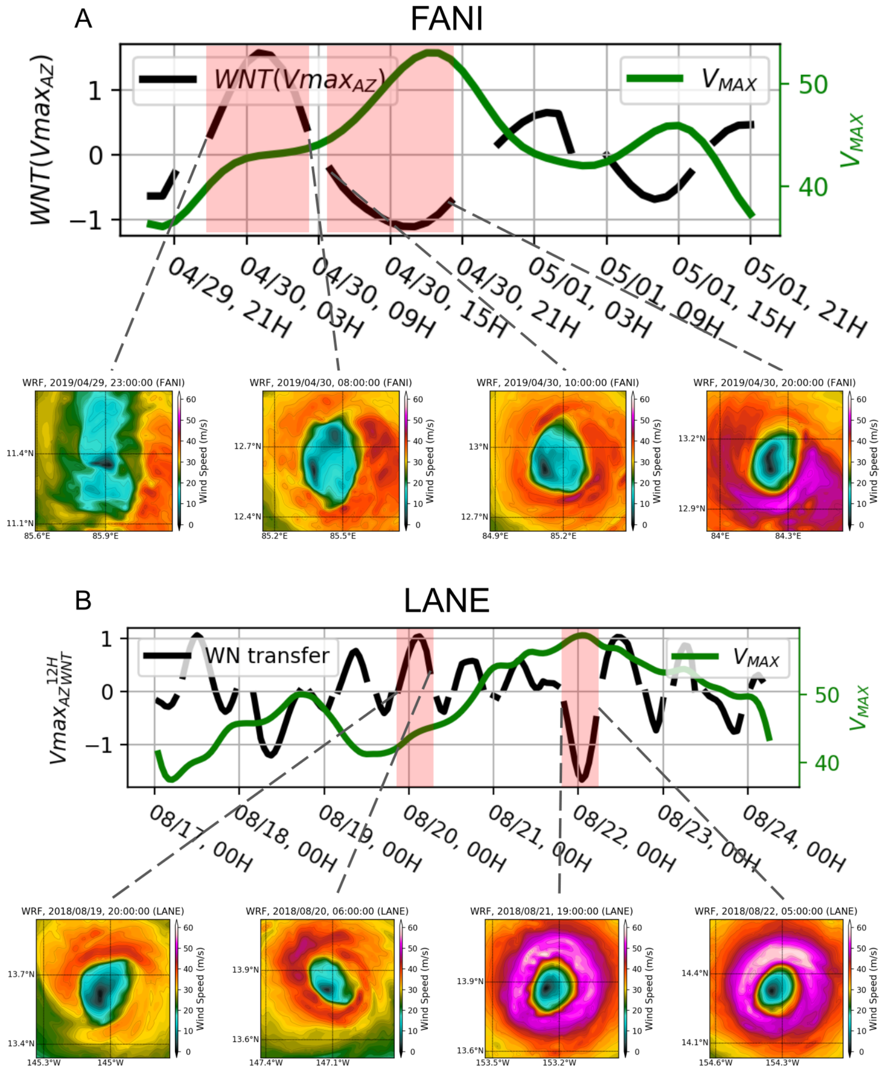

Figure 4.10 – Superimposed time series of $V_{MAX}$ (black curves) and $WNT(Vmax_{AZ})$ (green curves) for simulations of (A) LANE and (B) FANI. Strongest phases of positive and negative transfer are denoted by a red shading for each simulation, along with the corresponding snapshots of surface wind field.

situation. Moreover, it appears from the LANE life cycle that, when intensity variations are numerous and on small time scales, the relationship is less evident. Thus, although pattern emerges from these specific cases, a clear correlation seems difficult to obtain.

### 4.4.3 Statistical assessment of all case studies

When computed over all simulated cases, the cross-correlations between the various radial and azimuthal parameters, and intensity variations, shown on Fig. 4.11 reflect the previously illustrated behaviors.

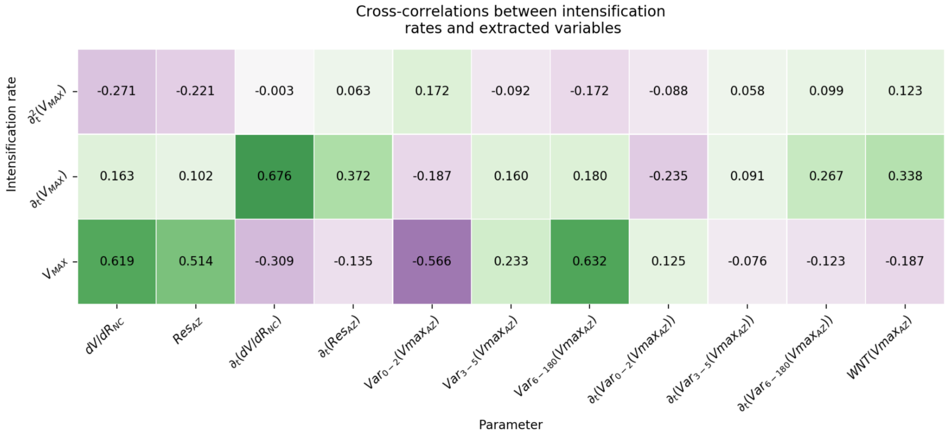

| | $dV/dR_{NC}$ | $Res_{AZ}$ | $\partial_t(dV/dR_{NC})$ | $\partial_t(Res_{AZ})$ | $Var_{0-2}(Vmax_{AZ})$ | $Var_{3-5}(Vmax_{AZ})$ | $Var_{6-180}(Vmax_{AZ})$ | $\partial_t(Var_{0-2}(Vmax_{AZ}))$ | $\partial_t(Var_{3-5}(Vmax_{AZ}))$ | $\partial_t(Var_{6-180}(Vmax_{AZ}))$ | $WNT(Vmax_{AZ})$ |
|---|---|---|---|---|---|---|---|---|---|---|---|
| $\partial_t^2(V_{MAX})$ | -0.271 | -0.221 | -0.003 | 0.063 | 0.172 | -0.092 | -0.172 | -0.088 | 0.058 | 0.099 | 0.123 |
| $\partial_t(V_{MAX})$ | 0.163 | 0.102 | 0.676 | 0.372 | -0.187 | 0.160 | 0.180 | -0.235 | 0.091 | 0.267 | 0.338 |
| $V_{MAX}$ | 0.619 | 0.514 | -0.309 | -0.135 | -0.566 | 0.233 | 0.632 | 0.125 | -0.076 | -0.123 | -0.187 |

Figure 4.11 – Table of cross-correlations between $V_{MAX}$ and its variations (vertical axis) and internal structure descriptors (horizontal axis).

The largest correlations are found between $V_{MAX}$ and $dV/dR_{NC}$ (61.9%), $\partial_t(V_{MAX})$ and $\partial_t(dV/dR_{NC})$ (67.6%), $V_{MAX}$ and $Vmax_{AZWNs6-180\%EV}$ (63.2%), and anti-correlation between $V_{MAX}$ and $Vmax_{AZWNs0-2\%EV}$ (-56.6%). Other correlations are quite low. In particular, no notable correlations are found with $\partial_t^2(V_{MAX})$, and WNTs show no significant correlation with neither of the three intensity variations descriptors. This can either indicate a lack of statistical significance, a lag between variables, or a different dynamical content.

To refine the statistical characterization of intensity variations, we perfomed a composite analysis of $V_{MAX}$, $\partial_t(V_{MAX})$, and $\partial_t^2(V_{MAX})$ local minima and maxima, shown on Figs. 4.12 and 4.13. This way, we isolate only the life cycle phases corresponding to marked intensity variations. The composite analysis consists in computing median values of the parameters of interest from 10h before to 10h after the minima or maxima. The composites of radial gradient time evolution ($\partial_t(dV/dR_{EW})$ and $\partial_t(dV/dR_{NC})$) appear tightly in phase with $\partial_t(V_{MAX})$ maxima and minima (Fig. 4.12C,D). They are also shown to decrease during $V_{MAX}$ peaks and $\partial_t^2(V_{MAX})$ minima, and increase during $V_{MAX}$ minima and $\partial_t^2(V_{MAX})$ maxima. Compared to the radial gradients that evolve in phase with the TC intensity, azimuthal WNTs interestingly show a phase lag with intensity variations (Fig.

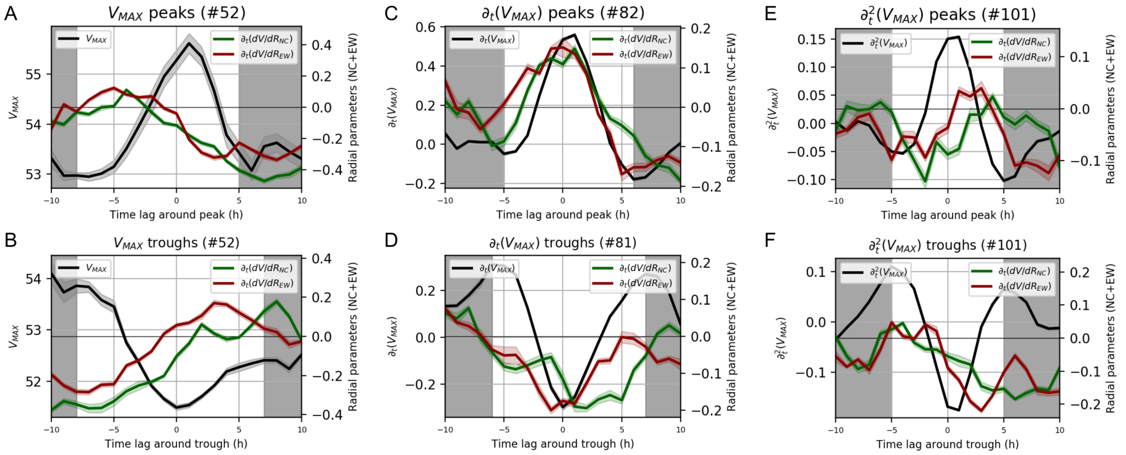

Figure 4.12 – Composites of $\partial_t(dV/dR_{NC})$ (green) and $\partial_t(dV/dR_{EW})$ (red) over all local maxima (upper panels) and minima (lower panels) of (left) $V_{MAX}$, (center) $\partial_t(V_{MAX})$, and (right) $\partial_t^2(V_{MAX})$, along with corresponding composites of (left) $V_{MAX}$, (center) $\partial_t(V_{MAX})$, and (right) $\partial_t^2(V_{MAX})$. Grey shadings denote the average start and end dates of maxima and minima. Number of WRF in each composite are indicated by (#)

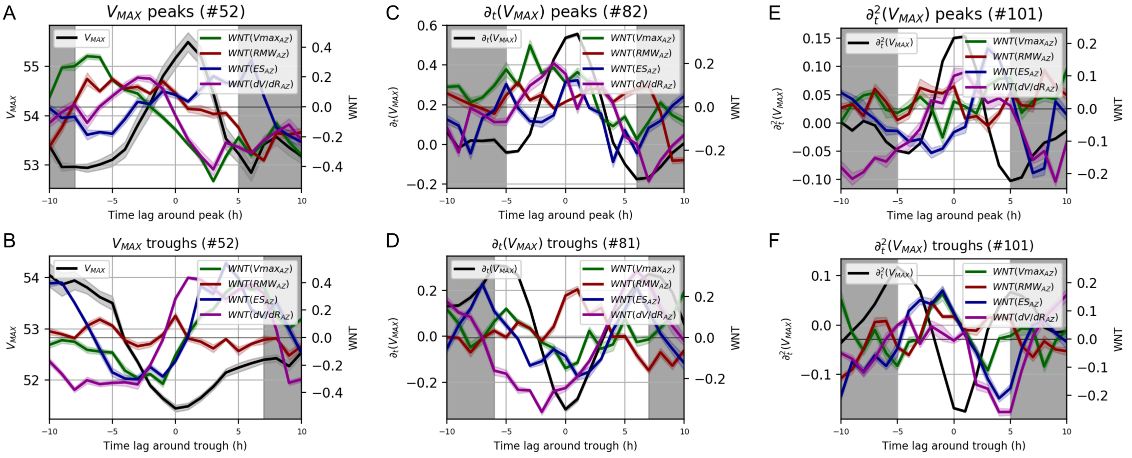

Figure 4.13 – Same as Fig. 4.12 for $WNT(Vmax_{AZ})$ (green), $WNT(RMW_{AZ})$ (red), $WNT(ES_{AZ})$ (blue) and $WNT(dV/dR_{AZ}$ (purple).

4.13) . Positive transfers occur before intensity ($V_{MAX}$) and intensification ($\partial_t(V_{MAX})$) peaks, and conversely negative transfers before $V_{MAX}$ and $\partial_t(V_{MAX})$ troughs. WNTs are also shown to notably increase during intensity trough and ($\partial_t^2(V_{MAX})$) maxima, that is before and during re-intensification phases. Conversely, they decrease during intensity peaks, and intensification weakening phases. This analysis suggests that azimuthal WNTs variables may have a potential for predictability as they are lagged with short-scale intensity changes, and are associated more to intensity modulations than to its magnitude in itself. These observations are made on the eyewall gradient, and eye shape. They are also mostly true for the maximum wind ring intensity but with less marked trends (not shown). On the other hand, $RMW_{AZ}$ composites do not show significant changes regarding intensity changes. The spatial asymmetry of the maximum wind ring thus does not seem to be a good proxy for characterizing intensity variations. The specificity of the eyewall area thus emerges consistently with intensity restoration studies of eyewall dynamics and VRWs: the eyewall is indeed the most sensitive area of the vortex, as any perturbation can cause vorticity mixing and, subsequently, lead to the generation of VRWs that eventually allow intensity restoration.

### 4.4.4 Prediction score improvement including azimuthal structure evolution

Following the previous observation of the particular connection between azimuthal spectral transfers, and intensification variations, the machine learning classification method described in section 4.2.2 was applied to WRF outputs with two goals: assess the connection between azimuthal structure parameters and intensity variations, clarify the characteristic time scales at which these connections occur. Two classifications were run. One to dissociate intensifying and declining TCs, and another to dissociate re-intensifications and intensification weakenings (i.e. positive and negative $\partial_t^2(V_{MAX})$). These classifications were performed using subgroups of 4 variables taken among instantaneous mean vortex parameters (i.e. latitude, maximum wind, RMW, and eyewall radial gradient), time-dependent azimuthal structure parameters (i.e. time derivatives of explained variance by WN groups, or spectral low-to-high WN transfer for each of the four azimuthal signals), or a random control variable. Results are synthetized in Fig. 4.14, showing the 5 best prediction scores compared to a control combination of instantaneous variables (i.e. $V_{MAX} + RMW + Latitude + dV/dR_{EW}$, first score on the left). The score evolution is evaluated and compared for different values of smoothing cutoff period considered: 3, 6, 12, and 18h. Moreover, Tables 4.2 and 4.3 show, for the two classifications and for each time smoothing reference, the most contributing variables sorted by number of occurrences among the 5 best combinations.

The prediction scores of intensifications and declines (Fig. 4.14A) shows improve-

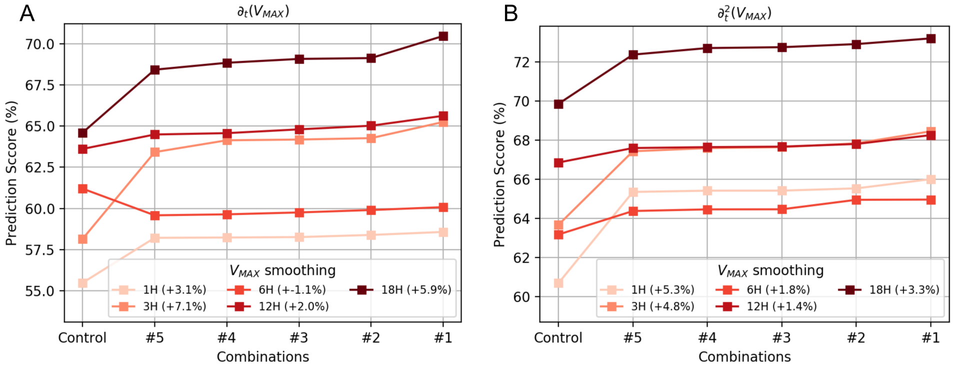

Figure 4.14 – (A) Evolution of prediction scores for the classification of positive/negative $\partial_t(V_{MAX})$ (i.e. intensifications/declines). Classes are defined as the lower and upper thirds of the $\partial_t(V_{MAX})$ distribution. Each line shows the score of the control combination $V_{MAX} + RMW + Latitude + dV/dR_{EW}$ (on the left), and the 5 best scores obtained by integrating internal structure time-derivative predictors, for different values of smoothing applied to the $V_{MAX}$ signal (colored lines). The relative difference between the control and the best combination scores is written in the legend. (B) same as (A) for the classification of $\partial_t^2(V_{MAX})$.

Table 4.2 – Summary of the top #5 most contributing vectors to the classification of positive and negative $\partial_t(V_{MAX})$ (i.e. intensification and declines) for different values of smoothing cutoff period $T_c$ (left column). The number of occurrences among the 5 best combinations is displayed.

| Time Reference | #1 | #2 | #3 | #4 | #5 |
|---|---|---|---|---|---|
| $T_c = 3h$ | $WNT(dV/dR_{AZ})$ (#5) | Abs. latitude (#5) | $WNT$ $(Vmax_{AZ})$ (#4) | $WNT$ $(RMW_{AZ})$ (#2) | $dV/dR_{NC}$ (#2) |
| $T_c = 6h$ | RMW (#5) | Abs. latitude (#5) | $Var_{6-180}$ $(Vmax_{AZ})$ (#4) | $Var_{6-180}$ $(ES_{AZ})$ (#2) | $dV/dR_{NC}$ (#2) |
| $T_c = 12h$ | Abs. latitude (#5) | $WNT$ $(Vmax_{AZ})$ (#4) | $WNT$ $(dV/dR_{AZ})$ (#3) | $WNT$ $(ES_{AZ})$ (#2) | $WNT$ $(RMW_{AZ})$ (#2) |
| $T_c = 18h$ | $WNT(Vmax_{AZ})$ (#5) | Abs. latitude (#4) | $WNT$ $(RMW_{AZ})$ (#3) | $dV/dR_{NC}$ (#3) | $WNT$ $(dV/dR_{AZ})$ (#3) |

ment when adding azimuthal parameters compared to mean-vortex properties, for all time smoothings except the 6h one. The highest improvements are observed for cutoff periods of 3h (+7.1%), and 18h (+5.9%). Moreover, the most contributing parameters are: absolute latitude (always 4 or 5 occurrences among the 5 best combinations whatever the smoothing, which are explained by the large number of declining TCs at high latitudes), $WNT(Vmax_{AZ})$ (4 or 5 occurences among the 5 best combinations with 3h, 12h, and

18h smoothing), and $WNT(dV/dR_{AZ})$ (3 to 5 occurences in the 5 best combinations). What comes out from this classification is thus the decisive role of $WNT(Vmax_{AZ})$ and $WNT(dV/dR_{AZ})$ in the dissociation of intensification rates: indeed, on the two classification yielding the highest improvement (3h and 18h), these two parameters are the most contributing to the classification. Moreover, intrestingly, the $WNT(dV/dR_{AZ})$ distribution is predominant at short time scale ($T_c = 3h$), while $WNT(Vmax_{AZ})$ takes over at $T_c = 12h$ and $T_c = 18h$. A different dynamical scale thus seems to characterize the eyewall and the maximum wind area, which confirms the observations made on time spectra (section 4.4.1), and is in agreement with eyewall dynamics studies that describe this area as subject to very short-scale changes and more spontaneous vorticity mixing processes (Schubert et al., 1999; Kossin and Schubert, 2001).

Table 4.3 – Same as table 4.2 for the classification of $\partial_t^2(V_{MAX})$ positive and negative phases

| Time Reference | #1 | #2 | #3 | #4 | #5 |
|---|---|---|---|---|---|
| $T_c = 3h$ | $V_{MAX}$ (#5) | Random (#4) | $WNT$ ($ES_{AZ}$) (#3) | $WNT$ ($RMW_{AZ}$) (#2) | $WNT$ ($Vmax_{AZ}$) (#2) |
| $T_c = 6h$ | $WNT$ ($Vmax_{AZ}$) (#5) | $V_{MAX}$ (#5) | $WNT$ ($ES_{AZ}$) (#3) | $WNT$ ($RMW_{AZ}$) (#2) | $dV/dR_{NC}$ (#2) |
| $T_c = 12h$ | $WNT$ ($Vmax_{AZ}$) (#5) | $dV/dR_{NC}$ (#4) | $V_{MAX}$ (#4) | $WNT$ ($RMW_{AZ}$) (#2) | $WNT(dV/dR_{AZ})$ (#2) |
| $T_c = 18h$ | $V_{MAX}$ (#5) | Abs. latitude (#5) | $WNT$ ($ES_{AZ}$) (#3) | $WNT$ ($Vmax_{AZ}$) (#3) | RMW (#2) |

The evolution of prediction scores of changes in intensification rate (positive and negative values of $\partial_t^2(V_{MAX})$), shown on Fig. 4.14B with best predictors summarized in Table4.3, indicates improvement for all time references with respect to the mean-vortex control combination. The best improvements are observed at $T_c = 3h$ (+4.8%), and $T_c = 18h$ (+3.3%). The best combinations yielding these improvements mostly include absolute $V_{MAX}$ (in 4 or 5 combinations out of the best 5 at all time scales, logically indicating the fact that intense TCs have more chances to weaken, and conversely), and $WNT(Vmax_{AZ})$ (present in 3 to 5 of the best combinations). $WNT(ES_{AZ})$ also regularly appears in the best combinations highlighting the significance of the eye shape signal. The 3h scale seems irrelevant given the presence of the random variable in 4 of the 5 best combinations. This second classification thus also shows the notable contribution of WNTs, even at large time scales of 18h, indicating that they consistently describe the evolution of the internal energy distribution (especially the maximum wind distribution WNT).

Overall, the classification highlights the significant role of azimuthal WNTs in dissociating TC intensification variations. Intensification rates are better dissociated preferably using eyewall dynamics at small time scales, and maximum wind ring properties at larger scales. Small-scale intensity variations (i.e. second derivative sign changes) consistently show better score improvements at scales larger for 6, 12 and 18h time scales, with a prevalent role of $WNT(Vmax_{AZ})$ and $WNT(ES_{AZ})$.

## 4.5 Summary and Discussion

### 4.5.1 Summary

In this study, seven major TC cases (reaching at least cat. 4 during their life cycle) are simulated with the WRF model at the high resolution of 1km thanks to a grid-nesting strategy using vortex-following moving nests. These simulations are designed to statistically evaluate the evolution of the TC surface wind field structure in relation with intensity variations. This work follows a recent study (Vinour et al., 2021) showing that newly available kilometer-resolution surface wind fields, retrieved from Synthetic Aperture Radars (SARs), have the potential to improve the statistical predictability of TC intensification rates. The present study evaluates the added-value of having the temporal evolution of the wind field structure, and particularly its fine scales, to further analyze the connections between vortex internal changes, and TC intensity modulation.

The simulations are shown to fairly represent the average TC contraction with intensity, with though an underestimation of the eyewall and near-core gradients, and an overestimation of the RMW for the strongest winds (when $V_{MAX}$ reaches cat. 4 and above). The azimuthal asymmetry of the eye shape, the eyewall gradient, the RMW, and the maximum wind is also realistically modeled, with only a slight shift towards a lower maximum wind variability than observed with SAR. This may be attributable to limitations associated to the model resolution, and parameterizations, which are discussed in the next section. Apart from the underestimated radial gradients for highest wind speeds, the model simulations are shown to realistically represent the TC internal structure, and its variability, as well as intensity variations.

The radial eyewall and near-core gradients are shown to evolve on a charateristic time scale similar to intensity, while the evolution of the azimuthal structure, and especially the transfer of energy within its spectrum, is shown to match the timescale of intensity variations. This suggests a separation between radial and azimuthal descriptors: while radial gradients tend to describe the state of the vortex, roughly following its maximum intensity, azimuthal WNTs have a larger connection with short-scale intensity changes, and are associated more to intensity modulations than to its magnitude.

Positive WNTs are observed during re-intensification phases, and negative transfers before and during intensity peaks, that is when intensification weakens. This is consistent with previous studies associating, on the one hand, the eyewall and maximum wind area distortions with external events perturbating the vortex intensity, and, on the other hand, restoration of intensity with symmetrization and homogenization of the vortex (Montgomery and Kallenbach, 1997; Schubert et al., 1999). Compared to the radial gradients that evolve in phase with the TC intensity, azimuthal WNTs show a phase lag with intensity variations, suggesting a predictability potential, although the time lag can vary significantly. Modeling and observational case studies suggested that polygonal eyewalls (approximated in this study by $ES_{AZ}$ middle wave numbers) might be favourable to rapid intensifications (Lee and Wu, 2018; Cha et al., 2020). Our analyses however indicate no statistical correlation between polygonal eye shapes and intensification rate on the considered time scales (i.e. larger than 6h). However, a higher correlation is evidenced for low-to-high wave number transfers suggesting that the azimuthal structure spectral decomposition shall be considered more dynamically than as a state of the vortex: what matters to the life cycle might not be the presence or the absence of polygonal eyewalls, low wave number asymmetry, or ring-like TCs, but the evolution of this structure in time, i.e. the fact that it is being either disrupted or restored. Our definition of azimuthal WN transfer is thus comforted as it is indeed a measurement of persistent changes through the inner-core. Moreover, eyewall signals (shape and gradient) appeared more sensitive to intensity variations than the maximum wind area, and in particular than the RMW. This highlights the specificity of the eyewall area as being the most sensitive area of the vortex, as any perturbation can cause vorticity mixing, impact the eyewall convection's stability and, subsequently, lead to the generation of VRWs that eventually allow intensity restoration.

All these observations indicate that including internal structure variations quantified through azimuthal WN transfer and homogenization might have a positive impact on TC intensity forecasts. To further assess this impact, we used an empirical machine learning framework to estimate the individual contribution of these variables and the other internal structure descriptors to the dissociation of TCs given the sign of $\partial_t(V_{MAX})$ and $\partial_t^2(V_{MAX})$.

We showed that both classifications are improved when using time evolution of the TC internal structure, notably thanks to $Vmax_{AZ}$, $dV/dR_{AZ}$, and $ES_{AZ}$ WNTs Moreover, the classification was shown to be very sensitive to the smoothing applied to the $V_{MAX}$ time serie to compute its variations, showing a more notable importance of the eyewall radial gradient at shorter time scales (under 6h), while the maximum wind distribution was more predominant at larger scales (12, and 18h).

Although we showed that our description of the internal structure has the potential to improve predictability through case studies, statistical comparisons, and classification score improvement, we did not truly assess the predictability of the life cycle. Indeed, our classification did not evaluate the future intensity changes, and did not include all the parameters usually used to predict TC life cycle, notably environmental parameters such as vertical wind shear, ocean surface temperature or atmospheric humidity (DeMaria, Knaff, and Sampson, 2007; DeMaria et al., 2014; Kaplan et al., 2015; Neetu et al., 2017; Neetu et al., 2020). An interesting perspective would thus to use our newly developed TC internal structure evolution descriptors as additional inputs of usual statistical forecast models. In an operational forecast perspective, it could also be interesting to compute these descriptors from real-time observations (such as SAR for instance, supposing a sufficient time continuity), or operational forecast models, and use them as a likelihood index for TC intensity restoration or decline, for instance.

### 4.5.2 Model setup limitations

#### Resolution

The spatial resolution of 1km might clearly be a factor preventing TC intensification at high categories, as several studies have shown that the spatial resolution can cause large differences in the simulated maximum intensity (Fierro et al., 2009; Gentry and Lackmann, 2010; Gopalakrishnan et al., 2011; Gopalakrishnan et al., 2012). For instance, Gopalakrishnan et al., 2011 show that a change of resolution from 9km to 3km can cause a difference in maximum intensity of $10 m.s^{-1}$. A spatial resolution of 1km means an effective resolution of approximately 5km, which means small-scale features and eyewall radial gradients are not totally resolved.

### Parameterizations

The set of parameterizations chosen to solve sub-grid processes, while widely used for TC simulations (Lengaigne et al., 2019; Hill, Lackmann, and Aiyyer, 2008), can also impact the maximum intensity, and the ability of the TC to intensify, in particular the Planetary Boundary Layer (Nolan, Zhang, and Stern, 2009; Nolan, Stern, and Zhang, 2009b; Smith and Thomsen, 2010; Kepert, 2012; Zhang et al., 2015), and microphysics (Zhu and Zhang, 2006; Park et al., 2020) schemes. The cumulus convection parameterization, which is a quite sensitive one in TC cases (Rao and Prasad, 2007; Raju, Potty, and Mohanty, 2011; Srinivas et al., 2013), only impacts the large domain, as convection is explicitly solved in the nested domains.

### Forcing conditions

The data used to initialize the model, force the boundary conditions, and spectrally nudge the synoptic flow in the parent domain can also impact the simulated TC evolutions. If they feature errors in the synoptic evolution, these errors will be transmitted to the simulations. Additionally, another impact of spectral nudging was identified in our simulations. While spectral nudging was applied only on the large domain, and only on the large wavelengths of the domain, i.e. synoptic scale, to avoid directly impacting the TC internal dynamics, it is shown to causes little curls in the TC track of a few simulations (CEBILE and FANI, cf. Fig. 4.3). These track curls appear as unrealistic as they do not appear in any of the real tracks, and seem to be a track response to the nudging. They may have an impact on the internal TC evolution, though, we assume that they are not impacting the consistence of the vortex's evolution with intensity variations.

All these aspects of the simulation set up can cause issues in the representativeness of our dataset. We notably observed a lower variability of the maximum wind contour, and weaker radial gradients for very high wind speeds, indicating the modeled surface wind field is smoother than SAR observations, and thus features less small-scale internal activity. Moreover, TC intensification can be conditioned by these eyewall dynamics: according to Kossin and Eastin, 2001, the structure of the eyewall profile and the alternation of phases of strong vorticity mixing, and phases of sharper profile and clearer eye are an important process in the formation and intensification of TCs, partly conditioning their ability to reach high intensity. An inaccurate representation of these processes may thus partly explain the lower intensity of simulated TCs compared to observations. On the other hand, we also saw that the spatial variability was well featured, that most dynamical processes were well-represented for TCs up to cat. 4, and that the distribution of life cycle variations (i.e. values of intensification rate) in our simulations was coherent with observational datasets, which are the main focus of this paper. Thus, although our interpretation is limited and might be incomplete for very high intensities, we can rely on a realistic dynamical behaviour of our simulated TCs, and on realistic interactions between their internal structure and intensity variations.

### Perspectives within the designed framework

While we use 3D realistic simulations, the presented analyses rely on a specific framework notably designed to allow a direct comparison with SAR observations. The TC vortex description is thus limited to the surface wind field, and more specifically to a subset of radial and azimuthal descriptors of the vortex, so that our results and methods are applicable to SAR observations, or to any other observational source providing surface wind fields. Each of these descriptors characterizes an aspect of TC dynamics. The eyewall radial gradient compared to Rankine ideal vortex is a proxy for vorticity mixing in the eye, and is related to the generation of mesovortices. The near-core gradient is related to the primary circulation broadness, and thus to the vortex resilience to shear and propension to intensify. Azimuthal transfers measure the homogenization of the internal structure and are thus tightly connected to restoration processes such as eyewall mesovortices and Vortex Rossby Waves that impact the vortex's symmetry and spectral decomposition. However, this synthetic view does not capture the whole complexity of the vortex's internal activity: this activity is a continuous succession of interactions going through the vortex's vertical and horizontal structure (cf. radial and vertical propagation of VRWs (Montgomery and Kallenbach, 1997; Wang, 2002a; Wang, 2002b), or importance of convective bursts and eyewall updrafts in rapid intensifications (Chen and Zhang, 2013; Hazelton, Hart, and Rogers, 2017; Zheng et al., 2020)). Applying similar analyses to those performed here on the surface wind to different vertical levels could certainly bring interesting insights, and an estimation of the relative importance of the Boundary Layer with respect to the rest of the vertical structure. Studying other output fields such as potential vorticity, precipitation, or vertical wind speed for instance, could also provide a more direct connection to convection or VRWs propagation (Wang, 2002a; Wang, 2002b). Both these perspectives could also suggest a synergetic use of observations from various sensors to provide various parameters and at several vertical levels.

Chapter 5

# CONCLUSION AND PERSPECTIVES

## 5.1 Summary

### 5.1.1 An original framework

In recent years, an important effort was made by the TC community to apprehend the dynamics controlling TC intensity, motivated by the lack of performance of TC intensity forecasts and the still important casualties that TCs cause every season. With the improvement of observational and modeling technologies came a new theoretical framework, focused notably on TC internal energetic processes and asymmetric features. The aggregation and merging of VHTs and vorticity anomalies and the resulting upscale cascade of cyclonic vorticity; their dissipation through VRWs propagation and the subsequent axisymmetrization and intensification or restoration of intensity; the implications of these asymmetric processes on the mean vortex's structure (resilience to shear) and fundamental dynamics (i.e. BL dynamics and wind spin-up process): all these features contribute to build a comprehensive view of the TC vortex as a coherent energetic system whose intensity and lifecycle are driven by internal processes. In this context, I used recently gathered SAR surface wind speed observations along with dynamical simulations performed with the WRF model to carry out a statistical study of TC surface wind field properties. Parameters were extracted to measure, on one hand, the asymmetric structure of the vortex and its evolution in time, drawing links with axisymmetrization processes and vorticity anomalies in the inner-core and eyewall. On the other hand, the symmetric structure was also studied to approximate vortex parameters such as eyewall vorticity mixing and baroctropic instabilities, and vortex resilience in the near-core area. These parameters were then related to intensity changes, with specific metrics defined to characterize several time scales of intensity modulations and life cycle phases.

### High-resolution observations of the TC surface wind field

The observational dataset is composed of 200 SAR-derived ocean surface wind fields with a spatial resolution of 1km resampled on a 3km grid, and an extent between 200 and 400km encompassing the whole vortex inner-core. Wind speed inversion is based on an algorithm combining the dual-polarization modes available with recent SAR missions (Mouche et al., 2017). These measurements have proven to be reliable and efficient to measure very high wind speeds in previous studies compared to airborne measurements, and best-track datasets (Combot et al., 2020). While these studies mostly focus on best-track typical parameters such as maximum wind, RMW, or 34-knot radius, I used the SAR wind fields to study finer-scale properties: radial gradients extracted from the radial wind profile ; and spectral decompositions of azimuthal distributions of eye shape, eye-eyewall surface wind gradient, and maximum wind. Each of these descriptors is related to a specific aspect of asymmetric theories on TC intensification and intensity variations: the vortex resilience to external shear depends on the radial gradient of vorticity and can thus be approximated through the slope of the radial wind profile outside the RMW; the development and propagation of eyewall mesovortices is observable as eye shape asymmetries, and the subsequent barotropic instabilities and vorticity mixing between the eye and the eyewall impact the radial gradient of the wind profile in this region; finally the propagation of Vortex Rossby Waves (VRWs) acting to axisymmetrize the vortex impacts the azimuthal wind distribution and sign as specific discrete wave numbers. To achieve this characterization of the TC, an important part of my work consisted in properly defining and estimating these parameters with a robust method (i.e. independent from artifacts or specific features of SAR acquisitions) suited for a statistical analysis. Original algorithms were developed in order to:

- retrieve TC center position from each image
- extract radial profile and characteristic azimuthal signals i.e. eye shape, maximum wind, radius of maximum wind and eyewall radial wind gradient distributions
- process and filter these signals to ignore artifacts and outliers caused by partially missed eyes, rain features, local wind anomalies, or double eyewalls.
- define synthetic parameters characterizing various aspects of the internal structure as described by the asymmetric theory: mean surface wind radial gradients, profile curvature in the eyewall and near-core areas, wave number decompositions or variances of azimuthal signals.

These analyses provided a unified SAR database of 200 samples, and 40 descriptive variables.

### High-resolution TC simulations

A modeling framework was designed to complement SAR analyses by providing a TC life cycle time continuity. The comparison of SAR and model also allows to evaluate the ability of high-resolution dynamical models to feature the variability and complexity of the internal structure compared to high-resolution 2D measurements. I used the WRF-ARW dynamical solver, which is extensively used in both TC research and forecasting communities, to simulate TC events in their mature life cycle phase. Seven TCs were simulated, chosen to feature all basins, and several configurations of life cycle: short ones with intensification, peak and decline, and more complex ones with re-intensifications, and several peaks of intensity. As the goal was to draw direct comparisons with SAR observations, I chose a fine resolution of 1km, which allows to reach an effective resolution of 5km, a reasonable compromise between computation time and comparability with SAR. To achieve this high-resolution, simulations were run with two successive vortex-following nests at respectively 3 and 1 km resolution, in a larger domain with a 9km resolution encompassing the whole TC trajectory. I processed model outputs similarly to SAR images, that is focusing on the surface wind field (taken as the 10-m wind speed in the model), and I extracted the same radial and azimuthal descriptors as defined for SAR. To exploit the time continuity of the model, I computed time derivatives of these descriptors, and defined new variables describing the evolution of the internal structure in time. In particular, I defined transfers in the spectral distribution of azimuthal signals, as the transfer of explained variance between low wave numbers (1,2) to high ones (6 to 180). These transfers can be interpreted as variations of the energetic distribution in the azimuthal dimension: they quantify the homogenization of the TC's azimuthal structure in time, and the changes in the vortex asymmetry degree. Such joint framework combining observations and simulations is very valuable in the context of TC research, as it allows a direct comparison of both sources. It also allows to assess the improvements that would be allowed by continuous SAR measurements, as hourly outputs simulate regular acquisitions.

### Machine learning classification

The joint statistical study of WRF and SAR datasets was complemented by an original machine learning classification method, designed to estimate the individual contributions of internal structure parameters to the dissociation of intensity variations, either through the value of intensification rate (i.e. separating phases of intensification and decline) or intensity time serie second derivative (i.e. separating phases of increasing intensification rates from decreasing ones, not applied to SAR due to insufficient time continuity). This method was used to assess the connection of surface wind field predictors with intensity changes, their characteristic time scale, and thus their potential for intensity predictability.

### 5.1.2 Description of internal structure

The mature TC evolution is very complex as it is highly multi-scale, linking large-scale synoptical events to kilometric features, air-sea interactions, and processes in the TC's inner-core. As SAR images only describe the sea surface wind field, and as their major asset is their high resolution and coverage, my goal was to capture the complexity of kilometer to vortex-scale inner-core processes through this partial view of the TC. The parameters extracted from SAR and WRF surface wind fields were thus designed in priority to:

- characterize or be related to processes involved in the regulation of TC intensity;
- synthesize through single value parameters the TC radial and azimuthal structure of the surface wind field to enable the use of these parameters in a statistical model
- be generically and automatically estimable, with a minimal dependence on SAR individual image artifacts such as rain impact, double eyewalls, image border, etc. Double eyewalls, outer rainbands and other features that are associated to specific events or not systematically measurable on all images were thus ignored.

#### Radial structure

The mean radial profile was used to retrieve the radius of maximum winds (RMW), and mean gradients in the eyewall (R<RMW), and in the near-core (RMW<R<3*RMW) areas. RMW and mean gradients provide a first order characterization of the vortex. The RMW, i.e. the size of the vortex, is a purely symmetric parameter, responding to intensification with a contraction due to increasing baroclinicity and inertial stability (Shapiro and Willoughby, 1982). In contrast, the radial profile in the near-core denotes the propagation and damping of VRWs: the broader the profile is, the more resilient the vortex is to external shear, the better it realigns after a perturbation and restores its intensity (Reasor, Montgomery, and Grasso, 2004; Mallen, Montgomery, and Wang, 2005). In the eye-eyewall area, the slope of the wind profile denotes the degree barotropic instability and vorticity mixing of the eyewall: according to Kossin and Eastin, 2001 and Nguyen et al., 2011, a vortex with a U-shaped profile in the eye-eyewall area is more likely to intensify than a linear one.

The analysis of SAR-extracted mean radial profiles by category showed the expected decrease in RMW with intensity with a log-normal trend. A clear sharpening of the eyewall mean profile was also observed, with a trend towards U-shaped profiles at high intensity indicating lower vorticity mixing (consistent with the higher frontogenesis associated with increased eyewall convection (Emanuel, 1997)), although the asymmetric regime with a linear profile (Nguyen et al., 2011) can also be observed even at highest intensity. The near-core profile was also observed to sharpen with intensity with a slightly superlinear trend: normalized with $V_{MAX}$, intense TC profiles are thus sharper than weak TCs profiles in the near-core. According to the theory of vortex resilience (Reasor, Montgomery, and Grasso, 2004), this indicates relative lower resilience of intense TCs: indeed, a sharper profile means a faster decreasing PV profile, and a higher likelihood of a positive PV gradient at the critical radius, which is the condition for a growing tilt asymmetry (Mallen, Montgomery, and Wang, 2005). This might also indicate a reduced VRW activity at high intensity, suggesting the vortex's stability is ensured by more symmetric processes as intensity increases (which was also suggested by Nguyen et al., 2011).

The radial wind profile was also studied with respect to intensity variations: intensifying TCs showed higher gradients on average both in the eyewall, and in the near-core areas. A sharper eyewall associated preferably to intensifying TCs is consistent with the symmetric phase described by Nguyen et al., 2011. On the other hand, larger values of near-core gradient, i.e. thinner radial profile outside the RMW, suggests a trend of lower resilience to external shear for intensifying TCs.

These observations can thus be summarized as follows: the more intense and/or intensifying the TC, the smaller and thinner its eyewall, the lower the vorticity mixing between the eye and eyewall. While the lower mixing indicates a lower generation of mesovortices and subsequent lower VRW activity, the thinner eyewall points at both a lower barotropic stability (Schubert et al., 1999) and lower resilience to external shear (Reasor, Montgomery, and Grasso, 2004). This suggests a kind of negative feedback process in which a TC that intensifies becomes more and more able to intensify (as lower voticity mixing goes with an annular vorticity structure and maximum wind occurring closer to the RMW (Nguyen et al., 2011)), while in the same time becoming more vulnerable to external shear and thus more susceptible to undergo perturbations (due to its thinner eyewall vorticity ring and lower resilience to external shear). Similarly, a declining TC, although less susceptible to intensify due to the higher mixing between its eye and eyewall, is more resilient to external shear and thus develops an internal VRW activity that is more likely to allow its axisymmetrization and its return to a symmetric phase with a U-shaped profile (as observed by Nguyen et al., 2011).

The radial profiles extracted from WRF outputs showed similar results, but with an increase in radial gradients that remained significantly limited above category 3. This may have several causes: 1) the horizontal resolution, which is effectively  5km still limiting the resolution of very sharp, and fine-scale gradients, 2) the limits due to parameterizations (the full BL dynamics representation may be questioned, as well as the role of surface fluxes and microphysics schemes), 3) the dataset was limited to a small number of TCs, and thus could not encompass the full variety of possible cases (chosen cases might not be the most favorable to strongest TCs, and were constrained by the initial and boundary conditions provided by a lower resolution global model).

Besides these limitations, both SAR and WRF datasets evidenced that properties of the mean radial profile are structural properties of the vortex that are related to TC intensity and its variations, which indicates their importance as a diagnostic of the vortex's internal structure. The defined near-core and eyewall gradients reflect, in a sense, the symmetric part of the asymmetric theory on TC intensification, approximating both energetic propagation and damping of VRWs in the near-core (Reasor, Montgomery, and Grasso, 2004), and generation of mesovortices and VHTs in the eyewall that cause vorticity mixing (Kossin and Eastin, 2001).

### Asymmetry and azimuthal variability

The degree of asymmetry, described in this work through the variance of azimuthal distributions of the eye shape, the eyewall radial gradient, the maximum wind, and the RMW, shows a strong dependence on intensity, noted both on SAR and WRF estimates. As for the sharpness of the mean radial profile, the degree of symmetry of the vortex is observed as primarily connected to TC intensity magnitude, in agreement with previous studies relating vortex symmetry to its internal stability (and thus to its intensity). In addition to these first order evidences, a finer analysis of the azimuthal structure was carried out through spectral decompositions of extracted azimuthal signals. The computation of wave number explained variances allows to separate dynamical scales, as low wave numbers characterize vortex-scale distortions mostly linked to external forcings (Beta-drift, external shear), or strong internal perturbations such as VRWs or asymmetric rain bands, while higher wave numbers contain more local and short timescale asymmetries (such as eyewall mesovortices or VHTs for instance), and generally assess the degree of homogeneity and disruption (more energy in high WNs means broader spectrum, i.e. more homogeneous energy distribution) inside the structure.

SAR observations revealed that the energy distribution in the maximum wind ring tends to homogenize with intensity (through decrease of low WN explained variance, and increase of middle and high WNs), while the distribution of eyewall radial gradient (approximate eyewall mixing) does not depend on it, indicating a decoupling between the maximum wind and eyewall areas. The gradual fueling of middle and high WNs at the expense of low WNs with intensity indicates an increasing role of internal processes, with an increased generation of VRWs and mesovortices but, in the same time, a lower importance of strong persistent VRWs, and a more homogeneous structure, consistent with the fact that intensity restoration in major TCs is also monitored by other processes such as eyewall replacement cycles (ERCs).

The characterization of azimuthal structure variability thus appeared as a diagnostic of the vortex dynamical behavior and internal activity. This aspect was also highlighted by the strong contribution of eye shape and eyewall radial gradient wave numbers 4-5 explained variances in the machine learning classification applied to dissociate intensification rates with SAR-extracted parameters.

### 5.1.3 Dynamics and predictability

The description of the internal structure provided by SAR observations and WRF outputs was evidenced to be related to the magnitude of intensity and to the ongoing intensity variations: the radial structure summarizes the symmetric aspects of VRW propagation and eye-eyewall mixing, while the azimuthal structure is a more instantaneous measurement of the asymmetry and thus of ongoing axisymmetrization processes in the maximum wind area and mesovortices generation in the eyewall. One exciting objective was thus to evaluate the potential of our surface wind field descriptors in providing relevant information for understanding, and predicting TC intensity fluctuations, in the context of asymmetric theory that links the internal transport and dissipation of energy from the eyewall to outside the RMW, to intensity of the vortex and its external interactions. SAR acquisitions being snapshots, with a relatively sparse sampling, they do not allow for a continuous monitoring of each TC evolution, and prevent estimating the short-range dynamical changes in the internal structure. Two tools were therefore used to cope with this limitation: 1) the WRF simulations, which provide a temporal continuous evolution (every 1h) of the simulated cases, 2) a machine-learning statistical classification of positive (>+5m.s-1.day-1) and negative (<-5m.s-1.day-1) intensification rates, which in the case of SAR are thus estimated from external best-track files.

WRF surface wind fields provided further insights into the dynamical control of the internal surface-level structure on the vortex's intensity. The various extracted parameters were shown to describe different time scales of TC internal changes. Radial gradients are linked to longer time-scale intensity variations than radially localized azimuthal asymmetry, which is quite logical given the larger spatial scale described by radial signals (they have a larger radial extent than azimuthal signals which describe only one specific radius for each azimuth) and their averaged (i.e. symmetric) nature. Azimuthal spectrum energy transfers describing the time evolution of azimuthal homogeneity in the eyewall and maximum wind area showed a higher connection with intensity short-scale modulations, both on statistical mean values and on case studies, than radial gradients. Positive transfers (from low to high WNs, i.e. spectral broadening and azimuthal symmetrization) were found to be on average associated with phases of intensification and/or increasing intensification rate, while the opposite trend was observed for negative transfers. This is consistent with the axisymmetrization theory (Montgomery and Kallenbach, 1997): intensity restoration indeed occurs through a re-distribution of localized vorticity anomalies present in the eyewall (i.e. VHTs, and eyewall mesovortices) by VRWs that propagate outward and act to axisymmetrize the vortex. Thus, while the declining TC is characterized by the generation and growth of asymmetry inside the structure (i.e. fueling of low-WN asymmetries), intensification and re-intensification are characterized by an axisymmetrizing structure (i.e. fueling of high WNs and dissipation of low-WN asymmetries). The connection noted between azimuthal WN transfers and the intensity second derivative (which characterizes fluctuations in the intensification rate such as re-intensifications for instance, instead of just intensifications/declines) confirms this interpretation and the capacity of SAR and WRF surface wind fields parameters to assess the ongoing internal axisymmetrization/asymmetrization processes on a short scale (around 6-12$\sim$h). This suggested that such energy transfers may be interesting predictors for short-range intensity changes.

To evaluate the predictability potential of all the extracted parameters characterizing the vortex (intensity, size, radial profiles, azimuthal degree of asymmetry, and energy distribution) on both SAR and WRF datasets, a machine learning classification was performed to separate intensifying and weakening TCs, and the scores were compared to evaluate the added value of the various parameters. SAR classification showed that eye shape, and eyewall radial gradient wave numbers 4-5 explained variances notably improve the classification, indicating their connection to the TC intensification regime. This spectral band was associated in the literature to the formation of mesovortices (Schubert et al., 1999), VRWs propagation (Schubert et al., 1999; Wang, 2002a), and rain bands (Judt, Chen, and Berner, 2016). WRF classification implemented spectral transfers and derivatives of radial profile gradients, and also showed consistent improvements of all scores thanks to these temporal internal structure predictors. Thanks to the better time continuity and coherence with internal structure provided by the model (as it is not necessary to add external best-track data that generate additional uncertainty), the classification was also performed on groups of intensity second derivative (i.e. separating increasing and decreasing intensification rates). Sensitivity tests were also performed on the values of temporal smoothing applied to intensity, enabling a comparison of characteristic time scales of the different predictors. These sensitivity tests revealed a larger importance of the eyewall (maximum wind) area at shorter (longer) time-scales. The classification improvements accounted both for intensification rate and intensity second derivative point at the importance of studying, and observing these small-scale (high wavenumber) events in the eyewall and maximum wind region. These suggestions are completely consistent with the rotating-convection paradigm and the new BL spin-up mechanism (Smith, Montgomery, and Van Sang, 2009; Montgomery and Smith, 2010), which consider the aggregation of asymmetric vorticity anomalies in the eyewall as the driving mechanism for BL spin-up during TC intensification and the BL spinup itself to be the driver for eyewall spinup above the BL (i.e. vortex intensity). Our results even suggest that surface-level asymmetric measurements near the eyewall are also of importance in the mature phase of the TC and not only in its intensification phase, supporting the hypothesis of a unified theory for the TC's life cycle including genesis, intensification and mature state under a same context of energetic internal distribution and upscale/downscale transfers modulating its intensification and declines.

Overall, the connections noted between intensity changes and internal modifications of the radial and azimuthal structure provide support for the recent theories on TC intensification based on an asymmetric view of the TC and on internal energy propagation and dissipation as the driving mechanism of TC intensity changes (Montgomery and Kallenbach, 1997; Reasor, Montgomery, and Grasso, 2004; Smith, Montgomery, and Van Sang, 2009; Montgomery and Smith, 2010; Montgomery and Smith, 2014). The accounted improvement of classification scores in statistical models dissociating intensifications and declines moreover advocates for the inclusion of such diagnoses into currently used statistical-dynamical models. These models indeed only include environmental variables (atmospheric humidity and temperature, vertical shear...) along with mean vortex parameters (intensity and size, translation speed and intensification rate mostly) with no consideration of fine-scale and asymmetric structures. Our analyses also emphasize the importance of high resolution, as azimuthal transfers, which appear as major contributors to score improvements, characterize the whole azimuthal spectrum (from kilometer to vortex-scale) and require the resolution of high wind gradients in the eyewall and maximum wind areas. These results thus have implications for TC forecast operational strategies, as well as for the future strategies of TC observations: the need for regular, and frequent observations of TC boundary layer winds at high resolution should be considered of great interest in the perspective of a better understanding and forecasting of TC intensity. This original work gathering observations, and simulations brings a consistent framework for studying TC internal structure. Though many of its aspects and limitations were analyzed throughout the discussions of the previous chapters, it also raises awareness on several areas of improvement and future perspectives, that are presented hereafter.

## 5.2 Applications and Perspectives

### 5.2.1 Applications

#### A new parametric profile

An application of SAR radial profile analyses could be the development of a new parametric wind profile. Parametric profiles are extensively used for storm waves and surge forecasts, as they allow to rapidly represent a forcing wind field with only few parameters such as maximum intensity and size, that are usually available from TC forecast agencies. The realism of these profiles is however regularly questioned and improved. For instance, Olfateh et al., 2017 proposed an implementation of TC asymmetry, Emanuel et al., 2004; Emanuel and Rotunno, 2011; Chavas, Lin, and Emanuel, 2015 developed theory on the properties of the radial profile to get rid of empirical formulations. Although this theory

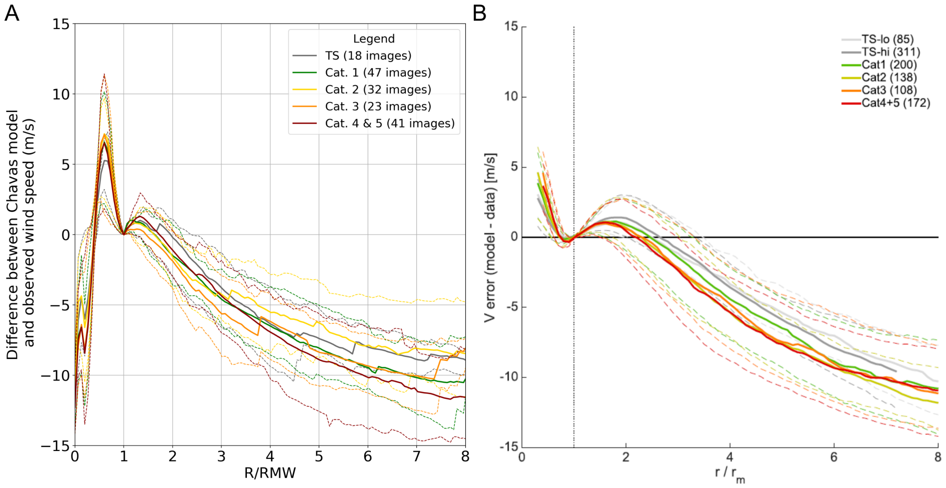

Figure 5.1 – (A) Reproduction of Fig. 8 from Chavas, Lin, and Emanuel, 2015 shown on panel (B), using SAR observations instead of HWind reanalyses. The median of differences between the fitted ER11 model (Emanuel and Rotunno, 2011) and SAR-extracted mean radial profiles is featured on the y-axis as a function of normalized radius. Profiles are composited intensity categories, with quartiles of each composite denoted by dashed lines

has notable inconsistencies (Montgomery, Persing, and Smith, 2019), the attempt made by Chavas, Lin, and Emanuel, 2015 to transcribe a theory for hurricane dynamics into a parametric radial profile allows, unlike other usual profiles, to discuss the underlying TC dynamics. Following our comparison of SAR-extracted profiles to the Rankine vortex idealized model, I reproduced the analysis of Chavas, Lin, and Emanuel, 2015 (cf. the reproduction and comparison with their fig. 8 showed on fig. 5.1), which compared the ER11 (Emanuel and Rotunno, 2011) model profiles to WindSAT averaged wind profiles. ER11 profiles are obtained by fitting the ER11 model parameters (i.e. $C_K/C_D$) to the observed data. This is done by minimizing RMSEs for different values of the ER11 profile parameters. Then comparison with the actual observed averaged profiles is performed, and the realism of the model profile in the inner eyewall region can be discussed. In our case, the observed data are SAR mean radial profiles.

The differences observed between SAR and ER11 profiles, especially in the eyewall area, are larger than the ones observed by Chavas, Lin, and Emanuel, 2015. Although the reasons for these discrepancies were not furtherly investigated, it is very likely that a more thorough analysis of SAR-extracted mean profiles properties could provide guidance and material for an observation-based discussion of the ER11 model, based on their original study and the following critique by Montgomery, Persing, and Smith, 2019.

## TC predictability

### Distribution of a product to operational centers

The methods developed in this thesis could be adapted to create a new SAR product distributable to weather forecast centers. The TC center research method is generically processed by the algorithm, and yields precise values of the eye position on all SAR images. These could be used by meteorological centers to compare and correct other data thanks to this surface-level estimation with kilometer accuracy, when SAR images are available. Similarly, the retrieved $V_{MAX}$ and RMW, that were shown to be accurately estimated (Combot et al., 2020), could be included in best-track analyses. Fitted parametric profiles and smoothed vortex-centered wind fields (obtained by filtering high wave numbers from the polar wind field decomposition) could also be processed generically, and included in a new product, providing SAR estimated bulk vortices that could be assimilated by forecast models or merged in wind reanalyses to provide more realistic wind fields in TCs for ocean and wave model forcing (Vincent et al., 2012). The multiplication of SAR acquisitions under TCs could certainly generalize the distribution of such products, and provide useful material for both weather and climate forecasters.

### Including SAR-extracted parameters into statistical forecast models

The predictive potential of internal structure variables was investigated in the thesis through the development of a machine learning framework based on the dissociation of positive and negative intensification rates at the time of measurement. Such estimation is related to intensity predictability, as it assessed the importance of a predictor to discriminate intensity variations. It is however not comparable to statistical forecast models that evaluate the future intensity variations, and take into account all the available environmental and climatological conditions (such as vertical shear, MPI, tropospheric relative humidity and temperature, low-level equivalent potential temperature, low-level relative vorticity), as well as current intensity and intensification rate (Knaff, Sampson, and DeMaria, 2005; Knaff and Sampson, 2009; Neetu et al., 2017).

I suggest that including the SAR-extracted descriptors of the TC fine-scale structure into existing statistical models could potentially improve their forecast scores.

### 5.2.2 Improving our understanding of TC intensity changes

#### Advanced simulations of internal dynamics

One of the main perspectives that arise from the comparison of SAR and WRF is the improvement of model resolution. Indeed, I showed in chapter 4 that simulated TCs are generally smoother and do not manage to feature the strong gradients estimated with SAR. As discussed previously, the main reasons for this are the lower spatial resolution of the model, and potential inconsistencies in the representation of boundary layer dynamics. We saw that the resolution of 1km yields an effective resolution of 5km. Reaching a resolution comparable to SAR would thus request a grid resolution of approximately 200m. A good way to improve resolution without increasing the computational cost too much would be to reduce large domain size by focusing or smaller phases of the life cycle, and specific events such as re-intensifications or intensity peaks for instance.

Otherwise, the use of Large Eddy Simulations (LES) is also considered as a potential application, as they allow to simulate idealized or realistic TCs with a horizontal grid spacing of the order of 40m (Rotunno et al., 2009; Wu, Liu, and Li, 2018). As spatial resolution strongly impacts both the radial structure and the azimuthal variability (Gentry and Lackmann, 2010)), LES would certainly bring more realism both in the structure and in the life cycle of simulated TCs.

#### Vortex wave propagation assessment through 2D Fourier decompositions

The synthetic view of the vortex developed in this thesis described the wind field with a limited set of parameters computed on 1D signals, in given separated areas. To further study the propagation of waves across the vortex extent requires to consider the full 2D structure. 2D Fourier decompositions of the TC polar wind field are widely used for TC asymmetry and internal dynamics studies (Wang, 2002a; Wang, 2002b; Olfateh et al., 2017), notably to compute asymmetric wind fields as the wavenumber-1 component (Peng, Jeng, and Williams, 1999). They allow to study the radial distribution of asymmetry and intensity. The phase and power distributions of the different wave numbers throughout the radial extent of the vortex are of interest to study VRW propagation, as they propagate radially and thus sign in the radial structure of the vortex. I performed 2D Fourier decompositions on both SAR and WRF polar wind fields. An example for a SAR-derived wind field is shown on Fig. 5.2, and reveals interesting properties regarding the azimuthal continuity of wave number distributions. Our preliminary analysis indicates

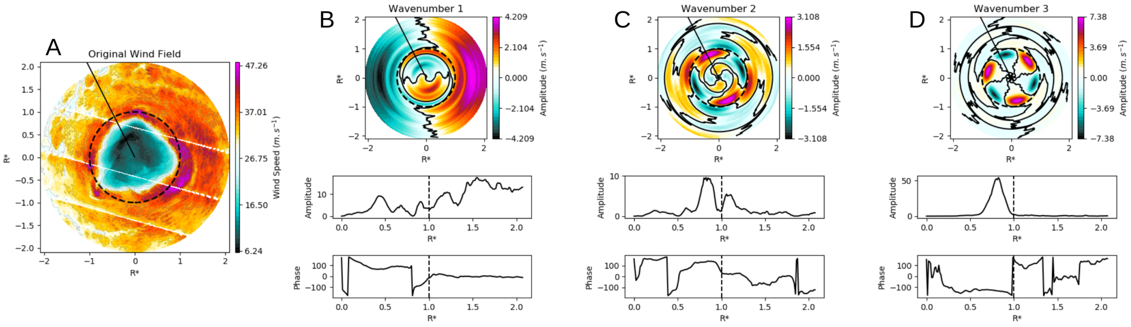

Figure 5.2 – 2D-Fourier decomposition of a SAR polar-projected wind field (acquisition on TC TRAMI (2018/09/28,09:35)). (A) Original wind field. (B) WN1 component 2D amplitude distribution, along with the radial distributions of amplitude and phase computed from the Fourier coefficients at each radius. (C) and (D): same as (B) for WNs 2 and 3. black line shows the TC direction (retrieved from IBTrACs) and dashed circle denotes the RMW position.

that in some cases, wave number asymmetries are continuous throughout the whole radial structure (such as the wavenumber-1 that is almost aligned beyond the RMW (Fig. 5.2B), while sometimes they experience several phase shifts between the vortex's center and its periphery (such as the wavenumber-2 which maximum has several phase shifts between the RMW and the periphery).

These parameters were not included in the analyses presented in my thesis to simplify the internal structure description. As a consequence, their relationship to the TC life cycle and their dynamical content was not investigated properly, but are considered as a great perspective for TC internal structure studies through SAR. Indeed, they are the only variables with the potential to describe a temporal evolution (i.e.signatures of radially propagating energy) through an instantaneous snapshot. Their study through SAR and WRF is a priority in my future studies, as they might enrich diagnoses used in this thesis.

### Vorticity estimates from SAR

Retrieving wind directions from SAR products is a current concern in the SAR community, and could bring interesting additional information to the measurement of internal structure and dynamics from SAR. Several projects are currently carried out in my lab to try to estimate wind directions from the wind streaks (i.e. signature of the organized large eddies in the marine atmospherique boundary layer on the small scales waves) extracted from SAR images. This estimation is not straightforward as wind streaks leave a 180°

ambiguity, and sometimes produce inconsistent estimations (notably in the case of rain signatures that distort the streaks in heavy rain bands). It thus has to be backed up by model-estimated directions. This yields many issues regarding the interpolation of these models on SAR wind fields, and the degree of realism and smoothing produced by this interpolation (as models used are much less resolved, and may have temporal lag with SAR data). Current attempts to estimate directions are focused on the development of optimal interpolation algorithms to set up the model arbitration, and on deep learning algorithms to estimate the directions automatically training on simulated fields with available directions. The implementation of wind directions would allow to compute the surface wind vorticity. This variable is very useful to describe internal processes, as it allows to directly spot convective structures, to study the intensity of convection in the eyewall (for instance to differentiate monopoles of vorticity from annular TCs which characterize different TC intensification regimes (Kossin and Eastin, 2001)), and to better estimate the propagation of internal waves such as VRWs which propagate along potential vorticity gradients, and thus disturb the symmetric surface vorticity field (Montgomery and Kallenbach, 1997; Wang, 2002a; Wang, 2002b).

#### Vertical structure

Although several perspectives exist to improve SAR images diagnoses and deliver a more complete estimation of internal structure dynamics, the SAR description of the TC is limited to the sea surface. This is a notable limitation, as intensity changes highly depend on its vertical structure, notably through the degree of eyewall tilt, the distribution of convection in the eyewall and maximum wind areas (cf. vortical hot towers that contribute to rapid intensifications (Montgomery et al., 2006; Guimond, Heymsfield, and Turk, 2010)), or the structure of inner and outer rain bands.

The properties of the vertical structure can be directly retrieved from WRF simulations, along with a wide range of other variables (precipitation, temperature, pressure, etc.). These variables would allow a much more complete description of the TC than the limited range of variables considered in this work, as performed in usual modeling studies.

The colocation of SAR with geostationnary visible or infrared images of the top of clouds TC structure, or with dropwindsondes and airborne dual-Doppler vertical cross sections, could certainly bring interesting insights into the connections between SAR-extracted surface properties and vortex vertical structure. An exciting perspective that could complement SAR measurements to bring a detailed description of the vertical struc-

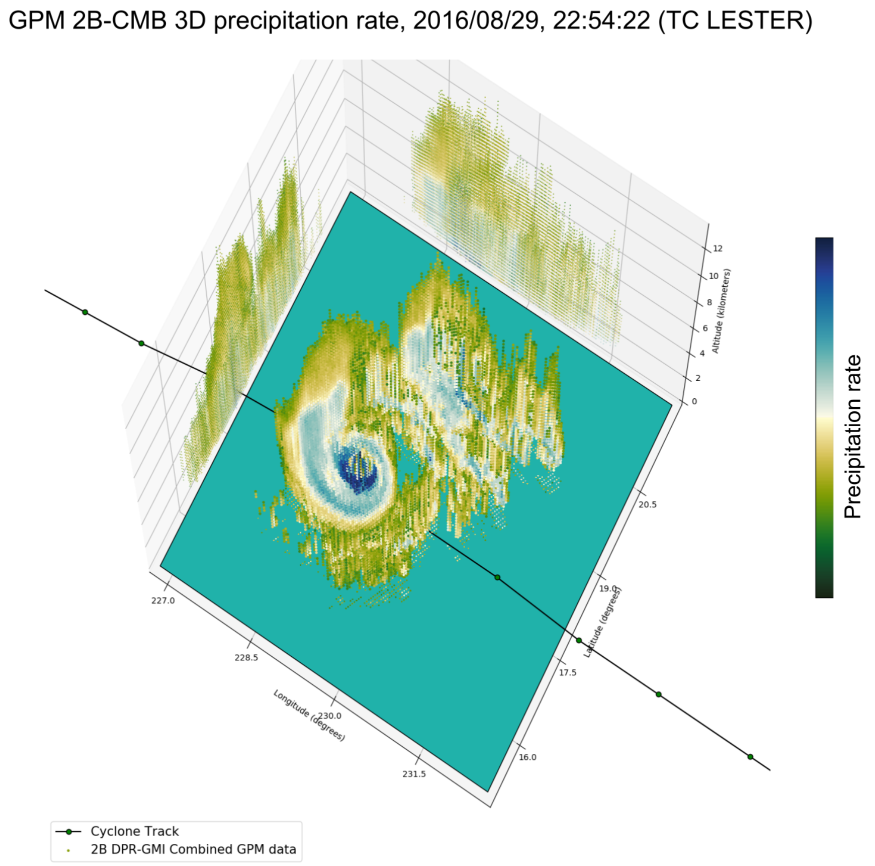

GPM 2B-CMB 3D precipitation rate, 2016/08/29, 22:54:22 (TC LESTER)

Figure 5.3 – Example of GPM 3D combined product: acquisition on TC LESTER (2016/08/29, 22:54:22)

ture is the implementation of measurements from the GPM 2B-CMB dataset (`https://disc.gsfc.nasa.gov/datasets/GPM_2BCMB_06/summary`), which provides estimates of surface rainfall and vertical precipitation on 3D grids with a resolution of 5km on the horizontal and 125 m on the vertical. Such data are extremely valuable as they compare to SAR in terms of resolution, and grant access to the vertical structure of the vortex in its whole instead of only vertical cross-sections that could be obtained from airborne dual-Doppler for instance. An example GPM combined product is shown on Fig. 5.3, showing an accurate description of the vertical TC structure through precipitation rate estimates. Although colocated acquisitions are not frequent as both SAR and GPM provide a sparse sampling of TCs, an effort of gathering SAR-GPM colocalized acquisitions is a perspective for a future investigation of small-scale TC internal structure under intensity changes.

The comparison of SAR with precipitation measurements such as GPM or, at a lower resolution, SSMI, would also be interesting for SAR processing and applications: indeed, many efforts are made throughout the SAR community to deal with rain signatures impacting the wind field. In the products used here, rain artifacts are spotted through the high local heterogeneity they generate: on most images, strong rain bands are visible on wind fields as they cause very strong localized gradients. However, their signature is not constantly the same, depending notably on the wind intensity: under high winds, rain will tend to attenuate the signal, whereas it will increase it under lower winds. Colocating SAR with surface precipitation measurements would thus bring insightful true estimates on the location of heavy rains, which would help correct the wind field. In a secondary step, it could also be used as a validation tool to estimate the topology of inner and outer rain bands from SAR: once the signatures are spotted, they can be related to rain and thus provide high-resolution estimates of the locations and properties of these rain bands.

### Boundary layer rolls and inflow angle measured from SAR

The very high resolution of SAR observations provides the ability to observe and study very fine-scale features of the TC. Several SAR studies have notably focused on the properties of Boundary Layer rolls (Katsaros et al., 2002; Morrison et al., 2005; Foster, 2005; Huang et al., 2018), which are kilometer wavelength coherent enhanced convective structures present at the sea surface, within which large wind speed variations (approx. 3-5 $m.s^{-1}$ according to Katsaros et al., 2002) can occur. These structures are poorly represented by current model parameterizations, and are suggested to have notable impacts for the representation of boundary layer enthalpy and momentum fluxes. Given the large database of SAR images gathered and studied here, a systematic assessment of BL rolls typical scale and properties (wave length, size, intensity) could be an interesting asset to my statistical analyses, and could certainly bring further insights to the pre-existing studies of their characteristics.

Another aspect of the BL dynamics which could benefit from future SAR wind direction retrievals is the computation of radial distributions of angular momentum and radial wind speed, which could be related to the extended spin-up theory proposed by Smith, Montgomery, and Van Sang, 2009. Indeed, they show that, if the convergence of the flow (i.e. radial wind speed) in the BL was faster than the loss of momentum due to surface friction during this convergence, the tangential wind defined as $V_t = \frac{M}{r} - \frac{1}{2}fr$ would increase with decreasing radius. Under these conditions, they show that wind spin-up occurs inside the BL and BL winds are supergradient, i.e. stronger than gradient winds located above the BL. The study of BL angular momentum and radial wind speed distributions, which presupposes a reliable estimation of wind directions and amplitude from SAR images, would thus enable one to determine from observations where and when the BL spin-up occurs (i.e. in which radial and azimuthal areas of the vortex, and during what phases of its life cycle), and in which conditions it is stronger/weaker, with great implications for the understanding of TC symmetric and asymmetric intensification and maximum intensity theories (Smith, Montgomery, and Vogl, 2008; Bryan and Rotunno, 2009).

# BIBLIOGRAPHY

Abarca, Sergio F and Kristen L Corbosiero (2011), « Secondary eyewall formation in WRF simulations of Hurricanes Rita and Katrina (2005) », *in*: *Geophys. Res. Lett.* 38.*7*.

Abarca, Sergio F and Michael T Montgomery (2013), « Essential dynamics of secondary eyewall formation », *in*: *J. Atmos. Sci.* 70.*10*, pp. 3216–3230.

Aberson, Sim D (2001), « The ensemble of tropical cyclone track forecasting models in the North Atlantic basin (1976–2000) », *in*: *Bulletin of the American Meteorological Society* 82.*9*, pp. 1895–1904.

Aberson, Sim D et al. (2006), « Thirty years of tropical cyclone research with the NOAA P-3 aircraft », *in*: *Bulletin of the American Meteorological Society* 87.*8*, pp. 1039–1056.

Ackerman, SA et al. (2019), « Satellites see the world's atmosphere », *in*: *Meteorological Monographs* 59, pp. 4–1.

Alvey III, George R, Jonathan Zawislak, and Edward Zipser (2015), « Precipitation properties observed during tropical cyclone intensity change », *in*: *Mon. Wea. Rev.* 143.*11*, pp. 4476–4492.

Andreas, Edgar L and Kerry A Emanuel (2001), « Effects of sea spray on tropical cyclone intensity », *in*: *Journal of the atmospheric sciences* 58.*24*, pp. 3741–3751.

Atlas, David (1994a), « Footprints of storms on the sea: A view from spaceborne synthetic aperture radar », *in*: *Journal of Geophysical Research: Oceans* 99.*C4*, pp. 7961–7969.

— (1994b), « Origin of storm footprints on the sea seen by synthetic aperture radar », *in*: *Science* 266.*5189*, pp. 1364–1366.

Bandeen, WR, V Kunde, and HP Thompson (1964), « TIROS III meteorological satellite radiation observations of a tropical hurricane », *in*: *Tellus* 16.*4*, pp. 481–502.

Bao, JW et al. (2000), « Numerical simulations of air–sea interaction under high wind conditions using a coupled model: A study of hurricane development », *in*: *Monthly Weather Review* 128.*7*, pp. 2190–2210.

Bell, Michael M and Michael T Montgomery (2019), « Mesoscale processes during the genesis of Hurricane Karl (2010) », *in*: *Journal of the Atmospheric Sciences* 76.*8*, pp. 2235–2255.

Bender, Morris A and Isaac Ginis (2000), « Real-case simulations of hurricane–ocean interaction using a high-resolution coupled model: Effects on hurricane intensity », *in*: *Mon. Wea. Rev.* 128.*4*, pp. 917–946.

Bender, Morris A et al. (2007), « The operational GFDL coupled hurricane–ocean prediction system and a summary of its performance », *in*: *Monthly Weather Review* 135.*12*, pp. 3965–3989.

Bentamy, Abderrahim, Denis Croize-Fillon, and C Perigaud (2008), « Characterization of ASCAT measurements based on buoy and QuikSCAT wind vector observations », *in*: *Ocean Science* 4.*4*, pp. 265–274.

Bhalachandran, Saiprasanth et al. (2019), « The relative importance of factors influencing tropical cyclone rapid intensity changes », *in*: *Geophysical Research Letters* 46.*4*, pp. 2282–2292.

Bister, Marja and Kerry A Emanuel (1998), « Dissipative heating and hurricane intensity », *in*: *Meteorology and Atmospheric Physics* 65.*3*, pp. 233–240.

Black, PG (1991), « The structure of an eyewall meso-vortex in Hurricane Hugo (1989) », *in*: *Preprints, 19th Conf. on Hurricanes and Tropical Meteorology, Miami, FL, Amer. Meteor. Soc., 1991*, pp. 579–582.

Braun, Scott A (2002), « A cloud-resolving simulation of Hurricane Bob (1991): Storm structure and eyewall buoyancy », *in*: *Monthly weather review* 130.*6*, pp. 1573–1592.

Braun, Scott A, Michael T Montgomery, and Zhaoxia Pu (2006), « High-resolution simulation of Hurricane Bonnie (1998). Part I: The organization of eyewall vertical motion », *in*: *Journal of the atmospheric sciences* 63.*1*, pp. 19–42.

Braun, Scott A and Liguang Wu (2007), « A numerical study of Hurricane Erin (2001). Part II: Shear and the organization of eyewall vertical motion », *in*: *Monthly weather review* 135.*4*, pp. 1179–1194.

Brunet, Gilbert and Michael T Montgomery (2002), « Vortex Rossby waves on smooth circular vortices: Part I. Theory », *in*: *Dyn. Atmos. Oceans* 35.*2*, pp. 153–177.

Bruyère, Cindy L, Greg J Holland, and Erin Towler (2012), « Investigating the use of a genesis potential index for tropical cyclones in the North Atlantic basin », *in*: *Journal of Climate* 25.*24*, pp. 8611–8626.

Bryan, George H and Richard Rotunno (2009), « Evaluation of an analytical model for the maximum intensity of tropical cyclones », *in*: *J. Atmos. Sci.* 66.*10*, pp. 3042–3060.

Camargo, Suzana J, Kerry A Emanuel, and Adam H Sobel (2007), « Use of a genesis potential index to diagnose ENSO effects on tropical cyclone genesis », *in*: *Journal of Climate* 20.*19*, pp. 4819–4834.

Camargo, Suzana J and Adam H Sobel (2005), « Western North Pacific tropical cyclone intensity and ENSO », *in*: *Journal of Climate* 18.*15*, pp. 2996–3006.

Cangialosi, John P and JL Franklin (2012), « National Hurricane Center forecast verification report », *in*: *NOAA National Hurricane Center Tech. Rep.*

— (2019), « National Hurricane Center forecast verification report », *in*: *NOAA National Hurricane Center Tech. Rep*, `http://www.nhc.noaa.gov/verification/pdfs/Verification_2014.pdf`.

Carnot, Sadi (1824), « Reflections on the motive power of fire, and on machines fitted to develop that power », *in*: *Paris: Bachelier* 108.

Carr, L. E. and Russell L. Elsberry (1990), « Observational Evidence for Predictions of Tropical Cyclone Propagation Relative to Environmental Steering », *in*: *J. Atmos. Sci.* 47.*4*, `https://doi.org/10.1175/1520-0469(1990)047<0542:OEFPOT>2.0.CO;2`, pp. 542–546.

Cha, Ting-Yu et al. (2020), « Polygonal eyewall asymmetries during the rapid intensification of Hurricane Michael (2018) », *in*: *Geophysical Research Letters* 47.*15*, e2020GL087919.

Chan, Johnny (Jan. 2005), « The physics of tropical cyclone motion », *in*: *Annu. Rev. Fluid Mech.* 37, pp. 99–128, DOI: `10.1146/annurev.fluid.37.061903.175702`.

Charney, Jule G. and Arnt Eliassen (1964), « On the Growth of the Hurricane Depression », *in*: *J. Atmos. Sci.* 21.*1*, `https://doi.org/10.1175/1520-0469(1964)021<0068:OTGOTH>2.0.CO;2`, pp. 68–75.

Chavas, Daniel R and Kerry Emanuel (2014), « Equilibrium tropical cyclone size in an idealized state of axisymmetric radiative–convective equilibrium », *in*: *J. Atmos. Sci.* 71.*5*, pp. 1663–1680.

Chavas, Daniel R, Ning Lin, and Kerry Emanuel (2015), « A model for the complete radial structure of the tropical cyclone wind field. Part I: Comparison with observed structure », *in*: *J. Atmos. Sci.* 72.*9*, pp. 3647–3662.

Chen, Hua and Da-Lin Zhang (2013), « On the rapid intensification of Hurricane Wilma (2005). Part II: Convective bursts and the upper-level warm core », *in*: *Journal of the Atmospheric Sciences* 70.*1*, pp. 146–162.

Chen, Rui, Weimin Zhang, and Xiang Wang (2020), « Machine learning in tropical cyclone forecast modeling: A review », *in*: *Atmosphere* 11.*7*, p. 676.

Chen, Shuyi S and William M Frank (1993), « A numerical study of the genesis of extratropical convective mesovortices. Part I: Evolution and dynamics », *in*: *Journal of Atmospheric Sciences* 50.*15*, pp. 2401–2426.

Chen, Yongsheng, Gilbert Brunet, and MK Yau (2003), « Spiral bands in a simulated hurricane. Part II: Wave activity diagnostics », *in*: *Journal of the atmospheric sciences* 60.*10*, pp. 1239–1256.

Chen, Yongsheng and MK Yau (2001), « Spiral bands in a simulated hurricane. Part I: Vortex Rossby wave verification », *in*: *Journal of the atmospheric sciences* 58.*15*, pp. 2128–2145.

Chou, Kun-Hsuan, Chun-Chieh Wu, and Shu-Zheng Lin (2013), « Assessment of the ASCAT wind error characteristics by global dropwindsonde observations », *in*: *Journal of Geophysical Research: Atmospheres* 118.*16*, pp. 9011–9021.

Chou, Kun-Hsuan et al. (2010), « Validation of QuikSCAT wind vectors by dropwindsonde data from Dropwindsonde Observations for Typhoon Surveillance Near the Taiwan Region (DOTSTAR) », *in*: *Journal of Geophysical Research: Atmospheres* 115.*D2*.

Combot, Clement et al. (2020), « Extensive High-Resolution Synthetic Aperture Radar (SAR) Data Analysis of Tropical Cyclones: Comparisons with SFMR Flights and Best Track », *in*: *Monthly Weather Review* 148.*11*, pp. 4545–4563.

Corbosiero, Kristen L and John Molinari (2002), « The effects of vertical wind shear on the distribution of convection in tropical cyclones », *in*: *Monthly Weather Review* 130.*8*, pp. 2110–2123.

— (2003), « The relationship between storm motion, vertical wind shear, and convective asymmetries in tropical cyclones », *in*: *J. Atmos. Sci.* 60.*2*, pp. 366–376.

Corbosiero, Kristen L et al. (2006), « The structure and evolution of Hurricane Elena (1985). Part II: Convective asymmetries and evidence for vortex Rossby waves », *in*: *Mon. Wea. Rev.* 134.*11*, pp. 3073–3091.

Croxford, Mark and Gary M Barnes (2002), « Inner core strength of Atlantic tropical cyclones », *in*: *Mon. Wea. Rev.* 130.*1*, pp. 127–139.

Davies, DA (1979), « Operational Techniques for Forecasting Tropical Cyclone Intensity and Movement », *in*: *WORLD WEATHER WATCH WMO TROPICAL CYCLONE PROJECT SUB-PROJECT No. 6 WMO-No. 528*.

Davis, Christopher A (2015), « The formation of moist vortices and tropical cyclones in idealized simulations », *in*: *Journal of the Atmospheric Sciences* 72.*9*, pp. 3499–3516.

Delden, Aarnout van (1989), « On the deepening and filling of balanced cyclones by diabatic heating », *in*: *Meteorology and Atmospheric Physics* 41.*3*, pp. 127–145.

DeMaria, M, JA Knaff, and C Sampson (2007), « Evaluation of long-term trends in tropical cyclone intensity forecasts », *in*: *Meteorology and Atmospheric Physics* 97.*1*, pp. 19–28.

DeMaria, Mark (1985), « Tropical Cyclone Motion in a Nondivergent Barotropic Model », *in*: *Mon. Wea. Rev.* 113.*7*, `https://doi.org/10.1175/1520-0493(1985)113<1199:TCMIAN>2.0.CO;2`, pp. 1199–1210.

DeMaria, Mark and John Kaplan (1994), « A statistical hurricane intensity prediction scheme (SHIPS) for the Atlantic basin », *in*: *Wea. Forecasting* 9.*2*, pp. 209–220.

— (1999), « An updated statistical hurricane intensity prediction scheme (SHIPS) for the Atlantic and eastern North Pacific basins », *in*: *Wea. Forecasting* 14.*3*, pp. 326–337.

DeMaria, Mark, John A Knaff, and Bernadette H Connell (2001), « A tropical cyclone genesis parameter for the tropical Atlantic », *in*: *Weather and Forecasting* 16.*2*, pp. 219–233.

DeMaria, Mark et al. (2014), « Is tropical cyclone intensity guidance improving? », *in*: *Bulletin of the American Meteorological Society* 95.*3*, pp. 387–398.

Donelan, MA et al. (2004), « On the limiting aerodynamic roughness of the ocean in very strong winds », *in*: *Geophys. Res. Lett.* 31.*18*.

Du, Yong and Paris W Vachon (2003), « Characterization of hurricane eyes in RADARSAT-1 images with wavelet analysis », *in*: *Canadian JOURNAL of Remote Sensing* 29.*4*, pp. 491–498.

Duan, Boheng et al. (2017), « Assimilation of typhoon wind field retrieved from scatterometer and SAR based on the Huber norm quality control », *in*: *Remote Sensing* 9.*10*, p. 987.

Dunkerton, Timothy J, MT Montgomery, and Z Wang (2009), « Tropical cyclogenesis in a tropical wave critical layer: Easterly waves », *in*: *Atmospheric Chemistry and Physics* 9.*15*, pp. 5587–5646.

Dvorak, Vernon F (1975), « Tropical cyclone intensity analysis and forecasting from satellite imagery », *in*: *Mon. Wea. Rev.* 103.*5*, pp. 420–430.

Eliassen, Arnt and Magne Lystad (1977), « The Ekman layer of a circular vortex-A numerical and theoretical study », *in*: *Geophysica Norvegica* 31.*7*, pp. 1–16.

Elsberry, Russell L, Thomas S Fraim, and Robert N Trapnell Jr (1976), « A mixed layer model of the oceanic thermal response to hurricanes », *in*: *Journal of Geophysical Research* 81.*6*, pp. 1153–1162.

Elsberry, Russell L, Tara DB Lambert, and Mark A Boothe (2007), « Accuracy of Atlantic and eastern North Pacific tropical cyclone intensity forecast guidance », *in*: *Weather and Forecasting* 22.*4*, pp. 747–762.

Elsberry, Russell L et al. (1990), *ONR Tropical cyclone motion research initiative: Field experiment summary*, tech. rep., NAVAL POSTGRADUATE SCHOOL MONTEREY CA.

Elsberry, Russell L et al. (2013), « Advances in understanding and forecasting rapidly changing phenomena in tropical cyclones », *in*: *Tropical Cyclone Research and Review* 2.*1*, pp. 13–24.

Emanuel, Kerry (2010), « Tropical cyclone activity downscaled from NOAA-CIRES reanalysis, 1908–1958 », *in*: *Journal of Advances in Modeling Earth Systems* 2.*1*.

— (2017), « A fast intensity simulator for tropical cyclone risk analysis », *in*: *Natural hazards* 88.*2*, pp. 779–796.

— (2018), « 100 YEARs of progress in tropical cyclone research », *in*: *Meteor. Monogr.* 59, pp. 15–1.

Emanuel, Kerry and David Nolan (May 2004a), « Tropical cyclone activity and global climate », *in*: *Bulletin of the American Meteorological Society* 85.

Emanuel, Kerry and David S Nolan (2004b), « Tropical cyclone activity and the global climate system », *in*: *26th Conference on Hurricanes and Tropical Meteorolgy.*

Emanuel, Kerry and Richard Rotunno (2011), « Self-stratification of tropical cyclone outflow. Part I: Implications for storm structure », *in*: *J. Atmos. Sci.* 68.*10*, pp. 2236–2249.

Emanuel, Kerry and Fuqing Zhang (2016), « On the predictability and error sources of tropical cyclone intensity forecasts », *in*: *Journal of the Atmospheric Sciences* 73.*9*, pp. 3739–3747.

Emanuel, Kerry et al. (2004), « Environmental control of tropical cyclone intensity », *in*: *Journal of the atmospheric sciences* 61.*7*, pp. 843–858.

Emanuel, Kerry A. (1986), « An Air-Sea Interaction Theory for Tropical Cyclones. Part I: Steady-State Maintenance », *in*: *J. Atmos. Sci.* 43.*6*, `https://doi.org/10.1175/1520-0469(1986)043<0585:AASITF>2.0.CO;2`, pp. 585–605.

Emanuel, Kerry A. (1987), « The dependence of hurricane intensity on climate », *in*: *Nature* 326.*6112*, pp. 483–485, ISSN: 1476-4687, DOI: `https://doi.org/10.1038/326483a0`.

Emanuel, Kerry A (1988), « The maximum intensity of hurricanes », *in*: *Journal of the Atmospheric Sciences* 45.*7*, pp. 1143–1155.

Emanuel, Kerry A. (1991), « The Theory of Hurricanes », *in*: *Annu. Rev. Fluid Mech.* 23.*1*, `https://doi.org/10.1146/annurev.fl.23.010191.001143`, pp. 179–196.

Emanuel, Kerry A (1995), « The behavior of a simple hurricane model using a convective scheme based on subcloud-layer entropy equilibrium », *in*: *J. Atmos. Sci.* 52.*22*, pp. 3960–3968.

Emanuel, Kerry A (1997), « Some aspects of hurricane inner-core dynamics and energetics », *in*: *Journal of the Atmospheric Sciences* 54.*8*, pp. 1014–1026.

Emanuel, Kerry A (1999), « Thermodynamic control of hurricane intensity », *in*: *Nature* 401.*6754*, pp. 665–669.

Enagonio, Janice and Michael T Montgomery (2001), « Tropical cyclogenesis via convectively forced vortex Rossby waves in a shallow water primitive equation model », *in*: *J. Atmos. Sci.* 58.*7*, pp. 685–706.

Fierro, Alexandre O et al. (2009), « The impact of horizontal grid spacing on the microphysical and kinematic structures of strong tropical cyclones simulated with the WRF-ARW model », *in*: *Monthly Weather Review* 137.*11*, pp. 3717–3743.

Fisher, Ronald A (1936), « The use of multiple measurements in taxonomic problems », *in*: *Annals of eugenics* 7.*2*, pp. 179–188.

Fore, Alexander G et al. (2018), « SMAP radiometer-only tropical cyclone intensity and size validation », *in*: *IEEE Geoscience and Remote Sensing Letters* 15.*10*, pp. 1480–1484.

Foster, Ralph C (2005), « Why rolls are prevalent in the hurricane boundary layer », *in*: *J. Atmos. Sci.* 62.*8*, pp. 2647–2661.

Frank, William M and Elizabeth A Ritchie (1999), « Effects of environmental flow upon tropical cyclone structure », *in*: *Monthly weather review* 127.*9*, pp. 2044–2061.

— (2001), « Effects of vertical wind shear on the intensity and structure of numerically simulated hurricanes », *in*: *Monthly weather review* 129.*9*, pp. 2249–2269.

Franklin, James L, Michael L Black, and Krystal Valde (2003), « GPS dropwindsonde wind profiles in hurricanes and their operational implications », *in*: *Weather and Forecasting* 18.*1*, pp. 32–44.

Franklin, James L, Stephen J Lord, and Frank D Marks Jr (1988), « Dropwindsonde and radar observations of the eye of Hurricane Gloria (1985) », *in*: *Mon. Wea. Rev.* 116.*5*, pp. 1237–1244.

Friedman, Karen S and Xiaofeng Li (2000), « Monitoring hurricanes over the ocean with wide swath SAR », *in*: *Johns Hopkins APL Technical Digest* 21.*1*, pp. 80–85.

Fu, JY et al. (2020), « Field measurements of Tropical Storm Aere (1619) via airborne GPS-dropsondes over the South China Sea », *in*: *Meteorological Applications* 27.*5*, e1958.

Fu, Lee-Lueng et al. (2019), « 50 years of satellite remote sensing of the ocean », *in*: *Meteorological Monographs* 59, pp. 5–1.

Gaiser, Peter W et al. (2004), « The WindSat spaceborne polarimetric microwave radiometer: Sensor description and early orbit performance », *in*: *IEEE Transactions on Geoscience and Remote Sensing* 42.*11*, pp. 2347–2361.

Gall, Robert et al. (2013), « The hurricane forecast improvement project », *in*: *Bulletin of the American Meteorological Society* 94.*3*, pp. 329–343.

Gamache, John F (1997), « Evaluation of a fully three-dimensional variational Doppler analysis technique », *in*: *Conference on Radar Meteorology, 28 th, Austin, TX*, p. 1997.

Gentry, Megan S and Gary M Lackmann (2010), « Sensitivity of simulated tropical cyclone structure and intensity to horizontal resolution », *in*: *Mon. Wea. Rev.* 138.*3*, pp. 688–704.

Ginis, Isaac (2002), « Tropical cyclone-ocean interactions », *in*: *Advances in Fluid Mechanics* 33, pp. 83–114.

Goni, Gustavo et al. (2009), « Applications of satellite-derived ocean measurements to tropical cyclone intensity forecasting », *in*: *Oceanography* 22.*3*, pp. 190–197.

Gopalakrishnan, Sundararaman G et al. (2011), « The experimental HWRF system: A study on the influence of horizontal resolution on the structure and intensity changes in tropical cyclones using an idealized framework », *in*: *Monthly Weather Review* 139.*6*, pp. 1762–1784.

Gopalakrishnan, Sundararaman G et al. (2012), « Toward improving high-resolution numerical hurricane forecasting: Influence of model horizontal grid resolution, initialization, and physics », *in*: *Weather and Forecasting* 27.*3*, pp. 647–666.

Gray, Willaim M (1979), « Hurricanes: their formation, structure and likely role in the tropical circulation. Meteorology over the tropical oceans », *in*: *Roy. Meteor. Soc.*, pp. 155–218.

Gray, William M (1968), « Global view of the origin of tropical disturbances and storms », *in*: *Monthly Weather Review* 96.*10*, pp. 669–700.

— (1975), « Tropical cyclone genesis », PhD thesis, Colorado State University. Libraries.

Guimond, Stephen R, Gerald M Heymsfield, and F Joseph Turk (2010), « Multiscale observations of Hurricane Dennis (2005): The effects of hot towers on rapid intensification », *in*: *Journal of the atmospheric sciences* 67.*3*, pp. 633–654.

Guinn, Thomas A and Wayne H Schubert (1993), « Hurricane spiral bands », *in*: *J. Atmos. Sci.* 50.*20*, pp. 3380–3403.

Hall, Jonathan D et al. (2013), « High-resolution modeling of Typhoon Morakot (2009): Vortex Rossby waves and their role in extreme precipitation over Taiwan », *in*: *Journal of the atmospheric sciences* 70.*1*, pp. 163–186.

Harr, Patrick A and Jonathan M Dea (2009), « Downstream development associated with the extratropical transition of tropical cyclones over the western North Pacific », *in*: *Monthly weather review* 137.*4*, pp. 1295–1319.

Harr, Patrick A and Russell L Elsberry (2000), « Extratropical transition of tropical cyclones over the western North Pacific. Part I: Evolution of structural characteristics during the transition process », *in*: *Monthly Weather Review* 128.*8*, pp. 2613–2633.

Harr, Patrick A, Russell L Elsberry, and Timothy F Hogan (2000), « Extratropical transition of tropical cyclones over the western North Pacific. Part II: The impact of midlatitude circulation characteristics », *in*: *Monthly Weather Review* 128.*8*, pp. 2634–2653.

Hazelton, Andrew T, Robert E Hart, and Robert F Rogers (2017), « Analyzing simulated convective bursts in two Atlantic hurricanes. Part II: Intensity change due to bursts », *in*: *Monthly Weather Review* 145.*8*, pp. 3095–3117.

Hazelton, Andrew T, Robert Rogers, and Robert E Hart (2015), « Shear-relative asymmetries in tropical cyclone eyewall slope », *in*: *Monthly Weather Review* 143.*3*, pp. 883–903.

Hendricks, Eric A, Michael T Montgomery, and Christopher A Davis (2004), « The role of "vortical" hot towers in the formation of Tropical Cyclone Diana (1984) », *in*: *Journal of the atmospheric sciences* 61.*11*, pp. 1209–1232.

Hendricks, Eric A and Wayne H Schubert (2010), « Adiabatic rearrangement of hollow PV towers », *in*: *Journal of Advances in Modeling Earth Systems* 2.*4*.

Hendricks, Eric A et al. (2009), « Life cycles of hurricane-like vorticity rings », *in*: *Journal of the atmospheric sciences* 66.*3*, pp. 705–722.

Hendricks, Eric A et al. (2014), « Hurricane eyewall evolution in a forced shallow-water model », *in*: *Journal of the Atmospheric Sciences* 71.*5*, pp. 1623–1643.

Hersbach, Hans (2010), « Comparison of C-band scatterometer CMOD5. N equivalent neutral winds with ECMWF », *in*: *Journal of Atmospheric and Oceanic Technology* 27.*4*, pp. 721–736.

Hill, Kevin A, GM Lackmann, and A Aiyyer (2008), « Model simulated changes in maximum TC intensity due to global warming », *in*: *Preprints, 28th Conf. on Hurricanes and Tropical Meteorology, Orlando, FL, Amer. Meteor. Soc. B*, vol. 7.

Holland, Greg J (1980), « An analytic model of the wind and pressure profiles in hurricanes », *in*: *Mon. Wea. Rev.* 108.*8*, pp. 1212–1218.

Holland, Greg J. (1983), « Tropical Cyclone Motion: Environmental Interaction Plus a Beta Effect », *in*: *J. Atmos. Sci.* 40.*2*, `https://doi.org/10.1175/1520-0469(1983)040<0328:TCMEIP>2.0.CO;2`, pp. 328–342.

— (1984), « Tropical Cyclone Motion. A Comparison of Theory and Observation », *in*: *J. Atmos. Sci.* 41.*1*, `https://doi.org/10.1175/1520-0469(1984)041<0068:TCMACO>2.0.CO;2`, pp. 68–75.

Holland, Greg J. (1997), « The Maximum Potential Intensity of Tropical Cyclones », *in*: *J. Atmos. Sci.* 54.*21*, `https://doi.org/10.1175/1520-0469(1997)054<2519:TMPIOT>2.0.CO;2`, pp. 2519–2541.

Holland, Greg J, James I Belanger, and Angela Fritz (2010), « A revised model for radial profiles of hurricane winds », *in*: *Mon. Wea. Rev.* 138.*12*, pp. 4393–4401.

Houze Robert A., Jr. (Feb. 2010), « Clouds in Tropical Cyclones », *in*: *Monthly Weather Review* 138.*2*, pp. 293–344, ISSN: 0027-0644, DOI: `10.1175/2009MWR2989.1`, eprint: `https://journals.ametsoc.org/mwr/article-pdf/138/2/293/4254202/2009mwr2989\_1.pdf`, URL: `https://doi.org/10.1175/2009MWR2989.1`.

Houze, Robert A et al. (2007), « Hurricane intensity and eyewall replacement », *in*: *Science* 315.*5816*, pp. 1235–1239.

Huang, Lanqing et al. (2018), « Tropical cyclone boundary layer rolls in synthetic aperture radar imagery », *in*: *JOURNAL of Geophysical Research: Oceans* 123.*4*, pp. 2981–2996.

Huang, Yi-Hsuan, Michael T Montgomery, and Chun-Chieh Wu (2012), « Concentric eyewall formation in Typhoon Sinlaku (2008). Part II: Axisymmetric dynamical processes », *in*: *Journal of the Atmospheric Sciences* 69.*2*, pp. 662–674.

Jaimes, Benjamin and Lynn K Shay (2009), « Mixed layer cooling in mesoscale oceanic eddies during Hurricanes Katrina and Rita », *in*: *Monthly Weather Review* 137.*12*, pp. 4188–4207.

Jiang, Haiyan (2012), « The relationship between tropical cyclone intensity change and the strength of inner-core convection », *in*: *Monthly Weather Review* 140.*4*, pp. 1164–1176.

Jin, Qingwen et al. (2019), « Using eXtreme Gradient BOOSTing to predict changes in tropical cyclone intensity over the western North Pacific », *in*: *Atmosphere* 10.*6*, p. 341.

Jin, Shaohui, Shuang Wang, and Xiaofeng Li (2014), « Typhoon eye extraction with an automatic SAR image segmentation method », *in*: *International JOURNAL of Remote Sensing* 35.*11-12*, pp. 3978–3993.

Jin, Shaohui et al. (2017), « Tropical Cyclone Center Location in SAR Images Based on Feature Learning and Visual Saliency », *in*: *Hurricane Monitoring With Spaceborne Synthetic Aperture Radar*, Springer, pp. 141–181.

Jones, Sarah C (1995), « The evolution of vortices in vertical shear. I: Initially barotropic vortices », *in*: *Quarterly Journal of the Royal Meteorological Society* 121.*524*, pp. 821–851.

— (2000), « The evolution of vortices in vertical shear. III: Baroclinic vortices », *in*: *Quarterly Journal of the Royal Meteorological Society* 126.*570*, pp. 3161–3185.

Jones, Sarah C et al. (2003), « The extratropical transition of tropical cyclones: Forecast challenges, current understanding, and future directions », *in*: *Weather and Forecasting* 18.*6*, pp. 1052–1092.

Jordan, Charles L (1961), « Marked changes in the characteristics of the eye of intense typhoons between the deepening and filling stages », *in*: *J. Meteor.* 18.*6*, pp. 779–789.

Jorgensen, David P (1984), « Mesoscale and convective-scale characteristics of mature hurricanes. Part II. Inner core structure of Hurricane Allen (1980) », *in*: *Journal of Atmospheric Sciences* 41.*8*, pp. 1287–1311.

Judt, Falko and Shuyi S Chen (2010), « Convectively generated potential vorticity in rainbands and formation of the secondary eyewall in Hurricane Rita of 2005 », *in*: *Journal of Atmospheric Sciences* 67.*11*, pp. 3581–3599.

Judt, Falko, Shuyi S Chen, and Judith Berner (2016), « Predictability of tropical cyclone intensity: scale-dependent forecast error growth in high-resolution stochastic kinetic-energy backscatter ensembles », *in*: *Quarterly JOURNAL of the Royal Meteorological Society* 142.*694*, pp. 43–57.

Jullien, Swen et al. (2012), « Impact of tropical cyclones on the heat budget of the South Pacific Ocean », *in*: *Journal of Physical Oceanography* 42.*11*, pp. 1882–1906.

Jullien, Swen et al. (2014), « Ocean feedback to tropical cyclones: climatology and processes », *in*: *Climate Dyn.* 43.*9-10*, pp. 2831–2854.

Kaplan, John et al. (2015), « Evaluating environmental impacts on tropical cyclone rapid intensification predictability utilizing statistical models », *in*: *Weather and Forecasting* 30.*5*, pp. 1374–1396.

Katsaros, Kristina B et al. (2000), « Wind fields from SAR: Could they improve our understanding of storm dynamics? », *in*: *Johns Hopkins APL Technical Digest* 21.*1*, pp. 86–93.

Katsaros, Kristina B et al. (2002), « Microwave remote sensing of tropical cyclones from space », *in*: *JO* 58.*1*, pp. 137–151.

Kepert, Jeffrey D (2006a), « Observed boundary layer wind structure and balance in the hurricane core. Part I: Hurricane Georges », *in*: *J. Atmos. Sci.* 63.*9*, pp. 2169–2193.

— (2006b), « Observed boundary layer wind structure and balance in the hurricane core. Part II: Hurricane Mitch », *in*: *J. Atmos. Sci.* 63.*9*, pp. 2194–2211.

— (2012), « Choosing a boundary layer parameterization for tropical cyclone modeling », *in*: *Monthly Weather Review* 140.*5*, pp. 1427–1445.

Kieu, Chanh (2015), « Revisiting dissipative heating in tropical cyclone maximum potential intensity », *in*: *Quarterly Journal of the Royal Meteorological Society* 141.*692*, pp. 2497–2504.

Kilroy, Gerard, Roger K Smith, and Michael T Montgomery (2016), « Why do model tropical cyclones grow progressively in size and decay in intensity after reaching maturity? », *in*: *Journal of the Atmospheric Sciences* 73.*2*, pp. 487–503.

— (2017), « A unified view of tropical cyclogenesis and intensification », *in*: *Quarterly Journal of the Royal Meteorological Society* 143.*702*, pp. 450–462.

Klein, Peter M, Patrick A Harr, and Russell L Elsberry (2000), « Extratropical transition of western North Pacific tropical cyclones: An overview and conceptual model of the transformation stage », *in*: *Weather and Forecasting* 15.*4*, pp. 373–395.

Kleinschmidt, Ernst (1951), « Grundlagen einer Theorie der tropischen Zyklonen », *in*: *Archiv für Meteorologie, Geophysik und Bioklimatologie, Serie A* 4.*1*, pp. 53–72.

Klotz, Bradley W and Eric W Uhlhorn (2014), « Improved stepped frequency microwave radiometer tropical cyclone surface winds in heavy precipitation », *in*: *Journal of Atmospheric and Oceanic Technology* 31.*11*, pp. 2392–2408.

Knaff, John A and Charles R Sampson (2009), « Southern hemisphere tropical cyclone intensity forecast methods used at the Joint Typhoon Warning Center, Part II: Statistical–Dynamical forecasts », *in*: *Australian Meteorological and Oceanographic JOURNAL* 58.*1*, p. 9.

Knaff, John A, Charles R Sampson, and Mark DeMaria (2005), « An operational statistical typhoon intensity prediction scheme for the western North Pacific », *in*: *Wea. Forecasting* 20.*4*, pp. 688–699.

Knapp, Kenneth R et al. (2010), « The international best track archive for climate stewardship (IBTrACS) unifying tropical cyclone data », *in*: *Bull. Amer. Meteor. Soc.* 91.*3*, pp. 363–376.

Kossin, James P and Matthew D Eastin (2001), « Two distinct regimes in the kinematic and thermodynamic structure of the hurricane eye and eyewall », *in*: *Journal of the atmospheric sciences* 58.*9*, pp. 1079–1090.

Kossin, James P and Wayne H Schubert (2001), « Mesovortices, polygonal flow patterns, and rapid pressure falls in hurricane-like vortices », *in*: *J. Atmos. Sci.* 58.*15*, pp. 2196–2209.

Kucas, Matthew E (2010), « 9C. 6 Challenges of forecasting tropical cyclone intensity change at the Joint Typhoon Warning Center », *in*.

Kuo, HC et al. (2004), « The formation of concentric vorticity structures in typhoons », *in*: *J. Atmos. Sci.* 61.*22*, pp. 2722–2734.

Kuo, Hung-Chi, RT Williams, and Jen-Her Chen (1999), « A possible mechanism for the eye rotation of Typhoon Herb », *in*: *J. Atmos. Sci.* 56.*11*, pp. 1659–1673.

Kuo, Hung-Chi et al. (2008), « Vortex interactions and barotropic aspects of concentric eyewall formation », *in*: *Mon. Wea. Rev.* 136.*12*, pp. 5183–5198.

Kwon, Young C and William M Frank (2005), « Dynamic instabilities of simulated hurricane-like vortices and their impacts on the core structure of hurricanes. Part I: Dry experiments », *in*: *Journal of the atmospheric sciences* 62.*11*, pp. 3955–3973.

— (2008), « Dynamic instabilities of simulated hurricane-like vortices and their impacts on the core structure of hurricanes. Part II: Moist experiments », *in*: *Journal of the atmospheric sciences* 65.*1*, pp. 106–122.

Lee, Isabella K et al. (2016), « Extracting hurricane eye morphology from spaceborne SAR images using morphological analysis », *in*: *ISPRS JOURNAL of Photogrammetry and Remote Sensing* 117, pp. 115–125.

Lee, Jae-Deok and Chun-Chieh Wu (2018), « The role of polygonal eyewalls in rapid intensification of Typhoon Megi (2010) », *in*: *Journal of Atmospheric Sciences* 75.*12*, pp. 4175–4199.

Lee, Wen-Chau and Michael M Bell (2007), « Rapid intensification, eyewall contraction, and breakdown of Hurricane Charley (2004) near landfall », *in*: *GRL* 34.*2*.

Leipper, Dale F (1967), « Observed ocean conditions and Hurricane Hilda, 1964 », *in*: *J. Atmos. Sci.* 24.*2*, pp. 182–186.

Lengaigne, Matthieu et al. (2019), « Influence of air–sea coupling on Indian Ocean tropical cyclones », *in*: *Climate Dynamics* 52.*1*, pp. 577–598.

Lewis, BM and HF Hawkins (1982), « Polygonal eye walls and rainbands in hurricanes », *in*: *Bull. Amer. Meteor. Soc.* 63.*11*, pp. 1294–1300.

Li, Qingqing and Yuqing Wang (2012), « A comparison of inner and outer spiral rainbands in a numerically simulated tropical cyclone », *in*: *Mon. Wea. Rev.* 140.*9*, pp. 2782–2805.

Li, Tsung-Han and Yuqing Wang (2021), « The role of boundary layer dynamics in tropical cyclone intensification. Part I: Sensitivity to surface drag coefficient », *in*: *Journal of the Meteorological Society of Japan. Ser. II.*

LI, Tsung-Han and Yuqing WANG (2021), « The role of boundary layer dynamics in tropical cyclone intensification. Part II: Sensitivity to initial vortex structure », *in*: *Journal of the Meteorological Society of Japan. Ser. II.*

Li, Xiaofeng et al. (2013), « Tropical cyclone morphology from spaceborne synthetic aperture radar », *in*: *Bull. Amer. Meteor. Soc.* 94.*2*, pp. 215–230.

Li, Yuanlong, Yuqing Wang, and Yanluan Lin (2019), « Revisiting the dynamics of eyewall contraction of tropical cyclones », *in*: *J. Atmos. Sci.* 76.*10*, pp. 3229–3245.

Lin, II et al. (2005), « The interaction of Supertyphoon Maemi (2003) with a warm ocean eddy », *in*: *Monthly Weather Review* 133.*9*, pp. 2635–2649.

Liu, Antony K et al. (2014), « Observations of typhoon eye using SAR and IR sensors », *in*: *International JOURNAL of remote sensing* 35.*11-12*, pp. 3966–3977.

Liu, W Timothy (2002), « Progress in scatterometer application », *in*: *Journal of Oceanography* 58.*1*, pp. 121–136.

Long, DG and C Nie (2017), « Hurricane precipitation observed by SAR », *in*: *Hurricane Monitoring With Spaceborne Synthetic Aperture Radar*, Springer, pp. 1–24.

Macdonald, Norman J (1968), « The evidence for the existence of Rossby-like waves in the hurricane vortex », *in*: *Tellus* 20.*1*, pp. 138–150.

Malkus, J. S. and H. Riehl (1960), « On the Dynamics and Energy Transformations in Steady-State Hurricanes », *in*: *Tellus* 12.*1*, `https://doi.org/10.3402/tellusa.v12i1.9351`, pp. 1–20.

Mallen, Kevin J, Michael T Montgomery, and Bin Wang (2005), « Reexamining the near-core radial structure of the tropical cyclone primary circulation: Implications for vortex resiliency », *in*: *J. Atmos. Sci.* 62.*2*, pp. 408–425.

Marks, Frank D (2003), « State of the science: Radar view of tropical cyclones », *in*: *Radar and Atmospheric Science: A Collection of Essays in Honor of David Atlas*, Springer, pp. 33–74.

Marks, Frank D. et al. (2008), « Structure of the Eye and Eyewall of Hurricane Hugo (1989) », *in*: *Mon. Wea. Rev.* 136.*4*, `https://doi.org/10.1175/2007MWR2073.1`, pp. 1237–1259, DOI: `10.1175/2007MWR2073.1`, eprint: `https://doi.org/10.1175/2007MWR2073.1`.

Marks Jr, Frank D and Robert A Houze Jr (1984), « Airborne doppler radar observations in Hurricane Debby », *in*: *Bulletin of the American Meteorological Society* 65.*6*, pp. 569–582.

McWilliams, James C (1979), « A review of research on mesoscale ocean currents », *in*: *Reviews of Geophysics* 17.*7*, pp. 1548–1558.

McWilliams, James C, Lee P Graves, and Michael T Montgomery (2003), « A formal theory for vortex Rossby waves and vortex evolution », *in*: *Geophysical & Astrophysical Fluid Dynamics* 97.*4*, pp. 275–309.

Meissner, Thomas, Lucrezia Ricciardulli, and Frank J Wentz (2017), « Capability of the SMAP mission to measure ocean surface winds in storms », *in*: *Bulletin of the American Meteorological Society* 98.*8*, pp. 1660–1677.

Meissner, Thomas and Frank J Wentz (2009), « Wind-vector retrievals under rain with passive satellite microwave radiometers », *in*: *IEEE Transactions on Geoscience and Remote Sensing* 47.*9*, pp. 3065–3083.

Melsheimer, Christian, Werner Alpers, and Martin Gade (1998), « Investigation of multifrequency/multipolarization radar signatures of rain cells over the ocean using SIR-C/X-SAR data », *in*: *Journal of Geophysical Research: Oceans* 103.*C9*, pp. 18867–18884.

Menelaou, Konstantinos and MK Yau (2014), « On the role of asymmetric convective bursts to the problem of hurricane intensification: Radiation of vortex Rossby waves and wave–mean flow interactions », *in*: *Journal of the Atmospheric Sciences* 71.*6*, pp. 2057–2077.

Menelaou, Konstantinos, MK Yau, and Yosvany Martinez (2013a), « Impact of asymmetric dynamical processes on the structure and intensity change of two-dimensional hurricane-like annular vortices », *in*: *Journal of the atmospheric sciences* 70.*2*, pp. 559–582.

— (2013b), « On the origin and impact of a polygonal eyewall in the rapid intensification of Hurricane Wilma (2005) », *in*: *Journal of the atmospheric sciences* 70.*12*, pp. 3839–3858.

Menkes, Christophe E et al. (2012), « Comparison of tropical cyclogenesis indices on seasonal to interannual timescales », *in*: *Climate dynamics* 38.*1-2*, pp. 301–321.

Merrill, Robert T (1984a), « A comparison of large and small tropical cyclones », *in*: *Monthly Weather Review* 112.*7*, pp. 1408–1418.

Merrill, RT (1984b), « On the dynamics of tropical cyclone structure changes », *in*: *Quart. J. Roy. Meteor. Soc* 110, pp. 723–745.

Miller, Banner I. (1958), « On the Maximum Intensity of Hurricanes », *in*: *J. Meteor.* 15.*2*, `https://doi.org/10.1175/1520-0469(1958)015<0184:OTMIOH>2.0.CO;2`, pp. 184–195.

Miller, Banner I (1965), *A simple model of the hurricane inflow layer*, US Department of Commerce, Environmental Science Services Administration . . .

Miller, Ronald J et al. (1990), « The Automated Tropical Cyclone Forecasting System (ATCF) », *in*: *Wea. Forecasting* 5.*4*, pp. 653–660.

Molinari, J and D Vollaro (1993), « Environmental controls on eye wall cycles and intensity change in Hurricane Allen (1980) », *in*: *Tropical Cyclone Disasters* 328, p. 337.

Möller, J Dominique and Michael T Montgomery (1999), « Vortex Rossby waves and hurricane intensification in a barotropic model », *in*: *Journal of the atmospheric sciences* 56.*11*, pp. 1674–1687.

Montgomery, Michael T and Janice Enagonio (1998), « Tropical cyclogenesis via convectively forced vortex Rossby waves in a three-dimensional quasigeostrophic model », *in*: *J. Atmos. Sci.* 55.*20*, pp. 3176–3207.

Montgomery, Michael T and Randall J Kallenbach (1997), « A theory for vortex Rossby-waves and its application to spiral bands and intensity changes in hurricanes », *in*: *Quart. J. Roy. Meteor. Soc.* 123.*538*, pp. 435–465.

Montgomery, Michael T, John Persing, and Roger K Smith (2019), « On the hypothesized outflow control of tropical cyclone intensification », *in*: *Quarterly Journal of the Royal Meteorological Society* 145.*721*, pp. 1309–1322.

Montgomery, Michael T and Roger K Smith (2010), *Tropical-cyclone formation: Theory and idealized modelling*, tech. rep., NAVAL POSTGRADUATE SCHOOL MONTEREY CA DEPT OF METEOROLOGY.

— (2014), *Paradigms for tropical cyclone intensification*, tech. rep., NAVAL POSTGRADUATE SCHOOL MONTEREY CA DEPT OF METEOROLOGY.

— (2017), « Recent developments in the fluid dynamics of tropical cyclones », *in*: *Annual Review of Fluid Mechanics* 49, pp. 541–574.

— (2019), « Toward Understanding the Dynamics of Spinup in Emanuel's Tropical Cyclone Model », *in*: *Journal of the Atmospheric Sciences* 76.*10*, pp. 3089–3093.

Montgomery, Michael T, Holly D Snell, and Zongjun Yang (2001), « Axisymmetric spin-down dynamics of hurricane-like vortices », *in*: *Journal of the atmospheric sciences* 58.*5*, pp. 421–435.

Montgomery, Michael T, Zhuo Wang, and Timothy J Dunkerton (2010), « Coarse, intermediate and high resolution numerical simulations of the transition of a tropical wave critical layer to a tropical storm », *in*: *Atmospheric Chemistry and Physics* 10.*22*, pp. 10803–10827.

Montgomery, Michael T et al. (2009), « Do tropical cyclones intensify by WISHE? », *in*: *Quarterly Journal of the Royal Meteorological Society: A journal of the atmospheric sciences, applied meteorology and physical oceanography* 135.*644*, pp. 1697–1714.

Montgomery, Michael T et al. (2012), « The Pre-Depression Investigation of Cloud-Systems in the Tropics (PREDICT) experiment: Scientific basis, new analysis tools, and some first results », *in*: *Bulletin of the American Meteorological Society* 93.*2*, pp. 153–172.

Montgomery, MT et al. (2006), « A vortical hot tower route to tropical cyclogenesis », *in*: *J. Atmos. Sci.* 63.*1*, pp. 355–386.

Montgomery, MT et al. (2010), « The genesis of Typhoon Nuri as observed during the Tropical Cyclone Structure 2008 (TCS-08) field experiment–Part 1: The role of the easterly wave critical layer », *in*: *Atmospheric Chemistry and Physics* 10.*20*, pp. 9879–9900.

Morrison, Ian et al. (2005), « An observational case for the prevalence of roll vortices in the hurricane boundary layer », *in*: *J. Atmos. Sci.* 62.*8*, pp. 2662–2673.

Mouche, Alexis et al. (2019), « Copolarized and Cross-Polarized SAR Measurements for High-Resolution Description of Major Hurricane Wind Structures: Application to Irma Category 5 Hurricane », *in*: *J. Geophys. Res.* 124.*6*, pp. 3905–3922.

Mouche, Alexis A et al. (2017), « Combined co-and cross-polarized SAR measurements under extreme wind conditions », *in*: *IEEE Transactions on Geoscience and Remote Sensing* 55.*12*, pp. 6746–6755.

Muller, Caroline J and David M Romps (2018), « Acceleration of tropical cyclogenesis by self-aggregation feedbacks », *in*: *Proceedings of the National Academy of Sciences* 115.*12*, pp. 2930–2935.

Muramatsu, Teruo (1986), « The structure of polygonal eye of a typhoon », *in*: *J. Meteor. Soc. Japan* 64.*6*, pp. 913–921.

Naylor, Jason and David A Schecter (2014), « Evaluation of the impact of moist convection on the development of asymmetric inner core instabilities in simulated tropical cyclones », *in*: *Journal of Advances in Modeling Earth Systems* 6.*4*, pp. 1027–1048.

Neetu, S et al. (2017), « Global assessment of tropical cyclone intensity statistical–dynamical hindcasts », *in*: *Quart. J. Roy. Meteor. Soc.* 143.*706*, pp. 2143–2156.

Neetu, S et al. (2020), « Quantifying the Benefits of Nonlinear Methods for Global Statistical Hindcasts of Tropical Cyclones Intensity », *in*: *Weather and Forecasting* 35.*3*, pp. 807–820.

Nguyen, Mai C et al. (2011), « Inner-core vacillation cycles during the intensification of Hurricane Katrina », *in*: *Quarterly Journal of the Royal Meteorological Society* 137.*657*, pp. 829–844.

Nolan, D. S., D. P. Stern, and J. A. Zhang (2009b), « Evaluation of planetary boundary layer parameterizations in tropical cyclones by comparison of in situ data and high-resolution simulations of Hurricane Isabel (2003). Part II: Inner core boundary layer and eyewall structure », *in*: *Mon. Wea. Rev.* 137, pp. 3675–3698.

Nolan, David S and Michael G McGauley (2012), « Tropical cyclogenesis in wind shear: Climatological relationships and physical processes », *in*: *Cyclones: Formation, triggers, and control* 1, p. 36.

Nolan, David S and Michael T Montgomery (2002), « Nonhydrostatic, three-dimensional perturbations to balanced, hurricane-like vortices. Part I: Linearized formulation, stability, and evolution », *in*: *J. Atmos. Sci.* 59.*21*, pp. 2989–3020.

Nolan, David S, Eric D Rappin, and Kerry A Emanuel (2007), « Tropical cyclogenesis sensitivity to environmental parameters in radiative–convective equilibrium », *in*:

*Quarterly Journal of the Royal Meteorological Society: A journal of the atmospheric sciences, applied meteorology and physical oceanography* 133.*629*, pp. 2085–2107.

Nolan, David S, Jun A Zhang, and Daniel P Stern (2009), « Evaluation of planetary boundary layer parameterizations in tropical cyclones by comparison of in situ observations and high-resolution simulations of Hurricane Isabel (2003). Part I: Initialization, maximum winds, and the outer-core boundary layer », *in*: *Monthly weather review* 137.*11*, pp. 3651–3674.

Olander, Timothy L and Christopher S Velden (2007), « The advanced Dvorak technique: Continued development of an objective scheme to estimate tropical cyclone intensity using geostationary infrared satellite imagery », *in*: *WF* 22.*2*, pp. 287–298.

Olfateh, Mohammad et al. (2017), « Tropical cyclone wind field asymmetry—Development and evaluation of a new parametric model », *in*: *Journal of Geophysical Research: Oceans* 122.*1*, pp. 458–469.

Ooyama, K. (1964), « A dynamical model for the study of tropical cyclone development. », *in*: *Geofis. Int.* 4, `https://ci.nii.ac.jp/naid/10003556859/en/`, pp. 187–198.

Ooyama, Katsuyuki (1969), « Numerical simulation of the life cycle of tropical cyclones », *in*: *J. Atmos. Sci.* 26.*1*, pp. 3–40.

Palmen, Erik (1948), « On the formation and structure of tropical hurricanes », *in*: *Geophysica* 3.*1*, pp. 26–38.

Park, Jinyoung et al. (2020), « Impact of cloud microphysics schemes on tropical cyclone forecast over the western North Pacific », *in*: *Journal of Geophysical Research: Atmospheres* 125.*18*, e2019JD032288.

Peng, Ke, Richard Rotunno, and George H Bryan (2018), « Evaluation of a time-dependent model for the intensification of tropical cyclones », *in*: *Journal of the Atmospheric Sciences* 75.*6*, pp. 2125–2138.

Peng, Melinda S, Bao-Fong Jeng, and RT Williams (1999), « A numerical study on tropical cyclone intensification. Part I: Beta effect and mean flow effect », *in*: *Journal of the atmospheric sciences* 56.*10*, pp. 1404–1423.

Pianezze, Joris et al. (2018), « A new coupled ocean-waves-atmosphere model designed for tropical storm studies: example of tropical cyclone Bejisa (2013–2014) in the South-West Indian Ocean », *in*: *Journal of Advances in Modeling Earth Systems* 10.*3*, pp. 801–825.

Powell, Mark D, Peter J Vickery, and Timothy A Reinhold (2003), « Reduced drag coefficient for high wind speeds in tropical cyclones », *in*: *Nature* 422.*6929*, p. 279.

Price, James F (1981), « Upper ocean response to a hurricane », *in*: *Journal of Physical Oceanography* 11.*2*, pp. 153–175.

Qiu, Xin, Zhe-Min Tan, and Qingnong Xiao (2010), « The roles of vortex Rossby waves in hurricane secondary eyewall formation », *in*: *Monthly weather review* 138.*6*, pp. 2092–2109.

Quilfen, Yves, Jean Tournadre, and Bertrand Chapron (2006), « Altimeter dual-frequency observations of surface winds, waves, and rain rate in tropical cyclone Isabel », *in*: *Journal of Geophysical Research: Oceans* 111.*C1*.

Raju, PVS, Jayaraman Potty, and UC Mohanty (2011), « Sensitivity of physical parameterizations on prediction of tropical cyclone Nargis over the Bay of Bengal using WRF model », *in*: *Meteorology and Atmospheric Physics* 113.*3*, pp. 125–137.

Rankine, WJM (1882), « A manual of applied physics », *in*: *Charles Griff and Co.: London, UK.*

Rao, DV Bhaskar and Dasari Hari Prasad (2007), « Sensitivity of tropical cyclone intensification to boundary layer and convective processes », *in*: *Natural Hazards* 41.*3*, pp. 429–445.

Rappaport, Edward N (2014), « Fatalities in the United States from Atlantic tropical cyclones: New data and interpretation », *in*: *Bulletin of the American Meteorological Society* 95.*3*, pp. 341–346.

Raymond, David J and Sharon L Sessions (2007), « Evolution of convection during tropical cyclogenesis », *in*: *Geophysical research letters* 34.*6*.

Raymond, DJ (1992), « Nonlinear balance and potential-vorticity thinking at large Rossby number », *in*: *Quarterly Journal of the Royal Meteorological Society* 118.*507*, pp. 987–1015.

Reasor, Paul D, Matthew D Eastin, and John F Gamache (2009), « Rapidly intensifying Hurricane Guillermo (1997). Part I: Low-wavenumber structure and evolution », *in*: *Monthly Weather Review* 137.*2*, pp. 603–631.

Reasor, Paul D and Michael T Montgomery (2001), « Three-dimensional alignment and corotation of weak, TC-like vortices via linear vortex Rossby waves », *in*: *Journal of the atmospheric sciences* 58.*16*, pp. 2306–2330.

— (2015), « Evaluation of a heuristic model for tropical cyclone resilience », *in*: *Journal of the Atmospheric Sciences* 72.*5*, pp. 1765–1782.

Reasor, Paul D, Michael T Montgomery, and Lewis D Grasso (2004), « A new look at the problem of tropical cyclones in vertical shear flow: Vortex resiliency », *in*: *J. Atmos. Sci.* 61.*1*, pp. 3–22.

Reasor, Paul D et al. (2000), « Low-waveNUMBER structure and evolution of the hurricane inner core observed by airborne dual-Doppler radar », *in*: *Mon. Wea. Rev.* 128.*6*, pp. 1653–1680.

Receveur, Aurore et al. (2020), « Seasonal and spatial variability in the vertical distribution of pelagic forage fauna in the Southwest Pacific », *in*: *Deep Sea Research Part II: Topical Studies in Oceanography* 175, p. 104655.

Reul, N. et al. (2017), « A New Generation of Tropical Cyclone Size Measurements from Space », *in*: *Bull. Amer. Meteor. Soc.* 98.*11*, `https://doi.org/10.1175/BAMS-D-15-00291.1`, pp. 2367–2385, DOI: `10.1175/BAMS-D-15-00291.1`.

Reul, Nicolas et al. (2012), « SMOS satellite L-band radiometer: A new capability for ocean surface remote sensing in hurricanes », *in*: *Journal of Geophysical Research: Oceans* 117.*C2*.

Riehl, Herbert (1950), « A model of hurricane formation », *in*: *Journal of Applied physics* 21.*9*, pp. 917–925.

— (1958), « On the heat balance of the equatorial trough zone », *in*: *Geophysica* 6, pp. 503–538.

— (1963), « On the origin and possible modification of hurricanes », *in*: *Science* 141.*3585*, pp. 1001–1010.

Riemer, M, MT Montgomery, and ME Nicholls (2013), « Further examination of the thermodynamic modification of the inflow layer of tropical cyclones by vertical wind shear », *in*: *Atmospheric Chemistry and Physics* 13.*1*, pp. 327–346.

Riemer, Michael, Michael T Montgomery, and Melville E Nicholls (2010), « A new paradigm for intensity modification of tropical cyclones: Thermodynamic impact of vertical wind shear on the inflow layer », *in*: *Atmospheric Chemistry and Physics* 10.*7*, pp. 3163–3188.

Rogers, Robert et al. (2006), « The Intensity Forecasting Experiment: A NOAA multiyear field program for improving tropical cyclone intensity forecasts », *in*: *Bulletin of the American Meteorological Society* 87.*11*, pp. 1523–1538.

Rotunno, R et al. (2009), « Large-eddy simulation of an idealized tropical cyclone », *in*: *Bulletin of the American Meteorological Society* 90.*12*, pp. 1783–1788.

Rozoff, Christopher M et al. (2006), « Rapid filamentation zones in intense tropical cyclones », *in*: *Journal of the atmospheric sciences* 63.*1*, pp. 325–340.

Rozoff, Christopher M et al. (2012), « The roles of an expanding wind field and inertial stability in tropical cyclone secondary eyewall formation », *in*: *J. Atmos. Sci.* 69.*9*, pp. 2621–2643.

Ruf, Christopher S, Scott Gleason, and Darren S McKague (2018), « Assessment of CYGNSS wind speed retrieval uncertainty », *in*: *IEEE Journal of Selected Topics in Applied Earth Observations and Remote Sensing* 12.*1*, pp. 87–97.

Ruf, Christopher S et al. (2012), « The CYGNSS nanosatellite constellation hurricane mission », *in*: *2012 IEEE International Geoscience and Remote Sensing Symposium*, IEEE, pp. 214–216.

Ruf, Christopher S et al. (2018), « A new paradigm in earth environmental monitoring with the cygnss small satellite constellation », *in*: *Scientific reports* 8.*1*, pp. 1–13.

Ruiz-Salcines, Pablo et al. (2019), « On the Use of Parametric Wind Models for Wind Wave Modeling under Tropical Cyclones », *in*: *Water* 11.*10*, p. 2044.

Samson, Guillaume et al. (2014), « The NOW regional coupled model: Application to the tropical Indian Ocean climate and tropical cyclone activity », *in*: *Journal of Advances in Modeling Earth Systems* 6.*3*, pp. 700–722.

Schecter, David A (2015), « Response of a simulated hurricane to misalignment forcing compared to the predictions of a simple theory », *in*: *Journal of the Atmospheric Sciences* 72.*3*, pp. 1235–1260.

Schecter, David A and Michael T Montgomery (2003), « On the symmetrization rate of an intense geophysical vortex », *in*: *Dynamics of atmospheres and oceans* 37.*1*, pp. 55–88.

— (2007), « Waves in a cloudy vortex », *in*: *Journal of the atmospheric sciences* 64.*2*, pp. 314–337.

Schecter, David A, Michael T Montgomery, and Paul D Reasor (2002), « A theory for the vertical alignment of a quasigeostrophic vortex », *in*: *Journal of the atmospheric sciences* 59.*2*, pp. 150–168.

Schloemer, Robert W (1954), *Analysis and synthesis of hurricane wind patterns over Lake Okeechobee, Florida*, 31, US Department of Commerce, Weather Bureau.

Schubert, Wayne H and James J Hack (1982), « Inertial stability and tropical cyclone development », *in*: *J. Atmos. Sci.* 39.*8*, pp. 1687–1697.

Schubert, Wayne H et al. (1999), « Polygonal eyewalls, asymmetric eye contraction, and potential vorticity mixing in hurricanes », *in*: *J. Atmos. Sci.* 56.*9*, pp. 1197–1223.

Schwendike, Juliane and Jeffrey D Kepert (2008), « The boundary layer winds in Hurricanes Danielle (1998) and Isabel (2003) », *in*: *Mon. Wea. Rev.* 136.*8*, pp. 3168–3192.

Scoccimarro, Enrico et al. (2011), « Effects of tropical cyclones on ocean heat transport in a high-resolution coupled general circulation model », *in*: *Journal of Climate* 24.*16*, pp. 4368–4384.

Shapiro, Lloyd J (1983), « The asymmetric boundary layer flow under a translating hurricane », *in*: *Journal of Atmospheric Sciences* 40.*8*, pp. 1984–1998.

— (2000), « Potential vorticity asymmetries and tropical cyclone evolution in a moist three-layer model », *in*: *J. Atmos. Sci.* 57.*21*, pp. 3645–3662.

Shapiro, Lloyd J and Huch E Willoughby (1982), « The response of balanced hurricanes to local sources of heat and momentum », *in*: *J. Atmos. Sci.* 39.*2*, pp. 378–394.

Shay, Lynn K, Russell L Elsberry, and Peter G Black (1989), « Vertical structure of the ocean current response to a hurricane », *in*: *Journal of physical oceanography* 19.*5*, pp. 649–669.

Shay, Lynn K, Gustavo J Goni, and Peter G Black (2000), « Effects of a warm oceanic feature on Hurricane Opal », *in*: *Monthly Weather Review* 128.*5*, pp. 1366–1383.

Shea, Dennis J and William M Gray (1973), « The hurricane's inner core region. I. Symmetric and asymmetric structure », *in*: *J. Atmos. Sci.* 30.*8*, pp. 1544–1564.

Shepherd, William G. (1928), « Beating the hurricane », *in*: *Collier's*.

Skamarock, William C (2004), « Evaluating mesoscale NWP models using kinetic energy spectra », *in*: *Monthly weather review* 132.*12*, pp. 3019–3032.

Skamarock, William C and Joseph B Klemp (2008), « A time-split nonhydrostatic atmospheric model for weather research and forecasting applications », *in*: *Journal of computational physics* 227.*7*, pp. 3465–3485.

Small, David (2011), « Flattening gamma: Radiometric terrain correction for SAR imagery », *in*: *IEEE Transactions on Geoscience and Remote Sensing* 49.*8*, pp. 3081–3093.

Smith, Gerald B and Michael T Montgomery (1995), « Vortex axisymmetrization: Dependence on azimuthal wave-number or asymmetric radial structure changes », *in*: *Quarterly Journal of the Royal Meteorological Society* 121.*527*, pp. 1615–1650.

Smith, Roger K (1968), « The surface boundary layer of a hurricane », *in*: *Tellus* 20.*3*, pp. 473–484.

Smith, Roger K (2003), « A simple model of the hurricane boundary layer », *in*: *Quarterly Journal of the Royal Meteorological Society: A journal of the atmospheric sciences, applied meteorology and physical oceanography* 129.*589*, pp. 1007–1027.

Smith, Roger K, Gerard Kilroy, and MT Montgomery (2021), « Tropical cyclone life cycle in a three-dimensional numerical simulation », *in*: *Quarterly Journal of the Royal Meteorological Society* 147.*739*, pp. 3373–3393.

Smith, Roger K and Michael T Montgomery (2008), « Balanced boundary layers used in hurricane models », *in*: *Quarterly Journal of the Royal Meteorological Society* 134.*635*, pp. 1385–1395.

— (2012), « Observations of the convective environment in developing and non-developing tropical disturbances », *in*: *Quarterly Journal of the Royal Meteorological Society* 138.*668*, pp. 1721–1739.

Smith, Roger K, Michael T Montgomery, and Scott A Braun (2019), « Azimuthally averaged structure of Hurricane Edouard (2014) just after peak intensity », *in*: *Quarterly Journal of the Royal Meteorological Society* 145.*718*, pp. 211–216.

Smith, Roger K, Michael T Montgomery, and Nguyen Van Sang (2009), « Tropical cyclone spin-up revisited », *in*: *Quart. J. Roy. Meteor. Soc.* 135.*642*, pp. 1321–1335.

Smith, Roger K, Michael T Montgomery, and Stefanie Vogl (2008), « A critique of Emanuel's hurricane model and potential intensity theory », *in*: *Quart. J. Roy. Meteor. Soc.* 134.*632*, pp. 551–561.

Smith, Roger K and Gerald L Thomsen (2010), « Dependence of tropical-cyclone intensification on the boundary-layer representation in a numerical model », *in*: *Quarterly Journal of the Royal Meteorological Society* 136.*652*, pp. 1671–1685.

Smith, Roger K, Wolfgang Ulrich, and Graeme Sneddon (2000), « On the dynamics of hurricane-like vortices in vertical-shear flows », *in*: *Quarterly Journal of the Royal Meteorological Society* 126.*569*, pp. 2653–2670.

Smith, Roger K and Stefanie Vogl (2008), « A simple model of the hurricane boundary layer revisited », *in*: *Quarterly Journal of the Royal Meteorological Society: A journal of the atmospheric sciences, applied meteorology and physical oceanography* 134.*631*, pp. 337–351.

Smith, Stuart D et al. (1992), « Sea surface wind stress and drag coefficients: The HEXOS results », *in*: *Boundary-Layer Meteorology* 60.*1-2*, pp. 109–142.

Soisuvarn, Seubson et al. (2008), « Validation of NOAA's near real-time ASCAT ocean vector winds », *in*: *IGARSS 2008-2008 IEEE International Geoscience and Remote Sensing Symposium*, vol. 1, IEEE, pp. I–118.

Srinivas, CV et al. (2013), « Tropical cyclone predictions over the Bay of Bengal using the high-resolution Advanced Research Weather Research and Forecasting (ARW) model », *in*: *Quarterly Journal of the Royal Meteorological Society* 139.*676*, pp. 1810–1825.

Steranka, Joseph, Edward B Rodgers, and R Cecil Gentry (1986), « The relationship between satellite measured convective bursts and tropical cyclone intensification », *in*: *Monthly weather review* 114.*8*, pp. 1539–1546.

Stern, Daniel P and David S Nolan (2011), « On the vertical decay rate of the maximum tangential winds in tropical cyclones », *in*: *J. Atmos. Sci.* 68.*9*, pp. 2073–2094.

Stern, Daniel P and Fuqing Zhang (2013), « How does the eye warm? Part I: A potential temperature budget analysis of an idealized tropical cyclone », *in*: *J. Atmos. Sci.* 70.*1*, pp. 73–90.

Stern, Daniel P et al. (2015), « Revisiting the relationship between eyewall contraction and intensification », *in*: *J. Atmos. Sci.* 72.*4*, pp. 1283–1306.

Stith, Jeffrey L et al. (2018), « 100 years of progress in atmospheric observing systems », *in*: *Meteorological Monographs* 59, pp. 2–1.

Su, Hui et al. (2020), « Applying satellite observations of tropical cyclone internal structures to rapid intensification forecast with machine learning », *in*: *Geophysical Research Letters* 47.*17*, e2020GL089102.

Sugi, Masato, Akira Noda, and Nobuo Sato (2002), « Influence of the global warming on tropical cyclone climatology: An experiment with the JMA global model », *in*: *Journal of the Meteorological Society of Japan. Ser. II* 80.*2*, pp. 249–272.

Sumner, Howard C (1943), « North Atlantic hurricanes and tropical disturbances of 1943 », *in*: *Monthly Weather Review* 71.*11*, pp. 179–183.

Tang, Brian and Kerry Emanuel (2010), « Midlevel ventilation's constraint on tropical cyclone intensity », *in*: *Journal of the Atmospheric Sciences* 67.*6*, pp. 1817–1830.

Terwey, Wesley D and Michael T Montgomery (2008), « Secondary eyewall formation in two idealized, full-physics modeled hurricanes », *in*: *Journal of Geophysical Research: Atmospheres* 113.*D12*.

Thomsen, Gerald L, Roger K Smith, and Michael T Montgomery (2015), « Tropical cyclone flow asymmetries induced by a uniform flow revisited », *in*: *Journal of Advances in Modeling Earth Systems* 7.*3*, pp. 1265–1284.

Tippett, Michael K, Suzana J Camargo, and Adam H Sobel (2011), « A Poisson regression index for tropical cyclone genesis and the role of large-scale vorticity in genesis », *in*: *Journal of Climate* 24.*9*, pp. 2335–2357.

Uhlhorn, Eric W et al. (2007), « Hurricane surface wind measurements from an operational stepped frequency microwave radiometer », *in*: *Monthly Weather Review* 135.*9*, pp. 3070–3085.

Uhlhorn, Eric W et al. (2014), « Observed hurricane wind speed asymmetries and relationships to motion and environmental shear », *in*: *Mon. Wea. Rev.* 142.*3*, pp. 1290–1311.

Vachon, Paris W and John Wolfe (2010), « C-band cross-polarization wind speed retrieval », *in*: *IEEE Geoscience and Remote Sensing Letters* 8.*3*, pp. 456–459.

Van Sang, Nguyen, Roger K Smith, and Michael T Montgomery (2008), « Tropical-cyclone intensification and predictability in three dimensions », *in*: *Quart. J. Roy. Meteor. Soc.* 134.*632*, pp. 563–582.

Velden, Christopher S and Derrick Herndon (2020), « A consensus approach for estimating tropical cyclone intensity from meteorological satellites: SATCON », *in*: *Weather and Forecasting* 35.*4*, pp. 1645–1662.

Vickery, Peter J et al. (2000), « Hurricane wind field model for use in hurricane simulations », *in*: *Journal of Structural Engineering* 126.*10*, pp. 1203–1221.

Vickery, Peter J et al. (2009), « Hurricane hazard modeling: The past, present, and future », *in*: *Journal of Wind Engineering and Industrial Aerodynamics* 97.*7-8*, pp. 392–405.

Vigh, Jonathan L and Wayne H Schubert (2009), « Rapid development of the tropical cyclone warm core », *in*: *J. Atmos. Sci.* 66.*11*, pp. 3335–3350.

Vincent, Emmanuel M et al. (2012), « Processes setting the characteristics of sea surface cooling induced by tropical cyclones », *in*: *Journal of Geophysical Research: Oceans* 117.*C2*.

Vinour, Léo et al. (2021), « Observations of Tropical Cyclone Inner-Core Fine-Scale Structure, and Its Link to Intensity Variations », *in*: *Journal of the Atmospheric Sciences* 78.*11*, pp. 3651–3671.

Vukicevic, Tomislava et al. (2014), « A novel multiscale intensity metric for evaluation of tropical cyclone intensity forecasts », *in*: *Journal of the Atmospheric Sciences* 71.*4*, pp. 1292–1304.

Wada, Akiyoshi (2009), « Idealized numerical experiments associated with the intensity and rapid intensification of stationary tropical-cyclone-like vortex and its relation to initial sea-surface temperature and vortex-induced sea-surface cooling », *in*: *J. Geophys. Res.* 114.*D18*.

Wadler, Joshua B, Robert F Rogers, and Paul D Reasor (2018), « The relationship between spatial variations in the structure of convective bursts and tropical cyclone intensification as determined by airborne Doppler radar », *in*: *Monthly Weather Review* 146.*3*, pp. 761–780.

Wang, Hui, Yuqing Wang, and Haiming Xu (2013), « Improving simulation of a tropical cyclone using dynamical initialization and large-scale spectral nudging: A case study of Typhoon Megi (2010) », *in*: *Acta Meteorologica Sinica* 27.*4*, pp. 455–475.

Wang, Hui et al. (2019), « The axisymmetric and asymmetric aspects of the secondary eyewall formation in a numerically simulated tropical cyclone under idealized conditions on an f plane », *in*: *Journal of the Atmospheric Sciences* 76.*1*, pp. 357–378.

Wang, Y and C-C Wu (2004), « Current understanding of tropical cyclone structure and intensity changes–a review », *in*: *Meteor. Atmos. Phys.* 87.*4*, pp. 257–278.

Wang, Yi-Fan and Zhe-Min Tan (2020), « Outer Rainbands–Driven Secondary Eyewall Formation of Tropical Cyclones », *in*: *Journal of the Atmospheric Sciences* 77.*6*, pp. 2217–2236.

Wang, Yuqing (2001), « An explicit simulation of tropical cyclones with a triply nested movable mesh primitive equation model: TCM3. Part I: Model description and control experiment », *in*: *Mon. Wea. Rev.* 129.*6*, pp. 1370–1394.

— (2002a), « Vortex Rossby waves in a numerically simulated tropical cyclone. Part I: Overall structure, potential vorticity, and kinetic energy budgets », *in*: *J. Atmos. Sci.* 59.*7*, pp. 1213–1238.

— (2002b), « Vortex Rossby waves in a numerically simulated tropical cyclone. Part II: The role in tropical cyclone structure and intensity changes », *in*: *J. Atmos. Sci.* 59.*7*, pp. 1239–1262.

— (2008), « Rapid filamentation zone in a numerically simulated tropical cyclone », *in*: *J. Atmos. Sci.* 65.*4*, pp. 1158–1181.

Wang, Yuqing (2009), « How do outer spiral rainbands affect tropical cyclone structure and intensity? », *in*: *Journal of the Atmospheric Sciences* 66.*5*, pp. 1250–1273.

Wang, Yuqing and Greg J Holland (1996), « Tropical cyclone motion and evolution in vertical shear », *in*: *J. Atmos. Sci.* 53.*22*, pp. 3313–3332.

Wang, Zhuo and Isaac Hankes (2016), « Moisture and precipitation evolution during tropical cyclone formation as revealed by the SSM/I–SSMIS retrievals », *in*: *Journal of the Atmospheric Sciences* 73.*7*, pp. 2773–2781.

Wang, Zhuo, MT Montgomery, and TJ Dunkerton (2010a), « Genesis of pre–Hurricane Felix (2007). Part I: The role of the easterly wave critical layer », *in*: *Journal of the atmospheric sciences* 67.*6*, pp. 1711–1729.

— (2010b), « Genesis of pre–Hurricane Felix (2007). Part II: Warm core formation, precipitation evolution, and predictability », *in*: *Journal of the atmospheric sciences* 67.*6*, pp. 1730–1744.

Weatherford, Candis L and William M Gray (1988a), « Typhoon structure as revealed by aircraft reconnaissance. Part I: Data analysis and climatology », *in*: *Mon. Wea. Rev.* 116.*5*, pp. 1032–1043.

— (1988b), « Typhoon structure as revealed by aircraft reconnaissance. Part II: Structural variability », *in*: *Monthly Weather Review* 116.*5*, pp. 1044–1056.

Williams, Brent A and David G Long (2011), « A reconstruction approach to scatterometer wind vector field retrieval », *in*: *IEEE transactions on geoscience and remote sensing* 49.*6*, pp. 1850–1864.

Willoughby, HE (1990), « Temporal changes of the primary circulation in tropical cyclones », *in*: *J. Atmos. Sci.* 47.*2*, pp. 242–264.

— (1998), « Tropical cyclone eye thermodynamics », *in*: *Mon. Wea. Rev.* 126.*12*, pp. 3053–3067.

Willoughby, HE, JA Clos, and MG Shoreibah (1982), « Concentric eye walls, secondary wind maxima, and the evolution of the hurricane vortex », *in*: *J. Atmos. Sci.* 39.*2*, pp. 395–411.

Willoughby, HE, RWR Darling, and ME Rahn (2006), « Parametric representation of the primary hurricane vortex. Part II: A new family of sectionally continuous profiles », *in*: *Mon. Wea. Rev.* 134.*4*, pp. 1102–1120.

Willoughby, HE and ME Rahn (2004), « Parametric representation of the primary hurricane vortex. Part I: Observations and evaluation of the Holland (1980) model », *in*: *Mon. Wea. Rev.* 132.*12*, pp. 3033–3048.

Wing, Allison A, Suzana J Camargo, and Adam H Sobel (2016), « Role of radiative–convective feedbacks in spontaneous tropical cyclogenesis in idealized numerical simulations », *in*: *Journal of the Atmospheric Sciences* 73.*7*, pp. 2633–2642.

Wu, Chun-Chieh, Chia-Ying Lee, and II Lin (2007), « The effect of the ocean eddy on tropical cyclone intensity », *in*: *Journal of the Atmospheric Sciences* 64.*10*, pp. 3562–3578.

Wu, Chun-Chieh et al. (2009), « A numerical investigation of the eyewall evolution in a landfalling typhoon », *in*: *Monthly weather review* 137.*1*, pp. 21–40.

Wu, Chun-Chieh et al. (2016), « The role of convective heating in tropical cyclone eyewall ring evolution », *in*: *Journal of the Atmospheric Sciences* 73.*1*, pp. 319–330.

Wu, Liguang, Qingyuan Liu, and Yubin Li (2018), « Prevalence of tornado-scale vortices in the tropical cyclone eyewall », *in*: *Proceedings of the National Academy of Sciences* 115.*33*, pp. 8307–8310.

Xu, Jing and Yuqing Wang (2010a), « Sensitivity of the simulated tropical cyclone inner-core size to the initial vortex size », *in*: *Monthly Weather Review* 138.*11*, pp. 4135–4157.

— (2010b), « Sensitivity of tropical cyclone inner-core size and intensity to the radial distribution of surface entropy flux », *in*: *Journal of the atmospheric sciences* 67.*6*, pp. 1831–1852.

— (2018), « Dependence of tropical cyclone intensification rate on sea surface temperature, storm intensity, and size in the western North Pacific », *in*: *Weather and Forecasting* 33.*2*, pp. 523–537.

Yang, Bo, Yuqing Wang, and Bin Wang (2007), « The effect of internally generated inner-core asymmetries on tropical cyclone potential intensity », *in*: *Journal of the atmospheric sciences* 64.*4*, pp. 1165–1188.

Yang, Xiaofeng et al. (2011), « Comparison of ocean surface winds from ENVISAT ASAR, MetOp ASCAT scatterometer, buoy measurements, and NOGAPS model », *in*: *IEEE Transactions on Geoscience and Remote Sensing* 49.*12*, pp. 4743–4750.

Yang, Xiaofeng et al. (2017), « Tropical Cyclone Wind Field Reconstruction from SAR and Analytical Model », *in*: *Hurricane Monitoring With Spaceborne Synthetic Aperture Radar*, Springer, pp. 69–84.

Yau, MK et al. (2004), « A multiscale numerical study of Hurricane Andrew (1992). Part VI: Small-scale inner-core structures and wind streaks », *in*: *Monthly weather review* 132.*6*, pp. 1410–1433.

Zabolotskikh, Elizaveta V, Leonid M Mitnik, and Bertrand Chapron (2013), « New approach for severe marine weather study using satellite passive microwave sensing », *in*: *Geophysical Research Letters* 40.*13*, pp. 3347–3350.

Zabolotskikh, Elizaveta V, Nicolas Reul, and Bertrand Chapron (2015), « Geophysical model function for the AMSR2 C-band wind excess emissivity at high winds », *in*: *IEEE Geoscience and Remote Sensing Letters* 13.*1*, pp. 78–81.

Zhang, Biao and William Perrie (2012), « Cross-polarized synthetic aperture radar: A new potential measurement technique for hurricanes », *in*: *Bulletin of the American Meteorological Society* 93.*4*, pp. 531–541.

— (2017), « High Wind Speed Retrieval from Multi-polarization SAR », *in*: *Hurricane Monitoring With Spaceborne Synthetic Aperture Radar*, Springer, pp. 85–98.

Zhang, Fuqing and Dandan Tao (2013), « Effects of vertical wind shear on the predictability of tropical cyclones », *in*: *Journal of the Atmospheric Sciences* 70.*3*, pp. 975–983.

Zhang, Guosheng, Xiaofeng Li, and William Perrie (2017), « Synthetic Aperture Radar Observations of Extreme Hurricane Wind and Rain », *in*: *Hurricane Monitoring With Spaceborne Synthetic Aperture Radar*, Springer, pp. 299–346.

Zhang, Guosheng et al. (2016), « A hurricane morphology and sea surface wind vector estimation model based on C-band cross-polarization SAR imagery », *in*: *IEEE Transactions on Geoscience and Remote Sensing* 55.*3*, pp. 1743–1751.

Zhang, Jun A and Xiaofeng Li (2017), « Tropical cyclone multiscale wind features from spaceborne synthetic aperture radar », *in*: *Hurricane monitoring with spaceborne synthetic aperture radar*, Springer, pp. 25–39.

Zhang, Jun A et al. (2011), « On the characteristic height scales of the hurricane boundary layer », *in*: *Mon. Wea. Rev.* 139.*8*, pp. 2523–2535.

Zhang, Jun A et al. (2015), « Evaluating the impact of improvements in the boundary layer parameterization on hurricane intensity and structure forecasts in HWRF », *in*: *Monthly Weather Review* 143.*8*, pp. 3136–3155.

Zheng, Gang et al. (2015), « Comparison of typhoon centers from SAR and IR images and those from best track data sets », *in*: *IEEE Transactions on Geoscience and Remote Sensing* 54.*2*, pp. 1000–1012.

Zheng, Gang et al. (2017), « Observing Typhoons from Satellite-Derived Images », *in*: *Hurricane Monitoring With Spaceborne Synthetic Aperture Radar*, Springer, pp. 183–214.

Zheng, Yan et al. (2020), « Simulation of Extreme Updrafts in the Tropical Cyclone Eyewall », *in*: *Advances in Atmospheric Sciences* 37, pp. 781–792.

Zhong, Wei, Da-Lin Zhang, and Han-Cheng Lu (2009), « A theory for mixed vortex Rossby–gravity waves in tropical cyclones », *in*: *J. Atmos. Sci.* 66.*11*, pp. 3366–3381.

Zhu, Ping (2008), « Simulation and parameterization of the turbulent transport in the hurricane boundary layer by large eddies », *in*: *Journal of Geophysical Research: Atmospheres* 113.*D17*.

Zhu, Tong and Da-Lin Zhang (2006), « Numerical simulation of Hurricane Bonnie (1998). Part II: Sensitivity to varying cloud microphysical processes », *in*: *Journal of the Atmospheric Sciences* 63.*1*, pp. 109–126.

DOCTORAT BRETAGNE LOIRE
SCIENCES DE LA MER ET DU LITTORAL

UBO
Université de Bretagne Occidentale

**Titre :** Liens entre structure interne et variations d'intensité des cyclones tropicaux : apports combinés des observations SAR et des simulations numériques à haute résolution

**Mot clés :** Cyclones tropicaux ; Observations satellite ; Modélisation numérique ; Classification

**Résumé :** La dynamique interne des cyclones tropicaux joue un rôle fondamental dans leur intensification et leur réponse aux perturbations externes. Bien que principalement symétrique à l'échelle du vortex, cette dynamique est aussi fortement régie par des processus asymétriques. Ces processus sont toutefois difficiles à observer car proches de la surface et de la zone de vents maximum, et multi-échelles. Cette thèse analyse conjointement images SAR et sorties de modèles dynamiques régionaux à résolution kilométrique afin d'estimer des paramètres internes du champ de vent de surface, et de relier ces paramètres à la théorie asymétrique des variations d'intensité des cyclones. L'analyse des images SAR permet d'observer la structure interne instantanée et de la relier à l'intensité (et à ses variations) à cet instant, à travers l'utilisation de données de best-track. Des propriétés telles que la contraction du vortex et sa symétrie accrue avec l'intensité et durant les phases de ré-intensification sont ainsi observées. Le modèle permet lui de diagnostiquer les variations temporelles de la structure interne, reliant ainsi statistiquement la symétrisation ou la perturbation du champ de vent de surface aux variations d'intensité du cyclone, en cohérence avec les récentes théories sur les processus de restauration d'intensité. Dans une perspective d'amélioration de la prédictabilité de l'intensité des cyclones, une méthode originale de machine learning permet de mettre en valeur l'impact positif de l'inclusion de la haute résolution (en particulier quantifiant le mixage entre l'oeil et le mur de l'oeil et l'asymétrie de la distribution des vents maximum) sur la prédiction statistique des taux d'intensification.

**Title:** Tropical cyclones internal structure and intensity variations: insights from high-resolution observations and modeling

**Keywords:** Tropical cyclones ; Satellite observations ; Numerical analysis / modeling ; Classification

**Abstract:** Tropical cyclones (TCs) internal dynamics play a fundamental role in their intensification and their response to external perturbations. Although mainly symmetric on a vortex scale, these dynamics are also strongly controlled by asymmetric processes. These processes are however difficult to observe, as they are multi-scale and occur mainly in the atmospheric boundary layer and the eyewall where strongest winds are located. This thesis jointly analyses SAR images and regional dynamical model outputs with a kilometric resolution, in order to estimate internal parameters of the surface wind field and relate them to the asymmetric theory of TC intensity variations. The analysis of SAR images allows to observe the internal structure at the time of acquisition and to relate it to ongoing intensity changes through the use of best-track data. Properties such as vortex contraction and increased symmetry with intensity and during re-intensification phases are observed this way. The model is used in turn to study the evolution in time of the internal structure, and relate statistically the symmetrization or perturbation of the surface wind field to corresponding intensity variations, denoting an agreement with recent theory on intensification and intensity restoration processes. In a perspective of predictability improvement, an original machine learning method shows the capacity of high-resolution internal structure measurements (notably, parameters quantifying the eye-eyewall mixing and the maximum wind ring asymmetry) to improve the statistical prediction of intensification rates.